Neutron-Capture Nucleosynthesis and the Chemical Evolution of Globular Clusters

Luke Jeremy Shingles

A thesis submitted for the degree of

Doctor of Philosophy

of the Australian National University

Australian National University

NATURAM PRIMUM COGNOSCERE RERUM

Research School of Astronomy & Astrophysics

Disclaimer

I hereby declare that, except where acknowledged appropriately either below or in the text, this thesis is my original work undertaken at the Australian National University between February 2012 and August 2015. It has not been submitted for a higher degree at any other university or institution.

This thesis has been submitted as a 'Thesis by Compilation' in accordance with the relevant ANU policies. Each of the three main chapters (2, 3, and 4) is therefore a completely self-contained article that has been published in a peer-reviewed journal.

Chapter 2 has been published in Monthly Notices of the Royal Astronomical Society as Shingles & Karakas (2013). This article includes some results that were previously included in the candidate's Honours thesis in 2011. In 2012, the candidate calculated new nucleosynthesis models to study the impact of the ^{13}C and ^{22}Ne neutron sources and developed the text and figures for publication. Amanda Karakas guided the scientific content of the paper and contributed some sections of text in the Discussion and Conclusions section.

Chapter 3 has been published in Astrophysical Journal as Shingles, Karakas, Hirschi, Fishlock, Yong, Da Costa, & Marino (2014). The main scientific insights, analysis, figures, and the manuscript were the produced by the candidate with minor revisions in response to feedback from coauthors and the referee. The chemical evolution code used in this project was developed solely by the candidate. The chemical evolution model incorporated tables of yields for massive stars provided by Raphael Hirschi and yields for AGB stars provided by Cherie Fishlock. Machine-readable abundance measurements for M4 and M5 were provided by David Yong.

Chapter 4 has been published in Monthly Notices of the Royal Astronomical Society as Shingles, Doherty, Karakas, Stancliffe, Lattanzio, & Lugaro (2015). All evolution and nucleosynthesis models were calculated by the candidate except for the 6 $M_\odot$, $Y = 0.40$ nucleosynthesis model, which was calculated by Carolyn Doherty. The figures and all sections of the text were drafted by the candidate and revised with suggestions from coauthors and the referee.

The remainder of this thesis was drafted solely by the candidate and revised in response to comments by Amanda Karakas.

Luke Jeremy Shingles
30th July 2015

Supplementary Research

In addition to the work presented in this thesis, the candidate has contributed to several other research projects during the PhD program. A complete list of peer-reviewed journal articles authored or co-authored by the candidate during the 3.5 year program are listed here in reverse chronological order:

"Evolution and nucleosynthesis of helium-rich asymptotic giant branch models"
Luke J. Shingles, Carolyn L. Doherty, Amanda I. Karakas, Richard J. Stancliffe, John C. Lattanzio, Maria Lugaro, 2015, MNRAS, 452, 2804

"Iron and s-element abundance variations in NGC 5286: comparison with 'anomalous' globular clusters and Milky Way satellites"
A. F. Marino, A. P. Milone, A. I. Karakas, L. Casagrande, D. Yong, L. Shingles, G. Da Costa, J. Norris, P. B. Stetson, K. Lind, M. Asplund, R. Collet, H. Jerjen, L. Sbordone, A. Aparicio, & S. Cassisi, 2015, MNRAS, 450, 815

"The s-process enrichment of the globular clusters M4 and M22"
Luke J. Shingles, Amanda I. Karakas, Raphael Hirschi, Cherie K. Fishlock, David Yong, Gary S. Da Costa, & Anna F. Marino, 2014, ApJ, 795, 34

"Iron and neutron-capture element abundance variations in the globular cluster M2 (NGC 7089)"
David Yong, Ian U. Roederer, Frank Grundahl, Gary S. Da Costa, Amanda I. Karakas, John E. Norris, Wako Aoki, Cherie K. Fishlock, A. F. Marino, A. P. Milone, & Luke J. Shingles, 2014, MNRAS, 441, 3396

"Augmented reality in astrophysics"
Frédéric Vogt & Luke J. Shingles, 2013, Ap&SS, 347, 47

"Is the sulphur anomaly in planetary nebulae caused by the s-process?"
Luke J. Shingles & Amanda I. Karakas, 2013, MNRAS, 431, 2861

Acknowledgements

I am thankful for the knowledge, techniques, and culture of science that were developed before my time. Growing up, I had learnt a fair number of scientific facts, but I did so without really believing that these ideas could describe the workings of daily life outside of specialised laboratory experiments. It was far too long before I understood that the known laws of physics are either consistent with literally every aspect of human experience, or we would have evidence that they are wrong and they need to be revised. For me, science then became more important as a way to understand the world while avoiding flawed or irrational thinking.

I am grateful to my primary supervisor, Amanda Karakas for her expert guidance of my research programme. Having observed how heavily other students' progress has been influenced by their supervisors and chosen research topics, I feel very fortunate to have been supervised by Amanda on the topic of stellar evolution and nucleosynthesis. Although she encouraged me to work independently where possible, Amanda has also been very generous with her time and knowledge throughout my PhD. Her excellent teaching skills clearly have applications beyond stellar astrophysics, as she has given me a solid foundation in workplace soft skills such as cocktail making. I'm sure this knowledge will continue to serve me well as I make the transition to postdoctoral life.

Thank you to the rest of my advisory panel, Gary Da Costa, David Yong, Richard Stancliffe, and John Lattanzio. Each of them has given their time to provide me with useful feedback and advice. Thank you also to my collaborators (especially Carolyn Doherty) who have helped me to improve the quality and scientific rigour of my papers.

Thank you to everyone at Stromlo for contributing to a friendly work environment. I would list people by name, but I would inevitably forget someone important, so I will just single out my office mates: Christopher Nolan and Chris Owen. Thanks for waiving the entrance requirements and letting me join the 'Chris' office. Thanks to my climbing buddies for helping me to get more exercise and spend less time sitting down. Thanks to everyone at cosmology lunch and supernova tea for welcoming me into the field of supernovae and helping me to prepare for my job interview (and now postdoc) at Queen's University Belfast.

Thank you to my immediate family, Mum, Dad, my sister Tegan, and my brother, Josh. Dr. Joshua Shingles gave me no excuses not to succeed in my doctorate after he completed his while simultaneously working full-time and raising four children with his wife Natalie.

Thank you to Louise for being with me during the best and worst times of our PhD years. I'll remember the great times we spent having tea after work (at exactly 5pm!), spending nights eating in and watching TV at our apartment, having chicken schnitzels and

microwaved vegetables ridiculously often, going out for lunch or coffee on the weekends, and our holiday trips together (especially Christmases!). Thank you for introducing me to much of the culture, accents, phrases, and retail stores of the UK ahead of my move to Belfast. I'm reminded of you when I go to a Caffé Nero, Boots, Tesco, or Pizza Express, and whenever I have no idea whether a British person is joking or not.

Abstract

Elements heavier than iron are almost entirely produced in stars through neutron captures and radioactive decays. Of these heavy elements, roughly half are produced by the *slow* neutron-capture process (*s*-process), which takes place under extended exposure to low neutron densities. Most of the *s*-process production occurs in stars with initial masses between roughly 0.8 and 8 $M_\odot$, which evolve through the Asymptotic Giant Branch (AGB) phase.

This thesis explores several topics related to AGB stars and the *s*-process, with a focus on comparing theoretical models to observations in the literature on planetary nebulae, post-AGB stars, and globular cluster stars. A recurring theme is the uncertainty of ^{13}C-pocket formation, which is crucial for building accurate models of *s*-process nucleosynthesis.

We first investigated whether neutron-capture reactions in AGB stars are the cause of the low sulphur abundances in planetary nebulae and post-AGB stars relative to the interstellar medium. Accounting for uncertainties in the size of the partial mixing zone that forms ^{13}C pockets and the rates of neutron-capture and neutron-producing reactions, our models failed to reproduce the observed levels of sulphur destruction. From this, we concluded that AGB nucleosynthesis is not the cause of the sulphur anomaly. We also discovered a new method to constrain the extent of the partial mixing zone using neon abundances in planetary nebulae.

We next aimed to discover the stellar sites of the *s*-process enrichment in globular clusters that have inter- and intra-cluster variation, with the examples of M4 (relative to M5) and M22, respectively. Using a new chemical evolution code developed by the candidate, we tested models with stellar yields from rotating massive stars and AGB stars. We compared our model predictions for the production of *s*-process elements with abundances from s-poor and s-rich populations. We found that rotating massive stars alone do not explain the pattern of abundance variations in either cluster, and that a contribution from AGB stars with ^{13}C pockets is required. We derived a minimum enrichment timescale from our best-fitting chemical evolution models and, although the value depends on the assumptions made about the formation of ^{13}C pockets, our estimate of 240–360 Myr for M22 is consistent with the upper limit of 300 Myr inferred by isochrone fitting.

Lastly, there is accumulating evidence that some stars (e.g., in ω Centauri) have been born with helium mass fractions as high as 40%. This motivated us to explore the impact of helium-rich abundances on the evolution and nucleosynthesis of intermediate-mass (3–6 $M_\odot$) AGB models. We found that the stellar yields of *s*-process elements are substantially lower in He-rich models, largely as a result of less intershell material being mixed into the envelope. We also found evidence that high He abundances could restrict the *s*-process production by ^{13}C pockets to stars with lower initial masses.

Contents

List of Figures

List of Tables

CHAPTER 1

Introduction

> The best that most of us can hope to achieve in physics is simply
> to misunderstand at a deeper level.
>
> – Wolfgang Pauli[1]

1.1. The Origins of the Chemical Elements

Atoms are the basic building blocks of matter. Within each atom is a nucleus of protons
and neutrons that traces back to its formation at a particular time during the 13.8 billion
year history of our universe. Most of the hydrogen and helium nuclei were formed in the
high temperature early universe just minutes after the Big Bang. Thereafter, successive
generations of stars hosted the nuclear furnaces needed to produce the heavier elements
that make up planets, complex molecules, and life. Today, we are continuing to find new
applications for the rich set of chemical elements left behind by ancient stars. Our modern
computer revolution is taking place only because stars have synthesised elements such as
copper, silicon, and literally dozens of metals including gallium and arsenic (National
Research Council 2008).

The complex processes of stellar nucleosynthesis were first described in detail by Burbidge
et al. (1957) and Cameron (1957a). Despite decades of improvements to our theoretical
models, there remain large uncertainties in our understanding of processes such as mass

---

[1]To Jagdish Mehra, in Berkeley, California (May 1958), as quoted in *The Historical Development of Quantum Theory* (2000) by Jagdish Mehra.
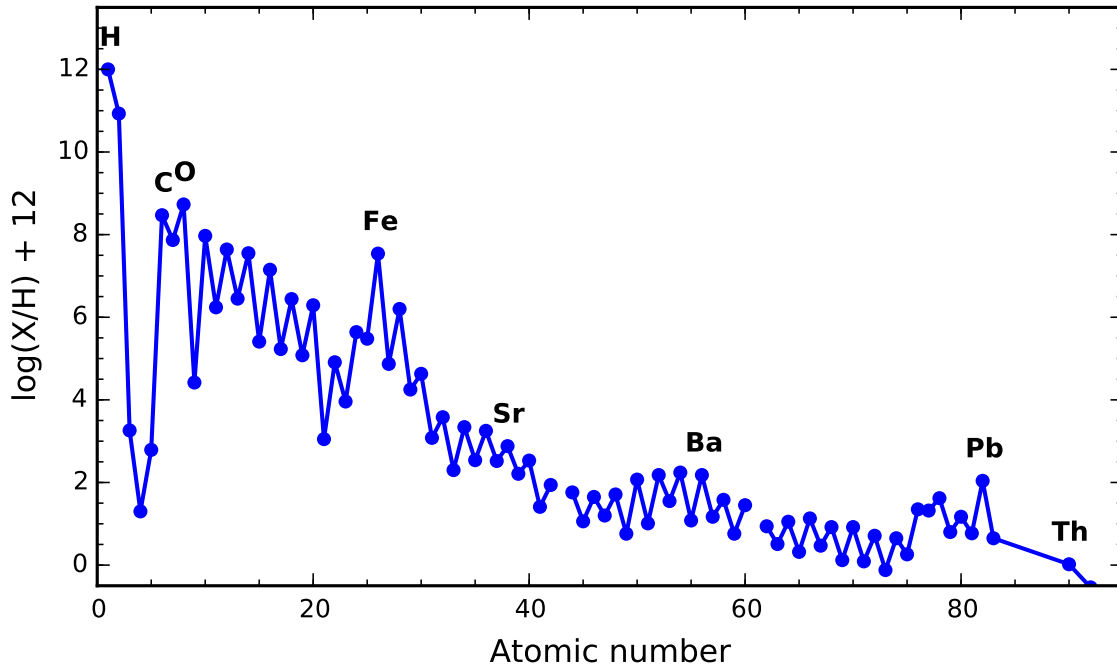
Figure 1.1 The solar system abundances by number relative to hydrogen. Data from Asplund et al. (2009).

loss, convection, and rotation in stars. These uncertainties in stellar physics propagate to uncertainties in our understanding of the universe's chemical enrichment history (see e.g., Romano et al. 2010). Nevertheless, we currently have a general qualitative understanding of how chemical enrichment takes place.

Figure 1.1 shows the abundances of the chemical elements in the solar system. Broadly, these elements can be classified into: hydrogen and helium created soon after the Big Bang, lithium, beryllium, and boron mostly from cosmic ray spallation, carbon up to iron (Fe) produced by thermonuclear fusion, and elements heavier than the Fe-peak ($Z > 30$; hereafter, heavy elements), which are almost entirely produced by neutron captures onto Fe-peak elements. Beyond lead, instability to α- and β-decays prevents further nucleosynthesis via slow neutron captures (Clayton & Rassbach 1967) and only a very small amount is synthesised via rapid neutron captures. We explore these types of nucleosynthesis in the following sections, with a particular focus on neutron-capture nucleosynthesis.

1.2.   Nuclear Reactions

Before discussing nuclear reactions, we must introduce some common notation. Consider the example of a reaction between an X nucleus and an A particle that produces a Y

nucleus and a B particle. This reaction can be represented by the formula

$$X + A \longrightarrow Y + B.$$
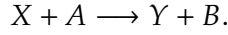
The left-hand side is known as the entrance channel (or the reactants) and the right-hand side is the exit channel (or the products). The same reaction can be represented even more compactly by the shorthand notation $X(A, B)Y$. If there is no comma to separate the entrance and exit channels, then the bracketed particles belong to the exit channel, as in the example β^+ decay reaction $^{13}\text{N}(\beta^+\nu)^{13}\text{C}$.

The factors determining the rate at which a reaction proceeds include the densities and relative velocities of the particles in the entrance channel as well as the cross section for the reaction, which accounts for the detailed nuclear physics that affect the probability of the reaction taking place. If the number densities of two reactants are n_X and n_A respectively, then the number of reactions per unit time, per unit volume is

$$R = \frac{n_X n_A \sigma v}{1 + \delta_{XA}},$$

where v is relative velocity of the incident particles, σ is the reaction cross section (usually a function of v), and δ_{XA} is equal to one if X and A are identical particles and zero otherwise.

In a system in thermal equilibrium (such as a stellar interior), particles move at a range of speeds described by a Maxwell-Boltzmann distribution. For these applications, it is useful to integrate σv over the velocity distribution so that the reaction rate can be expressed as a function of temperature, i.e.,

$$R(T) = n_X n_A \int \sigma(v) v \cdot \frac{\mathrm{d}N(v, T)}{\mathrm{d}v} \mathrm{d}v$$
$$= n_X n_A \langle \sigma v \rangle_T .$$

Tables of reaction rates often provide the 'reduced reaction rate', which is $N_A \langle \sigma v \rangle$, where N_A is Avogadro's number.

1.3.   Big Bang Nucleosynthesis

The solutions to Einstein's equations of General Relativity that describe a dynamic and expanding universe (Friedmann 1922; Lemaître 1927) first began to be taken seriously by many astronomers after it was discovered that the speeds with which galaxies recede from us are proportional to their distances (Lemaître 1927; Hubble 1929). One interpretation, the Big Bang theory, holds that the universe has been expanding and cooling from a very definite beginning in time. An alternative cosmology, the steady-state theory (Hoyle 1948), posited that the universe is in a perpetual state of expansion with no beginning.

The Big Bang came to be the preferred explanation, especially after the confirmation of one major prediction: that at some time between the Big Bang and now, the universe would have first become cool enough for protons and electrons to recombine into neutral hydrogen atoms. This would have made the universe largely transparent to radiation for the first time, meaning that photons emitted by the hot plasma would have begun freely streaming through the universe carrying the characteristic blackbody signature of the high-temperature earlier state. A microwave background with a temperature of about 3 K was detected by Penzias & Wilson (1965), and this was widely accepted to be the redshifted radiation from the Big Bang (Dicke et al. 1965).

The Big Bang theory has further consequences for the abundances of the elements. The question of which nuclear reactions took place in the high-temperature early universe had begun to be explored by Gamow (1946), Alpher et al. (1948), and others, even before the cosmic microwave background had been detected. Although these early works incorrectly assumed that Big Bang Nucleosynthesis (BBNS) was the source of all elements, we now know that the production of carbon and heavier elements are largely due to stellar nucleosynthesis. However, Big Big nucleosynthesis is still required to explain the abundances of several light nuclides.

For the first few minutes after the Big Bang, the universe was filled with a hot plasma of neutrons and protons that could freely interconvert at their equilibrium ratio via weak interactions (Hayashi 1950; Alpher et al. 1953). The higher masses of neutrons meant that they were outnumbered by protons with a precise ratio that can be calculated from the temperature. As the universe cooled, the rate of weak interactions became small at a neutron/proton ratio of about 1/6. At this time, the temperature was approximately 10^{10} K, too high for deuterium nuclei to stay bound, so the only decrease in n/p was due to neutron β^- decays ($t_{1/2} = 617$ sec). These decays reduced the n/p ratio to about 1/7 before the temperature had become low enough for deuterium to start accumulating, which locked up the neutrons into stable nuclei. Because the vast majority of free neutrons were paired up with protons to form ^{4}He nuclei, the primordial mass fraction of helium (Y_p) can be approximated as two times the mass fraction of neutrons. The primordial helium mass fraction is then given approximately by

$$Y_P = \frac{2n/p}{1 + n/p} = 0.25.$$

This is remarkably close to the value of $Y_P = 0.2534 \pm 0.0083$ inferred from spectroscopy of regions of ionised hydrogen (H ɪɪ regions; Aver et al. 2012).

From the perspective of understanding the origins of the elements, the most important consequences of BBNS are: (1) BBNS sets a lower limit on the initial helium abundance of the first stars and (2) BBNS is the source of virtually all deuterium nuclei, which are easily destroyed in stellar interiors, and (3) BBNS also produced trace amounts of ^{7}Li, and

almost nothing beyond this (Wagoner et al. 1967; Tytler et al. 2000). The majority of nuclei are produced by nucleosynthesis in stars.

1.4.   Stellar Evolution and Nucleosynthesis

1.4.1.   Basic assumptions and the stellar structure equations

The physical complexity of stars, together with the incredibly long timescales over which they evolve (up to tens of billions of years), make simulating their evolution computationally difficult. For this reason, computer models of stars require a number of simplifying assumptions to be made, even where a more fundamental understanding of the physics is known. For example, three-dimensional models of magneto-hydrodynamics are widely used in several areas of astrophysics such as star formation and accretion modelling, but their application to stellar models is extremely limited in practice. Even without considering magnetic fields, three-dimensional hydrodynamical models of stars are presently limited to extremely short simulation times (e.g., a few hours of real-time, Mocák et al. 2011; Stancliffe et al. 2011; Woodward et al. 2015).

For models of complete stellar evolution, we use four stellar structure equations that follow from the assumptions of spherical symmetry, hydrostatic equilibrium, and the diffusive transport of radiation. Using numerical methods to solve these differential equations (Henyey et al. 1959, 1964), the stellar structure can be modelled on computers.

The first assumption of spherical symmetry requires that the physical conditions in a star depend only on the radius from the centre, or equivalently the enclosed mass (m). Stellar evolution codes (and the equations shown here) typically use a Lagrangian mesh where mass is the independent variable, which improves the numerical stability during expansion and contraction of the stellar structure.

With spherical symmetry, the mass continuity equation is

$$\frac{\mathrm{d}r}{\mathrm{d}m} = \frac{1}{4\pi\rho r^2},$$

(1.1)

where r is the radius, m is the mass coordinate, and ρ is the volumetric mass density.

The difference between the luminosity entering and exiting a given mass shell is affected by several sources and sinks within the shell: the rate of energy generation by nuclear reactions (ϵ_{nuc}), the rate of energy loss by neutrinos (ϵ_ν), and the rate of energy emitted or absorbed by non-adiabatic contraction or expansion, where all of these quantities are per unit mass. By combining these terms, the equation of energy conservation can be

expressed as

$$\frac{\mathrm{d}L}{\mathrm{d}m} = \epsilon_{\mathrm{nuc}} - \epsilon_{\nu} - \left(\frac{\partial u}{\partial t} - P \frac{\partial}{\partial t} \frac{1}{\rho} \right), \tag{1.2}$$

where L is the luminosity, u is the internal energy per unit mass, and P is the pressure.

The assumption of a hydrostatic equilibrium requires that each mass shell not be accelerating. This is achieved by a difference in pressure between the top and bottom of the shell that precisely balances the inwards gravitational force. In differential form, the pressure gradient is given by

$$\frac{\mathrm{d}P}{\mathrm{d}m} = -\frac{Gm}{4\pi r^4}. \tag{1.3}$$

The energy transport equation is

$$\frac{\mathrm{d}T}{\mathrm{d}m} = -\frac{Gm}{4\pi r^4} \frac{T}{P} \nabla, \tag{1.4}$$

where ∇ represents the temperature gradient $(\mathrm{d}\ln T)/(\mathrm{d}\ln P)$. In order to solve Equation 1.4, the radiative and adiabatic temperature gradients must first be calculated. The radiative temperature gradient is

$$\nabla_{\mathrm{rad}} = \frac{\mathrm{d}\ln T}{\mathrm{d}\ln P}\bigg|_{rad} = \frac{3}{16\pi 4\sigma c} \frac{\kappa L P}{Gm T^4}, \tag{1.5}$$

where σ is the Stefan-Boltzmann constant and κ is the mass attenuation coefficient for radiation (with units of cross-sectional area per unit mass), commonly called the stellar opacity. Next, the adiabatic gradient is

$$\nabla_{\mathrm{ad}} = \frac{\gamma - 1}{\gamma}, \tag{1.6}$$

where γ is the adiabatic exponent of the gas (5/3 for a monatomic ideal gas).

According to the Schwarzschild criterion (which ignores the effect of a mean molecular weight gradient), an adiabatic gradient that is steeper than the radiative gradient at some location indicates that the material is stable against convection and the radiative gradient should be used. In the opposite case where the radiative gradient is larger, the fluid is unstable to convective motions and the value of ∇ is often calculated from the mixing length theory (MLT; Böhm-Vitense 1958). In the Mount Stromlo stellar evolution code, the chemical abundances in convective regions are instantaneously mixed, which is a valid approximation if the convective turnover timescale is much shorter than the nuclear burning timescale. A time-dependent alternative is to use diffusive mixing in convective zones (Cannon 1993, as implemented in the nucleosythesis code used in this thesis).

To calculate the rates of energy generation and neutrino losses in Equation 1.2, we must calculate the rates of all nuclear reactions that generate a significant amount of energy and therefore will affect the stellar structure.

1.4.2.   Hydrogen and helium burning

The fusion of hydrogen into helium is one the most efficient sources of nuclear energy. Per hydrogen nucleus, fusion into helium releases 6.68 MeV of energy (minus neutrino losses), which is about 0.7% of the 938 MeV rest mass energy of one proton. This, together with the high abundance of hydrogen and the relatively low temperatures at which it fuses ($\sim 10^7$ K) mean that stars spend most of their nuclear-burning lifetimes powered by hydrogen burning in their cores. The net reaction is

$$4\,{}^1\mathrm{H} \longrightarrow {}^4\mathrm{He} + 2\,e^+ + 2\,\nu_e + 24.7\ \mathrm{MeV}.$$
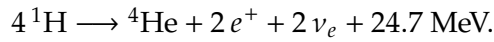
The two positrons produced in this reaction rapidly annihilate with nearby electrons, thereby releasing an additional 1.02 MeV of energy each.

The two most energetically important sets of reactions by which hydrogen is converted into helium are the proton-proton (pp-)chains and the Carbon-Nitrogen-Oxygen (CNO) cycles. In stars less than about 1.2 M$_\odot$, core hydrogen burning takes place via the pp chain reaction (Iliadis 2007), which first produces ^{3}He via

$$^1\mathrm{H} + {}^1\mathrm{H} \longrightarrow {}^2\mathrm{H} + e^+ + \nu_e + 0.16\ \mathrm{MeV},\ \mathrm{and}$$
$$^2\mathrm{H} + {}^1\mathrm{H} \longrightarrow {}^3\mathrm{He} + \gamma.$$
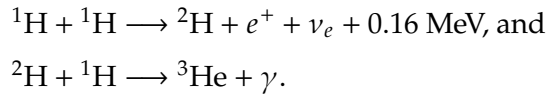
There are several ways for the resulting ^{3}He to be converted into ^{4}He, which correspond to the different branches of the pp-chain. The first and most active branch (responsible for 90% of the energy generation in the Sun, Iliadis 2007) is the pp I branch, which produces ^{4}He via the reaction

$$^3\mathrm{He} + {}^3\mathrm{He} \longrightarrow 2\,{}^1\mathrm{H} + {}^4\mathrm{He}.$$
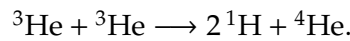
The other branches, pp II and pp III, alter the abundances of lithium, beryllium, and boron, but produce negligible energy in stars.

In stars with masses higher than about 1.2 M$_\odot$ and with some enrichment of carbon, nitrogen, or oxygen, hydrogen burning takes place primarily through the CNO cycles, which take over from the pp-chains as the dominant hydrogen-burning pathway at high temperatures ($\gtrsim$ 20 MK). The most active branch is the CN cycle (Bethe 1939), which consists of the reactions

$$^{12}\mathrm{C} + {}^1\mathrm{H} \longrightarrow {}^{13}\mathrm{N} + \gamma,$$
$$^{13}\mathrm{N} \longrightarrow {}^{13}\mathrm{C} + e^+ + \nu_e, \qquad\qquad (\tau_{1/2} = 9.965\ \mathrm{min})$$
$$^{13}\mathrm{C} + {}^1\mathrm{H} \longrightarrow {}^{14}\mathrm{N} + \gamma,$$
$$^{14}\mathrm{N} + {}^1\mathrm{H} \longrightarrow {}^{15}\mathrm{O} + \gamma,$$
$$^{15}\mathrm{O} \longrightarrow {}^{15}\mathrm{N} + e^+ + \nu_e,\ \mathrm{and} \qquad\qquad (\tau_{1/2} = 122.24\ \mathrm{s})$$
$$^{15}\mathrm{N} + {}^1\mathrm{H} \longrightarrow {}^{12}\mathrm{C} + {}^4\mathrm{He}.$$
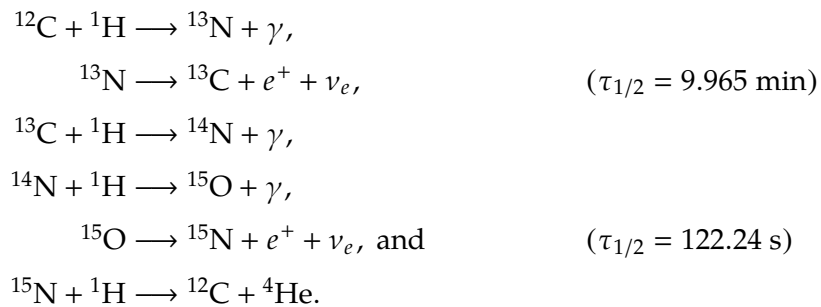
The slowest reaction of the CN cycle (at temperatures below ~ 100 MK) is proton capture onto ^{14}N, so typically the effect of the CN cycle is to convert abundant ^{12}C nuclei into ^{14}N.

Other branches of the CNO cycle produce very little energy in stars, so they have a negligible effect on the stellar structure. Higher order proton-capture reactions such as the NeNa cycle and MgAl chain, which operate in the envelopes of massive Asymptotic Giant Branch (AGB) stars, are described in Section 4.4.4.

After the exhaustion of hydrogen in the core, the next nuclear fuel for core burning is helium. With the absence of stable nuclides that have mass numbers of 5 and 8, He-burning bypasses boron and beryllium to produce ^{12}C via the triple-α reaction[2]. The triple-α reaction releases 7.27 MeV, or 0.049% of the 14.91 GeV rest mass energy of three α particles. This is only roughly 7% as efficient as hydrogen burning. The triple-α reaction can be separated into two parts:

$$^4\text{He} + {}^4\text{He} \longrightarrow {}^8\text{Be} - 93.7 \text{ KeV, and}$$
$$^8\text{Be} + {}^4\text{He} \longrightarrow {}^{12}\text{C} + 7.367 \text{ MeV.}$$
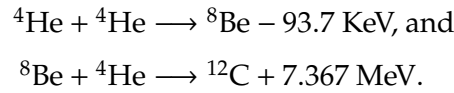
The intermediate ^{8}Be nuclei rapidly dissociate back into two ^{4}He nuclei with a half-life of 6.7×10^{-17} seconds. The fact that this reaction proceeds to ^{12}C at the rate required to explain the present abundance of carbon is due to an excited state of ^{12}C, which was predicted by the astronomer Fred Hoyle in 1953 (later published as Hoyle 1954) and then confirmed experimentally by Dunbar et al. (1953).

Once a reservoir of ^{12}C has accumulated in the core, further α-capture produces ^{16}O, leading to a core composed of roughy equal parts of carbon and oxygen. Of the other α-capture reactions, most are not important for energy production but can be highly important for nucleosynthesis, such as the neutron-producing reactions $^{13}\text{C}(\alpha, n)^{16}\text{O}$, and $^{22}\text{Ne}(\alpha, n)^{25}\text{Mg}$ which we discuss in the following sections.

The most massive AGB stars also ignite carbon off-centre in their cores, which is discussed in Section 4.4.6.

1.4.3. The rapid and slow neutron-capture processes

For nuclei heavier than the Fe-group, the addition of nucleons typically reduces the amount of binding energy per nucleon. Consequently, the fusion of these heavy nuclei is not a source of energy for sustained hydrostatic burning in stars. Of further importance for nucleosynthesis, the Coulomb repulsion of their strong nuclear charges means that extremely high temperatures are required for fusion to take place. At the high temperatures required, the nuclei become susceptible to spontaneous decay, thus preventing charged

---

[2]For historical reasons, ^{4}He nuclei are also known as α particles.
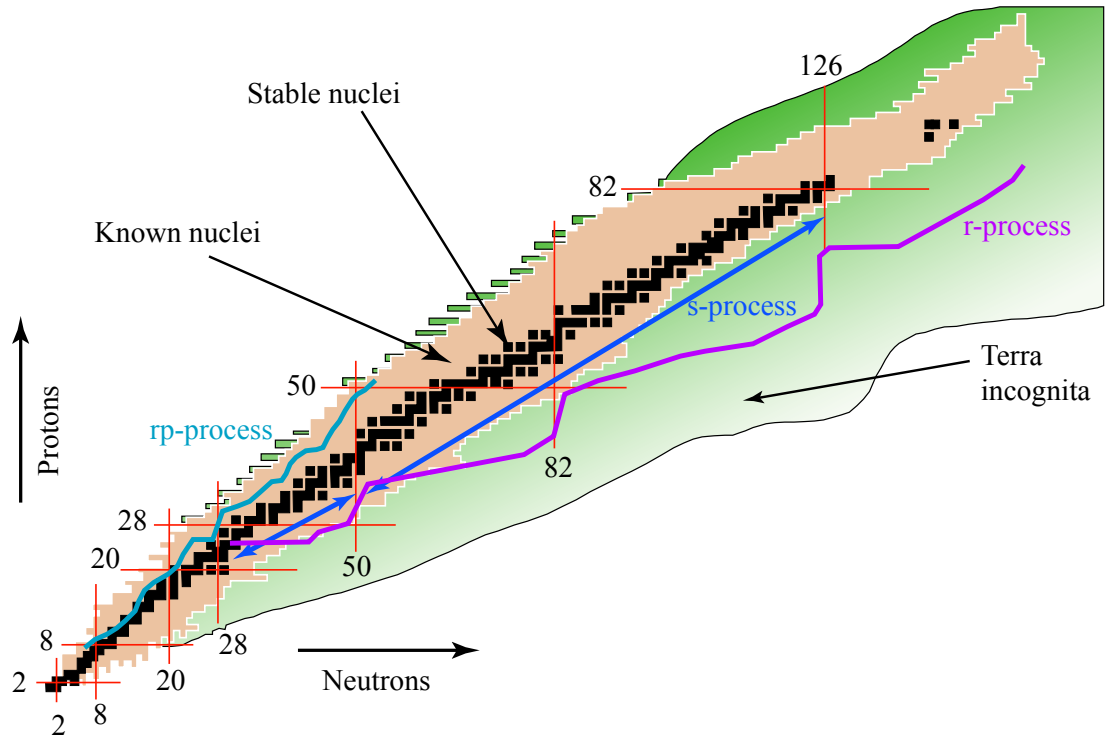
Figure 1.2 A chart of the nuclides showing the s- and r-process paths. Figure by Frank Timmes.

particle reactions from producing significant quantities of heavy elements. Instead, the heavy elements are almost entirely synthesised by the capture of neutrons (aside from a small number of proton-rich nuclides, Arnould & Goriely 2003), which are not sensitive to the Coulomb barrier due to their zero charge.

Free neutrons are most readily captured by nuclei that are both abundant and have a high neutron-capture cross section. For this reason, neutrons are mostly captured onto ^{56}Fe nuclei, which are abundant due to their production by the ^{56}Ni–^{56}Co–^{56}Fe decay chain in supernovae. The neutron-rich isotopes produced by neutron captures are typically unstable to decay through the β^- channel, which converts a neutron into a proton (and emits an electron and an antineutrino) thereby producing a nucleus with a higher atomic number. The neutron captures and β^--decays can be chained together into many different paths. However, they are generally divided into the two extremes of neutron-capture rates: the r- (rapid) and s- (slow) process paths (Burbidge et al. 1957; Cameron 1957a,b). The nuclei involved in these two processes are shown in Figure 1.2.

In the r-process, Fe-seed nuclei are bombarded with an extremely high flux of neutrons, which produces highly unstable neutron-rich isotopes out to the neutron drip line (at which neutrons can no longer be captured). This process, which is the only way to produce the heaviest elements such as Th and U, requires extremely high neutron densities of 10^{20}–10^{25} cm^{-3} that most likely occur in the explosive conditions of core-collapse supernovae or neutron star mergers (for a recent review of possible r-process sites, see Thielemann

et al. 2011). The *r*-process produces some of the most unstable nuclides in nature, so measurements of the lifetimes and decay channels of the relevant nuclei are extremely difficult to make with laboratory experiments. For this reason, the *r*-process component of an abundance distribution is often inferred from solar system material by subtracting the *s*-process component, which itself may be determined either theoretically (e.g., Arlandini et al. 1999; Goriely 1999; Sneden et al. 2008) or empirically (e.g., Simmerer et al. 2004). For this reason, improvements to our understanding of the *s*-process provide important constraints on the *r*-process.

The *s*-process refers to the opposite extreme of neutron capture rates, in which unstable nuclei typically have time to undergo β^- decay before capturing a neutron. The *s*-process is far better understood than the *r*-process, and today we have a good qualitative picture of the *s*-process in nature (e.g., Busso et al. 1999; Herwig 2005; Karakas & Lattanzio 2014).

The *s*-process takes place in low- to intermediate-mass stars (with *M* between about 0.8 and 8 $M_\odot$) in the He-intershell region during the thermally pulsing AGB phase (Sanders 1967; Straniero et al. 1995; Busso et al. 1999). Perhaps the clearest evidence of this is the detection of the unstable element Tc, whose longest-lived isotope has a half-life of 4.2 million years, in the atmospheres of AGB stars that are billions of years old (Merrill 1952; Uttenthaler et al. 2007).

The *s*-process also takes place in massive stars (Raiteri et al. 1993), which is discussed in Section 3.3.

1.4.4.   The *s*-process in AGB stars

The structure of an AGB star is characterised by dual burning shells that surround a degenerate CO core. Outside of the CO core is a thin He-burning shell at the base of the He-rich intershell region. The He-rich intershell is surrounded by a H-burning shell beneath a hydrogen-rich deep convective envelope.

The He-burning shell is thermally unstable, leading to a recurring series of structural changes every 10^2–10^5 years that make up a thermal-pulse cycle. Figure 1.3 shows the first two thermal pulses in a 3 $M_\odot$, $Z = 0.0006$ model[3]. The He-burning shell ignites in a flash, a runaway reaction caused by a combination of the increasing temperature, the extreme temperature-sensitivity ($\epsilon \propto T^{40}$) of the triple-α reaction, and the lack of thermal regulation. The degeneracy and thinness of the He-burning shell prevent it from expanding sufficiently to quench the reaction until the luminosity has become very high (Schwarzschild & Harm 1965; Weigert 1966; Rose 1966), often exceeding 10^8 $L_\odot$ (as shown

---

[3]Here, *Z* means the total mass fraction of all elements other than hydrogen and helium. Not to be confused with the atomic number *Z*.
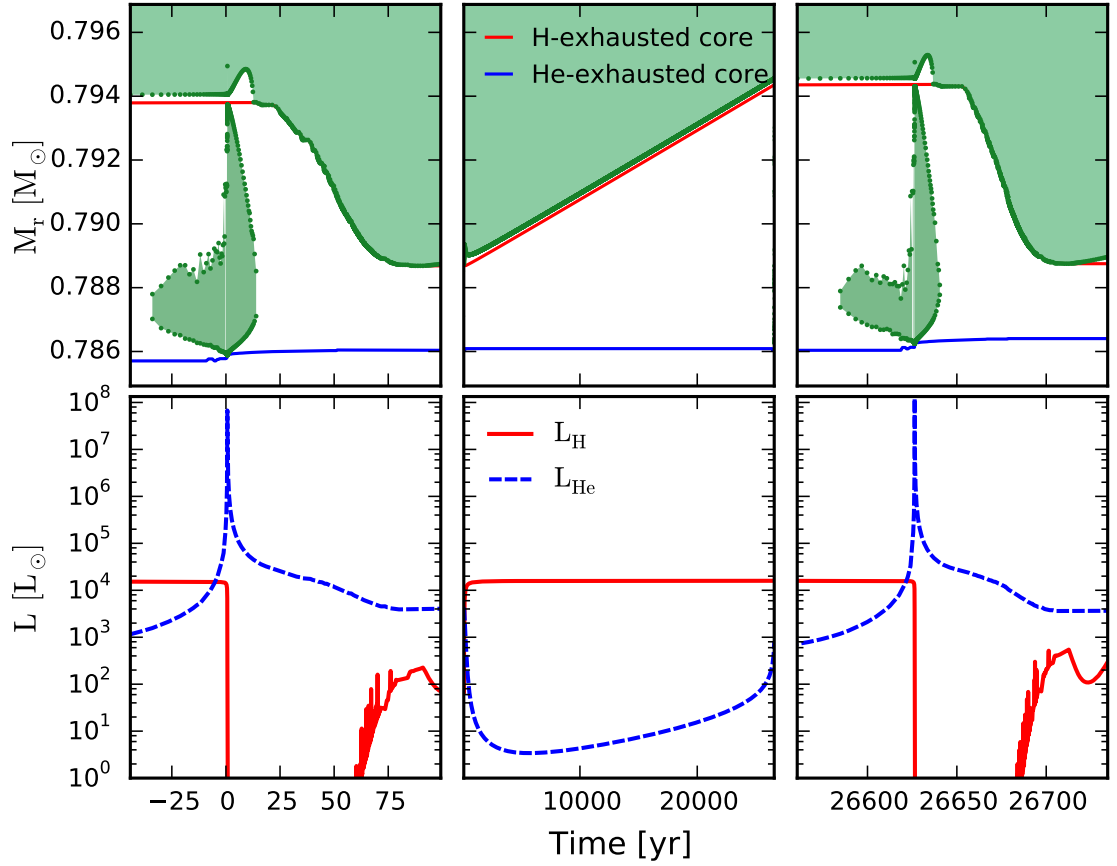
Figure 1.3 The AGB thermal pulse cycle illustrated with a 3 $M_\odot$, $Z = 0.0006$ model. Green shaded areas indicate convective regions. The style of the plot was inspired by Herwig (2005, Figure 3).

in the lower panel of Figure 1.3). The steep temperature gradient produced by the shell flash leads to convective motions in the He-intershell, which becomes well-mixed.

The energy from the He-flash causes the star to expand, which pushes the H-burning shell outwards and extinguishes it. In the left-hand panel of Figure 1.3, we can see that with the H-burning barrier removed, the lower boundary of the envelope convection zone can extend into the intershell, which is known as a 'third dredge-up' (TDU) episode. The TDU transports nuclear burning products (such as ^{12}C and s-process elements) to the stellar surface, where they affect the stellar spectrum and enrich the surrounding medium after being ejected by mass loss.

Most of the free neutrons available for the s-process in low-mass ($\lesssim$ 3–4 $M_\odot$) stars are produced via the ^{13}C$(\alpha, n)^{16}$O reaction under radiative conditions (Cameron 1957c; Scalo 1978; Straniero et al. 1995; Gallino et al. 1998). Producing the seed ^{13}C nuclei in stellar models requires the existence of a layer at the top of the ^{12}C-rich intershell in which protons are 'partially mixed' down from the envelope, thus enabling the CN cycle reaction ^{12}C$(p, \gamma)^{13}$N$(\beta^+\nu)^{13}$C to occur. The number of protons mixed into the region must be low because further proton capture completes the CN cycle to ^{14}N, which is an efficient
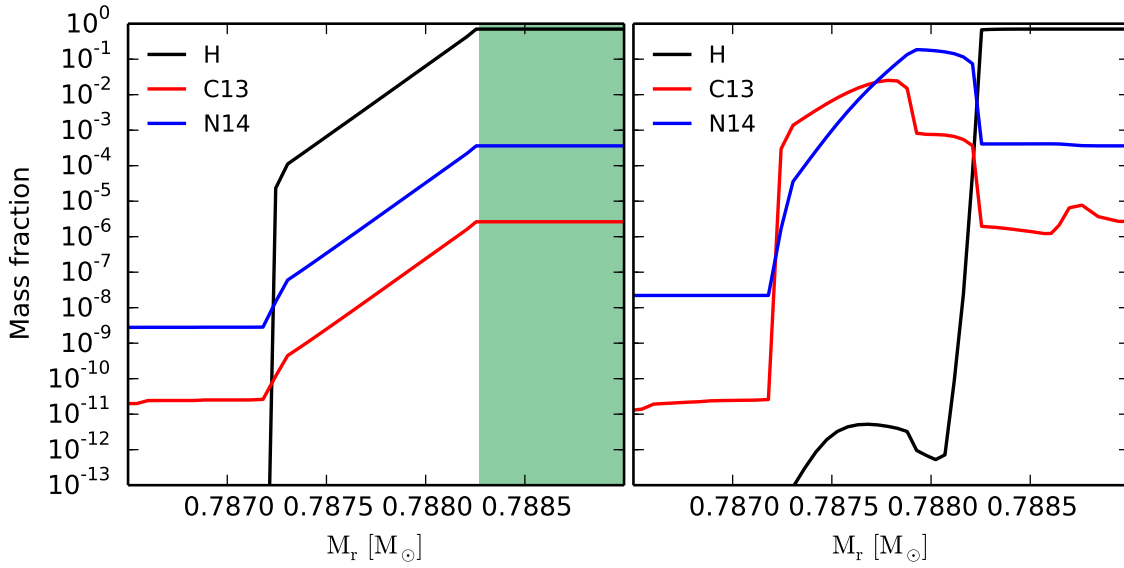
Figure 1.4 Composition profiles for H, ^{13}C, and ^{14}N showing the formation of a ^{13}C pocket in a 3 M$_\odot$, Z = 0.0006 model with M$_{pmz}$ = 10^{-3} M$_\odot$. Left panel: Immediately after insertion the the protons as the convective envelope retreats (green shaded). Right panel: Approximately 1000 years later, a ^{13}C pocket has formed below a ^{14}N pocket.

absorber of free neutrons.

The treatment of ^{13}C-pocket formation in our models is shown in Figure 1.4. The left-hand panel shows the exponential profile of protons that is added below the base of the envelope at the deepest extent of TDU. The right-hand panel, which displays the composition approximately 1000 years later, shows the resulting ^{13}C pocket that forms below a pocket of ^{14}N. The uncertainty surrounding the physical process that mixes protons into the intershell to form ^{13}C pockets is a recurring theme in this thesis, and each of the main chapters go into further detail on this topic.

The major neutron source in intermediate-mass stars ($\gtrsim$ 4 M$_\odot$) is the ^{22}Ne(α, n)^{25}Mg reaction (Iben 1975a; Scalo 1978). In the high temperatures of He-burning shell, ^{22}Ne is produced via ^{14}N(α, γ)^{18}F($\beta^+\nu$)^{18}O(α, γ)^{22}Ne. Above temperatures of about 300×10^6 K, the ^{22}Ne(α, n)^{25}Mg reaction starts to become active, producing a burst of neutrons at the base of the intershell during convective pulses. An important byproduct of the ^{22}Ne + α reactions is the production of ^{25}Mg and ^{26}Mg. These isotopes are particularly significant because Mg isotope ratios can be derived from the spectra of cool stars (with T$_{eff}$ $\lesssim$ 5000 K), which can then be used to obtain clues about chemical evolution (e.g., Yong et al. 2003).

Another diagnostic of neutron-capture environments are the abundances of elements that are affected by s-process branching points (Ward et al. 1976). Some unstable nuclides close to the valley of stability have half-lives on the order of days or years, resulting in β-decay rates that are similar to the neutron-capture rates. Two examples of nuclides with these immediate lifetimes are ^{85}Kr ($\tau_{1/2}$ = 10.8 yr) and ^{86}Rb ($\tau_{1/2}$ = 18.6 days) (van Raai et al.
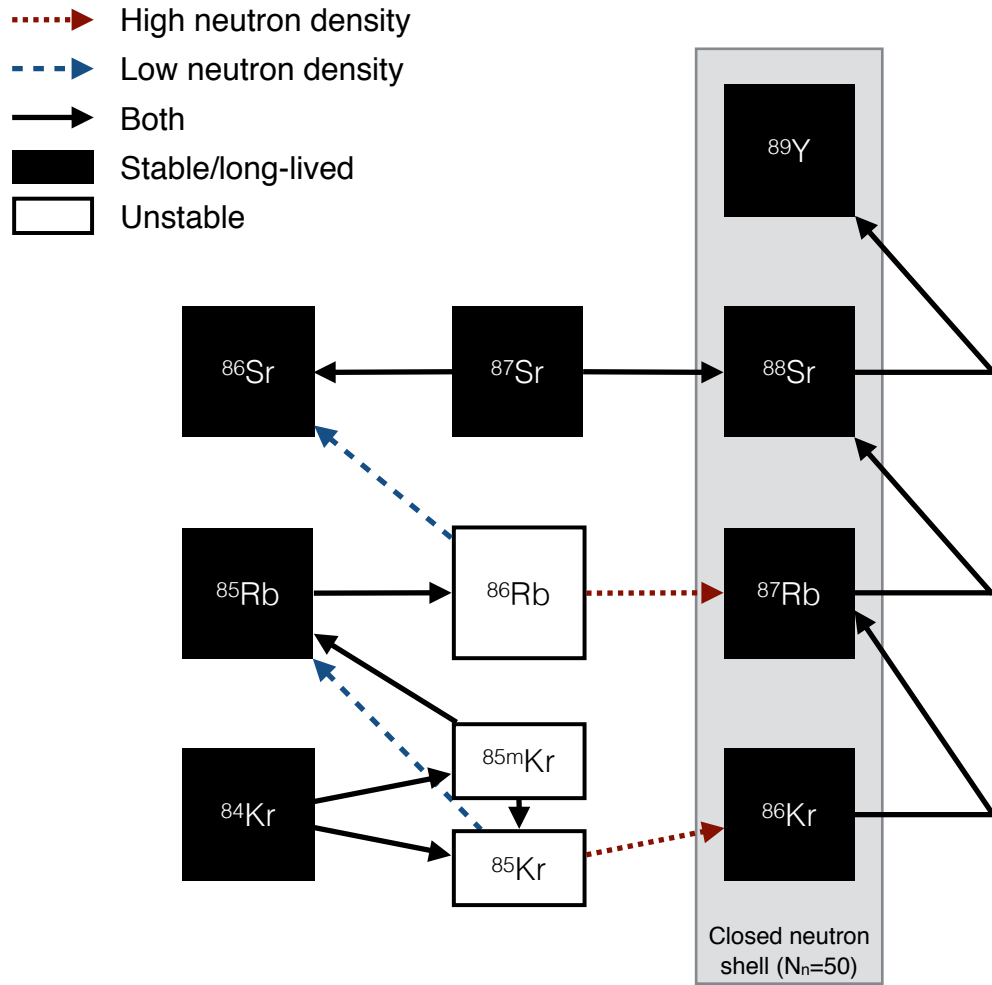
Figure 1.5 The *s*-process path near the branchings at ^{85}Kr and ^{86}Rb. Similar to van Raai et al. (2012, Figure 1)

2012; Karakas et al. 2012). Figure 1.5 illustrates the different *s*-process paths near these nuclides that operate under high and low neutron densities. With neutron densities above 10^8–10^9 cm^{-3}, neutron captures on to ^{85}Kr and ^{86}Rb cause the *s*-process path to produce ^{87}Rb. ^{87}Rb has a closed shell of neutrons, which gives it a very small neutron-capture cross section relative to ^{85}Rb and neighbouring nuclides, causing it to accumulate (Heil et al. 2008). At the high neutron densities resulting from the ^{22}Ne neutron source, there is a larger production of Rb than Sr and Zr.

Figure 1.6 shows the final surface abundances (in [X/Fe] notation[4]) of two example models with initial stellar masses of 1.7 and 6 M$_\odot$, where the *s*-process production is dominated by the ^{13}C and ^{22}Ne neutron sources, respectively. The *s*-process in general tends to cause an accumulation of elements with stable isotopes whose neutrons form a closed shell configuration (magic numbers of neutrons), and therefore have a relatively small

---

[4]This is the standard spectroscopic abundance notation $[A/B] = \log_{10}(n_A/n_B)_\star - \log_{10}(n_A/n_B)_\odot$, where $\odot$ denotes the solar abundance ratio.
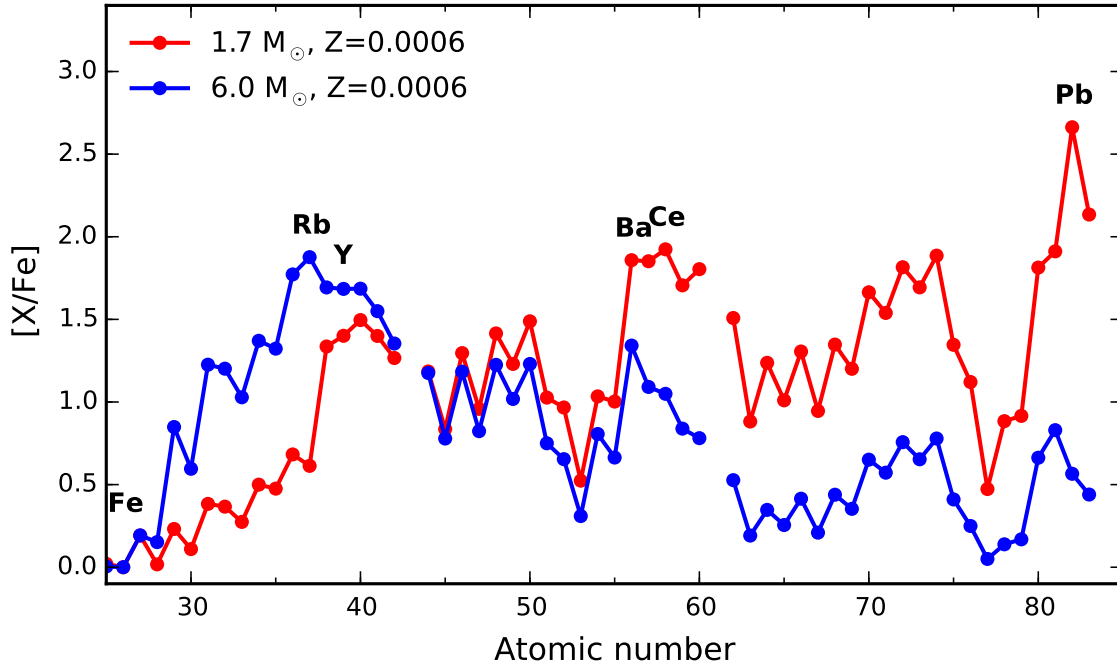
Figure 1.6 Final [X/Fe] surface abundances (except for $Z = 26$, which is [Fe/H]) for AGB models of 1.7 and 6.0 $M_\odot$. The 1.7 $M_\odot$ model is an example of s-process production via $^{13}C(\alpha, n)^{16}O$ reaction, and the 6 $M_\odot$ model of production via the $^{22}Ne(\alpha, n)^{25}Mg$ reaction.

neutron-capture cross sections compared to their neighbours. The peak near Rb–Zr is caused by the accumulation of nuclides with 50 neutrons: ^{87}Rb, ^{88}Sr, ^{89}Y, and ^{90}Zr. A second peak forms around Ba–Ce due to nuclides with 82 neutrons: ^{138}Ba, ^{139}La, and ^{140}Ce. A third peak forms at Pb due to the doubly-magic ^{208}Pb nuclide with 82 protons and 126 neutrons.

In low-mass ($\lesssim 3\,M_\odot$) stars such as the 1.7 $M_\odot$ model in Figure 1.6, the s-process distribution is particularly enhanced near the Ba-peak elements and Pb (as discussed in Lugaro et al. 2012). In contrast, the s-process in intermediate-mass stars such as the 6 $M_\odot$ model results in a heavy-element distribution that is dominated by the first s-process peak near Sr, Y, and Zr. The effect of the s-process branching is evident in the 6 $M_\odot$ model from the enhancement in [Rb/Fe] relative to [(Sr,Y,Zr)/Fe].

After being dredged-up into the envelope via TDU, s-process nuclei are released into the surrounding medium by mass loss through stellar winds. The contribution of a particular chemical species i (e.g., an element or nuclide) to the interstellar medium by a star over its lifetime is known as the stellar yield. We calculate this quantity using the formula

$$M_i^{\text{yield}} = \int_0^\tau X_i(t)\dot{M}(t)\,dt, \qquad (1.7)$$

where $X_i(t)$ is the mass fraction of species i at time t, $\dot{M}(t)$ is the stellar mass-loss rate at time t, and τ is the total stellar lifetime. For models with a non-zero envelope mass at the end of our calculations, we assume that all mass exterior to the core is ejected with

the composition of the surface at the last computed model. A set of stellar yields are a prerequisite for constructing models of chemical evolution.

1.5.   Chemical Evolution

Our knowledge of single stellar evolution and nucleosynthesis lays the groundwork for understanding chemical evolution, i.e., how the interstellar medium changes in chemical composition as it is enriched by dying stars. Observationally, the historical composition of the interstellar medium can be traced by low-mass stars. This is because of their extremely long lifetimes (tens of billions of years) and the fact that their atmospheres preserve their chemical compositions at birth, making them ideal 'stellar fossils'.

1.5.1.   Chemical evolution modelling

By accounting for the major processes that affect star formation and the composition of the interstellar medium, we can construct theoretical models whose abundance evolution can be compared with the abundances from real stars measured by spectroscopy.

The basic components of a chemical evolution model are:

- initial conditions: the starting gas mass and chemical composition,

- $\phi(m)$: the initial mass function,

- ψ: the star formation rate (in $M_\odot$/year) as a function of time or gas density,

- $\tau(m)$: the stellar lifetime (in years) as a function of initial mass,

- $m_{rem}(m)$: the remnant mass (in $M_\odot$) as a function of initial mass, and

- $q_i(m)$: the stellar yield of species i from a star with initial mass m (in $M_\odot$).

The initial mass function is a distribution function for the initial masses of stars produced by star formation. For chemical evolution purposes, it is typically normalised such that $\phi(m)\,dm$ is the number of stars with masses between m and $m + dm$ per $M_\odot$ of star formation. Common choices for the initial mass function include the classical Salpeter (1955) power law, or more recent forms such at the broken power law of Kroupa et al. (1993).

The star formation rate is often estimated by a power law function of the gas density (Schmidt 1959; Kennicutt & Evans 2012) or even more simply, an exponentially decreasing rate that models a single initial burst.

The results from a grid of stellar evolution and nucleosynthesis models spanning a range of initial masses at the relevant metallicity are interpolated to fix several more of the required functions: the stellar lifetime function, the remnant mass function, and the stellar yields. We ignore the dependence on metallicity here for simplicity (and because star formation ends before the metallicity increases in our models), but more complex models can use interpolated yields from a grid that spans a range of metallicities.

With these ingredients, we can write a set of differential equations to be solved in order to model the chemical composition as a function of time. Here we describe a single-zone chemical evolution model for simplicity, although the model can be straightforwardly extended to multiple zones or two or three dimensional models. This would be achieved by solving the chemical evolution equations separately for each zone, with extra terms that account for the transfer of gas and stars across zone boundaries. The following summary of the equations of chemical evolution is based on Pagel (2009, Chapter 7).

The total mass of the system is the divided up into the gas mass (g) and the stellar mass (s). These variables evolve according to

$$\frac{\mathrm{d}s}{\mathrm{d}t} = \psi(t) - e(t),$$

and

$$\frac{\mathrm{d}g}{\mathrm{d}t} = F(t) - E(t) + e(t) - \psi(t),$$

where F is the galactic accretion rate, E is the galactic ejection rate, e is the rate of mass ejection from the stellar population, and ψ is the star formation rate. The stellar mass ejection rate, $e(t)$ is

$$e(t) = \int_{m_{\tau=t}}^{m_U} (m - m_{rem}(m))\, \psi(t - \tau(m))\, \phi(m)\, \mathrm{d}m,$$

where $m_{\tau=t}$ is the initial mass of a star with a lifetime of t, m_U is the upper limit mass, $m_{rem}(m)$ is the mass of a remnant left by a star with an initial mass m, and $\tau(m)$ is the stellar lifetime.

For each chemical species i the ejection rate is

$$e_i(t) = \int_{m_{\tau=t}}^{m_U} q_i(m)\, \psi(t - \tau(m))\, \phi(m)\, \mathrm{d}m,$$

where $q_i(m)$ is the stellar yield of i from a star with an initial mass of m.

The gas mass fractions $X_i(t)$ evolve according to:

$$\frac{\mathrm{d}}{\mathrm{d}t}[gX_i] = e_i - X_i\psi + X_{i,F}F - X_iE$$

where $X_{i,F}$ represents the mass fraction of species i in the in-falling material.

1.5.2.   Globular clusters

Some of the oldest objects in the local universe are globular clusters, which are very dense, roughly spherical groups of about 10^5–10^6 stars located mostly in the halo of galaxies. Our Milky Way galaxy hosts over 150 globular clusters (Harris 1996, 2010 edition) and many of these clusters are over ten billion years old (Dotter et al. 2009).

Historically, the ages of globular clusters have provided a useful constraint on cosmology by setting a lower limit on the age of the universe (Chaboyer et al. 1996; Dotter et al. 2010). Their simplicity as single stellar populations has also made them extremely valuable for testing theories of stellar evolution (Johnson & Sandage 1955), where a simple stellar population is defined as a group of stars that formed at the same time in a single burst of star formation within a gas cloud of a uniform chemical composition. The assumption that this described globular clusters made the age dating of clusters relatively straightforward; the age of the cluster is simply the lifetime of the stars that are currently leaving the main sequence, and these stars can be identified from a colour-magnitude diagram.

Detailed abundances studies have revealed that globular clusters show significant spreads in the abundances of light elements such as He, C, N, O, F, Na, Mg, and Al (Cohen 1978; Peterson 1980; Gratton et al. 2004). The variations of these elements are correlated in a way that is almost exclusive to globular clusters (i.e., it is rarely seen in field stars and open clusters, as shown by Kraft et al. 1982; Shetrone 1996; Kraft et al. 1997; Gratton et al. 2000; De Silva et al. 2009) with anti-correlations between the abundances of C and N, Na and O, and sometimes Mg and Al (Shetrone 1996), typically with a C+N+O abundance that is constant within observational errors. These abundance patterns point to a H-burning process at high temperature ($\gtrsim 80\,\mathrm{MK}$) and dilution with varying amounts of unprocessed material, although the stellar sites where this burning takes place and the mechanism of dilution are presently not understood (Prantzos et al. 2007). Some current candidates for the hot hydrogen-burning environment are massive AGB (5–8 $\mathrm{M_\odot}$) stars (Cottrell & Da Costa 1981; Ventura et al. 2001), rotating massive stars (Prantzos & Charbonnel 2006; Decressin et al. 2007), massive binaries (de Mink et al. 2009; Bastian et al. 2013), and supermassive ($>10^4$ $\mathrm{M_\odot}$) stars (Denissenkov & Hartwick 2014; Denissenkov et al. 2015b).

The Milky Way globular clusters have metallicities ranging from [Fe/H] ≈ -2.4 to -0.3, with remarkably little variation within each cluster in almost all cases. A survey of 19 globular clusters by Carretta et al. (2009a) found no more than 0.05 dex scatter in [Fe/H] measurements, which is consistent with all of the clusters in their sample being mono-metallic. There are a few ($\sim 10\%$) exceptional clusters that do feature metallicity variation, and these are also some of the most massive clusters. Examples include M22, which has an intrinsic scatter in [Fe/H] of 0.10–0.15 dex (Marino et al. 2009; Da Costa et al. 2009) and ω Centauri, although the latter could be the tidally-stripped nucleus of a dwarf galaxy (Freeman 1993; Bekki & Freeman 2003) and might therefore formed differently to

other globular clusters (see the discussion in Gratton et al. 2004).

The abundances of neutron-capture elements ($Z > 30$) are constant within most clusters (Gratton et al. 2004; Yong et al. 2006, 2008a; D'Orazi et al. 2010). However, there are exceptions to this, including M15, which shows variations in r-process elements such as Eu (Sneden et al. 2000). M22 shows two distinct populations with distinct abundances of s-process elements (Y, Zr, Ba) (Marino et al. 2009; Villanova et al. 2010b). Among globular clusters with constant abundances of neutron-capture elements, there exist cluster-to-cluster differences. For example, M4 is a fairly typical mono-metallic metal-poor GC ([Fe/H] $= -1.18$; Carretta et al. 2009a), except that it has super-solar abundances of s-process peak elements (e.g., Rb, Y, Zr, La, Ba, Pb; Brown & Wallerstein 1992; Ivans et al. 1999). This makes M4 more enriched with s-process elements than M5, another GC with a similar metallicity.

In Chapter 3, we will construct new chemical evolution models that incorporate yields from AGB stars and rotating massive stars to investigate the internal s-process enrichment within the cluster M22, as well as the global s-process enrichment of M4.

1.5.3.   Chemical evolution code

The candidate has developed a basic one-zone chemical evolution code in modern Fortran named 'Evel ChemEvol'.

The Evel ChemEvol code solves the equations of chemical evolution (described in Section 1.5.1) with a Simpson rule integration and an adaptive time step. To estimate the integration error at each step, the Simpson rule calculation is compared with a lower-order integration using the mid-point rule. If any of the integration stages exceed their configured error thresholds, the current step is recalculated with a shorter time step.

To ensure that the Evel ChemEvol code produces valid output, the software must be able to reproduce the results of an existing chemical evolution model. We chose to reproduce the model of the globular cluster NGC 6752 by Fenner et al. (2004, hereafter, F04).

Following F04, the initial gas abundances are set by polluting primordial gas (roughly 75% H and 25% He) with the ejecta of massive stars until [Fe/H] increases to -1.4, the observed metallicity of NGC 6752. Many of initial these abundances were then manually adjusted to match F04, since the massive star yields of Kobayashi et al. (2006) that we used were different to those of Chieffi & Limongi (2002) that were used in F04. The initial gas mass is set to 1.4×10^5 M$_\odot$, and star formation is triggered with an exponential falloff on a timescale of 10^7 years. Figure 1.7 illustrates the output of the chemical evolution model.

As shown in Figure 1.7, the stellar ejection rate is separated into retained ejecta from stars
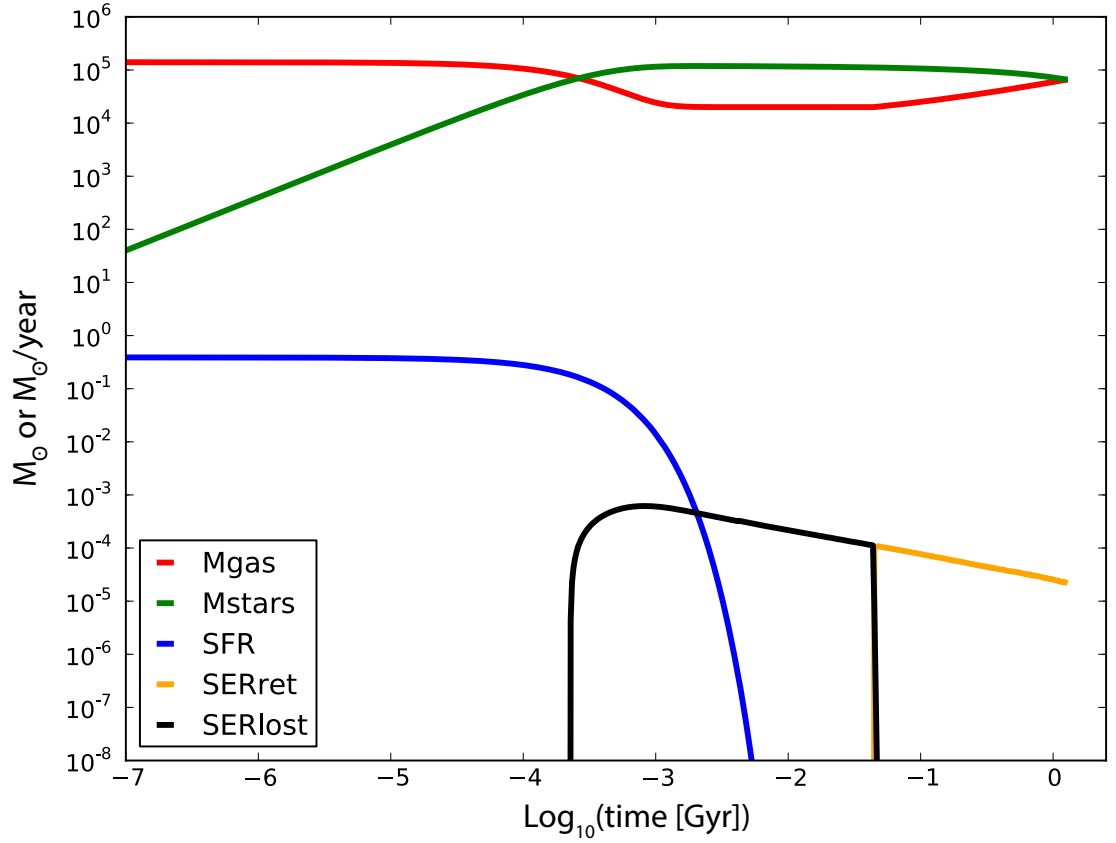
Figure 1.7 Time evolution of Evel ChemEvol model variables. The plot shows the gas mass (M_{gas}, in $M_\odot$), the stellar mass (M_{stars}, in $M_\odot$), the star formation rate (SFR, in $M_\odot$/yr), the stellar ejection rate of retained and lost ejecta (SERret and SERlost, in $M_\odot$/yr). In this model, ejecta from stars < 6.5 $M_\odot$ is assumed to retained, while ejecta from more massive stars is lost.

less massive than 6.5 $M_\odot$, and ejecta from more massive stars, whose high-speed winds are assumed to escape the cluster system. The cutoff at 6.5 $M_\odot$ is chosen for consistency with F04.

We use the same Kroupa et al. (1993) initial mass function and AGB stellar yields specified in F04. The stellar lifetime function is not described in F04 and is approximated here by a power law with the index −2.9. The results are in good agreement when assuming the same AGB yields for C, N, O (Figure 1.8), Na and O (Figure 1.9), and Al and Mg (Figure 1.10).
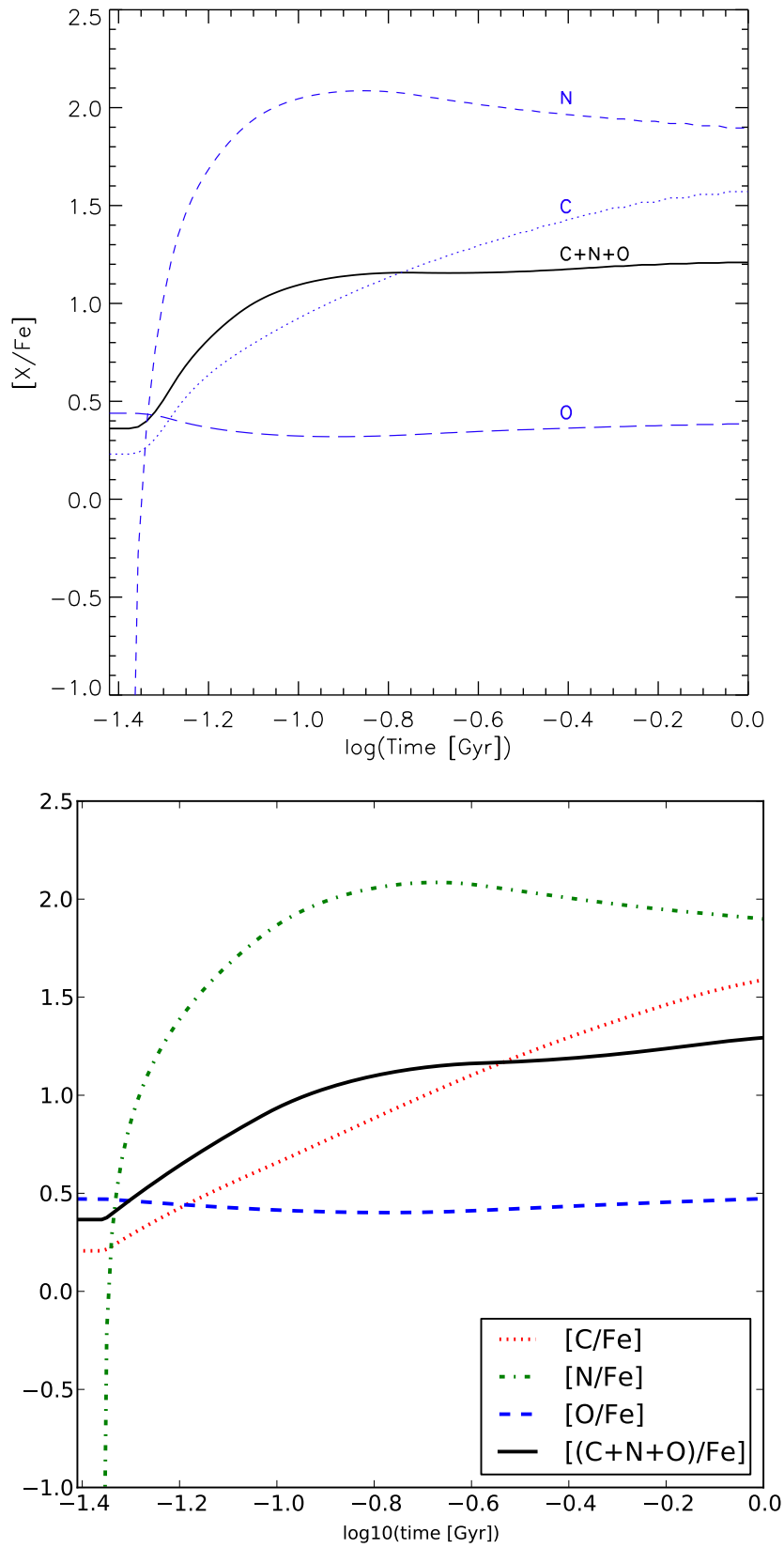
Figure 1.8 Evolution of C, N, and O abundances from Fenner et al. (2004) (top) and with Evel ChemEvol (bottom).
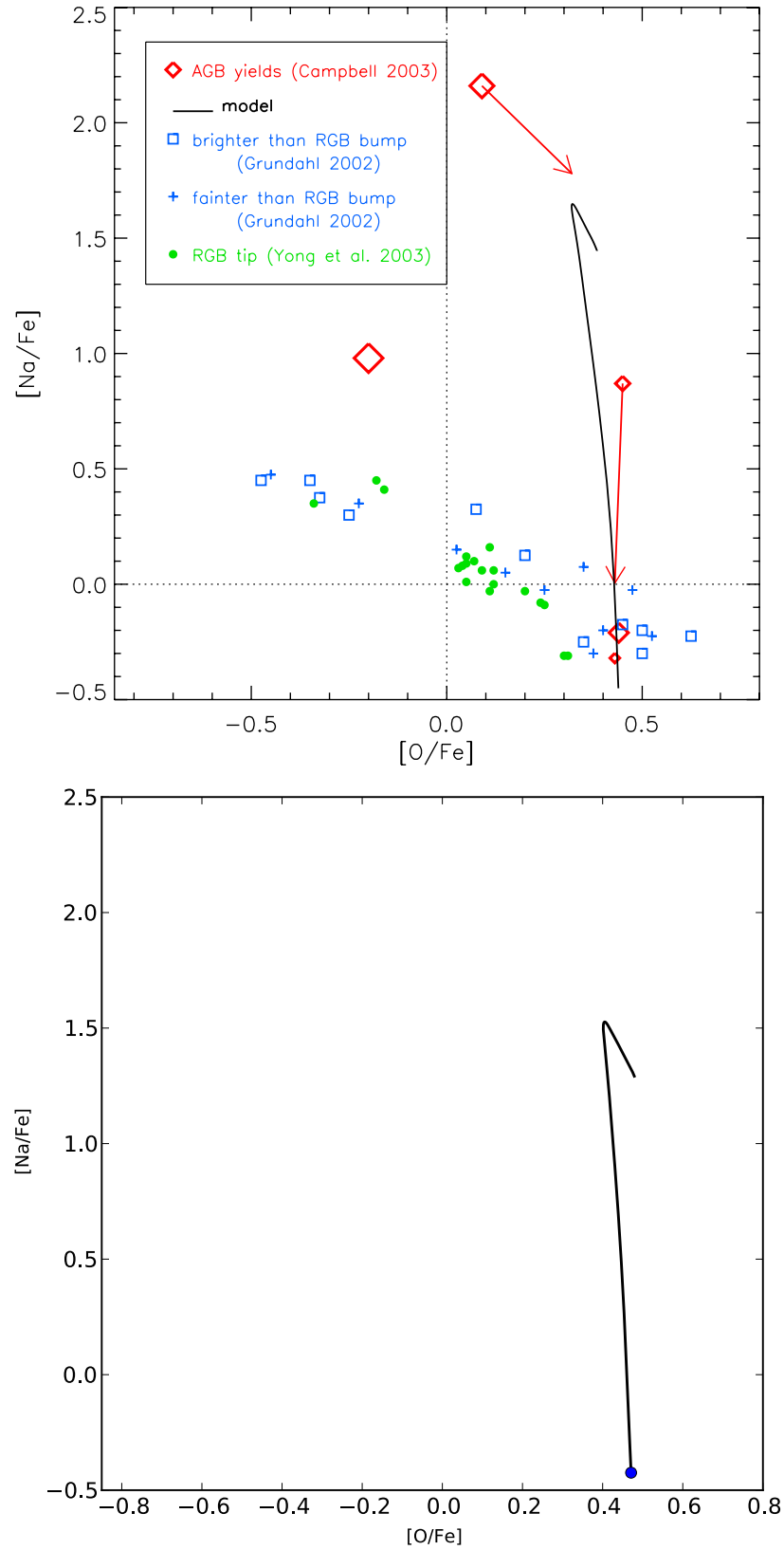
Figure 1.9 Evolution of Na and O abundances from Fenner et al. (2004) (top) and with Evel ChemEvol (bottom).
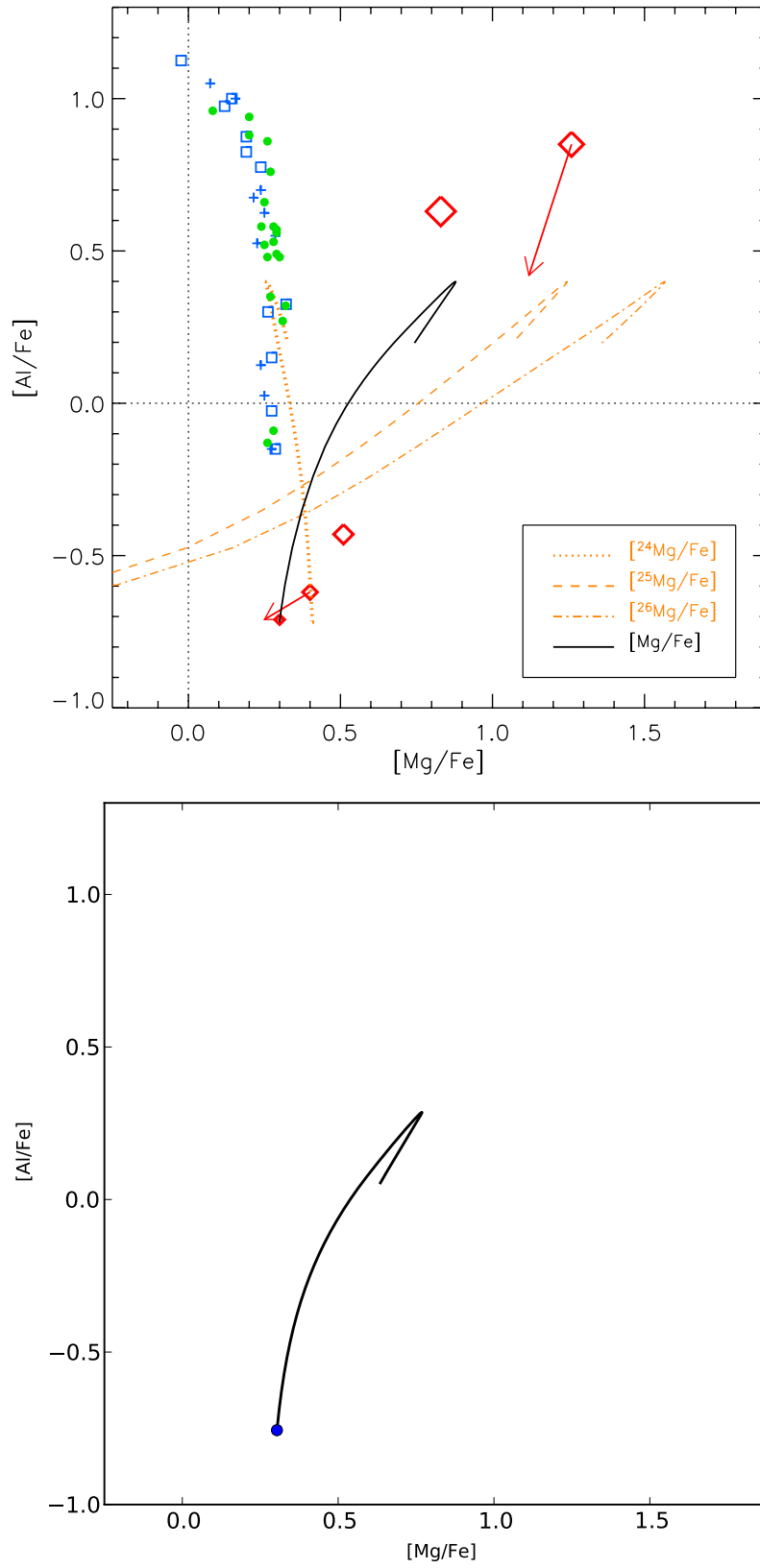
Figure 1.10 Evolution of Al and Mg abundances from Fenner et al. (2004) (top) and with Evel ChemEvol (bottom).

1.6.   Outline of the Thesis

This thesis presents new theoretical models of stellar evolution, nucleosynthesis, and chemical evolution, which we compare with observational data in the literature on planetary nebulae, post-AGB stars, and globular clusters.

We address the following questions:

- Are the low sulphur abundances in planetary nebulae and post-AGB stars caused by nuclear reactions in their precursor AGB stars?

- How can we constrain the mixing process that forms ^{13}C pockets in AGB stars?

- What is the origin of the *s*-process-rich material in M4 and M22?

- On what timescale did the *s*-process enrichment of M4 and M22 take place?

- How do high helium abundances affect the evolution, nucleosynthesis, and final fates of AGB stars?

- What are the chemical yields of He-rich intermediate-mass AGB stars?

Chapter 2 investigates the sulphur anomaly in planetary nebulae and post-AGB stars.

Chapter 3 analyses the *s*-process enrichment of the globular clusters M4 and M22 using a chemical evolution code developed by the candidate.

Chapter 4 focuses on the evolution and nucleosynthesis of stars with the high helium abundances found in globular cluster systems.

The main findings of these chapters are summarised in Chapter 5, where we also discuss the implications of this work and give some directions for future research.

CHAPTER 2

Is the sulphur anomaly in planetary nebulae caused by the s-process?

This chapter has been published as 'Is the sulphur anomaly in planetary nebulae caused by the s-process?',
Shingles, Luke J.; Karakas, Amanda I., 2013, MNRAS, 431, 3.

2.1. Chapter Summary

Motivated by unexplained observations of low sulphur abundances in planetary nebulae (PNe) and the PG1159 class of post asymptotic giant branch (AGB) stars, we investigate the possibility that sulphur may be destroyed by nucleosynthetic processes in low-to-intermediate mass stars during stellar evolution. We use a 3 $M_\odot$, Z = 0.01 evolutionary sequence to examine the consequences of high and low reaction rate estimates of neutron captures onto sulphur and neighbouring elements. In addition we have also tested high and low rates for the neutron producing reactions $^{13}C(\alpha,n)^{16}O$ and $^{22}Ne(\alpha,n)^{25}Mg$. We vary the mass width of a partially mixed zone (PMZ), which is responsible for the formation of a ^{13}C pocket and is the site of the $^{13}C(\alpha,n)^{16}O$ neutron source. We test PMZ masses from zero up to an extreme upper limit of the entire He-intershell mass at 10^{-2} $M_\odot$. We find that the alternative reaction rates and variations to the PMZ have almost no effect on surface sulphur abundances and do not reproduce the anomaly. To understand the effect of initial mass on our conclusions, 1.8 $M_\odot$ and 6 $M_\odot$ evolutionary sequences are also tested with similar results for sulphur abundances. We are able to set a constraint on the size of the PMZ, as PMZ sizes that are greater than half of the He-intershell mass

(in the 3 $M_\odot$ model) are excluded by comparison with neon abundances in planetary nebulae. We compare the 1.8 $M_\odot$ model's intershell abundances with observations of PG1159-035, whose surface abundances are thought to reflect the intershell composition of a progenitor AGB star. We find general agreement between the patterns of F, Ne, Si, P, and Fe abundances and a very large discrepancy for sulphur where our model predicts abundances that are 30-40 times higher than is observed in the star.

2.2.   Introduction

After leaving the asymptotic giant branch (AGB), a post-AGB star may evolve to high temperatures ($> 30,000$ K) on the timescale required to ionise the surrounding shell of ejected material and become visible as a planetary nebula (PN). As PNe are composed of envelope material from a progenitor AGB star, measurements of PN chemical abundances provide a way to test the predictions of AGB nucleosynthesis models (e.g., Marigo et al. 2003; Karakas et al. 2009; Pottasch & Bernard-Salas 2010; Karakas & Lugaro 2010).

Many planetary nebulae (PNe) with approximately solar oxygen abundance (±0.4 dex) have been found to have sulphur depletions of between 0.1 and 0.6 dex relative to the Sun (Marigo et al. 2003). A more detailed investigation with a larger sample of 85 PNe by Henry et al. (2004) discovered that sulphur abundances in PNe are systematically lower than HII regions at the same metallicity, where metallicity in PNe is measured indirectly through the oxygen abundance. Specifically, Henry et al. (2004) showed that the abundance trends between PNe and HII regions are co-linear in the Ne-O, Cl-O, and Ar-O planes, but are separated in the S-O plane, in which the trend-line of PNe is located below that of HII regions by 0.3 dex. The co-linear trends between Ne, Cl, Ar, and O, but not S single out sulphur as the anomalous element, and this has been labelled the 'sulphur anomaly'. The sulphur anomaly has been independently confirmed by the observations of Milingo et al. (2010).

Henry et al. (2004) argued that because AGB models do not predict significant depletion of sulphur and sulphur does not readily condense into dust grains, the most likely cause of the sulphur anomaly is a failure to correctly account for sulphur in the highly ionised S^{+3} state through the use of an Ionisation Correction Factor (ICF) and measurements of S^{+1} and S^{+2} abundances. However, infrared observations of PNe (e.g., Bernard-Salas et al. 2008) have directly measured S^{+3} abundances using the [S IV] emission line at 10.5 μm. This was done without the need for an ICF and these observations show that the sulphur anomaly still exists and is in need of explanation.

If the observed low gas phase abundance of sulphur in PNe relative to the interstellar medium (ISM; as sampled by HII regions) reflects a decrease in elemental sulphur between

the birth composition of a star and its surface layers at the final phases of stellar evolution, then an attractive solution would be to identify a nucleosynthetic process that is able to destroy sulphur during the intervening stages. The progenitors of planetary nebulae are typically low-mass stars (e.g., 1.0 to 2.5 $M_\odot$; Pottasch et al. 2011), which evolve through the AGB phase and experience nucleosynthesis through H and He burning and the slow neutron capture process (*s*-process) (e.g., Gallino et al. 1998; Busso et al. 1999). During the AGB, nucleosynthesis products are periodically dredged up into the convective hydrogen-rich envelope as part of the thermal pulse cycle, so a depletion of sulphur in the He-intershell of an AGB star would result in a (smaller) depletion of sulphur at the stellar surface. A review of AGB evolution and modelling is given by Herwig (2005).

Henry et al. (2012) provide an update on the status of the sulphur anomaly and discuss the still viable explanations, including gas phase depletion due to dust or molecule formation, and the nuclear processing in AGB stars. Although it was argued that the sulphur anomaly is inconsistent with the predictions of existing nucleosynthesis models (e.g., Karakas 2010), there has not been an investigation into how modelling uncertainties such as nuclear reaction rates and the treatment of mixing affect predictions of surface sulphur abundances.

There is a separate physical site with unexplained sulphur depletion in stars of the type PG1159. PG1159 stars are extremely hot (75,000-200,000 K) post-AGB stars that are hydrogen deficient and helium rich, likely because of a late or very late helium shell flash that has consumed their remaining hydrogen envelope and exposed He-intershell material to the stellar surface (van Winckel 2003; Werner et al. 1991). Although a very late thermal pulse and hydrogen ingestion episode may lead to some additional light element and *s*-process nucleosynthesis after the AGB (Herwig et al. 2011; Stancliffe et al. 2011), the resulting surface abundances are expected to largely reflect the intershell composition at the end of the AGB phase. With intershell matter at their surfaces, PG1159 stars provide a test of nucleosynthesis models that is relatively free of the uncertainties related to dredge-up efficiency that affect the surface abundances of AGB stars.

Werner & Herwig (2006) report that PG1159 stars have highly scattered and generally low sulphur abundances ranging from 0.01-1 times solar, while the models of Herwig show He-intershell sulphur abundances at the end of the AGB that are 0.6-0.9 times solar. They suggest that a study is needed to understand how the uncertainties of neutron capture cross sections affect intershell abundances. Werner et al. (2009) interprets the discrepancy between low sulphur observations of PG1159 stars and sulphur preserving theoretical models as a failure of stellar modelling. If the current models' failure to reproduce the sulphur anomaly is an indication that our understanding of stellar nucleosynthesis is in need of refinement, then a solution to the sulphur problem may lead to a better understanding of other aspects of stellar nucleosynthesis, such as the mixing near convective boundaries and nuclear reaction rates.
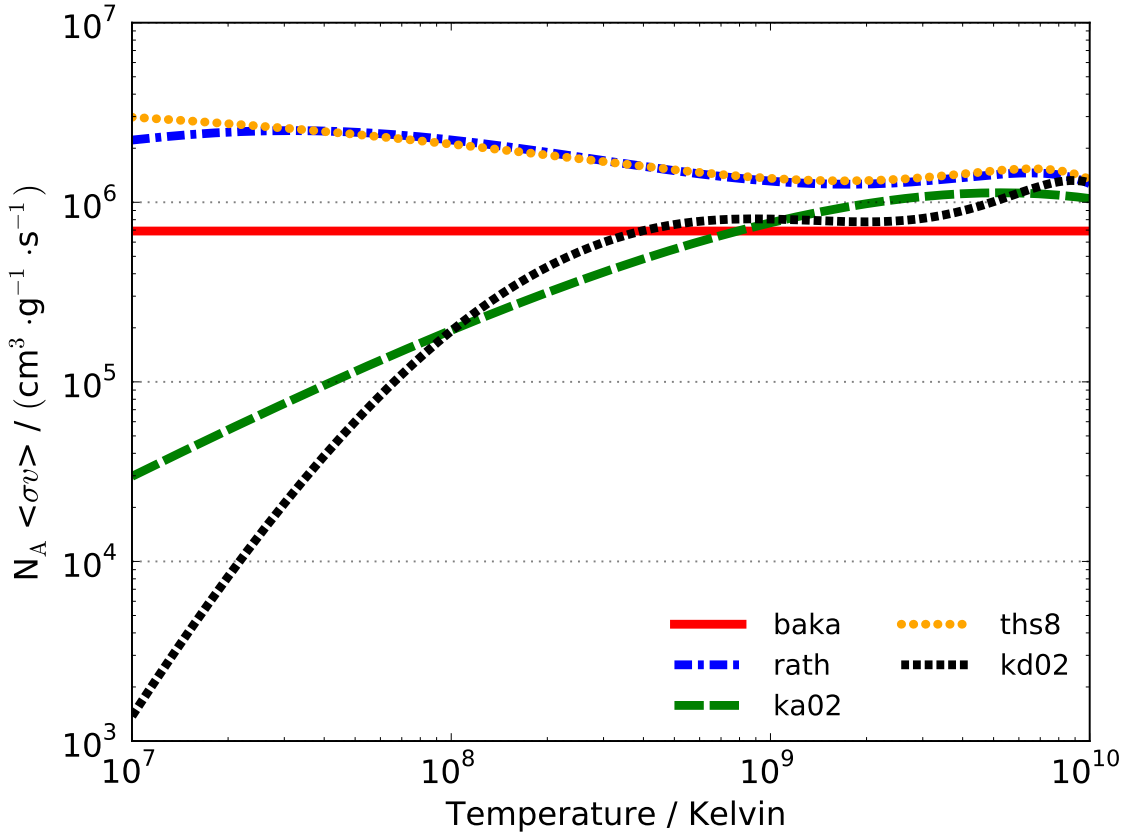
Figure 2.1 Reduced reaction rates for $^{32}S(n,\gamma)^{33}S$ as a function of temperature from several sources in the JINA Reaclib database (Cyburt et al. 2010). Source labels are defined in Section 2.3.1.

Sulphur has a significant nuclear charge ($Z = 16$) that prevents it from strongly participating in charged-particle reactions (e.g., p- and α-capture) at the temperatures and densities of AGB stellar interiors. For sulphur destruction, the much more likely pathway is neutron capture on S to produce the unstable isotopes ^{35}S and ^{37}S, which spontaneously decay via β^- to ^{35}Cl and ^{37}Cl, respectively. Although neutron-capture reactions with S are included in existing models, there is disagreement over the rates of these reactions that becomes particularly significant at temperatures below 10^9 K. The disparity is evident in Figure 2.1, which shows the rate of the $^{32}S(n,\gamma)^{33}S$ reaction as a function of temperature from several sources in the JINA Reaclib database (Cyburt et al. 2010). Most neutron captures at the top of the He-intershell take place at a temperature of the order of 10^8 K, and at this temperature the independently predicted rates disagree by up to factor of 10. At temperatures less than 10^7 K, the neutron capture rates diverge rapidly and differ by over three orders of magnitude.

In this paper, we aim to determine whether the sulphur anomaly in PNe is the consequence of the nucleosynthetic processes in PN-progenitor AGB stars. To do this, we calculate models that span the range of relevant uncertainties in modelling low-mass stars – neutron-capture reaction rates, neutron-producing reaction rates, and partial mixing zone profiles (which determine the size of the ^{13}C-pockets) and compare their surface abundances to

PNe observational data. We will examine the intershell abundances of our models in comparison with PG1159 observations and consider the significance that extra mixing (e.g., convective overshoot and rotation) could have reproducing the sulphur anomaly in PNe.

2.3.   Numerical Method & Models

We evolve our stellar evolutionary sequences from the zero-age main sequence to the tip of the AGB with the Mount Stromlo Stellar Structure Program, which has been updated to include C- and N-rich low temperature opacity tables from Lederer & Aringer (2009), as described in Karakas et al. (2010b) and references therein. We use Reimers' formula (Reimers 1975) with the parameter $\eta = 0.4$ for mass loss during the first red giant branch and the Vassiliadis & Wood (1993) prescription on the AGB.

The evolutionary code operates on a minimal set of nuclides that are involved in reactions that are highly exothermic (the pp-chains, CNO cycle, triple-α, and $^{12}C(\alpha,\gamma)^{16}O$ reactions) and hence affect the stellar structure. The structure model generated by the evolutionary code is used as input to a post-process nucleosynthesis code. With time- and mass-dependent variables such as temperature, density, and the locations of convective boundaries defined in the structure model, the nucleosynthesis code recalculates abundances for a detailed network with time-dependent diffusive mixing for all convective zones (Cannon 1993).

As the energy generation in the He-flash convective zone is completely dominated by the triple-α reaction included in the structure model, we are able to modify the rates of weakly energetic or endothermic α- and n-capture reactions and add a partially mixed zone (Section 2.3.2) in the nucleosynthesis post-process without having to recalculate the stellar structure. In this work, our detailed nuclear network consists of 125 species, which include many isotopes of P, S, and Cl to precisely account for the neutron-capture and β-decay reactions around sulphur.

Our chosen initial mass of 3.0 $M_\odot$ is near the upper end of PN progenitor masses. As shown in the results of Karakas & Lattanzio (2007), 3.0 $M_\odot$ models experience a greater number of thermal pulses and third dredge-up than lower mass models, so this choice will exaggerate the effect of any possible sulphur depletion on surface abundances.

For our initial composition, we scale the solar abundances of Asplund et al. (2009) ($Z_\odot = 0.0142$) such that the models' metallicity is $Z = 0.704\,Z_\odot = 0.01$. The models' final metallicity will be roughly a factor of two larger than the initial value (mostly due to the dredge-up of primary ^{12}C during the thermally pulsing AGB phase), so the model will lie

just above the centre of the PNe metallicity range of $0.3\,Z_\odot$ to $2\,Z_\odot$ (Sterling & Dinerstein 2008).

2.3.1.   Changes to Reaction Rates

To explore the effect of rate uncertainties for neutron-capture reactions with sulphur and its nuclear neighbours, we select the two sources in the JINA Reaclib database that predict the highest and lowest rates for ^{32}S(n,γ)^{33}S around the intershell temperature of 10^8 K. Our standard rate case is the ReaclibV0.5 release by Cyburt et al. (2010), which, for this reaction includes experimental estimates from the KADoNiS database (Dillmann et al. 2006) labelled 'ka02'. The source that predicts the lowest rate, 'kd02' is very similar to 'ka02', except that fitting formulae have been adjusted to maintain accuracy at low temperatures. The highest rate source, 'ths8' is comprised of theoretical estimates by Thomas Rauscher that were included as part of the REACLIB V1.0 release (Cyburt et al. 2010). The current ReaclibV2.0 release has adopted 'kd02' rates for the ^{32}S(n,γ)^{33}S reaction. Also included in Figure 2.1 are the experimental rates of Bao & Kappeler (1987) (labelled 'baka'), and the statistical model calculations by Rauscher & Thielemann (2000) ('rath'), however, these rates have not been adopted in this study.

2.3.2.   Partial Mixing Zone

The free neutrons available for the s-process in low-mass stars are primarily produced by ^{13}C burning under radiative conditions via the ^{13}C(α,n)^{16}O reaction (Straniero et al. 1995; Gallino et al. 1998). Producing the seed ^{13}C nuclei in stellar models requires the existence of a layer at the top of the ^{12}C-rich intershell in which protons are 'partially mixed' down from the envelope, thus enabling the CN cycle reaction ^{12}C(p,γ)^{13}N(β^+)^{13}C. The mixing process cannot be too efficient, or else the newly-created ^{13}C nuclei will be destroyed by further proton capture to make ^{14}N, which is a neutron poison, i.e., its large neutron-capture cross section significantly reduces the number of free neutrons available for the s-process. The physical mechanism behind the formation of a partially mixed zone (PMZ) is still a mystery, although some of the more likely possibilities include convective overshooting (Herwig 2000; Cristallo et al. 2004), rotational mixing (Herwig & Langer 2001), or gravity-wave driven mixing (Denissenkov & Tout 2003).

Some models in the literature insert a ^{13}C pocket directly at each thermal pulse, using a profile such as the Gallino et al. (1998) standard (ST) case, which has a ^{13}C pocket mass of 5×10^{-4} M$_\odot$. Herwig & Langer (2001) use a diffusive convective overshoot at the bottom of the envelope convection boundary with the parameter $f = 0.016$ and find a ^{13}C pocket width (where the ^{13}C mass fraction is above 10^{-4}) of about 2×10^{-5} M$_\odot$ in a 3 M$_\odot$ model.

To experiment with different ^{13}C pocket masses, the studies of Arlandini et al. (1999) and Bisterzo et al. (2010, 2012) insert a Gallino et al. (1998) ST profile ^{13}C (and ^{14}N) pocket that has been scaled in ^{13}C (and ^{14}N) abundance. We instead scale the width (in mass coordinate) of an inserted proton profile, which not only controls the total mass of protons inserted (and the mass of the resulting ^{13}C and ^{14}N pockets) but also changes the radial position and extent over which the resulting neutron-captures take place. For a comparison involving both of these treatments of the ^{13}C pocket, see the detailed discussion in Lugaro et al. (2012).

Figure 2.2 shows the ^{13}C and ^{14}N pockets that form as a result of an exponential profile of protons inserted below the envelope convection zone. The protons are inserted identically after every thermal pulse with third dredge-up, at the time when the envelope convection zone reaches its deepest extent during a third dredge-up episode. The proton profile matches the envelope abundance at top of the PMZ and decreases exponentially to a mass fraction of 10^{-4} across a mass interval we refer to as the 'PMZ mass'. This method is described in more detail in Lugaro et al. (2004) and is very similar to that used by Goriely & Mowlavi (2000).

To explore the results of exaggerated neutron capture nucleosynthesis, we test 3 M$_\odot$ models with PMZ masses of (1, 5, and 10) $\times 10^{-3}$ M$_\odot$ in addition to a model with no partial mixing zone. Unless otherwise stated, we use our standard PMZ with a mass of 1×10^{-3} M$_\odot$. The PMZ mass of 10×10^{-3} M$_\odot$ is included as an extreme upper limit for for the 3 M$_\odot$ model, as this profile spans the entire He-intershell and the partial mixing is not expected to penetrate into the degenerate C-O core.
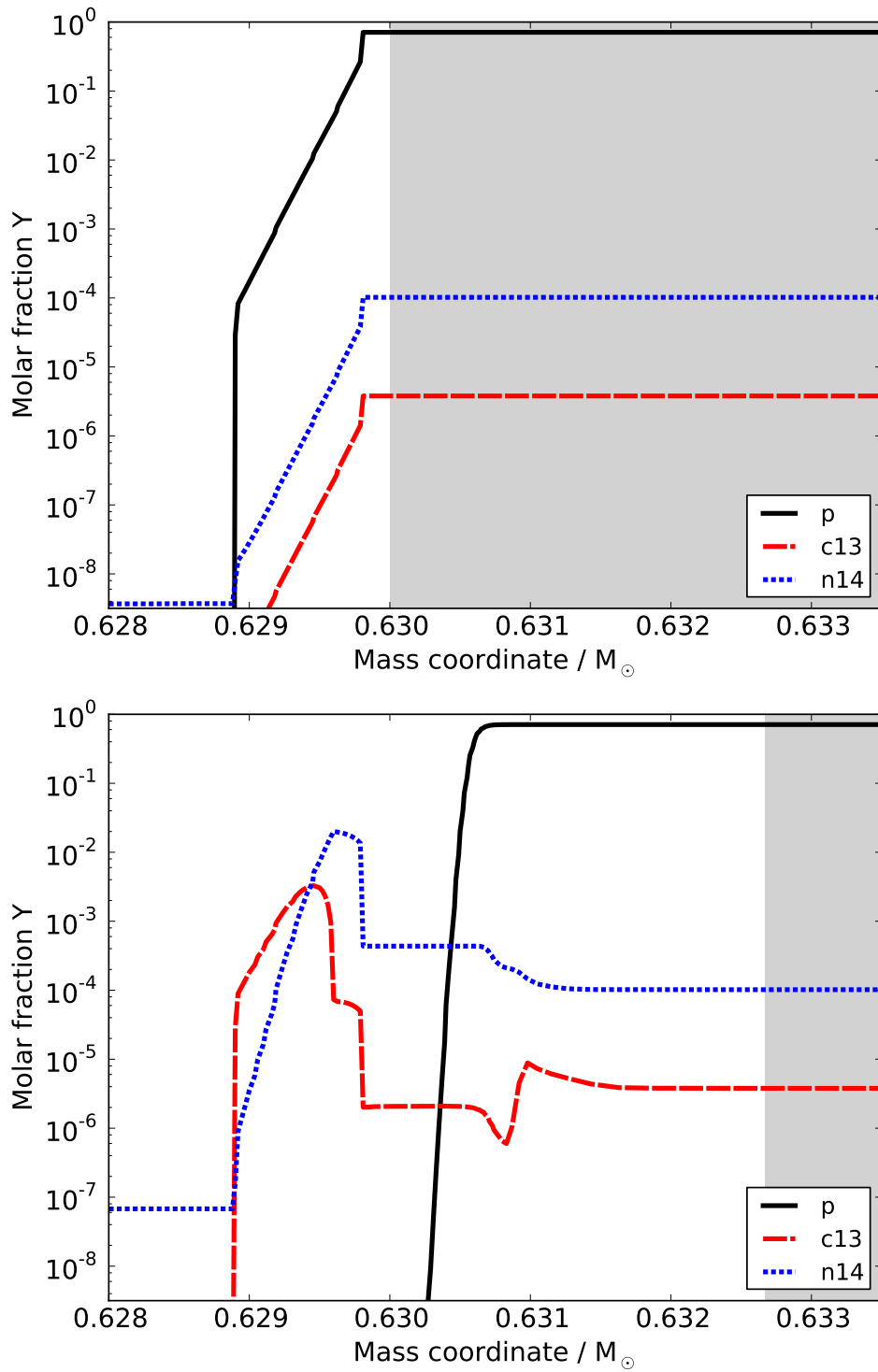
Figure 2.2 Upper panel: The 3 $M_\odot$ model proton profile immediately after inserting a 10^{-3} $M_\odot$ partial mixing zone. Lower panel: As the envelope convection zone (shaded) retreats outwards in mass, proton capture reactions result in adjacent pockets of ^{13}C and ^{14}N forming near the top of the intershell. Y denotes the molar fraction, equal to (mass fraction) / (atomic mass).

2.4.   Model Results

2.4.1.   New Stellar Evolutionary Models

The 1.8 $M_\odot$ model has previously been described in Karakas et al. (2010b). We present new 3 $M_\odot$ and 6 $M_\odot$ sequences at $Z = 0.01$ computed with Mount Stromlo evolutionary code.

Table 2.1 and Table 2.2 list the structural parameters of each thermal pulse (TP) in the 3 $M_\odot$ and 6 $M_\odot$ models, respectively. The parameters include the total mass (M_{tot}) and the H-exhausted core mass (M_H) measured at the beginning of the TP, the mass dredged-up into the envelope (ΔM_{DUP}) and the dredge-up efficiency parameter ($\lambda = \Delta M_{DUP}/\Delta M_H$, where Δ denotes the change between the previous and current TP) measured after the TP. Also included are the maximum temperatures of the He- and H-burning shells ($T_{He-shell}$, $T_{H-shell}$) during the TP. In the interpulse period (τ_{ip}), we sample the maximum temperature at the base of the convective envelope (T_{bce}), the minimum luminosity (L_{max}), the maximum stellar radius (R_{max}), the minimum bolometric magnitude (M_{bol}), the minimum effective temperature (T_{eff}), and the carbon-to-oxygen number ratio (C/O).

In our 3 $M_\odot$ model, the temperature at the base of the convective envelope never exceeds

Table 2.1   Structural and dredge-up parameters of the 3 $M_\odot$, $Z = 0.01$ sequence for each thermal pulse cycle during the AGB. Columns are described in Section 2.4.1.

TP #	M_{tot} [$M_\odot$]	M_H [$M_\odot$]	ΔM_{DUP} [$10^{-3} M_\odot$]	λ	$T_{He-shell}$ [10^6 K]	$T_{H-shell}$ [10^6 K]	T_{bce} [10^6 K]	τ_{ip} [10^3 yr]	L_{max} [$10^3 L_\odot$]	R_{max} [$R_\odot$]	M_{bol} [mag]	T_{eff} [K]	C/O
1	2.99	0.607	0.00	0.00	181.6	53.0	2.3	0.00	3.5	146	-4.15	3797	0.36
2	2.99	0.610	0.00	0.00	214.1	57.3	2.7	58.27	5.0	188	-4.52	3775	0.36
3	2.99	0.614	0.00	0.00	226.3	58.9	2.8	77.52	5.6	204	-4.65	3749	0.37
4	2.99	0.619	0.00	0.00	238.2	60.7	3.0	84.12	6.3	223	-4.78	3715	0.37
5	2.99	0.625	0.00	0.00	245.6	62.0	3.2	85.53	6.9	238	-4.87	3682	0.37
6	2.99	0.631	0.90	0.14	253.0	63.1	3.3	83.52	7.4	251	-4.95	3580	0.37
7	2.99	0.637	2.42	0.34	261.7	64.3	3.5	82.65	7.9	265	-5.03	3520	0.39
8	2.99	0.642	3.71	0.47	269.7	65.4	3.8	81.83	8.5	278	-5.10	3474	0.48
9	2.99	0.647	5.24	0.61	273.0	66.2	4.0	81.51	9.0	290	-5.16	3437	0.63
10	2.99	0.651	6.57	0.70	278.9	66.8	4.3	82.36	9.5	303	-5.22	3410	0.84
11	2.99	0.655	7.32	0.72	283.1	67.3	4.6	82.72	9.9	313	-5.27	3387	1.07
12	2.99	0.658	8.01	0.76	287.2	67.6	5.0	81.37	10.3	318	-5.31	3377	1.30
13	2.98	0.661	8.49	0.77	290.8	67.8	4.9	80.67	10.7	352	-5.35	3258	1.53
14	2.98	0.664	8.77	0.78	294.0	68.0	5.1	78.92	11.0	371	-5.38	3198	1.78
15	2.98	0.666	8.81	0.78	296.5	68.2	5.2	76.91	11.3	391	-5.41	3145	2.03
16	2.98	0.669	9.00	0.80	298.6	68.3	5.3	74.18	11.6	409	-5.44	3097	2.27
17	2.97	0.671	8.89	0.78	300.8	68.5	0.0	72.56	11.8	426	-5.46	3055	2.50
18	2.96	0.673	8.83	0.80	301.7	68.6	5.5	69.27	12.1	444	-5.48	3019	2.74
19	2.92	0.676	8.99	0.81	302.8	68.7	5.6	67.58	12.3	460	-5.50	2983	2.98
20	2.83	0.678	8.98	0.81	304.9	68.8	5.6	65.74	12.5	482	-5.52	2948	3.23
21	2.17	0.680	7.85	0.71	305.8	68.8	5.4	63.95	12.6	581	-5.53	2901	3.48
22	1.23	0.682	7.09	0.72	303.6	68.4	3.4	58.91	12.5	843	-5.52	2633	3.79

Table 2.2 Structural and dredge-up parameters of the 6 $M_\odot$, $Z = 0.01$ sequence for each thermal pulse cycle during the AGB. Columns are described in Section 2.4.1.

TP #	M_{tot} [$M_\odot$]	M_H [$M_\odot$]	ΔM_{DUP} [10^{-3} $M_\odot$]	λ	$T_{He-shell}$ [10^6 K]	$T_{H-shell}$ [10^6 K]	T_{bce} [10^6 K]	τ_{ip} [10^3 yr]	L_{max} [10^3 $L_\odot$]	R_{max} [$R_\odot$]	M_{bol} [mag]	T_{eff} [K]	C/O
1	5.95	0.911	0.00	0.00	236.7	76.9	31.4	0.00	23.1	436	-6.19	3518	0.37
2	5.95	0.912	0.07	0.09	247.3	78.1	38.6	3.23	24.0	449	-6.23	3494	0.37
3	5.95	0.913	0.28	0.30	256.5	79.3	46.9	3.36	25.0	462	-6.27	3486	0.37
4	5.95	0.914	0.54	0.51	264.9	80.4	56.0	3.44	26.2	478	-6.32	3475	0.37
5	5.95	0.914	0.71	0.60	272.7	81.4	62.7	3.53	27.6	498	-6.38	3465	0.38
6	5.95	0.915	0.93	0.73	279.6	82.2	66.6	3.65	29.0	519	-6.44	3457	0.38
7	5.95	0.915	1.10	0.79	286.7	83.0	69.4	3.77	30.4	537	-6.49	3449	0.38
8	5.95	0.916	1.26	0.84	293.0	83.7	71.6	3.92	31.7	554	-6.53	3446	0.35
9	5.95	0.916	1.41	0.87	299.2	84.4	73.5	4.10	32.7	569	-6.57	3426	0.31
10	5.95	0.917	1.56	0.90	304.8	85.0	75.3	4.28	33.6	580	-6.60	3398	0.25
11	5.95	0.917	1.56	0.84	310.3	85.7	77.0	4.49	34.3	590	-6.62	3376	0.18
12	5.95	0.917	1.65	0.88	313.8	86.2	78.5	4.55	34.7	596	-6.63	3347	0.13
13	5.94	0.917	1.83	0.90	319.6	86.9	80.0	4.85	35.4	603	-6.65	3344	0.09
14	5.94	0.918	1.95	0.93	323.6	87.5	81.2	4.99	35.7	609	-6.66	3326	0.07
15	5.94	0.918	2.06	0.93	328.0	88.0	82.1	5.19	36.3	616	-6.68	3319	0.06
16	5.93	0.918	2.11	0.92	330.6	88.3	82.8	5.30	36.9	625	-6.70	3308	0.06
17	5.93	0.918	2.19	0.93	334.7	88.6	83.2	5.42	37.4	631	-6.71	3294	0.06
18	5.92	0.919	2.25	0.93	338.0	88.9	83.6	5.52	37.9	638	-6.73	3288	0.06
19	5.91	0.919	2.30	0.93	340.4	89.1	83.9	5.62	38.4	644	-6.74	3278	0.06
20	5.90	0.919	2.36	0.94	342.8	89.3	84.1	5.69	38.8	651	-6.75	3269	0.06
21	5.88	0.919	2.41	0.94	344.7	89.4	84.4	5.79	39.2	657	-6.76	3265	0.06
22	5.86	0.920	2.21	0.84	346.1	89.5	84.5	5.86	39.6	663	-6.77	3257	0.06
23	5.84	0.920	2.22	0.84	347.4	89.6	84.6	5.92	39.9	668	-6.78	3251	0.06
24	5.80	0.920	2.54	0.95	347.5	89.7	84.7	5.94	40.2	673	-6.79	3244	0.07
25	5.75	0.920	2.56	0.94	348.5	89.8	84.8	6.06	40.4	678	-6.80	3237	0.07
26	5.69	0.920	2.57	0.94	350.8	89.8	84.8	6.06	40.5	682	-6.80	3228	0.07
27	5.60	0.921	2.35	0.86	354.2	89.8	84.7	6.05	40.5	686	-6.80	3216	0.07
28	5.46	0.921	2.45	0.89	350.2	89.7	84.5	6.04	40.4	690	-6.80	3205	0.08
29	5.17	0.921	2.63	0.95	352.0	89.6	84.1	6.10	40.1	695	-6.79	3193	0.08
30	4.85	0.921	2.67	0.94	352.3	89.4	83.3	6.25	39.3	700	-6.77	3169	0.08
31	4.54	0.921	2.69	0.94	348.0	89.0	82.4	6.27	38.0	704	-6.73	3137	0.09
32	4.23	0.921	2.72	0.94	351.0	88.7	81.2	6.32	36.7	709	-6.69	3104	0.11
33	3.94	0.922	2.75	0.95	347.9	88.2	79.5	6.38	35.4	712	-6.65	3072	0.13
34	3.64	0.922	2.80	0.95	354.1	87.8	77.4	6.51	34.0	715	-6.61	3042	0.15
35	3.36	0.922	2.86	0.95	351.3	87.3	74.3	6.65	32.6	717	-6.56	3011	0.20
36	3.08	0.922	2.90	0.94	352.5	86.7	69.1	6.91	31.1	720	-6.51	2981	0.29
37	2.79	0.923	2.97	0.95	354.6	86.0	57.5	7.24	29.6	730	-6.46	2944	0.41
38	2.50	0.923	3.03	0.95	352.9	85.3	39.2	7.67	28.5	754	-6.42	2901	0.56
39	2.21	0.923	3.05	0.93	357.7	84.7	22.3	7.99	27.7	783	-6.39	2856	0.74
40	1.92	0.923	3.11	0.97	359.2	84.1	6.7	7.92	27.2	809	-6.37	2817	0.95
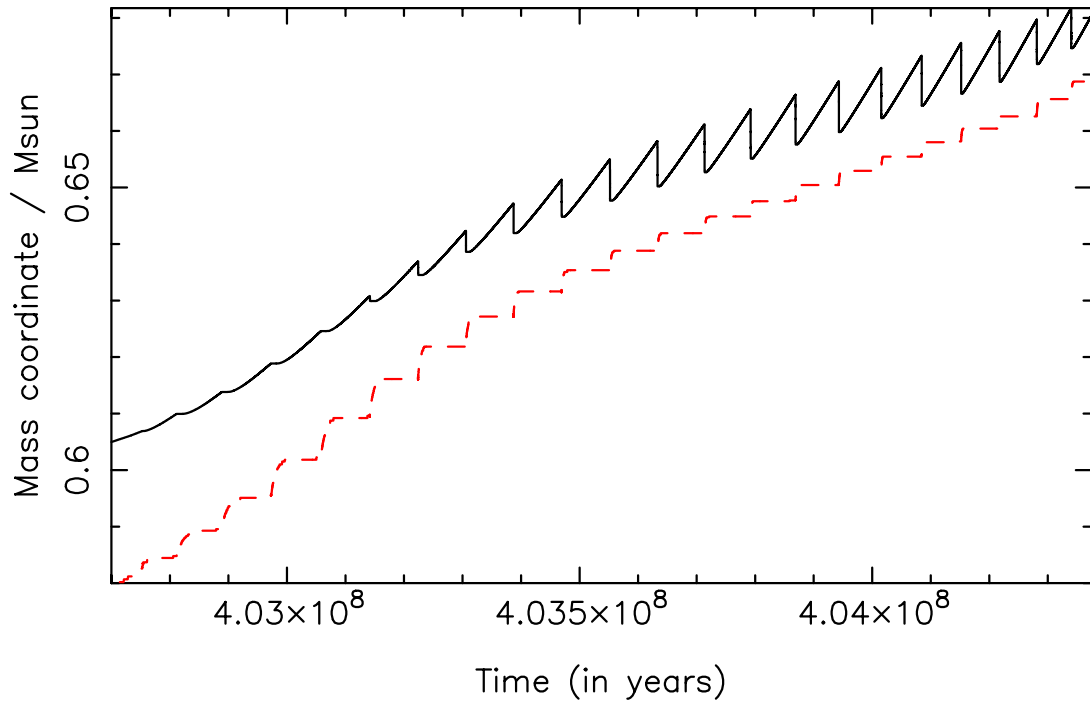
Figure 2.3 Mass of the He-exhausted (dashed) and H-exhausted (solid) cores during the thermally pulsing AGB phase as a function of time in the 3 M$_\odot$ model.

5.6×10^6 K, so there is no proton capture nucleosynthesis in the envelope (hot-bottom burning), which requires temperatures above about $(40–50) \times 10^6$ K. Without active CN-cycling in the envelope, third dredge-up raises the surface C/O ratio, eventually causing the model to become carbon-rich (C/O >1) after the 11th thermal pulse.

Envelope temperatures in the 6 M$_\odot$ model are in the range $(31–85) \times 10^6$ K, high enough that hot-bottom burning is active and prevents the surface from becoming carbon-rich up to the last (40th) thermal pulse, at which time the C/O ratio is 0.95. At the end of the AGB, the C/O ratio has increased to 1.16.

The maximum temperature in the helium burning shell generally increases with thermal pulse number in the 3 M$_\odot$ model, reaching a temperature of about 300×10^6 K after the 15th thermal pulse. Above about 300×10^6 K, the ^{22}Ne(α,n)^{25}Mg reaction starts to become active, producing a burst of neutrons at the base of the intershell during convective thermal pulses. The ^{22}Ne neutron source operates in addition to the ^{13}C source, so this indicates that the intershell matter will be subject to additional neutron captures over the last few thermal pulses.

The 3 M$_\odot$ model experiences a total of 22 thermal pulses before the AGB phase is terminated by mass loss at a final core mass of 0.68 M$_\odot$ (Figure 2.3). At this time, the total amount of intershell matter that has been dredged up into the envelope is 0.120 M$_\odot$. With an envelope mass of about 2 M$_\odot$ for most of the AGB, there is enough material dredged up

that the results of neutron capture nucleosynthesis in the He-intershell will be evident in the surface abundances of the model. This amount of dredge-up is a factor of a few compared to our evolutionary models with initial masses of 1.8 $M_\odot$ and 6 $M_\odot$, which dredge up a total of 0.041 $M_\odot$ and 0.082 $M_\odot$ of intershell matter, respectively.

The cumulative dredge-up quantity of 0.12 $M_\odot$ in our 3 $M_\odot$, $Z = 0.01$ model is comparable to other models of the same mass and similar metallicity. Lugaro et al. (2003) compare 3 $M_\odot$, $Z = 0.02$ models (the same mass but higher metallicity than our model) that have been computed independently with the Mount Stromlo stellar structure program, FRANEC (Gallino et al. 1998), and EVOL (as used by Herwig 2000, with hydrodynamic overshoot included at all convective boundaries), finding cumulative dredge-up quantities of 0.08 $M_\odot$, 0.044 $M_\odot$, and 0.10 $M_\odot$, respectively. A 3 $M_\odot$, $Z = 0.02$ model calculated with the Cambridge STARS code, which computes mixing and burning as a single step, dredges up a total of 0.13 $M_\odot$ after 20 thermal pulses in Stancliffe et al. (2004).

2.4.2.   Nucleosynthesis Model Results

Table 2.3 presents the final surface abundance results of the 3 $M_\odot$ model with standard ('ka02') and alternative neutron capture rates ('kd02' and 'ths8') and several partial mixing zone sizes (0, 1, 5, and 10 $\times 10^{-3}$ $M_\odot$), as illustrated in Figure 2.4. The alternative neutron capture rates are seen to have little effect (< 0.001 dex) on the surface abundance of sulphur at the end of the AGB phase. The variations to the partial mixing zone size also leave sulphur abundances virtually unchanged. In each of our cases, the surface abundance of sulphur is not depleted but instead shows a very slight increase (< 0.03 dex) from pre-main sequence to the end of the AGB (Figure 2.4).

In Figure 2.5, we show surface abundance evolution in the S vs. O plane for 3 $M_\odot$ models with a range of PMZ sizes, as well as the 1.8 and 6 $M_\odot$ models for comparison with observational PNe abundances from Pottasch & Bernard-Salas (2010). Although it is unlikely for a 6 $M_\odot$ star to produce a detectable planetary nebula, the 6 $M_\odot$ abundances are included to show the extent to which our results are dependent on the stellar initial mass. An enhancement in O by up to 0.2 dex is seen in the 1.8 and 3 $M_\odot$ models, but this is not enough to explain the observational trend of PNe. Figure 2.6 showing the results in the S versus Ar plane confirms that neither S nor Ar are significantly processed during low-mass evolution, and that none of the models can account for the trend of low S abundances in PNe.

The sulphur abundance not only changes very little at the surface, but remains relatively constant throughout the entire stellar interior at the end of the AGB. The abundance discontinuity (Figure 2.7) at the intershell-envelope boundary shows the results of a small ^{32}S depletion in the intershell by conversion into more neutron-rich isotopes, indicated by

Table 2.3 Log ϵ^* surface elemental abundances, carbon-to-oxygen ratio (by number) and ^{12}C/^{13}C isotopic ratios at the end of the AGB in our 3 M$_\odot$, $Z = 0.01$ model.

	Ne	Mg	Si	S	P	Cl	Ar	C/O	^{12}C/^{13}C
scaled solar initial ($Z = 0.01$)	7.802	7.472	7.382	6.992	5.242	5.062	6.272	0.550	89.4391
m3z01-standard-pmz1	8.266	7.546	7.416	7.024	5.326	5.133	6.302	4.279	305.146
m3z01-kd02-pmz1	8.267	7.547	7.416	7.023	5.318	5.134	6.302	4.279	305.329
m3z01-ths8-pmz1	8.265	7.545	7.417	7.022	5.313	5.152	6.302	4.280	305.278
m3z01-ths8-pmz0	8.167	7.531	7.417	7.023	5.280	5.136	6.302	4.549	318.118
m3z01-ths8-pmz5	8.502	7.602	7.418	7.020	5.391	5.179	6.301	3.467	259.238
m3z01-ths8-pmz10	8.627	7.640	7.419	7.021	5.407	5.186	6.300	2.874	219.838

$^*\log \epsilon(X) = \log(N_X/N_H) + 12$
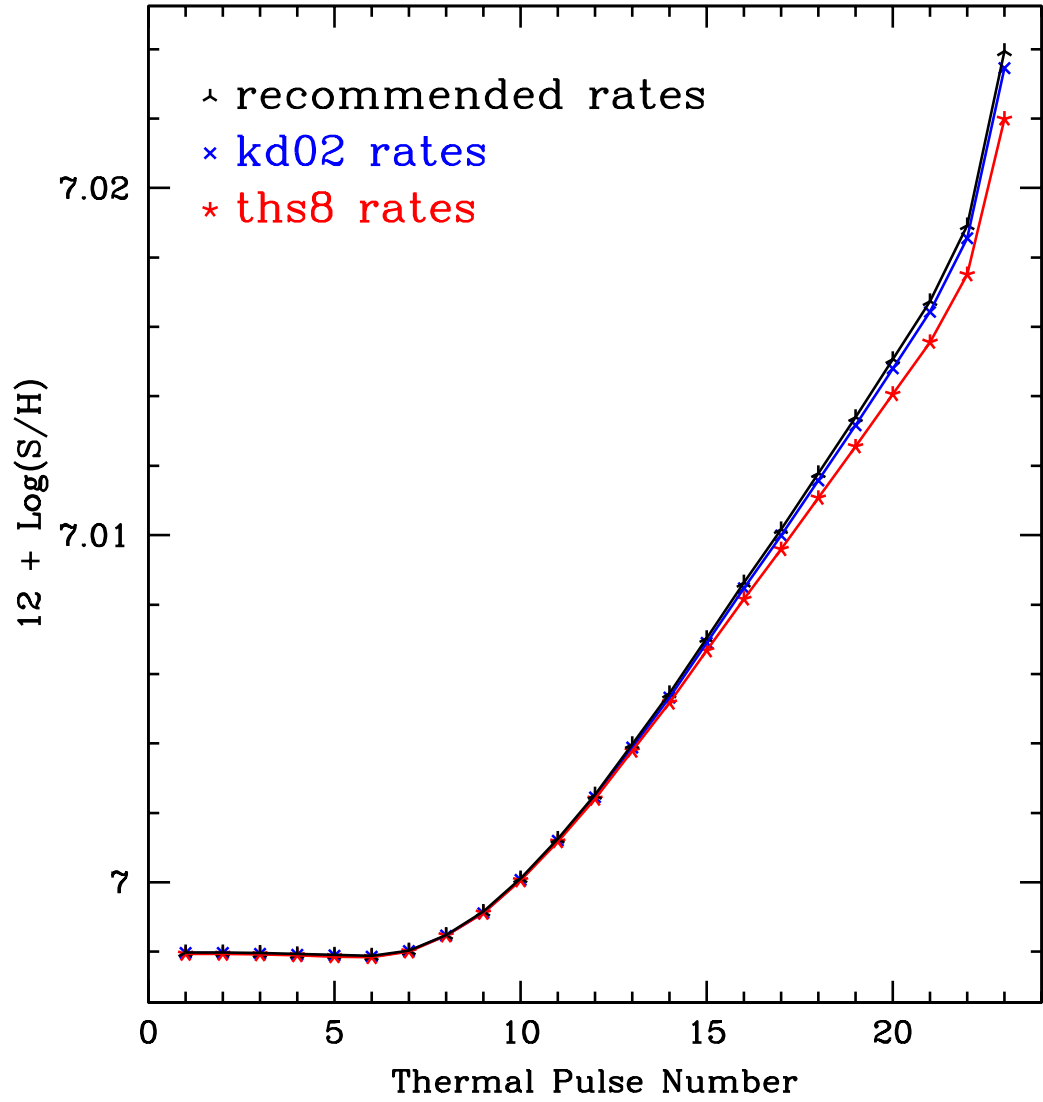
Figure 2.4 Surface sulphur abundance as a function of thermal pulse number during the AGB phase in the 3 M$_\odot$, $Z = 0.01$ model with a PMZ size of 10^{-3} M$_\odot$ and three neutron-capture rate sources.
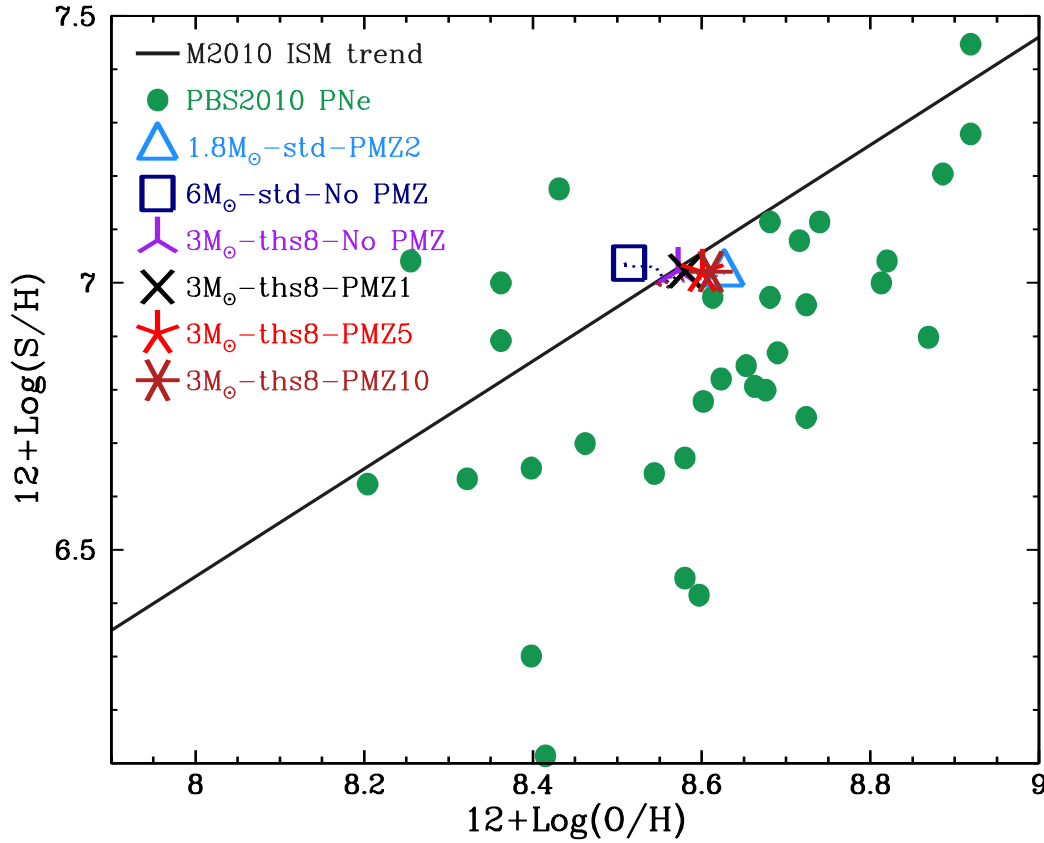
Figure 2.5 Surface abundance results in the S versus O plane for 3 $M_\odot$ models with PMZ sizes of (1, 5, and 10)$\times 10^{-3}$ $M_\odot$, the 1.8$M_\odot$ model with a 2×10^{-3} PMZ, and the 6 $M_\odot$ with no PMZ. Included for comparison are the PNe observational data of Pottasch & Bernard-Salas (2010) and the interstellar medium (ISM) trend of Milingo et al. (2010) from observations of HII regions and blue compact galaxies.

increase in ^{33}S, ^{34}S, ^{35}S, and ^{36}S abundances. The increase in ^{36}S abundance indicates that neutron captures onto unstable ^{35}S nuclei occur on a timescale comparable to its β^+-decay mean lifetime of 126.3 days (Audi et al. 2003). The sulphur depletion (by 22% or 0.1 dex) in the intershell is too small to resolve the sulphur anomaly in PNe, which requires sulphur depletions of typically 0.3 dex (and up to 0.6 dex) in the hydrogen-rich envelope.

From the results in Table 2.3, we see that the neon surface abundances increase significantly with increases to the mass of the partial mixing zone. The elemental increase in neon is due to ^{22}Ne production from primary ^{14}N in convective pulses via the reaction chain ^{14}N$(\alpha,\gamma)^{18}$F$(\beta^+)^{18}$O$(\alpha,\gamma)^{22}$Ne. The size of the PMZ correlates with the size of the resulting ^{14}N pocket, which adds to the quantity of ^{14}N available for the production of ^{22}Ne, as shown in Figure 2.8.

The position of our models with large PMZ sizes in the Ar versus Ne plane is far from the observational PNe data (Figure 2.8) and from this we conclude that the partial mixing zone widths larger than 5×10^{-3} $M_\odot$ (50% of the He-intershell mass in the 3 $M_\odot$ model)
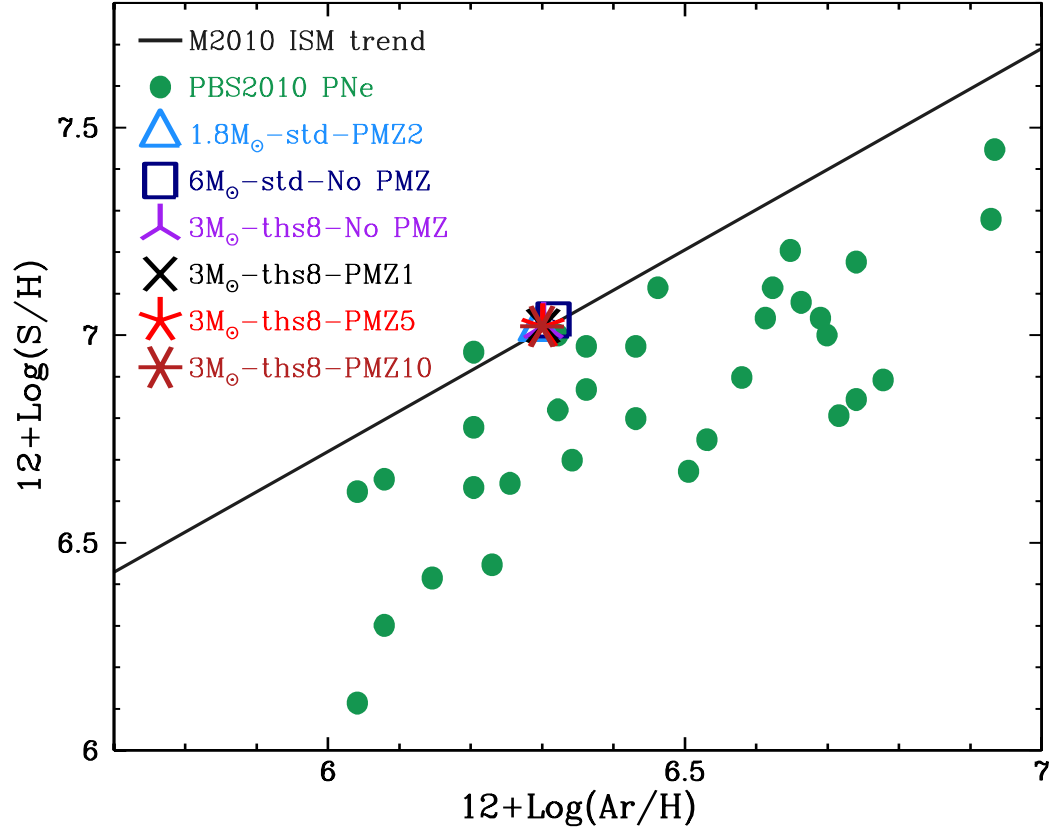
Figure 2.6 Same as Figure 2.5 but for S versus Ar.

Table 2.4 Final log ϵ^* surface abundances for 3 M$_\odot$, $Z = 0.01$ model with alternative rate sources: ^{13}C(α,n)^{16}O low and high estimates from Angulo et al. (1999, NACRE collaboration) and ^{22}Ne(α,n)^{25}Mg low, median, high, and high×600 rate tables from Iliadis et al. (2010). Our standard case for comparison uses the ReaclibV0.5 release, which includes fits to the NACRE adopted rates for both reactions.

	Ne	Mg	S	P	Cl	Ar
Initial	7.802	7.472	6.992	5.242	5.062	6.272
Standard (JINA ReaclibV0.5)	8.266	7.546	7.024	5.326	5.133	6.302
^{13}C(α,n)^{16}O NACRE-low	8.200	7.537	7.024	5.325	5.135	6.302
^{13}C(α,n)^{16}O NACRE-high	8.200	7.537	7.024	5.323	5.134	6.303
^{22}Ne(α,n)^{25}Mg Iliadis2010-low	8.207	7.516	7.024	5.319	5.128	6.303
^{22}Ne(α,n)^{25}Mg Iliadis2010-med	8.206	7.517	7.024	5.320	5.130	6.303
^{22}Ne(α,n)^{25}Mg Iliadis2010-high	8.205	7.517	7.024	5.320	5.130	6.303
^{22}Ne(α,n)^{25}Mg Iliadis2010-high-x600	7.868	8.068	7.017	5.686	5.146	6.295

* $\log \epsilon(X) = \log(N_X/N_H) + 12$

are excluded by the observations.

We have measured the effect of rate uncertainties on the two most important neutron-producing reactions by independently testing the high and low rates for ^{13}C(α,n)^{16}O
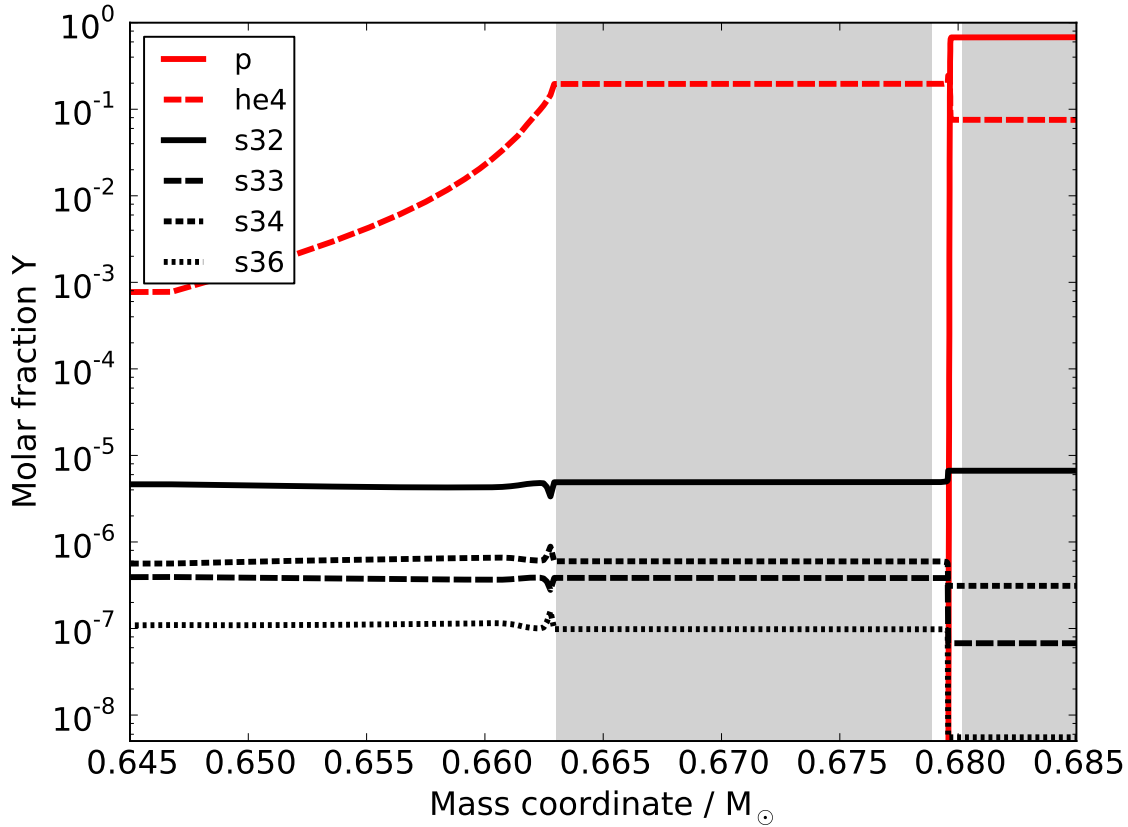
Figure 2.7   Abundances in the He-intershell after the second last thermal pulse of the 3 $M_\odot$, $Z = 0.01$ model with 'ths8' rates and a PMZ mass of 1×10^{-3} $M_\odot$. The shaded regions indicate convective zones.

from Angulo et al. (1999, NACRE collaboration) and high, low, and adopted rates for ^{22}Ne$(\alpha,$n$)^{25}$Mg from Iliadis et al. (2010). Table 2.4 shows that these alternative rates have little effect on sulphur.

As with most charged particle reactions, the rate of the ^{22}Ne$(\alpha,$n$)^{25}$Mg reaction is very highly temperature-sensitive. As an extreme example, if the He-burning shell temperature was significantly higher by 33% (0.4 GK[1] instead of 0.3 GK), then the Iliadis et al. (2010) high rate predicts a reaction rate increase from 3.01×10^{-11} to 1.80×10^{-8} cm$^3 \cdot$g$^{-1} \cdot$s^{-1}, i.e., a factor of 631. To simulate the effect of a highly increased He-shell temperature on neutron production, we test a model with ^{22}Ne$(\alpha,$n$)^{25}$Mg rates boosted by a factor of 600. The surface abundance results of the boosted reaction rates are listed in Table 2.4 and include: a reduction in Ne (0.3 dex), increase in Mg (0.5 dex), an increase in P (0.4 dex) and a small decrease in S (0.01 dex). The implications of these results discussed in Section 2.5.

Table 2.5 Top: observed surface abundances of PG1159 stars PG1159-035 and PG1144+005 with the Sun for comparison. Bottom: intershell abundance results of the models, measured during intershell convection at the last or second last thermal pulse. Rate definitions are given in the text.
References: (1) Asplund et al. (2009), (2) Jahn et al. (2007), (3) Werner et al. (2011), (4) Werner & Herwig (2006)

Stars

	Metallicity Z	Mass [M$_\odot$]	Mass Fractions C	O	F [10^{-7}]	Ne [10^{-2}]	Si [10^{-4}]	P [10^{-5}]	S [10^{-4}]	Fe [10^{-4}]
Solar[1]	0.014	1.00	0.003	0.006	3.66	0.14	7.3	0.58	3.4	14
Scaled Solar	0.010	-	0.002	0.004	2.44	0.09	4.9	0.39	2.3	9.5
PG1144+005[4]	-	0.60	0.570	0.016	100	2.00	-	-	-	-
PG1159-035[2,3]	$\simeq Z_\odot$	$0.536^{+0.068}_{-0.010}$	0.480	0.170	32.0	2.00	3.6	0.64	0.05	13

Models (Z = 0.01)

M$_{initial}$ [M$_\odot$]	Rates	M$_{PMZ}$ [M$_\odot$]	M$_f$ [M$_\odot$]	He-Intershell Mass Fractions C	O	F [10^{-7}]	Ne [10^{-2}]	Si [10^{-4}]	P [10^{-5}]	S [10^{-4}]	Fe [10^{-4}]
1.8	ka02	2×10^{-3}	0.59	0.167	0.012	202	2.19	5.0	2.2	2.2	8.3
3.0	kd02	1×10^{-3}	0.68	0.176	0.004	667	3.39	5.2	1.1	2.1	8.8
3.0	ka02	1×10^{-3}	0.68	0.175	0.004	657	3.39	5.1	1.2	2.2	8.9
3.0	ths8	No PMZ	0.68	0.183	0.002	547	2.56	5.3	5.2	2.0	9.4
3.0	ths8	1×10^{-3}	0.68	0.175	0.004	657	3.39	5.4	1.0	1.9	9.0
3.0	ths8	5×10^{-3}	0.68	0.146	0.006	809	6.26	5.6	2.4	1.8	7.8
3.0	ths8	10×10^{-3}	0.68	0.123	0.008	847	8.32	5.9	2.3	1.9	8.0
3.0	^{22}Ne-Il10-high-x600	1×10^{-3}	0.68	0.179	0.004	2700	0.18	12	13	1.6	1.6
6.0	ka02	No PMZ	0.98	0.201	0.004	65.1	1.22	9.8	3.5	1.7	4.4
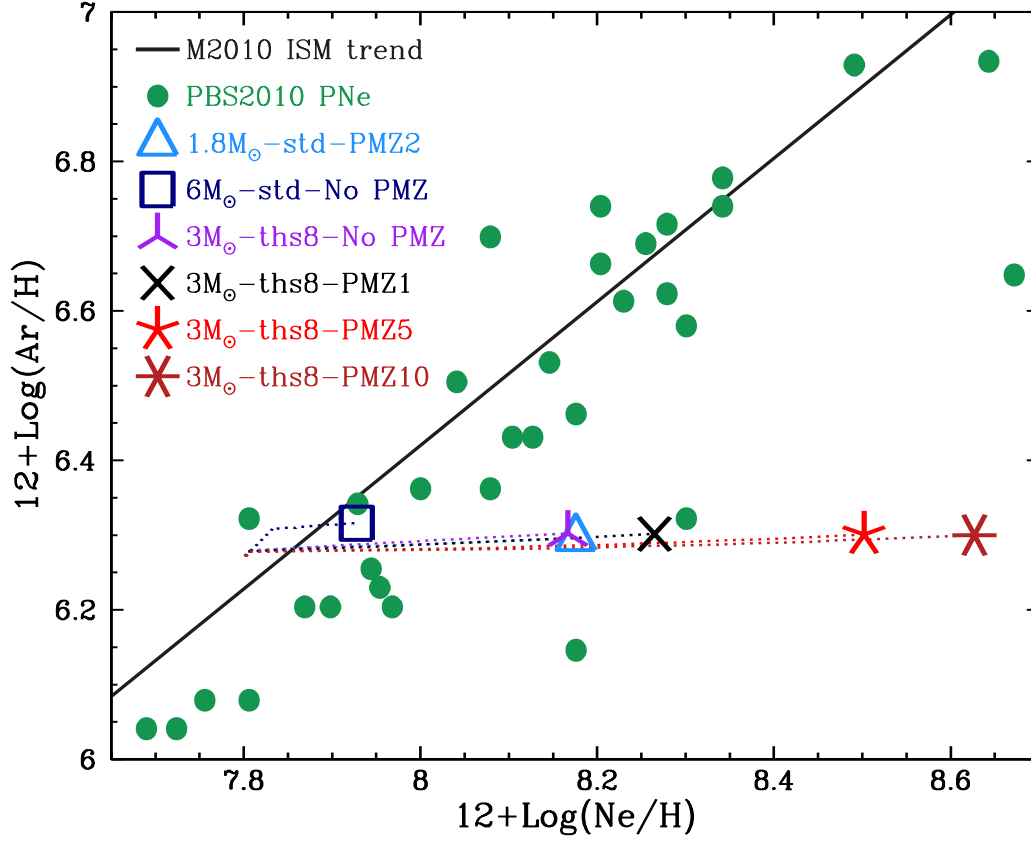
Figure 2.8   Same as Figure 2.5 but for Ar versus Ne.

2.4.3.   Comparison to PG1159-035

The hydrogen-deficient and helium-rich surface chemistry of PG1159 stars is likely caused by a late helium shell flash and consequent convection zone that extends into the hydrogen-rich surface layers (Schoenberner 1979; Iben et al. 1983; Herwig et al. 1999). The nucleosynthesis during post-AGB evolution is expected to be a relatively small addition to the nucleosynthesis during the preceding ~ 20 thermal pulses (Herwig et al. 1999), with the exception of a very late helium shell flash and proton ingestion episode, which may significantly affect the surface composition of light elements (up to oxygen) and heavy neutron-capture elements (Herwig et al. 2011; Stancliffe et al. 2011). Hence, although our stellar models terminate at the tip of the AGB, we expect that our intershell abundances of elements heavier than oxygen and much lighter than iron will approximately match the surface abundances of PG1159 stars. Abundance measurements for elements heavier than oxygen in PG1159 stars are rare in the literature. However, abundances in the prototype PG1159-035 have been measured for many elements including Si, P, S, and Fe (Jahn et al. 2007; Werner et al. 2011) and we include them in Table 2.5. Also shown in Table 2.5 are the intershell abundances of our 1.8 $M_\odot$, 3.0 $M_\odot$, and 6.0 $M_\odot$ models for comparison.

---

[1]Where 1 GK = 1×10^9 K.
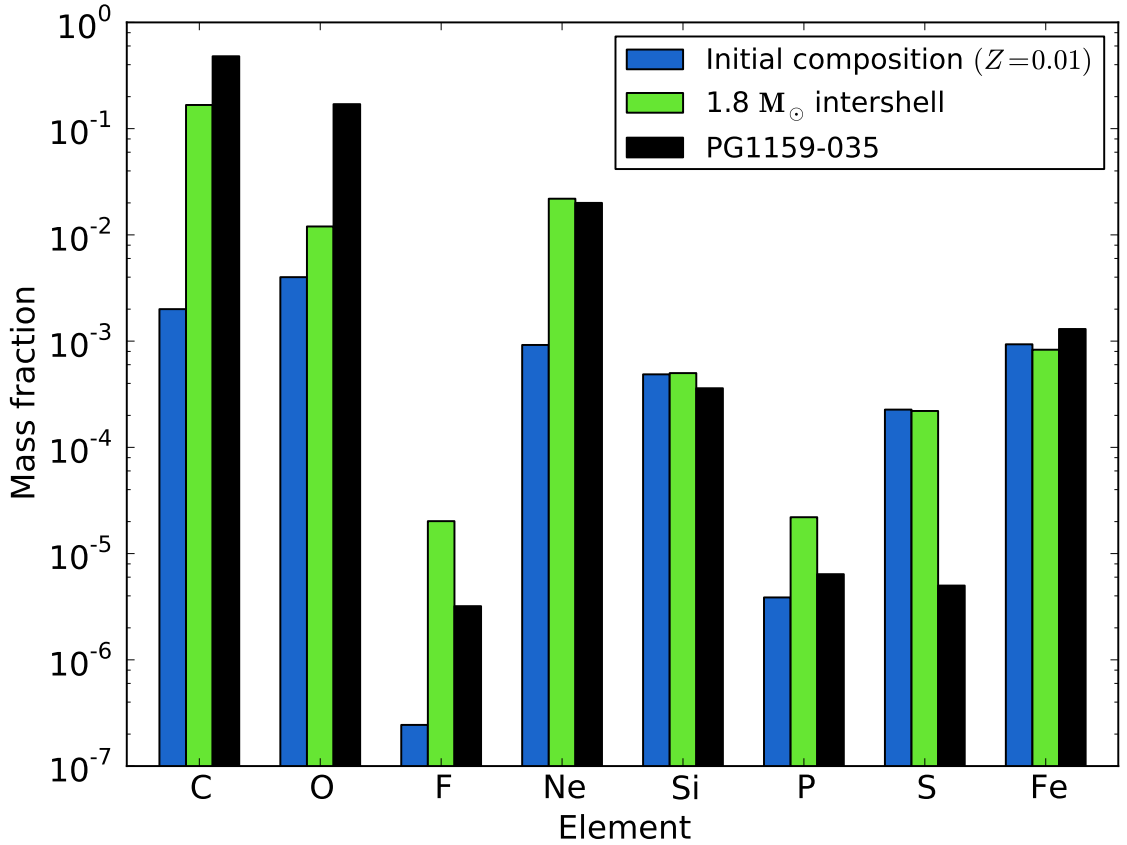
Figure 2.9   Comparison of our 1.8 M$_\odot$ intershell abundances with surface abundances of PG1159-035 from Jahn et al. (2007) and Werner et al. (2011).

Werner et al. (1991) estimated the mass of PG1159-035 at $0.605^{+.13}_{-.04}$ M$_\odot$ by comparison with the evolutionary tracks of Schoenberner (1979). The mass measured by Werner et al. (1991) is a close match to our 1.8 M$_\odot$ model, which has a mass at the end of the AGB of 0.59 M$_\odot$. However, based on more recent evolutionary calculations by Miller Bertolami & Althaus (2006), Werner et al. (2011) recently revised the mass of PG1159-035 downwards to $0.536^{+.068}_{-.010}$ M$_\odot$. The predicted final mass of our 1.8 M$_\odot$ model is still contained within the uncertainties of the revised measurement, although a better fit may be achieved by a model with a lower initial mass.

In Figure 2.9, we plot the abundances of PG1159-035 together with the intershell abundances of our 1.8 M$_\odot$ model. The closely matching Fe abundances indicate that our model has a similar initial metallicity to PG1159-035, as low mass stellar evolution leaves Fe abundances almost unchanged. We find that our model overproduces fluorine, with a resulting intershell mass fraction that is 2.0 times that of PG1159-035. This may be caused by our model having a higher initial mass than PG1159-035.

Our models do not include convective overshoot, and we therefore find carbon and oxygen abundances that are too low to match the surface of PG1159-035 (Werner et al. 1991). The high carbon and oxygen abundances of the PG1159 stars have been shown to be consistent

with overshoot into the C-O core (Herwig et al. 1999), whereas our abundance results match other standard models of AGB stars without convective overshoot (Boothroyd & Sackmann 1988a; Karakas et al. 2002). Overshoot into the C-O core could take place during a late helium shell flash, which is when the post-AGB star becomes helium-rich, or alternatively might occur during every thermal pulse on the AGB.

We find general agreement between the neon and silicon abundances, which match to within 10% and 40%, respectively. However, our model displays a large overabundance of phosphorus by 240%, and an even larger overabundance of sulphur, for which our model prediction is 44 times too high to match the observation. Our final intershell sulphur abundances are consistent with the models of Herwig that have no extra mixing into the C-O core during thermal pulses, which predict an abundance of 0.9 times solar (Werner & Herwig 2006).

2.5.   Discussion and Conclusions

The main finding of this study is that variation in the uncertainties that affect nucleosynthesis of AGB stars has little impact on the abundance of sulphur in AGB models. The uncertainties that we have explored include those associated with the nuclear network (e.g., neutron capture cross sections) and those that deal with the formation of a ^{13}C-rich region in the He-intershell of AGB models.

In terms of the nuclear network, we have measured the effect of rate uncertainties of the two most important neutron-producing reactions by independently testing the high and low rates for ^{13}C(α,n)^{16}O from Angulo et al. (1999, NACRE collaboration) and high, low, and recommended rates for ^{22}Ne(α,n)^{25}Mg from Iliadis et al. (2010). Table 2.4 shows that variations in these rates within the quoted uncertainties have little effect on sulphur. The rate of the ^{22}Ne(α,n)^{25}Mg reaction is highly uncertain, especially at the temperatures found in the He-shells of AGB stars (e.g., see discussions in Longland et al. 2009, 2012; Wiescher et al. 2012). At the temperatures of $T \lesssim 0.30$ GK found in the He-shell of low-mass AGB stars, this reaction is only marginally activated. However the uncertainties quoted at this temperature are considerable, for example, the rate given by Iliadis et al. (2010) varies by a factor of 1.24 at 0.300 GK, although in comparison the NACRE rate varies by a factor of 47 between the upper limit and the recommended values at the same temperature. In contrast, the NACRE rate for the ^{13}C(α,n)^{16}O reaction has smaller quoted uncertainties of only about 30% at temperatures up to 0.15 GK (Angulo et al. 1999, NACRE collaboration). Note that this reaction is ignited in the He-intershell between pulses, when the temperature is much lower than during convective thermal pulses. The rate for ^{13}C(α,n)^{16}O was recently re-determined by Pellegriti et al. (2008) and Guo et al. (2012). The uncertainties quoted in Guo et al. (2012) are now even lower, at $\lesssim 20$ per cent

at 1.0×10^8 K.

The temperature at the base of the He-flash convection zone is dependent on the numerical details of the AGB model and in particular on the treatment of the flash-driven convective boundaries (e.g., Herwig 2000). The inclusion of convective overshoot at the inner boundary of the pulse-driven convective zone (PDCZ) will transport additional ^{4}He downward to higher temperatures where it burns via the triple-α reaction, leading to increased temperatures in the He shell. In a 3 M$_\odot$, Z = 0.02 model, Herwig (2000) found that the inclusion of diffusive convective overshooting (with overshoot parameter $f = 0.016$) increased the maximum temperature at the base of the PDCZ by 13% from 0.24 GK to 0.27 GK (see also Fig. 3 in Lugaro et al. 2003). The application of diffusive overshoot to the base of the PDCZ can cause convective mixing to reach into the degenerate C-O core; however, this phenomenon is not seen in 3D hydrodynamic simulations of the core-intershell boundary by Stancliffe et al. (2011). Note that Herwig found modest sulphur depletion in the He-shell of his model, where the sulphur abundance was between 0.6–0.9 times the solar abundance. The sulphur depletion is directly related to the amount of convective overshoot (and therefore presumably the He-shell temperature). For example, Herwig's most recent models calculated with the MESA code (Paxton et al. 2011) and the NuGrid Multi-zone Post-Processing Network tool (Herwig et al. 2008; Bennett et al. 2012) and with a lower overshoot parameter applied to the PDCZ of $f = 0.008$, still show a very small sulphur depletion at about 0.8 times the solar abundance.

Our only reproduction of significant sulphur depletions in the He-intershell of our 3 M$_\odot$, Z = 0.01 model resulted from significantly increasing the rate of the ^{22}Ne(α,n)^{25}Mg reaction. By boosting the rate of ^{22}Ne(α,n)^{25}Mg by a factor of 600, we obtain a sulphur intershell abundance that is 0.47 times the solar abundance (but only ≈ 0.7 times the initial abundance) as shown in Table 2.5. As mentioned in Section 2.4.2, the corresponding surface abundance predictions relative to our standard rate case include: a reduction in Ne (0.3 dex), an increase in Mg (0.5 dex), an increase in P (0.4 dex), and only a small decrease in S (0.01 dex). Note that the factor of 600 is approximately equivalent to a 33% increase in the maximum He-shell temperature from 0.30 GK to 0.40 GK, where the upper-limit of the Iliadis et al. (2010) rate increases from 3.01×10^{-11} to 1.80×10^{-8} cm$^3 \cdot$g$^{-1} \cdot$s^{-1}, i.e., a factor of 631. An increase to the He-burning shell temperature of 33% is well beyond the 13% increase predicted by Herwig (2000) with the inclusion of diffusive convective overshoot. Furthermore, an increase to the reaction rate of this magnitude is well outside of experimental uncertainties, indicating the difficulty in depleting sulphur via neutron captures in AGB models.

In our investigation of the uncertainties related to ^{13}C pocket formation, we found that the insertion of a partially mixed zone (10^{-3} M$_\odot$ and larger) caused a very small reduction in the final intershell sulphur abundance by about 5-10% and that the use of larger PMZ masses does not necessarily result in greater sulphur depletions (Table 2.5). This is

because neutron captures at the top of the intershell produce sulphur via phosphorus decay at approximately the same rate as they deplete it via decay into chlorine. However, because the neutron capture rate of ^{30}Si decreases as a function of temperature while those of phosphorus and sulphur isotopes increase, activation of the ^{22}Ne(α,n)^{25}Mg reaction during convective thermal pulses at high temperature causes some depletion of phosphorus and sulphur.

Models in the narrow mass range of 2.5 to 3.5 M$_\odot$ are known to efficiently produce neon and increase their Ne/O ratio during AGB evolution (Karakas & Lattanzio 2003a). The elemental increase in neon is due to ^{22}Ne production from primary ^{14}N in convective pulses via the reaction chain ^{14}N(α,γ)^{18}F(β^+)^{18}O(α,γ)^{22}Ne. We find that the inclusion of a partial mixing zone significantly increases the final surface abundance of neon, and that larger PMZ sizes generally result in higher neon abundances (Table 2.3). The extent in mass of the PMZ correlates with the size of the resulting ^{14}N pocket, which contributes to the quantity of ^{14}N available for the production of ^{22}Ne.

The positions of our models with large PMZ sizes in the Ar versus Ne plane are far from the observational PNe data (Figure 2.8) and from this we conclude that the partial mixing zone masses larger than 5×10^{-3} M$_\odot$ (50% of the He-intershell mass in the 3 M$_\odot$ model) are excluded by the observations. However, this result is dependent on the uncertain physics associated with the formation of partially mixed zones and ^{13}C pockets. For example, when we inserted the protons into the post-processing code, we made the choice that the proton abundance decreases exponentially, i.e., linearly in a logarithmic scale. Studies of the formation of the ^{13}C pocket have found profiles that can slightly differ from this basic assumption, as well as from each other (e.g., see discussion in Lugaro et al. 2012).

To explain the abundances of young open cluster AGB stars, Maiorca et al. (2012) find that the effective ^{13}C required for the *s*-process in low-mass AGB stars is four times larger in models with $M \lesssim 1.5$M$_\odot$ than that required in more massive AGB stars (but see the discussion in D'Orazi et al. 2012). Kamath et al. (2012) find that PMZ masses of 1.2×10^{-2} M$_\odot$ or greater improve the fitting of AGB models to the C/O ratios and [F/Fe] abundances of stars in the Magellanic cluster NGC 1846. Kamath et al.'s best fitting PMZ mass represented a fraction of 80% of their 1.86 M$_\odot$ model's 1.5×10^{-2} M$_\odot$ intershell, with the large PMZ required to produce enough fluorine to match the observations. Our results for neon and argon in planetary nebulae data are not consistent with such a large partial mixing zone. The conflicting results of PMZ studies demonstrate the need for further work to identify the formation mechanism of ^{13}C pockets in AGB stars.

In general, AGB models are a good match to fluorine abundances in post-AGB stars (e.g., Werner et al. 2005), so the overproduction of fluorine in our 1.8 M$_\odot$ model relative to PG1159-035 may be indication that a lower initial mass is needed to model the star more accurately.

Although it was not the original aim of this investigation, our finding that neon abundances in PNe can be used to constrain the size of the ^{13}C pocket in low-mass stars is an important and unexpected result. Other investigations of ^{13}C pocket size in the literature exist (e.g., Bonačić Marinović et al. 2007a), but our method is independent from the uncertainties of AGB s-process abundances. To date, the extent and profile of the ^{13}C pocket are still highly uncertain, so the constraint set by neon abundances represents an additional clue to understanding this critical step in heavy element production via the s-process. A wider study with a finer grid of PMZ sizes and more accurate PNe data would likely find a smaller upper bound for the PMZ mass and could result in other, new constraints on mixing processes in AGB stars.

Our results show that variations within the known uncertainties of nuclear reaction rates and partial mixing zone masses are insufficient to reproduce the sulphur anomalies in PNe and PG1159-035 via low-mass stellar nucleosynthesis models. We conclude that our present knowledge of AGB stellar evolution and the relevant reaction rates does not support an explanation for the sulphur anomaly in terms of the nucleosynthesis in PN-progenitor AGB stars.

Acknowledgements

CHAPTER 3

The s-process enrichment of the globular clusters M4 and M22

3.1. Chapter Summary

We investigate the enrichment in elements produced by the slow neutron-capture process (s-process) in the globular clusters M4 (NGC 6121) and M22 (NGC 6656). Stars in M4 have homogeneous abundances of Fe and neutron-capture elements, but the entire cluster is enhanced in s-process elements (Sr, Y, Ba, Pb) relative to other clusters with a similar metallicity. In M22, two stellar groups exhibit different abundances of Fe and s-process elements. By subtracting the mean abundances of s-poor from s-rich stars, we derive s-process residuals or empirical s-process distributions for M4 and M22. We find that the s-process distribution in M22 is more weighted toward the heavy s-peak (Ba, La, Ce) and Pb than M4, which has been enriched mostly with light s-peak elements (Sr, Y, Zr). We construct simple chemical evolution models using yields from massive star models that include rotation, which dramatically increases s-process production at low metallicity. We show that our massive star models with rotation rates of up to 50% of the critical (break-up) velocity and changes to the preferred $^{17}O(\alpha,\gamma)^{21}Ne$ rate produce insufficient heavy s-elements and Pb to match the empirical distributions. For models that incorporate asymptotic giant branch yields, we find that intermediate-mass yields (with a ^{22}Ne neutron source) alone do not reproduce the light-to-heavy s-element ratios for M4

and M22, and that a small contribution from models with a ^{13}C pocket is required. With our assumption that ^{13}C pockets form for initial masses below a transition range between 3.0 and 3.5 M$_\odot$, we match the light-to-heavy s-element ratio in the s-process residual of M22 and predict a minimum enrichment timescale of between 240 and 360 Myr. Our predicted value is consistent with the 300 Myr upper limit age difference between the two groups derived from isochrone fitting.

3.2. Introduction

The assumption that globular clusters (GCs) are simple stellar populations (i.e., populations of stars that formed simultaneously from gas of a uniform chemical composition) has made them ideal laboratories for the study of low-mass stellar evolution (Moehler 2001) and enabled their ages to be accurately determined. This has aided cosmology by setting a lower limit on the age of the universe (Chaboyer et al. 1996; Dotter et al. 2010). However, the simple stellar population model of GCs has been undermined by spectroscopic studies that reveal significant star-to-star abundance variations ($\gtrsim 1$ dex) in the light elements from C to Al (e.g., Cottrell & Da Costa 1981; Carretta et al. 2009b; Denissenkov & Hartwick 2014). Similar variations found in unevolved stars show that the chemical variations were initially present in the star-forming gas rather than being the result of nucleosynthesis and mixing within the observed stars (Cannon et al. 1998; Gratton et al. 2001). More recently, photometric studies have independently confirmed the existence of multiple populations in the form of split main sequences and sub-giant branches in color-magnitude diagrams (e.g., Piotto et al. 2007; Piotto 2009; Milone et al. 2008).

The light element patterns that exist almost exclusively in GCs (i.e., rarely in field stars and open clusters, see Gratton et al. 2000; De Silva et al. 2009) include anti-correlations between the abundances of C and N, Na and O, and sometimes Mg and Al, typically with a C+N+O abundance that is constant within observational errors. The abundance patterns depict a H-burning process at high temperature (> 80 MK[1]) combined with dilution by varying amounts of unprocessed material, although the stellar sites where this burning takes place and the mechanism of dilution are presently not well understood (Denisenkov & Denisenkova 1990; Langer et al. 1993; Decressin et al. 2007; Prantzos et al. 2007; D'Orazi & Marino 2010; D'Ercole et al. 2011).

In contrast to the light elements which vary in abundance, GCs are typically homogenous in [Fe/H][2] ($\sigma < 0.05$ dex, Carretta et al. 2009a) and in the abundances of neutron-capture elements ($Z > 30$; Gratton et al. 2004; Yong et al. 2006, 2008a; D'Orazi et al. 2010).

---

[1] 1 MK = 10^6 K.

[2] We use the standard spectroscopic notation $[A/B] = \log(A/B) - \log(A/B)_\odot$, where A and B are abundances by number and $\odot$ denotes the solar abundance.

Exceptions are known, including ω Centauri (Norris & Da Costa 1995; Smith et al. 2000; Johnson & Pilachowski 2010), M22 (Marino et al. 2009), NGC 1851 (Yong & Grundahl 2008; Villanova et al. 2010a; Carretta et al. 2011), M2 (Yong et al. 2014), M15 (Sneden et al. 1997; Sobeck et al. 2011), and possibly NGC 2419 (Cohen & Kirby 2012).

Neutron-capture elements refer to elements with atomic number Z > 30, because production of these elements is almost entirely by a process of neutron captures and β^--decay reactions. Depending on whether the average neutron-capture rates are less than or greater than the average rate of β^--decay reactions, the processes are divided into the slow (s-process) and rapid (r-process) neutron-capture processes (Burbidge et al. 1957). Although most heavy elements can be synthesized by both processes, elements whose production is dominated by the r- or the s-process in solar system material are commonly referred to as r- and s-process elements.

Due to the large uncertainties involved in numerically modeling nucleosynthesis by the r-process, the r-only component of a heavy element distribution is often inferred from solar system material by subtracting the s-process component, which itself may be determined either theoretically (e.g., Arlandini et al. 1999; Goriely 1999; Sneden et al. 2008) or empirically (e.g., Simmerer et al. 2004).

The s-process takes place at low neutron densities ($\leq 10^{14}$ cm^{-3}; Busso et al. 1999) and operates exclusively on nuclides that are very close to stability, as nuclei that become unstable following neutron capture have time to β-decay back to stability before additional neutron captures occur. In the build-up of progressively heavier elements via the s-process, bottlenecks form around nuclides with 'magic' numbers of neutrons (e.g., 50, 82, 126) which form nuclear structures that are more stable against neutron capture than their neighbors (Busso et al. 1999). Three major peaks develop: a light s-peak (Sr, Y, Zr), a heavy s-peak (Ba, La, Ce), and a peak at Pb, with the light peak forming first and the heavier peaks forming later with increasing neutron exposure.

GCs provide laboratories to test and explore our understanding of stellar nucleosynthesis. One cluster that has been studied extensively is M22 (NGC 6656), which exhibits internal variation in [Fe/H] and s-process abundances that are bimodally distributed and neatly separate into two groups (Marino et al. 2009, 2011b; Da Costa & Marino 2011). While there are other well-studied clusters with Fe and s-process variation (e.g., ω Centauri), the simpler chemical evolution history of M22 relative to more complex systems like ω Centauri makes it an attractive system for testing theories about s-process variation in GCs more generally.

Even among GCs that are homogenous in their abundances of Fe and neutron-capture elements there exist puzzles surrounding the chemical evolution of the s-process elements. For example, M4 is a fairly typical mono-metallic metal-poor GC ([Fe/H] = -1.18; Carretta

et al. 2009a), except that it has super-solar abundances of *s*-process peak elements (e.g., Rb, Y, Zr, La, Ba, Pb; Brown & Wallerstein 1992; Ivans et al. 1999). The origin of the *s*-process elements in M4 and M22 is speculated on in the literature, but often on the basis of individual stellar yields (e.g., Roederer et al. 2011) rather than a full investigation using a chemical evolution model. Very recently, Straniero et al. (2014) presented the first comparison of the *s*-process distributions of M4 and M22 with the summed contribution from a generation of asymptotic giant branch (AGB) stars at the metallicity of M22 ([Fe/H]= −1.8).

In this paper, we present simplified chemical evolution models of the heavy elements in GCs and predict the abundance variations that arise from *s*-process production by (1) massive stars with rotation, or (2) a generation of AGB stars that span a range of stellar masses. We then compare our chemical abundance predictions with the observed abundances of stars in M4 and M22. The success or failure of the individual models gives us insight into the stellar sites and timescales of *s*-process enrichment in GCs, as well as highlighting the shortcomings of current stellar nucleosynthesis models.

3.3. The *s*-Process in Massive Stars

We define as massive stars those with sufficient mass to eventually form a collapsing core of Fe and end their lives as core-collapse supernovae. Current estimates for the lower-limit of initial mass required to meet this condition are around 8–12 $M_\odot$, with lower masses required at lower metallicities (Langer 2012; Nomoto et al. 2013; Jones et al. 2013).

In massive stars, neutron-capture nucleosynthesis takes place during pre-supernova evolution and possibly also during the supernova itself. During convective core He-burning and shell He- and C-burning, neutrons are released via the ^{22}Ne(α,n)^{25}Mg reaction (Peters 1968; Raiteri et al. 1992; Meyer 1994; The et al. 2007).

The production of ^{22}Ne occurs via He-burning of ^{14}N left over from H-burning in the CNO cycle. In models without rotation ^{22}Ne is secondary since its yield depends on the initial amount present plus any formed from α-capture onto ^{14}N, which itself is limited by the initial abundance of C+N+O. Hence, there is very little *s*-process production at low metallicity in non-rotating models. Some production of heavy elements in massive stars does take place (the weak *s*-process) but this is mainly concentrated around elements of the first *s*-peak near Y, with virtually no heavy *s*-elements or Pb being produced (Beer et al. 1992; Gallino et al. 2010).

In models of massive stars that do include rotation, rotationally-induced mixing transports primary ^{12}C and ^{16}O produced in the convective He-core to the H-burning shell, where it is then converted into ^{14}N via the CN-cycle (Ekström 2006). The primary ^{14}N is then
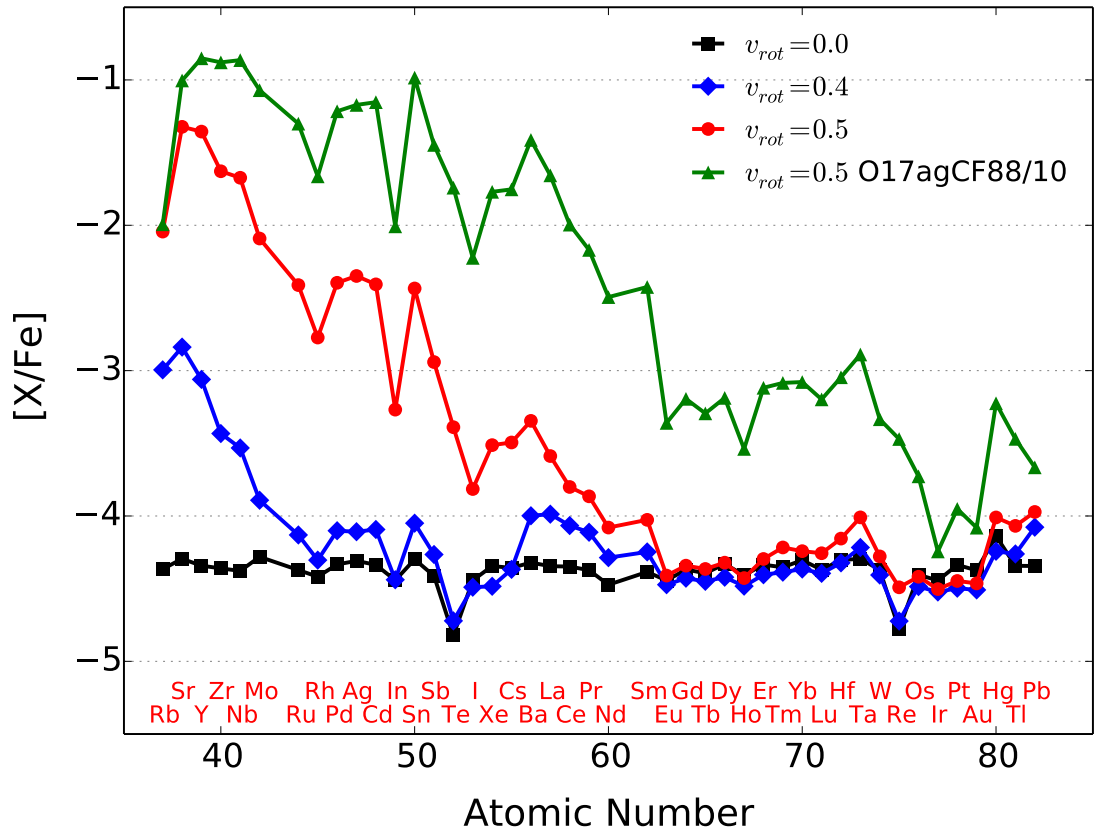
Figure 3.1 Abundance ratios with Fe relative to the solar values in the pre-supernova yields of 25 $M_\odot$ models at [Fe/H]= -3.8 with several initial rotation rates. The rotation rate is given in units of the critical velocity (v_{crit}). Yields from Frischknecht & Thielemann (2012) with zero-metallicity explosive Fe yields from Limongi & Chieffi (2012).

mixed into and burnt in the He core, resulting in an almost-primary production of ^{22}Ne (Hirschi 2007) that dramatically increases *s*-process yields at low metallicity.

Gallino et al. (2008) present the first *s*-process yields for a rotating massive star with their 25 $M_\odot$ model. They find that rotation increases *s*-process yields by orders of magnitude and alters the standard weak *s*-process distribution with a peak of production between Sr and Ba. The high production of heavy *s*-elements in their model is due to the use of the very low Descouvemont (1993) rate for the ^{17}O(α,γ)^{21}Ne reaction, which is disfavored by recent experiments. Frischknecht & Thielemann (2012) present *s*-process yields from a set of massive models with updated reaction rates and find that rotation leads to the complete consumption of Fe-seeds at metallicities below $Z = 10^{-3}$ and an increase to the production of elements near the Ba peak at the expense of the Sr peak as metallicity decreases.

Figure 3.1 presents the heavy-element yields of 25 $M_\odot$ massive star models with several initial rotation rates from Frischknecht & Thielemann (2012). This figure demonstrates that under the condition of fast rotation, the *s*-process production in massive stars at low metallicity begins to include elements that would otherwise be associated uniquely with

AGB stars (e.g., Ba, La, and Pb). For this reason, massive rotating stars must be considered as a possible source of the neutron-capture elements in GCs.

In this study we use the pre-supernova yields of neutron-capture elements calculated from a grid of rotating massive stars (including those used to generate Figure 3.1) with initial masses of 15, 20, 25, and 40 $M_\odot$ at initial metallicities of $Z = 10^{-5}$ ([Fe/H]= -3.8) and $Z = 10^{-3}$ ([Fe/H]= -1.8) with α-enhanced initial compositions as described in Frischknecht & Thielemann (2012). The rotation rates of the models are specified by their initial velocity at the equator as a fraction of the break-up velocity (v_{crit}, the velocity at which centrifugal force balances gravity).

For elements $Z \leq 26$, we use the zero-metallicity explosive yields of Limongi & Chieffi (2012). Although supernova yields presently carry large uncertainties, the effect of varying the Fe yields will be to scale our resulting heavy element distributions up and down while leaving the ratios between elements unchanged. The supernova shockwave will not significantly affect the s-process production and hence the s-process yields are approximated by their pre-supernova values although the mass yields and to a lesser extent the s-process distribution, will depend on the mass cut (Tur et al. 2009).

3.4.   The s-Process in AGB Stars

In low to intermediate mass (0.8–8 $M_\odot$) stars, the s-process takes place during the thermally-pulsing AGB phase of evolution. For further details on AGB stellar evolution and nucleosynthesis, we refer to the reviews by Herwig (2005) and Karakas & Lattanzio (2014).

Figure 3.2 shows the average composition of the stellar ejecta of AGB models selected from the full grid which includes masses of 2.5, 2.75, 3.00, 3.25, 3.5, 4.0, 4.5, 5.0, 6.0, and 7.0 $M_\odot$ at a metallicity of $Z = 0.001$ ([Fe/H]= -1.2 scaled solar), and are taken from Fishlock et al. (2014a). This figure displays the transition between the s-process yields from low-mass stars ($\lesssim 4 \, M_\odot$) to intermediate-mass stars as a result of the ^{22}Ne neutron source becoming active. This transition mass also roughly coincides with our assumed upper limit initial masses for ^{13}C pockets in AGB stars of 3 or 3.5 $M_\odot$ at [Fe/H] = -1.2. For the rest of this section, we briefly summarize the operation of the s-process in AGB stars.

With increasing initial mass, the maximum temperature in the intershell obtained during a thermal pulse also increases. A consequence is that in stars $\lesssim 4 \, M_\odot$, fewer thermal pulses are accompanied by a substantial activation of the ^{22}Ne$(\alpha,n)^{25}$Mg reaction. Instead, free neutrons for the s-process are mainly released by radiative ^{13}C-burning via the ^{13}C$(\alpha,n)^{16}$O reaction, which is active at temperatures as low as 90 MK (Cameron 1955; Straniero et al. 1995). Producing the required ^{13}C has been a challenge for stellar modelers,
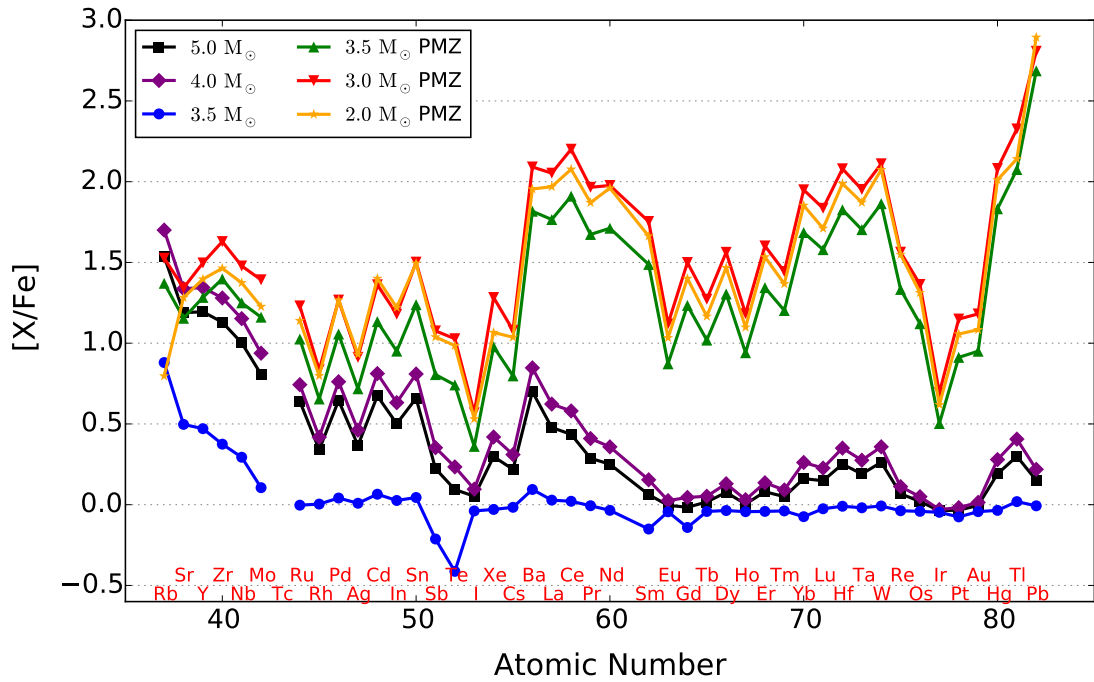
Figure 3.2 Abundance ratios with Fe relative to their solar values in the yields of AGB models at [Fe/H]= −1.2 with several different initial masses. Models labelled 'PMZ' include a partial mixing zone. Yields from Fishlock et al. (2014a).

as the ^{13}C abundance left behind by the H-burning shell is too low to allow for sufficient *s*-processing, and the convective region following a thermal pulse cannot extend into the H-rich region above the ^{12}C-rich intershell (Iben 1975b).

Current AGB models achieve s-process nucleosynthesis via a ^{13}C pocket in the following manner: protons from the envelope are "partially mixed" beyond the formal convective border into the ^{12}C-rich intershell region, thus enabling the CN cycle reactions ^{12}C(p,γ)^{13}N(β^+)^{13}C (Gallino et al. 1998; Arlandini et al. 1999). The mixing process is required to have only marginal efficiency, otherwise the newly-synthesized ^{13}C is readily destroyed by further proton captures to make ^{14}N, which is a neutron poison, i.e., its large neutron-capture cross section makes it an efficient absorber of free neutrons. For models that include a partial-mixing zone (PMZ) by inserting an exponential profile of protons below the inner edge of the envelope convective zone, a ^{13}C pocket is formed below a pocket of ^{14}N (Cristallo et al. 2009; Lugaro et al. 2012). In our post-process AGB nucleosynthesis models (including those used to calculate the yields shown in Figure 3.2) we include a PMZ of 2×10^{-3} M$_\odot$ at the deepest extent of each third dredge-up episode for initial masses ≤ 3.0 M$_\odot$ and a 1×10^{-3} M$_\odot$ PMZ for selected models at 3.25 and 3.5 M$_\odot$. The technique we use to include a PMZ is identical to Lugaro et al. (2012) and we refer the reader to that paper for more details. We discuss the uncertainties related to ^{13}C pockets in Section 3.5.

Figure 3.2 illustrates that low-mass stars produce significant quantities of heavy *s*-peak

elements and Pb at low metallicity and confirms previous results in the literature (Travaglio et al. 2001; Van Eck et al. 2001, 2003; Lugaro et al. 2012). This is because the neutron source ^{13}C is primary (independent of metallicity) while at low metallicity fewer Fe-seed nuclei (the most abundant heavy element) are available (Clayton 1988). With a large neutron supply per Fe-seed, neutrons are preferentially captured by heavier nuclei and the abundance distribution is shifted toward higher atomic numbers.

Figure 3.2 also shows that the yields of elements heavier than Sr are significantly lower in models with masses ≥ 4 $M_\odot$ at a metallicity of [Fe/H]$= -1.2$. This is because the dominant neutron source in these models is the ^{22}Ne(α,n)^{25}Mg reaction, which is active at temperatures above about 300 MK (Cameron 1960; Iben 1975a; Goriely & Mowlavi 2000). The high temperatures and ^{22}Ne nuclei required to activate this source are found near the base of the He intershell in convective zones driven by He-shell flashes. Thus, neutrons are briefly exposed to a relatively large number of Fe seeds at the base of the flash-driven convective zone, and the resulting *s*-process distribution in intermediate-mass stars is mostly weighted towards the light *s*-peak near Sr–Y–Zr, with lower yields of heavy *s*-elements compared to lower mass stars.

In summary, the change from the ^{22}Ne source operating in convective pulses to radiative ^{13}C-burning during the interpulse phase creates a dramatic change in the distribution of heavy elements between models above and below the transition mass of around 3–4 $M_\odot$. The precise mass of this transition is dependent on the choice of the highest mass to include a ^{13}C pocket, which is an uncertain parameter that is model and metallicity dependent (Goriely & Siess 2004; Herwig 2004).

3.5. Stellar Modeling Uncertainties

The uncertainties that have the greatest effect on the yields of heavy elements are the numerical treatments of convection, mass loss, and reaction rates, as well as the rotation in massive stars and low-temperature opacities in AGB stars (e.g., Marigo 2002; Fishlock et al. 2014b; Constantino et al. 2014).

In stellar models of all masses, convective mixing plays a crucial role in the transport of energy and chemical species. The construction of accurate stellar models requires a method to approximate the effects of convection in 1D stellar evolution codes, as the high computational demands of full 3D hydrodynamical models limit their simulation times to no more than a small fraction of a stellar lifetime (e.g., Stancliffe et al. 2011). The most common numerical treatment of convection is the mixing-length theory (MLT) that depends on the value of an uncertain parameter, α, which is the mixing length in units of the local pressure scale height. The value of α is usually assumed to be constant on the

AGB (e.g., the yields shown in Figure 3.2 use a value of 1.86), even though empirical and theoretical studies both suggest that the value changes with stellar evolution (Lebzelter & Wood 2007; Magic & Asplund 2014). Larger values of α have been shown to increase the depth of the third dredge-up (Boothroyd & Sackmann 1988b), which increases the yields of s-process elements (Cristallo et al. 2009, 2011).

An alternative treatment of convective mixing that has been applied to AGB stars is the full-spectrum of turbulence (FST; Canuto & Mazzitelli 1991; Canuto et al. 1996). FST predicts a higher rate of energy transport than MLT, which leads to increased surface luminosities and higher interior temperatures in stellar models. In the intermediate-mass (4 to 6 $M_\odot$) models of Ventura & D'Antona (2008) that use FST, temperatures at the base of the convective envelope reach 90–110 MK, which is hot enough for extensive H-burning nucleosynthesis (hot bottom burning). Combined with a luminosity-dependent mass-loss law, the high luminosities of these models drive rapid mass-loss rates that shorten the thermally-pulsing AGB phase and reduce the number of dredge-up episodes (Ventura & D'Antona 2005b; Ventura et al. 2013). The limited dredge-up in these models leads to a negligible net yield of C+N+O in the stellar wind. Presumably, this would also result in negligible yields of s-process elements, although yields from an FST model with a full s-process network are, to our knowledge, not published at present.

Another major uncertainty in stellar modeling is the mass-loss rate and its dependence upon stellar parameters. Indeed, massive stars can lose more than half of their mass by the end of core He burning (Chiosi & Maeder 1986). In massive stars with rotation, mass loss transports angular momentum away from the stellar surface (Hirschi 2007, to which we refer for details of the mass-loss prescription used in our massive star models). With the very low mass-loss rates expected at metallicities of $Z = 10^{-5}$ ([Fe/H]= -3.8) and below, extremely metal-poor massive stars will evolve differently from observable OB stars (Maeder & Meynet 2000). Adding further complexity, the mass-loss rate would also be increased by the presence of a binary companion. For AGB stars, mass loss is very difficult to determine empirically without an accurate understanding of the dust composition and detailed models of the radiative transfer physics. Because the rate of mass loss controls the amount of time spent on the AGB and the number of thermal pulses, changes to the mass-loss rate have a significant effect on the predictions of stellar yields. In our models, we use Vassiliadis & Wood (1993) mass-loss rates along the AGB, which includes the switch to a superwind phase of extremely rapid mass loss near the tip of the AGB. An alternative is the Bloecker (1995) formula derived from dynamical calculations of the atmospheres of Mira-like stars, which predicts higher mass-loss rates and shorter AGB lifetimes.

Our massive star models include rotationally-induced mixing in the form of meridional circulation and shear instabilities which dramatically alter the yields of CNO and s-process elements, depending on the rate of rotation (Frischknecht & Thielemann 2012). The best

constraints on the rotation rates of low-metallicity massive stars come from the comparison of chemical signatures in low-metallicity, low-mass stars with the predictions of rotating stellar models. In order to explain the existence of high N/O and C/O ratios at times too early for AGB stars to contribute, Ekström & Matteucci (2006) infer rotation rates of around 0.5 times the break-up velocity (v_{rot}/v_{crit} = 0.5) at [Fe/H]< −3. Ekström & Charbonnel (2008) claim that rotation is independently supported by the low ^{12}C/^{13}C ratios of metal-poor stars, which they report are consistent with models having rotational velocities of $v_{rot}/v_{crit} \simeq$ 0.5 to 0.6. Fabbian et al. (2009) reach a less-certain conclusion about rotation and interpret high C/O ratios as possible signatures of either Population III stars or rotating Population II stars. The effect of rotation on the s-process yields is illustrated in Figure 3.1 which shows that rotation is the dominant effect.

For rotating massive star models, another uncertainty with an effect on s-process yield predictions is the competition between the ^{17}O(α,γ)^{21}Ne and ^{17}O(α,n)^{20}Ne reactions. This is because ^{16}O is highly effective at capturing free neutrons, which produces ^{17}O. Neutrons are then either recycled via ^{17}O(α,n)^{20}Ne or lost via ^{17}O(α,γ)^{21}Ne. The rate of the ^{17}O(α,γ)^{21}Ne reaction is particularly uncertain at the relatively low energies of stellar interiors. The first experimental rates for this reaction were published by (Caughlan & Fowler 1988, hereafter CF88) and subsequently disputed by Descouvemont (1993), who predicted on theoretical grounds that the rate should be lowered by roughly a factor of 1000. However, more recent experimental work by Best et al. (2011) supports a rate similar to CF88. Best et al. (2013) report that the ratio between the (α,γ) and (α,n) reactions is best matched by using the CF88 rate divided by ten for ^{17}O(α,γ)^{21}Ne and the Angulo et al. (1999, NACRE) rate for ^{17}O(α,n)^{20}Ne, the combination of which we will refer to as CF88/10 rates.

For s-process yields of both intermediate-mass AGB models and massive-star models, the ^{22}Ne(α,n)^{25}Mg reaction plays a critical role in determining neutron fluxes, and for this reason it has been the subject of a number of studies (Angulo et al. 1999; Jaeger et al. 2001; Koehler 2002; Karakas et al. 2006b). Recent rates presented by Longland et al. (2012) have reduced the uncertainties in AGB model abundances caused by uncertainty in these reactions to less than a factor of two.

A major uncertainty for the s-process in low-mass models concerns the formation of a ^{13}C pocket. This is because the physical mechanism that leads to ^{13}C pockets in stars is yet to be identified. Currently proposed candidates include convective-boundary mixing (Herwig 2000; Cristallo et al. 2004), rotational mixing (Herwig & Langer 2001; Piersanti et al. 2013), or gravity-wave driven mixing (Denissenkov & Tout 2003). Eventually, a deeper understanding of the physics involved might completely eliminate the free parameter that determines the mass of the ^{13}C pocket. At present, a variety of constraints have been derived from observations of carbon-enhanced metal poor stars (Izzard et al. 2009; Bisterzo et al. 2012; Lugaro et al. 2012), planetary nebulae (Shingles & Karakas 2013; Miszalski et al.

2013), and post-AGB stars (Bonačić Marinović et al. 2007b; De Smedt et al. 2012).

Aside from the uncertain size of the partial mixing zone and resulting ^{13}C pocket, an additional uncertainty relates to the stellar initial masses in which a ^{13}C pocket can be formed. With increasing stellar mass, the size of the He-rich intershell region decreases and temperatures at the base of the convective envelope during the third dredge-up increase, inhibiting ^{13}C-pocket formation in more massive AGB stars. Goriely & Siess (2004) show that when the third dredge-up takes place with temperatures of around 40 to 70 MK ^{13}C-pocket formation can be suppressed, depending on the details of any diffusive mixing near the convective boundary. At our metallicity of Z = 0.001, the results of Goriely & Siess (2004) suggest that ^{13}C-pocket formation could become inhibited above around 3.0 to 3.5 M$_\odot$ (but see Straniero et al. (2014) for a different view on ^{13}C-pocket formation above this mass). To account for this uncertainty on our results, we separately consider two cases in which our nucleosynthesis post process includes a PMZ for all stellar masses up to 3.0 or 3.5 M$_\odot$. This is an approximation in the absence of a physically-accurate PMZ included in our stellar model calculations.

In this work we do not consider binary stars, although the presence of a binary companion will also alter the yields with a dependence on the period and mass ratio of the system.

3.6.   Observational Data

3.6.1.   Differential abundances and empirical s-process distributions

As an indication of how elemental abundances vary between two stars or stellar populations, it is common to subtract solar bracket [X/Fe] abundances (e.g., Yong et al. 2008a; Roederer et al. 2011). The difference [X/Fe]$_2$−[X/Fe]$_1$ is equal to $\log_{10}$[(X/Fe)$_2$/(X/Fe)$_1$], i.e., it measures of the number ratio of X to Fe in system 2 as a factor of the ratio in system 1. In the case that system 1 represents an initial composition that has undergone nucleosynthesis to make the abundances in system 2, a quantity that isolates the net production or destruction of elements is obtained by subtracting the number ratios in linear abundance space, i.e., Δ(X/Fe)=(X/Fe)$_2$ − (X/Fe)$_1$, assuming that Fe is either constant or only marginally produced. This quantity is analogous to the net yields of stellar nucleosynthesis models, which are computed by subtracting the abundances in the initial composition from the abundances in the stellar ejecta (e.g., Karakas 2010).

Using a linear abundance subtraction, Roederer et al. (2011, Table 8) calculate an s-process-only residual composition for M22 by subtracting the average X/H number ratios of s-poor from s-rich stars. We use the same technique to derive empirical s-process distributions for M4 and M22, except that we use number ratios relative to Fe. Our own
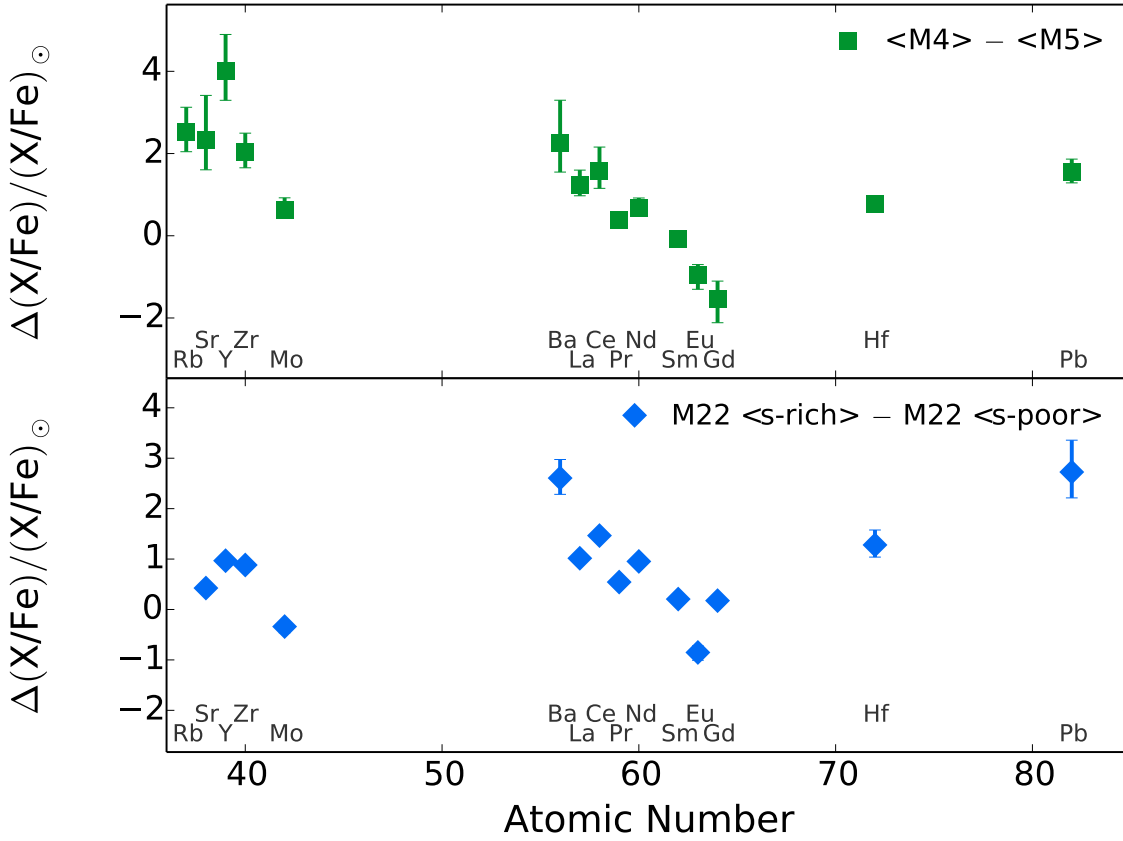
Figure 3.3 Abundance differences relative to solar with observational data. Abundances of M4 and M5 are from Yong et al. (2008a,b) except Cu from Simmerer et al. (2003) and Ba from Ivans et al. (2001). M22 abundances are from Roederer et al. (2011). $\Delta(X/Fe)=(X/Fe)_A - (X/Fe)_B$. Upper and lower bounds are calculated by multiplying and dividing by $10^{\sqrt{(\sigma A)^2+(\sigma B)^2}}$, where σA and σB are the logarithmic abundance dispersions of two systems whose abundances have been subtracted.

testing confirms that the resulting distributions look very similar regardless of whether abundances relative to Fe or H are used.

Figure 3.3 shows our calculated *s*-process-only residuals of M22 <s-rich> − <s-poor> and <M4> − <M5> relative to the solar abundances (Asplund et al. 2009). To visually emphasize small differences (that are significant within the errors), we plot on a linear scale. The distance from the zero point is related to the amount of dilution with *s*-poor material, while the shape of the distribution is relatively independent of this uncertain parameter and primarily depends on the relative abundances in the stellar ejecta. In agreement with Roederer et al. (2011), we interpret the empirical *s*-process distributions of M4 and M22 as representing enrichment by material of a similar but not identical composition. We suggest that the *s*-process distributions of these two clusters are distinguishable as representing the results of different nucleosynthetic sites or stellar mass ranges. We now discuss the observations, starting with M4.

3.6.2.   The s-rich globular cluster M4

M4 is a typical mono-metallic GC with a Na-O anti-correlation and constant abundances of Fe-group elements, neutron-capture elements (except possibly Y, see Villanova & Geisler 2011), and C+N+O (Drake et al. 1992; D'Orazi & Marino 2010; Marino et al. 2008, 2011a).

Although the neutron-capture element abundances show no star-to-star variations in M4, the entire cluster is moderately enriched with s-process elements compared to other GCs at a similar metallicity, such as M5. With [Fe/H] of -1.33 (Carretta et al. 2009a), M5 is a near metallicity-twin of M4 with similar abundances of Fe-peak (Fe, Co, Ni) and r-process (Eu) elements. Compared to M5, the s-process elements in M4 are overabundant by between 0.3 and 0.5 dex (Ivans et al. 2001; Yong et al. 2008a,b). Figure 3.3 shows that the s-process distribution of M4 (which is obtained by subtracting the abundances of M5) is dominated by the light s-peak around Y, with lower abundances of Ba and heavier s-process elements.

Karakas et al. (2010a) and Roederer et al. (2011) have suggested that the overabundances of Rb, Y, Ba, La, and Pb in M4 relative to M5 could result from intermediate-mass AGB stars (in which the neutron source is ^{22}Ne(α,n)^{25}Mg) by a comparison with individual stellar yields. However, this does not rule out a simultaneous contribution from less massive stars with ^{13}C pockets. The simultaneous contribution of the s-process from both ^{13}C pockets and the ^{22}Ne source is the conclusion drawn by Straniero et al. (2014), who fit to the s-process distribution of M4 to an IMF-weighted sum of stellar yields with AGB models from 3 to 6 $M_\odot$ at [Fe/H]$= -1.8$.

Although AGB stars have been suggested as the heavy elements producers in M4, the sequence of events that led to the peculiar s-process enrichment of M4 and not M5 (and many other GCs) is presently without a conclusive explanation in the literature.

3.6.3.   The two populations in M22

Marino et al. (2009) demonstrated that M22 exhibits two groups of stars separated by 0.15 dex in [Fe/H] and variations in s-process elements that are correlated with Fe.

The first group (s-poor) has a mean metallicity of [Fe/H]$= -1.82 \pm 0.02$ and [s/Fe] of -0.01 ± 0.01, where s represents an average over Y, Zr, Ba, La, and Nd. The second group (s-rich) has a metallicity of [Fe/H]$= -1.67 \pm 0.01$ and [s/Fe] of $+0.35 \pm 0.02$ (Marino et al. 2011b). Both populations independently show the Na-O and C-N anti-correlations (Marino et al. 2011b), indicating that whichever stars contributed to the enrichment of the s-rich population did not also produce the light element anomalies. In comparison with

M4, which is mostly enriched with light *s*-elements, Figure 3.3 shows that the *s*-process distribution of M22 is peaked at the heavy *s*-elements near Ba.

Marino et al. (2012) compare photometry of the two groups with isochrones and derive an upper-limit age spread of 300 Myr. The result is confirmed by Joo & Lee (2013), who find that their best-fitting isochrones predict an age difference of 0.3 ± 0.4 Gyr. Assuming that the gas cooling time is a negligible fraction of a stellar lifetime, the age difference of 300 Myr allows enough time for stellar masses as low as 3.0 $M_\odot$ to contribute to the chemical abundances in the *s*-rich group. The connection between the minimum contributing mass and the timescale for *s*-process enrichment is explored in more detail in Section 3.8.

3.7. Chemical Evolution Model and Results

We present abundance evolution results calculated using a new code, Evel ChemEvol to solve the equations of chemical evolution for a single-zone (for an review, we refer to Pagel 2009). Our testing with the AGB yields and self-pollution scenario described by Fenner et al. (2004) confirms that the code correctly reproduces the abundance results of an existing chemical evolution code. For more details of the output validation tests, see Appendix 3.10.

Our simplified chemical evolution model includes a single short burst of star formation as a first-order attempt at understanding the enrichment of GCs. The final abundance outputs of the chemical evolution model represent the IMF-weighted (Kroupa et al. 1993) sum of ejecta from a range of stellar masses with yields that are interpolated from a grid of stellar models.

Our derivation of an *s*-process-only component from the observational abundances and the similar subtraction of the initial abundances from the final abundances of the models (or the subtraction of the final abundances of two different models) enables us to compare our chemical evolution predictions with both cluster systems simultaneously, although the initial composition will affect the ratios of elements in the stellar yields (e.g., [ls/hs]).

For each stellar mass in the range from 15 to 40 $M_\odot$, massive star yields are interpolated from our grid of stellar models with initial rotation rates of 0.0 and 0.4 as a fraction of v_{crit} (Frischknecht & Thielemann 2012). For the particular initial mass of 25 $M_\odot$, we have also have yields from stellar models with rotation rates of 0.4 and 0.5 v_{crit} with and without alternative reaction rates (CF88/10). From the yields of the 25 $M_\odot$ stellar models, we calculate a set of factors (one per chemical species) that approximate the effect of these alternative parameters on the yields of the other models in the grid with different initial masses.
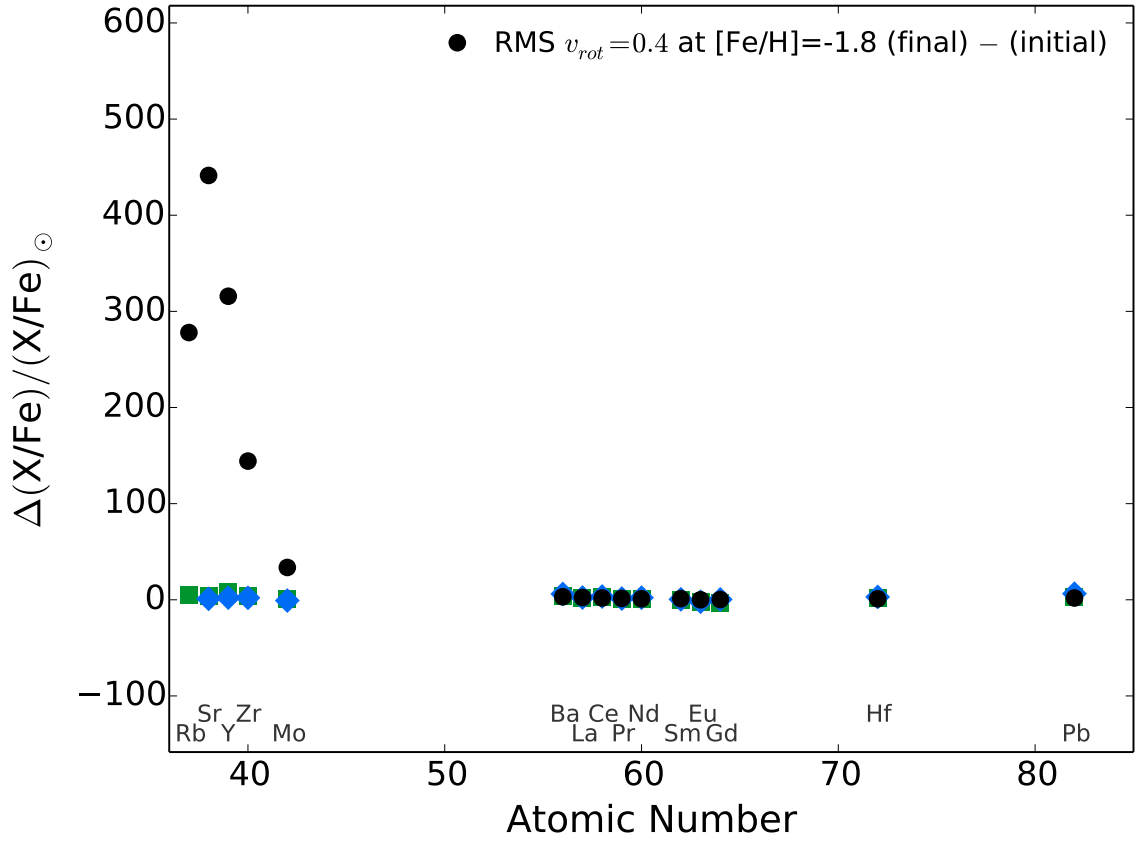
Figure 3.4 Chemical evolution results for rotating massive star yields at [Fe/H]= −1.8 with rotation rates at 40% of the break-up velocity. Also shown are the empirical distributions of M4 (green) and M22 (blue) scaled to match La abundance.

Table 3.1 and Figures 3.4–3.6 show the quantitative results of our chemical evolution models with rotating massive stars and AGB stars. The first two rows show the observation results in terms of [ls/hs][3] and [Pb/hs] ratios of the *s*-process residuals. A timescale is given for the models with AGB stars, which is the stellar lifetime of the lowest included mass.

3.7.1. Rotating Massive Stars

Figure 3.5 shows the chemical evolution results for rotating massive stars at very low metallicity ($Z = 10^{-5}$), where the abundances of models with low or no rotation have been subtracted from the abundances of faster rotating models to derive an *s*-process residual. These results correspond to the scenario of stochastic enrichment in which early generations of massive stars that formed M4 and M5 had a higher average rotation rate in the case of M4. For M22, these results correspond to a scenario in which the two groups chemically evolved separately. Although we only consider yields with a single

---

[3]We define [ls/Fe] = ([Y/Fe] + [Zr/Fe])/2, [hs/Fe] = ([Ba/Fe] + [La/Fe] + [Ce/Fe])/3, and [ls/hs] = [ls/Fe] - [hs/Fe].
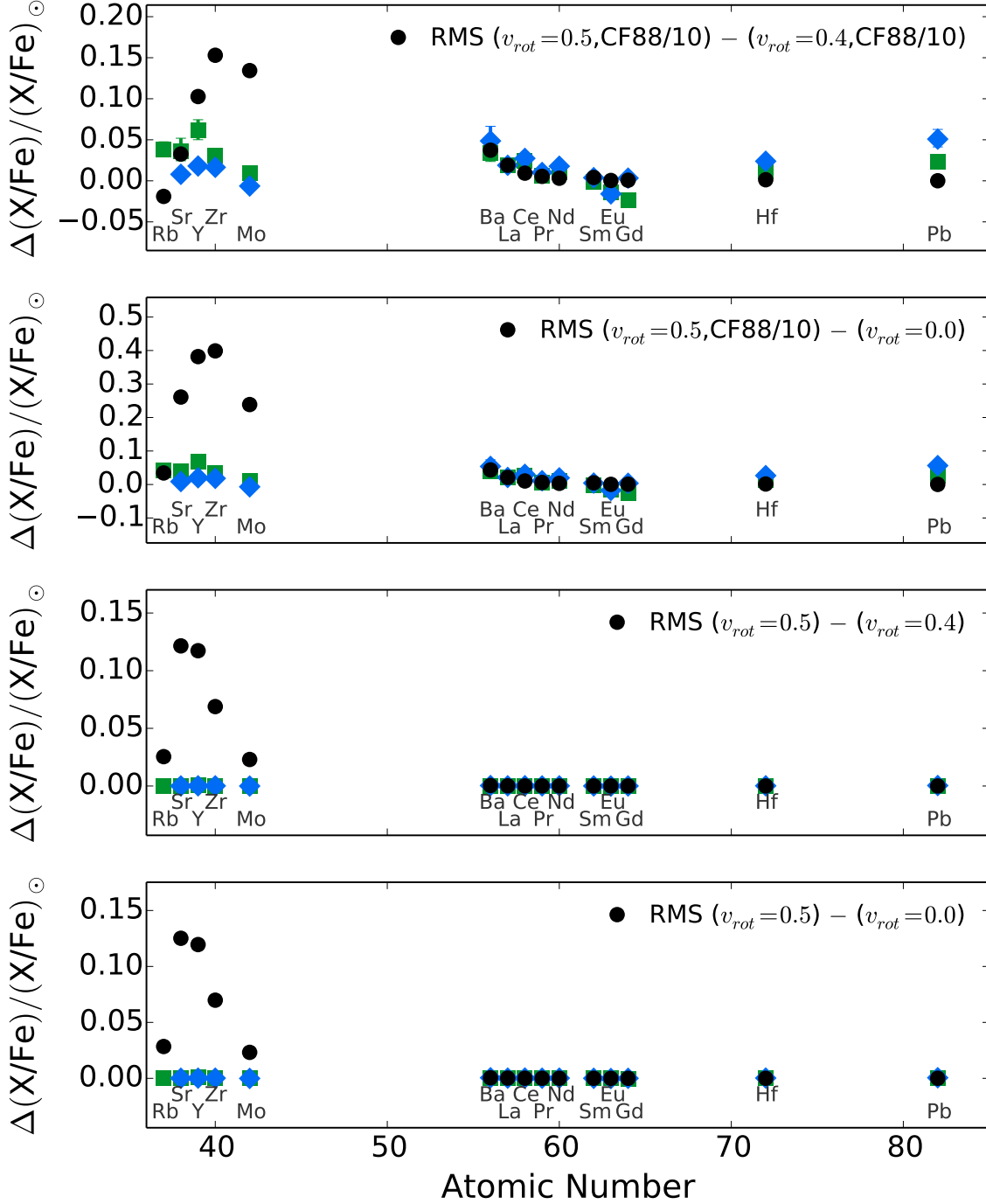
Figure 3.5 Chemical evolution abundance subtraction results for rotating massive star models at [Fe/H]= −3.8 with rotation rates of 0%, 40%, and 50% of the break-up velocity and an alternative reaction rate (CF88/10). Also shown are the empirical distributions of M4 (green) and M22 (blue) scaled to match La abundance.

value of v_{rot} in each chemical evolution model, future studies that model a distribution of rotational velocities would be of great interest. The resulting distributions are a poor match to the empirical distributions of both M4 and M22 (Figure 3.3), as they predict a very strong weighting toward light s-peak elements, even using the highest rotation rates and with an alternative reaction rate (CF88/10) that limits the effectiveness of ^{16}O as a neutron poison. The poor match to observations is also apparent from the high [ls/hs] ratios of 0.8–2.7 shown in Table 3.1, as compared with 0.24 in M4 − M5 and −0.23 in M22 (s-rich) − (s-poor).

To test the scenario for M22 in which rotating massive stars of the s-poor group have driven the increase in both [Fe/H] and the s-process abundances in the s-rich group, we present chemical evolution results from a generation of rotating massive stars at [Fe/H]= −1.8 that are shown in Figure 3.4. The abundances of the initial composition have been subtracted from the final (ejecta) abundances to derive an s-process residual using the same technique applied to M4 and M22. The s-process distribution is too strongly weighted toward elements at the first peak around Y (with an [ls/hs] ratio of 1.95) to match the observational distribution of M22.

3.7.2. AGB Stars

We test chemical evolution models that predict the output of a single generation of low-metallicity AGB stars, with the results provided in Figure 3.6 and Table 3.1. We vary the lower limit of the stellar mass range as a free parameter because this corresponds to the uncertain age difference between the s-process polluters and the s-process-rich stars (minus the gas cooling time). Because of the uncertainty over the upper mass limit for AGB stars to have a ^{13}C pocket, we separately test chemical evolution models in which the 3.25 and 3.5 $M_\odot$ yields are calculated from models with and without a PMZ of 1×10^{-3} $M_\odot$.

For M4, the [ls/hs] and [Pb/hs] ratios are bracketed from above and below by models with AGB yields that have lower limit masses of 3.00 and 3.25 $M_\odot$, respectively. From the stellar lifetimes, this corresponds to a minimum enrichment timescale 239–290 Myr. As the 3.00 $M_\odot$ stellar model includes a PMZ and the 3.25 $M_\odot$ model does not, this indicates a small contribution from stars with a ^{13}C pocket. If the models up to 3.5 $M_\odot$ include a PMZ, the [ls/hs] and [Pb/hs] ratios of M4 are bracketed by 3.5 and 4.0 $M_\odot$ lower-limit models, corresponding to a 140-200 Myr minimum enrichment timescale. With the uncertain upper mass limit for the ^{13}C pocket formation, the minimum enrichment timescale for M4 is likely around 140–290 Myr.

Although our AGB yields are not an exact match to the metallicity of M22 ([Fe/H] = −1.2 versus −1.8 in M22's s-poor group), we explore the similarities between our chemical
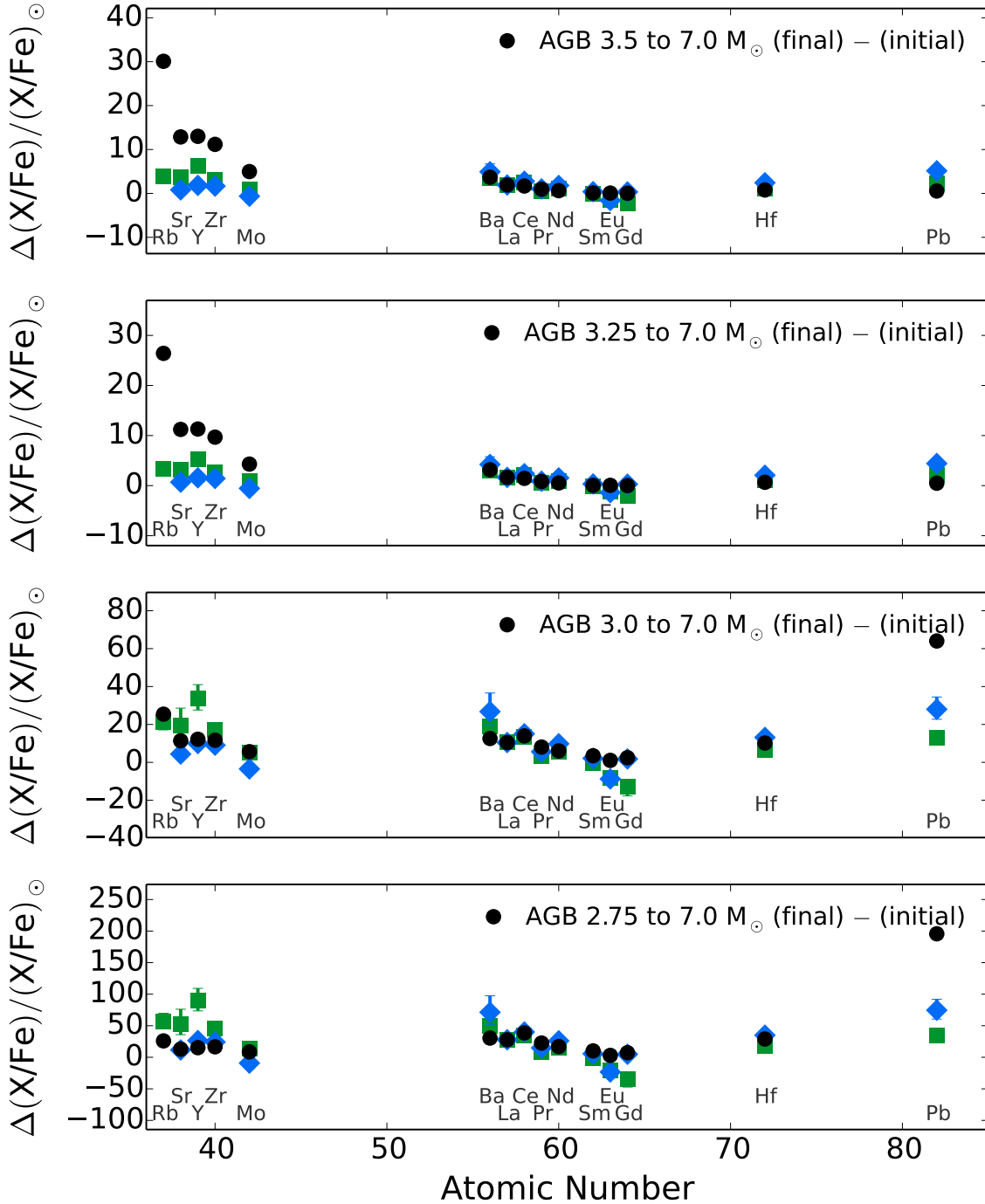
Figure 3.6 Chemical evolution results with several mass ranges of AGB yields at [Fe/H]= −1.2, and where the highest mass to include partial mixing zone is 3.0 M$_\odot$. Also shown are the empirical distributions of M4 (green) and M22 (blue) scaled to match La abundance.
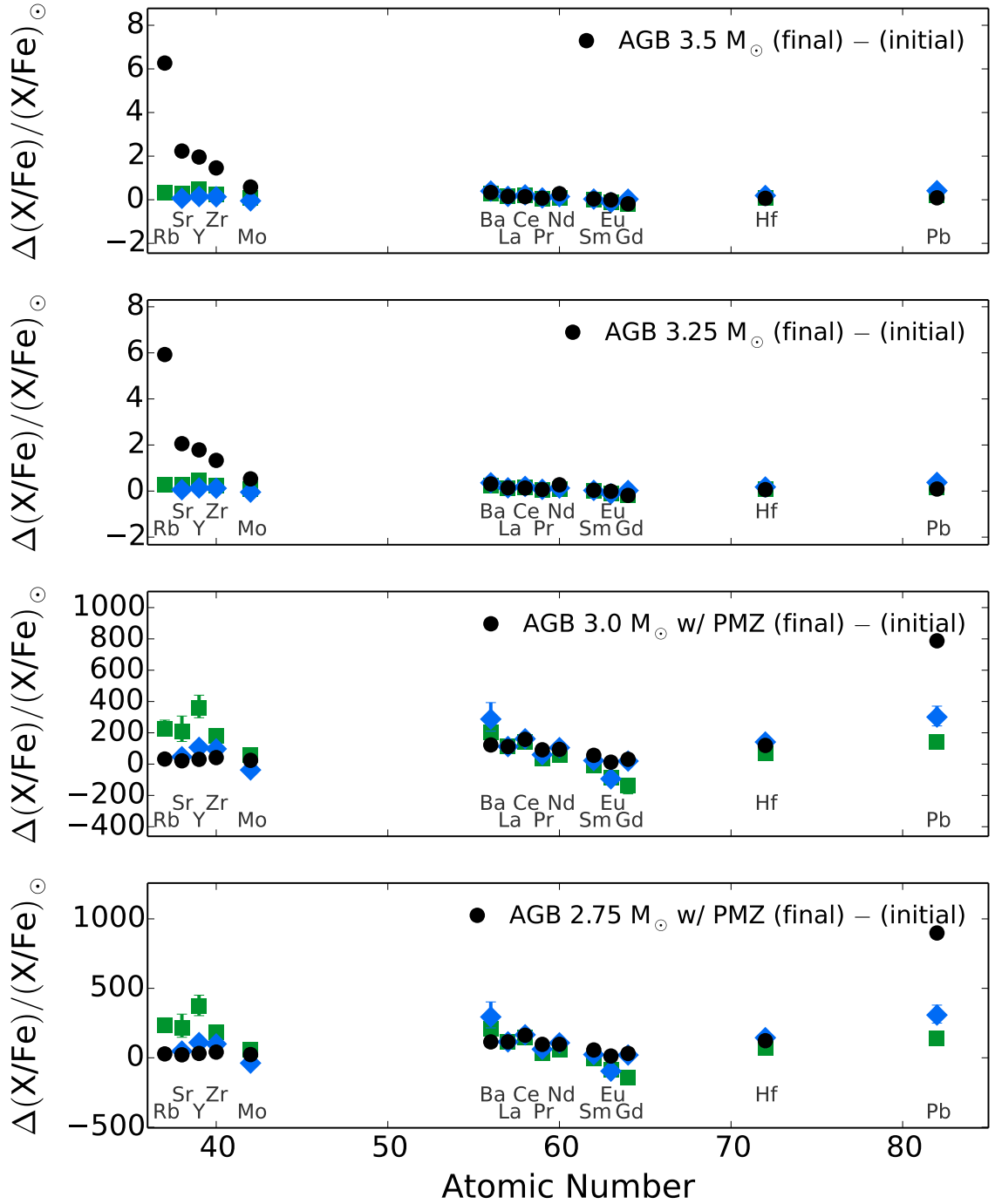
Figure 3.7 Results with single-mass AGB yields at [Fe/H]= −1.2. Also shown are the empirical distributions of M4 (green) and M22 (blue) scaled to match La abundance.

evolution results and the observational data. The chemical evolution of heavy elements in the *s*-rich group of M22 requires even lower mass stars than M4, however a simultaneous match of [ls/hs] and [Pb/hs] ratios is not found in our results. The [ls/hs] ratio in M22 is bracketed by 2.75 and 3.0 $M_\odot$ lower-limit models, while the [Pb/hs] ratio is bracketed by models with lower mass limits of 3.00 and 3.25 $M_\odot$. If the stellar masses up to 3.5 $M_\odot$ include a PMZ, we find that M22's [ls/hs] ratio is between those of the 3.00 and 3.25 $M_\odot$ lower-limit models, while the predicted [Pb/hs] of these models is still too high to match the data. In both of our test cases for the upper limit mass of ^{13}C pocket formation, the dual contribution from stars with a ^{13}C pocket as well as stars with a ^{22}Ne neutron source are required. With our assumption that ^{13}C pockets transition from fully developed to negligible between initial masses of 3.0 and 3.5 $M_\odot$, we predict a lower limit on the polluter masses of 2.75 to 3.25 $M_\odot$, which corresponds to a minimum enrichment timescale of 240–360 Myr.

A common method for comparing measured abundances with the predictions of stellar models is to use the yield results of a single stellar model rather than a grid covering a range of stellar masses that has been weighted by an initial mass function. In Table 3.1 and Figure 3.7, we present single-mass yield results for comparison with our chemical evolution results. The slope of the IMF means that the lowest contributing mass will have the largest contribution to the final abundances, however the single models with a ^{13}C pocket importantly lack the significant production of light *s*-elements that is due to intermediate-mass AGB stars. This difference is apparent in the high Rb/Sr ratio and overall higher abundances of Rb, Sr, Y, Zr, and Mo by the 3.0 to 7.0 $M_\odot$ model shown in Figure 3.6, as compared with same ratio from the single 3.0 $M_\odot$ model shown in Figure 3.7.

Table 3.1 Observational s-process residuals and the results of our chemical evolution models as well as individual AGB yields. The CF88/10 case is explained in Section 3.7.

A	B	$[ls/hs]_{A-B}$	$[Pb/hs]_{A-B}$	Timescale (Myr)
M4	M5	0.24	−0.03	-
M22 (s-rich)	M22 (s-poor)	−0.23	0.24	$\sim 300^a$
Results with [Fe/H] = −3.8 rotating massive star yields from 15 to 40 M$_\odot$				
RMS^b (v_{rot} = 0.5, CF88/10)	RMS(v_{rot} = 0.4, CF88/10)	0.82	−2.31	-
RMS (v_{rot} = 0.5, CF88/10)	RMS (v_{rot} = 0.0)	1.26	−2.02	-
RMS (v_{rot} = 0.5)	RMS (v_{rot} = 0.4)	2.73	−0.77	-
RMS (v_{rot} = 0.5)	RMS (v_{rot} = 0.0)	2.62	−0.50	-
Results with [Fe/H] = −1.8 rotating massive star yields from 15 to 40 M$_\odot$				
RMS (v_{rot} = 0.4v_{crit})	[Fe/H] = −1.8 (α-enhanced scaled solar)	1.95	−0.11	12
Results with [Fe/H] = −1.2 AGB yields (M ≤ 3.0 M$_\odot$ stellar models include a PMZ)				
AGB 3.50 to 7.0 M$_\odot$	[Fe/H] = −1.2 (scaled solar)	0.72	−0.62	199
AGB 3.25 to 7.0 M$_\odot$	[Fe/H] = −1.2 (scaled solar)	0.73	−0.61	239
AGB 3.00 to 7.0 M$_\odot$	[Fe/H] = −1.2 (scaled solar)	−0.01	0.72	290
AGB 2.75 to 7.0 M$_\odot$	[Fe/H] = −1.2 (scaled solar)	−0.30	0.79	364
Results with [Fe/H] = −1.2 AGB yields (M ≤ 3.5 M$_\odot$ stellar models include a PMZ)				
AGB 4.00 to 7.0 M$_\odot$	[Fe/H] = −1.2 (scaled solar)	0.72	−0.62	144
AGB 3.50 to 7.0 M$_\odot$	[Fe/H] = −1.2 (scaled solar)	0.09	0.86	199
AGB 3.25 to 7.0 M$_\odot$	[Fe/H] = −1.2 (scaled solar)	−0.10	0.92	239
AGB 3.00 to 7.0 M$_\odot$	[Fe/H] = −1.2 (scaled solar)	−0.25	0.89	290
AGB 2.75 to 7.0 M$_\odot$	[Fe/H] = −1.2 (scaled solar)	−0.37	0.86	364
[Fe/H] = −1.2 individual-mass AGB yields				
AGB 3.50 M$_\odot$	[Fe/H] = −1.2 (scaled solar)	0.94	−0.34	199
AGB 3.25 M$_\odot$	[Fe/H] = −1.2 (scaled solar)	0.94	−0.30	239
AGB 3.00 M$_\odot$ w/ PMZ	[Fe/H] = −1.2 (scaled solar)	−0.56	0.78	290
AGB 2.75 M$_\odot$ w/ PMZ	[Fe/H] = −1.2 (scaled solar)	−0.55	0.84	364

^{a}Derived from isochrone fitting of the subgiant branch region by Marino et al. (2012).
^{b}Rotating massive stars.

3.8.   Discussion and Conclusions

We have used the shape of the *s*-process distributions in M4 and M22 to identify the
s-process polluter mass range and the corresponding maximum stellar lifetime, which
places a lower limit on the timescale of *s*-process enrichment. As well as *s*-process
enrichment, M4 and the two groups in M22 also feature anti-correlated variations in O and
Na, which we do not attempt to explain. Although we match the *s*-process distribution of
M22's *s*-rich group with the ejecta of AGB stars, the coexistence of an Fe variation in M22
likely required some fraction of the ejecta from massive stars to be kept within the cluster
to form new stars with a higher Fe abundance.

The lower-limit mass range of 2.75–3.25 $M_\odot$ in our best-fitting models for M22 corresponds
to a stellar lifetime in the range 300 ± 60 Myr. Assuming that the time for the ejecta to cool
and form new stars is relatively small, this value is consistent with the 300 Myr upper
limit derived from isochrone fitting of the subgiant branch region by Marino et al. (2012)
and Joo & Lee (2013). A match between the inter-group age difference and the lifetime of
the minimum polluter mass supports a scenario in which the metal-rich group in M22 has
been self-enriched with material ejected from stars coeval with the present-day *s*-poor
group. Alternative scenarios in which the two metallicity groups in M22 (which have
independent light element anti-correlations) are the result of a merger of two separate GC
systems or the second generation is formed from *s*-process rich material accreted from
outside the cluster are also plausible. However, under both of these alternative scenarios,
the close match between timescales of pollution and the age difference between the stellar
groups would be a coincidence.

Further evidence for a lower mass limit of ≈ 3 $M_\odot$ and an enrichment timescale of ≈ 300
Myr for M22 is the measured 0.6 dex spread in F abundances (Alves-Brito et al. 2012;
D'Orazi et al. 2013b). D'Orazi et al. (2013b) report F abundances that correlate with O,
are anti-correlated with Na, and increase between the two groups. The authors suggest
that the *s*-rich group has been enriched by the ejecta of stars with masses between 4 and
5 $M_\odot$, as these stars would destroy (rather than produce) F while O is destroyed in the
early stages of GC formation. However, these measurements could be heavily affected by
systematic errors as is claimed by de Laverny & Recio-Blanco (2013), who argue that a
reliable detection of the HF line in M22 stars is unlikely due to errors in radial velocity
correction, continuum subtraction, and the removal of telluric absorption lines.

The matching of M4 − M5 to a model of AGB ejecta opens up the question of how the
formation of M4 differed to that of M5. A scenario similar to M22 in which an *s*-poor
generation of stars pollute the interstellar medium from which a second generation forms
is ruled out by observations of constant *s*-process abundances in M4, which do not feature
the same bimodality found in M22. A more likely scenario is that M4 and M5 formed out

of material in an inhomogeneous early Galactic halo. James et al. (2004) show that Ba and Eu abundances plotted as a function of [Fe/H] for mono-metallic GCs (including M4 and M5) fall within the spread of halo field star values, suggesting that they share a common origin or a similar enrichment process.

Our inferred enrichment timescales for M4 and M22 are roughly a factor of two larger than the 150 ± 50 Myr for both clusters inferred by Straniero et al. (2014). They require a larger minimum contributing mass (4.0 ± 0.5 $M_\odot$) due to their inclusion of a prescription for core-envelope convective boundary mixing (Cristallo et al. 2009) that predicts small ^{13}C pockets in AGB models with masses as high as 4.5 $M_\odot$. The predictions of Straniero et al. (2014) and those in this paper are both consistent within the uncertainty of the age spread in M22 derived from isochrone fitting. Our results support their conclusion that neutron captures from both ^{13}C pockets and the ^{22}Ne source operating in convective pulses are required to explain the s-process enrichment of M4 and M22.

While our massive star models could not reproduce the s-process enhancements seen in M4 and in M22, there are still large uncertainties on the yields of s-process elements from rotating massive star models. For example, the yields of Gallino et al. (2008) show a ratio between Y and Ba of approximately unity (see their Figure 2). This suggests that while AGB stars produce the best fit with our adopted stellar yields, other sets of yields may change our conclusions as to the nature of the polluters of heavy elements in GCs.

We consider the effect of a possible r-process difference between the s-rich and s-poor samples of up to [r/Fe] = 0.4. Using the solar system r-process fractions of Simmerer et al. (2004), the effect would be to increase [Y/Fe] by 0.15 dex, [Zr/Fe] by 0.07 dex, [Ba/Fe] by 0.09 dex, [La/Fe] by 0.14 dex, and [Ce/Fe] by 0.11 dex. The net result for the [ls/hs] ratio would be a change of less than 0.01 dex. The ratio [Pb/Fe] would increase by 0.12 dex, resulting in a [Pb/hs] change of less than 0.01 dex. We conclude that our results hold independently of a possible r-process difference between M4 and M5 or the two populations in M22. A dilution by pristine material would shift the [X/Fe] ratios in the s-process residual to closer to zero, but would not affect the relative abundances between elements.

Our models predict [Pb/hs] ratios that are too high to match the observations of M22. A similar phenomenon is reported by De Smedt et al. (2014) for metal-poor ([Fe/H]< −1) post-AGB stars in the Magellanic clouds, which they refer to as the "lead discrepancy;'. If the Pb measurements are correct, then a solution to the lead discrepancy will likely require a better understanding of the mixing that leads to the formation of a ^{13}C pocket, possibly by modeling it as an advective process, rather than the more typical diffusive treatment. One form of extra mixing that is not included in our AGB models (or in most AGB stellar models) is the mixing due to rotation. The study of AGB models with rotation by Piersanti et al. (2013) hints at a possible solution to the lead discrepancy, as they find

that rotation reduces the [Pb/hs] ratio in the stellar yields.

Rb is overproduced in our best-fitting model in comparison with the observational data for M4, while separate Rb abundances for the two groups in M22 are not available in the literature. An overproduction of Rb in AGB stellar models is also noted by D'Orazi et al. (2013) under the assumption that AGB stars are responsible for the light element variations in M4. Their 6 $M_{\odot}$ model with the mass-loss rate from Vassiliadis & Wood (1993) and a mixing-length parameter of $\alpha = 1.75$ produces too much variation in neutron-capture elements, for too little variation in Na. Their solution is to use the higher mass-loss rates of Bloecker (1995) and a boosted mixing-length parameter ($\alpha = 2.2$), which improves the fit to the abundances in M4 by increasing the temperature at the base of the convective envelope and reducing the cumulative dredge-up of *s*-process elements into the envelope.

The opposite case of a Rb underproduction is found when stellar models (5–9 $M_{\odot}$) are compared with AGB stars in the Galaxy and Magellanic clouds (van Raai et al. 2012; Karakas et al. 2012), although recent work by Zamora et al. (2014) suggests that the inferred Rb abundances may be systematically overestimated due to the presence of circumstellar envelopes. The implementation of a delayed superwind to increase Rb yields explored by Karakas et al. (2012) would likely worsen the discrepancy in our results, unless there was a simultaneous reduction in Rb production by the less massive (< 5 $M_{\odot}$) AGB models.

Future stellar models at the correct metallicity for M22, and more generally improvements to the numerical treatment of mixing and mass loss might help to reduce some of the discrepancies with observations of the *s*-process abundances in globular clusters. Even with present models, the application of similar techniques to other clusters with *s*-process variation such as M2 (Yong et al. 2014) and ω Centauri would enable us to characterize the full range of enrichment timescales and polluter masses among the anomalous GCs.

3.9. Acknowledgements

3.10.   Appendix: Verification of Evel ChemEvol code

To validate the output of the new chemical evolution code Evel ChemEvol used in this study, we use the stellar yields and GC self-pollution scenario described by Fenner et al. (2004). A metal-free initial composition is first polluted with the ejecta of massive stars up to a metallicity of [Fe/H]$= -1.4$. Subsequently, star formation takes place on a timescale of 10^7 yr. The ejecta from stars < 6 M$_\odot$ is kept within the system, while ejecta from more massive stars is lost.

Our chemical evolution results in Figures 3.8–3.10 for Evel ChemEvol correspond almost exactly to Figures 1, 3, and 4 of Fenner et al. (2004). Small differences in the output can be explained by differences in the stellar lifetime function and the treatment of the massive star pollution phase, which were not specified in detail in the original paper.

The results of this comparison give us confidence that the Evel ChemEvol is producing the correct abundance outputs and can be used to explore new chemical evolution scenarios.
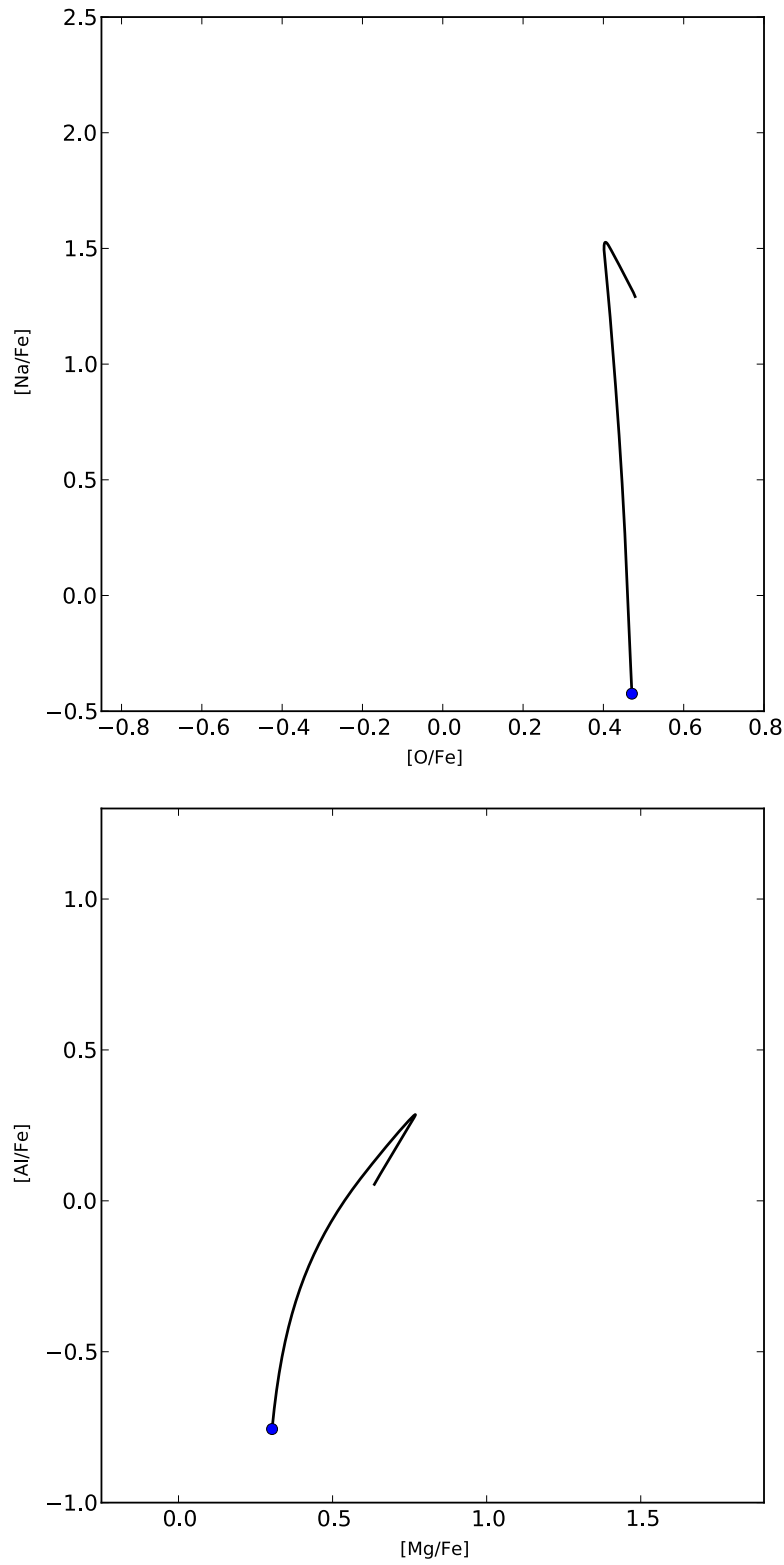
Figure 3.8 Chemical evolution results of Na, O, Al, and Mg with Evel ChemEvol for comparison with Fenner et al. (2004, Figure 1). The blue point indicates the composition after the massive star pollution phase and before ejecta from AGB stars has been produced.
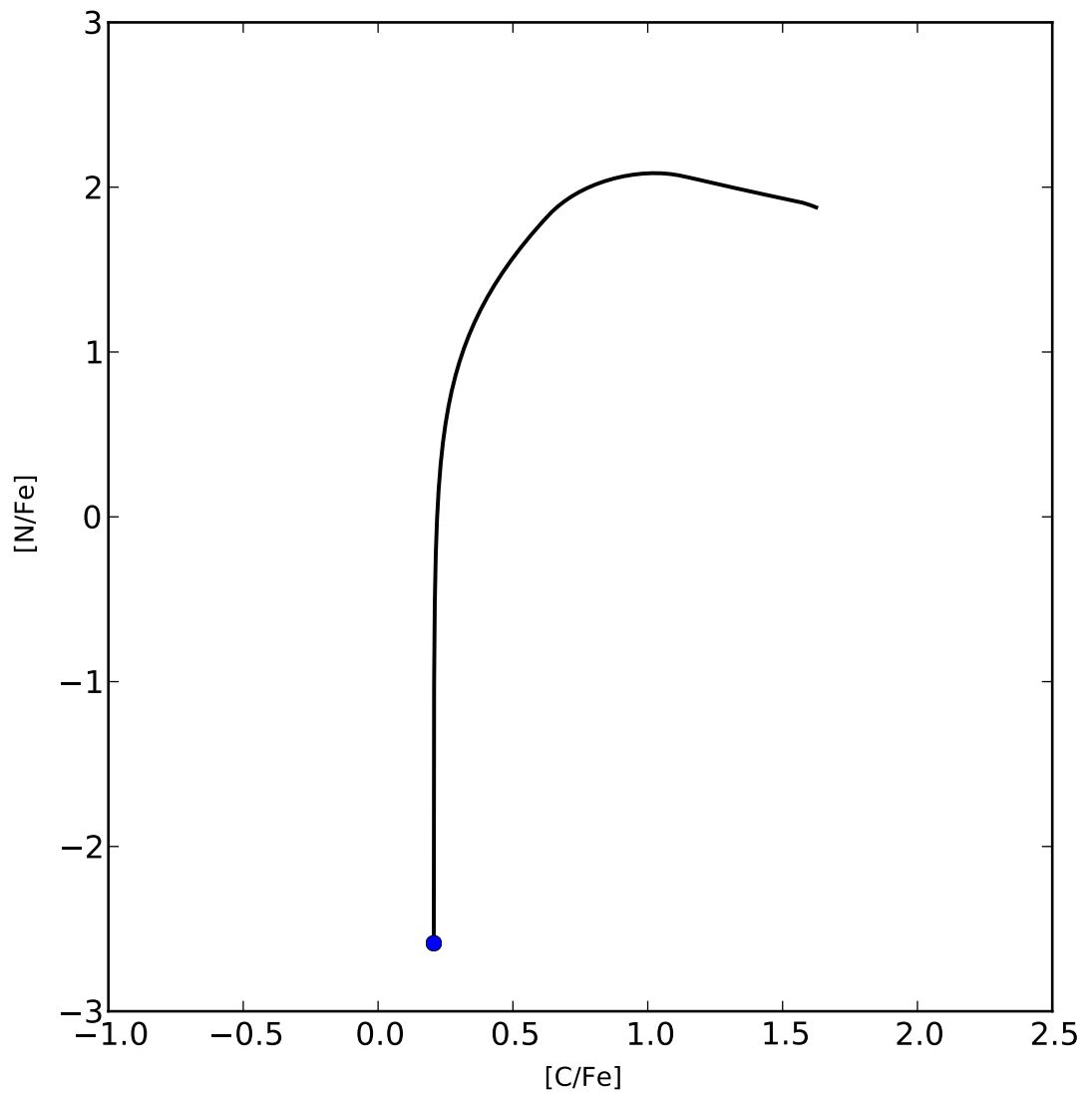
Figure 3.9   Chemical evolution results of N and C with Evel ChemEvol for comparison with Fenner et al. (2004, Figure 3).
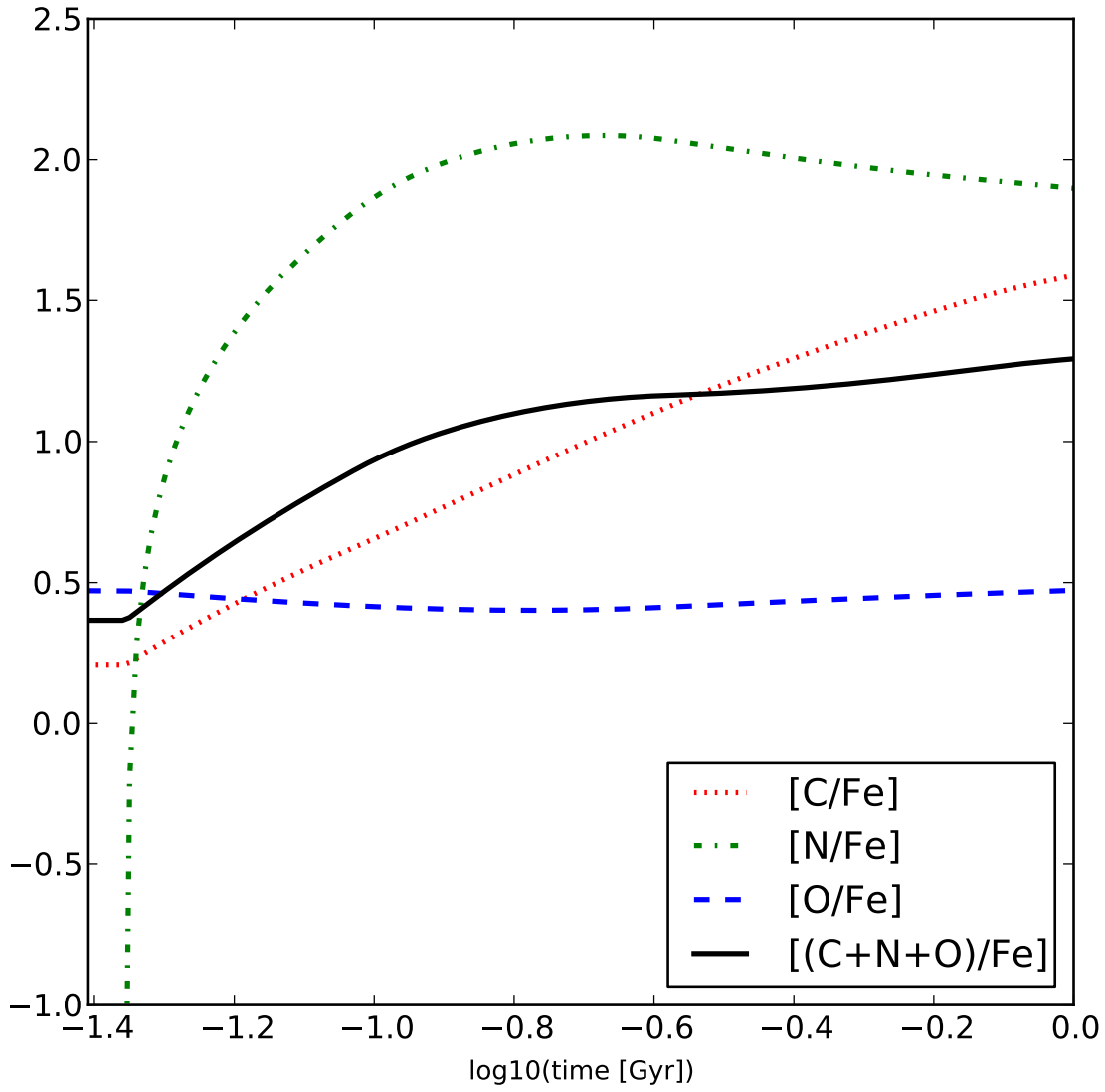
Figure 3.10 Chemical evolution results of C, N, and O with Evel ChemEvol for comparison with Fenner et al. (2004, Figure 4).

CHAPTER 4

Evolution and nucleosynthesis of helium-rich asymptotic giant branch models

4.1. Chapter Summary

There is now strong evidence that some stars have been born with He mass fractions as high as $Y \approx 0.40$ (e.g., in ω Centauri). However, the advanced evolution, chemical yields, and final fates of He-rich stars are largely unexplored. We investigate the consequences of He-enhancement on the evolution and nucleosynthesis of intermediate-mass asymptotic giant branch (AGB) models of 3, 4, 5, and 6 $M_{\odot}$ with a metallicity of $Z = 0.0006$ ([Fe/H] ≈ -1.4). We compare models with He-enhanced compositions ($Y = 0.30, 0.35, 0.40$) to those with primordial He ($Y = 0.24$). We find that the minimum initial mass for C burning and super-AGB stars with CO(Ne) or ONe cores decreases from above our highest mass of 6 $M_{\odot}$ to ~ 4–5 $M_{\odot}$ with $Y = 0.40$. We also model the production of trans-Fe elements via the *slow* neutron-capture process (*s*-process). He-enhancement substantially reduces the third dredge-up efficiency and the stellar yields of *s*-process elements (e.g., 90% less Ba for 6 $M_{\odot}$, $Y = 0.40$). An exception occurs for 3 $M_{\odot}$, where the near-doubling in the number of thermal pulses with $Y = 0.40$ leads to $\sim 50\%$ higher yields of Ba-peak elements and Pb if the ^{13}C neutron source is included. However, the thinner intershell and increased

temperatures at the base of the convective envelope with $Y = 0.40$ probably inhibit the ^{13}C neutron source at this mass. Future chemical evolution models with our yields might explain the evolution of s-process elements among He-rich stars in ω Centauri.

4.2. Introduction

Stars that evolve through the asymptotic giant branch (AGB) play a crucial role in the chemical evolution of stellar populations and galaxies. These stars experience a complex sequence of He-shell instabilities, mixing, and mass loss processes that combine to eject material that has undergone H and He burning, and enrichment in heavy elements produced by the *slow* neutron-capture process (s-process). Understanding the chemical contribution by stars to the interstellar medium is a prerequisite for building models of chemical evolution (e.g., Chiappini et al. 2001; Kobayashi et al. 2011).

The most important parameter governing stellar evolution is the initial mass, with a secondary role played by chemical composition. Chemical composition typically refers to the mass fraction of metals (Z), but the mass fraction of He (Y) also has major consequences for stellar evolution. However, the stellar evolution and nucleosynthesis that take place during the AGB phase are relatively unexplored for He-rich initial compositions. For a detailed introduction to AGB evolution and nucleosynthesis with normal He content, we refer the reader to the reviews by Herwig (2005) and Karakas & Lattanzio (2014).

There is strong evidence that some stars have been born with substantial He enrichments above the primordial He mass fraction of $Y \approx 0.24$ predicted from big bang nucleosynthesis. The most direct method to measure He abundances is to use spectroscopy, however the application to He is severely hindered by the lack of He lines in cool stars, and the effects of gravitational settling in hot stars. Still, direct detections of He have been made, such as those by Pasquini et al. (2011), who used the He I 10830 Å line in two stars with different Na and O abundances in NGC 2808 to derive a difference of $\Delta Y \geq 0.17$. The finding of He-enhanced second-generation stars in NGC 2808 is also supported by Marino et al. (2014) with a sample of 96 horizontal-branch stars, although they report a smaller average enhancement of $\Delta Y = 0.09 \pm 0.06$. The same He I 10830 Å line was also used by Dupree & Avrett (2013) to infer a variation of $\Delta Y \geq 0.17$ between red giants in ω Centauri.

A second, less-direct line of evidence for He-rich stars is the requirement of high He abundances to reconcile theoretical isochrones with the photometry of clusters in colour-magnitude diagrams (CMDs). For example, the split main sequence of ω Centauri can be explained by multiple populations that vary in both metallicity and He abundance (Bedin et al. 2004; Norris 2004; Piotto et al. 2005). King et al. (2012) report a best fit to the blue main sequence with a He abundance of $Y = 0.39 \pm 0.02$. The high He abundance also

persists when additional features of the CMD are incorporated in a simultaneous fit, such as the work of Joo & Lee (2013), who infer Y of up to 0.39 ± 0.02 for ω Centauri and up to 0.32 ± 0.04 for M22.

With relatively few theoretical studies of the detailed AGB evolution and nucleosynthesis of He-rich models (Campbell et al. 2013; Charbonnel et al. 2013; Karakas 2014; Karakas et al. 2014), the effects of high He abundances on chemical evolution are not well understood. An important set of observational clues is the s-process abundances in ω Centauri. In this cluster, [Ba/Fe][1] increases with metallicity up to about [Fe/H] = −1.4, above which [Ba/Fe] remains roughly constant (Norris & Da Costa 1995). Interestingly, this plateau occurs near the metallicity of the most He-rich population (Joo & Lee 2013), and one potential explanation is that Ba yields are lower in He-rich stars. Chemical evolution might play out similarly in other clusters such as M22, which follows the same rise of [Ba/Fe] (Da Costa & Marino 2011) but where a truncation of the chemical evolution at a metallicity below [Fe/H]= −1.4 prevents the possibility of a similar s-process plateau.

Karakas, Marino, & Nataf (2014, hereafter KMN14) present stellar yields of He-enhanced 1.7 and 2.36 $M_\odot$ AGB models with a metallicity of [Fe/H] $\approx$ −1.4. This metallicity is appropriate for the most metal-poor of the He-rich populations in ω Centauri (Joo & Lee 2013). Among the findings of KMN14 is a reduction in the third dredge-up (TDU) mass with increasing initial He abundance. Largely as a result of the less efficient dredge-up, their Ba yields decrease by roughly 50 per cent with $Y = 0.40$ in comparison with primordial-He models at the same initial mass.

In this work, we extend the study of He-enhanced AGB nucleosynthesis by KMN14 with new intermediate-mass models of 3, 4, 5, and 6 $M_\odot$ at the same metallicity of $Z = 0.0006$ and with similar input physics. For our primordial He models, we make a comparison with the models of Straniero, Cristallo, & Piersanti (2014, hereafter SCP14), which have $Y = 0.245$, $Z = 0.0003$ (before α-enhancement, [Fe/H] = −1.7), and [α/Fe] = 0.5. We also compare our evolutionary models with the primordial-He models of Ventura & D'Antona (2009, hereafter VD09), which have $Z = 0.0006$ and [α/Fe] = 0.4. The models of VD09 are calculated with the Full Spectrum of Turbulence (FST; Canuto & Mazzitelli 1991) treatment of convective mixing and energy transport rather than the more common Mixing Length Theory (MLT; Biermann 1948).

The stellar yields of He-rich models, including those presented in this study, will build a foundation for future work in understanding the chemical evolution of He-rich environments. Our comparison with other models in the literature allows us to estimate how sensitive our predictions for He-rich stellar evolution and yields are to uncertain modelling assumptions.

---

[1]We use the standard spectroscopic notation, [A/B] = $\log_{10}(N_A/N_B) - \log_{10}(N_A^\odot/N_B^\odot)$, where N_A and N_B are abundances by number and $\odot$ denotes the solar abundance.

In Section 4.3 we describe our computational method and stellar modelling assumptions. In Section 4.4 we present our stellar evolutionary models. In Section 4.5 we present the nucleosynthesis models and explore the impact of He-enhancement on the stellar yields. In Section 4.6 we discuss our results in the context of other studies in the literature and consider the implications for He-rich chemical evolution.

4.3.   Computational Method

We present evolutionary sequences for initial masses of 3, 4, 5, and 6 $M_\odot$ with a global metallicity of $Z = 0.0006$ ([Fe/H] ≈ -1.4 and [α/Fe]$= 0.0$), and initial He mass fractions of $Y = 0.24, 0.30, 0.35$, and 0.40.

We use the same input physics and stellar evolutionary code as KMN14 (the MOUNT STROMLO STELLAR STRUCTURE PROGRAM), except that we include the opacity treatment of Fishlock et al. (2014b), which accounts for changes to the C abundance and the C/O ratio at the surface. This opacity treatment improves the accuracy for models that experience hot bottom burning (HBB; discussed in Section 4.4.4). At low temperatures ($T < 10\,000$ K), we use the molecular opacity tables from AESOPUS (Marigo & Aringer 2009). At higher temperatures, we use OPAL tables (Iglesias & Rogers 1996) that have been updated to a Lodders (2003) scaled-solar composition.

The initial abundances of the models are scaled solar (Asplund et al. 2009) with a global metallicity of $Z = 0.0006$. With Z fixed and a chosen value of Y, the H mass fraction (X) is determined by $X = 1 - Y - Z$. A consequence of keeping the mass fraction of metals (including Fe) constant and exchanging mass between H and He is that the initial ratio of Fe to H varies slightly between our models of different He abundance. Specifically, the initial [Fe/H] is -1.41 in the models for $Y = 0.24$, and -1.31 in the models for $Y = 0.40$.

The search for stable convective borders uses the method of Lattanzio (1986) (see also Frost & Lattanzio 1996), and we assume no other form of extra mixing at convective boundaries. The convective velocities are calculated using MLT with a mixing length parameter of $\alpha = 1.86$. Although the constancy of α is a standard assumption, empirical and theoretical studies have found a variation of this parameter with stellar evolution (Lebzelter & Wood 2007; Magic & Asplund 2014). Larger values of α can increase the depth of the TDU (e.g., Boothroyd & Sackmann 1988b), which in turn typically increases the yields of C+N+O and s-process elements (Cristallo et al. 2009, 2011).

We do not include mass loss on the first red giant branch (RGB). This assumption is reasonable (in the context of stellar yield predictions) given recent results using *Kepler* data, which indicate that the total mass loss during the RGB is relatively small ($\Delta M = 0.09 \pm 0.03 \pm 0.04$ $M_\odot$; Miglio et al. 2012), at least near solar metallicity. Many of

our models do not reach the RGB and for the models that do, the inclusion of mass loss of the this order would have a minimal impact on our stellar yield predictions, which are subject to much larger uncertainties related to mass loss during the AGB phase (Stancliffe & Jeffery 2007). For mass loss on the AGB, we use the prescription given by Equations (1)–(4) of Vassiliadis & Wood (1993), which includes a superwind phase beginning at pulsation periods above approximately 500 d.

The output of the stellar evolution code (including the temperatures, densities, convective boundaries, and convective velocities) is used as input to a post-process code that performs the detailed nucleosynthesis calculations with a large network of 320 species up to Po. The two-pass method used in this work is different to the models of SCP14 calculated with the FUNS code (a descendant of FRANEC; Chieffi & Straniero 1989), which solves the stellar structure equations simultaneously with the full network of nuclear reactions.

Another difference is that our post-processing code solves simultaneously the abundance changes wrought by mixing and burning. To mix the convective regions in our nucleosynthesis models, we use the two-stream, time-dependent method devised by Cannon (1993). An upward and a downward-moving stream are treated separately, with the mass-flow rate at each mass shell calculated from the convective velocities in the evolutionary model. It is assumed that the material from an upward moving cell below flows into the upward moving cell above, and likewise the material in a downward moving cell flows into the downward moving cell below, as well as horizontally mixing from one stream to the other.

4.3.1.   The inclusion of ^{13}C pockets

For stars with initial masses $\lesssim 3$ M$_\odot$, the dominant neutron source driving s-process nucleosynthesis is the ^{13}C$(\alpha, n)^{16}$O reaction (Busso et al. 1999), while the ^{22}Ne$(\alpha, n)^{25}$Mg reaction becomes more important at higher initial masses (García-Hernández et al. 2013). For our 3 M$_\odot$ models which are near the mass of this transition, the treatment of ^{13}C-pocket formation is crucial for making accurate predictions of the stellar yields and surface abundances of neutron-capture elements.

In current theoretical models, the ^{13}C$(\alpha, n)^{16}$O reaction occurs in a thin layer of ^{13}C that results from the partial mixing of protons from the base of the envelope into the ^{12}C-rich intershell region during TDU (Straniero et al. 1995; Gallino et al. 1998). The protons then are captured by ^{12}C where they activate the CN cycle reactions ^{12}C$(p, \gamma)^{13}$N$(\beta^+\nu)^{13}$C. The number of protons mixed into the region must be low because further proton capture results in ^{14}N, which efficiently absorb free neutrons. The physical mechanism that produces the partially mixed zone (PMZ) has not been conclusively identified, but plausible candidates include convective-boundary mixing (Herwig 2000; Cristallo et al. 2009), rotational mixing (Langer et al. 1999; Herwig & Langer 2001), gravity-wave driven

mixing (Denissenkov & Tout 2003), and semiconvection (Iben & Renzini 1982; Hollowell & Iben 1989). Further, the important effect of rotationally induced mixing on the neutron release in the ^{13}C pocket has been investigated by Herwig et al. (2003), Siess et al. (2004), and Piersanti et al. (2013).

The nature of the transition away from ^{13}C pockets with increasing initial mass is also highly uncertain, although it is very likely connected with the shrinking of the He-rich intershell and the higher temperatures at the base of the convective envelope with larger core masses.

For example, the models of SCP14 assume that the convective velocity declines exponentially with distance beyond the formal convective boundary, with a free parameter describing the length scale of the velocity decline. This method is applied only to convective boundaries for which the velocity is discontinuous, which occurs at the base of the envelope during TDU episodes (Cristallo et al. 2009). The convective velocity is incorporated into a non-diffusive mixing scheme (Straniero et al. 2006) and results in ^{13}C pockets that smoothly decrease in size (and neutron production) with increasing initial mass.

Goriely & Siess (2004) show that a diffusive treatment of convective-boundary mixing can reduce the amount of neutron production by ^{13}C pockets (due to enhanced production of ^{14}N) when TDU takes place with temperatures above 40 MK, and can totally inhibit the s-process with temperatures above 70 MK. As shown in Table 4.2, the maximum temperatures at the base of the envelope during TDU for our 3 $M_\odot$ models with Y between 0.24 and 0.35 occupy this transition range of temperatures. For the 3 $M_\odot$ model with $Y = 0.40$ and the higher-mass models with all He abundances, temperatures above 70 MK during TDU would likely prevent a significant s-process production by ^{13}C pockets. For this reason, a PMZ leading to the formation of a ^{13}C pocket is not included in our models with $M \geq 4\,M_\odot$. For the initial mass of 3 $M_\odot$, we construct nucleosynthesis models with and without a PMZ at each He abundance.

In the absence of a deep physical understanding of the PMZ, we apply the simple parametrized treatment used by Lugaro et al. (2004) (similar to Goriely & Mowlavi 2000) in our nucleosynthesis post-processing models. For models that include a PMZ, we insert an exponential (in mass coordinate) profile of protons below the envelope at the deepest extent of each TDU episode. The proton abundance starts at the envelope value and decreases by a factor of 10^4 through a depth given by the parameter M_{pmz}. The value of M_{pmz} is uncertain, although a variety of constraints have been derived from observations of AGB stars (Abia et al. 2002), C-enhanced metal poor stars (Izzard et al. 2009; Bisterzo et al. 2012; Lugaro et al. 2012), planetary nebulae (Miszalski et al. 2013; Shingles & Karakas 2013), and post-AGB stars (Bonačić Marinović et al. 2007b; De Smedt et al. 2012). KMN14 presented 1.7 and 2.36 $M_\odot$ models with a range of PMZ sizes, but for comparison we

only use their results for a PMZ of 10^{-3} M$_\odot$. Except where stated otherwise, our 3 M$_\odot$ nucleosynthesis models include a PMZ with $M_{pmz} = 10^{-3}$ M$_\odot$.

4.4. Stellar Evolution Models

The evolutionary properties of our models and their dependencies on the initial He abundance are reported in Tables 4.1 and 4.2 and discussed below.
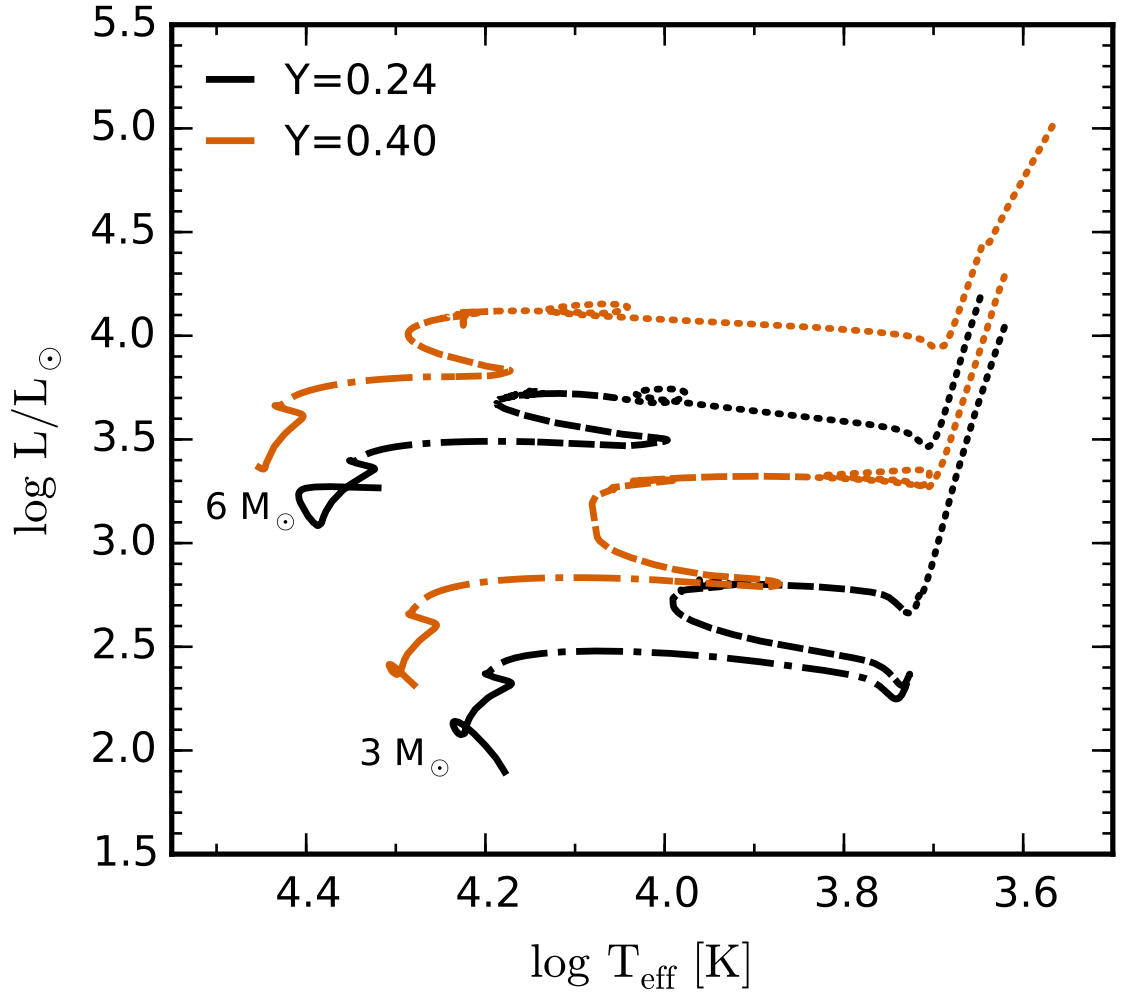
Figure 4.1 Evolutionary Hertzsprung–Russell tracks of 3 and 6 M$_\odot$ models at $Y = 0.24$ (black lines) and $Y = 0.40$ (orange lines) from the main sequence to the beginning of the thermally pulsing AGB phase. Line styles indicate the nuclear burning stages: core H burning (solid), shell H burning (dot dashed), core He burning (dashed), and shell He and H burning (dotted).

Table 4.1 Evolutionary lifetimes, first and second dredge-up masses, and final model properties. We include the initial stellar mass (M_{ini}), the initial He mass fraction (Y), the core H-burning lifetime (τ_{ms}), the core He-burning lifetime (τ_{coreHe}), the AGB lifetime measured from the exhaustion of core He until the end of calculations plus the estimated time to lose the remaining envelope (τ_{agb}), the total stellar lifetime ($\tau_{stellar}$), the innermost mass layer reached by first and second dredge-up (M_{FDU} and M_{SDU}), the final stellar mass (M^{final}), the final core mass (M_C^{final}), the final envelope mass (M_{env}^{final}), the final mass-loss rate ($\dot{M}^{final}$), and the class of white dwarf remnant formed. Final refers the state at the end of our calculations, which cease due to convergence problems before the envelope has been fully ejected.

M_{ini}	Y	τ_{ms} [Myr]	τ_{coreHe} [Myr]	τ_{agb} [Myr]	$\tau_{stellar}$ [Myr]	M_{FDU} [M$_\odot$]	M_{SDU} [M$_\odot$]	M^{final} [M$_\odot$]	M_C^{final} [M$_\odot$]	M_{env}^{final} [M$_\odot$]	$\dot{M}^{final}$ [10^{-5} M$_\odot$]	Remnant
3 M$_\odot$	0.24	213.2	59.6	0.81	290.1	1.79	0.786	1.462	0.801	0.661	2.64	CO WD
	0.30	161.2	45.5	0.29	219.5	2.28	0.844	1.182	0.858	0.324	3.06	CO WD
	0.35	126.1	35.9	0.23	172.5	2.94	0.863	1.628	0.880	0.748	3.39	CO WD
	0.40	97.5	29.0	0.20	134.8	–	0.888	1.641	0.914	0.727	3.98	CO WD
4 M$_\odot$	0.24	112.4	26.6	0.97	146.3	–	0.862	1.513	0.886	0.626	3.56	CO WD
	0.30	85.6	21.4	0.61	112.4	–	0.887	1.462	0.910	0.552	4.23	CO WD
	0.35	67.8	17.5	0.36	89.5	–	0.913	1.625	0.938	0.687	4.12	CO WD
	0.40	53.2	14.5	0.20	71.0	–	0.951	1.760	0.984	0.776	4.73	CO WD
5 M$_\odot$	0.24	71.1	14.6	0.67	89.3	–	0.913	1.671	0.940	0.731	4.02	CO WD
	0.30	54.8	11.9	0.33	69.4	–	0.951	1.597	0.976	0.621	4.32	CO WD
	0.35	43.7	10.3	0.18	56.0	–	0.998	1.603	1.025	0.578	4.92	CO WD
	0.40	34.5	8.9	0.11	45.0	–	1.073	1.911	1.125	0.786	5.99	CO(Ne) WD
6 M$_\odot$	0.24	50.0	9.5	0.39	61.4	–	0.996	1.569	1.021	0.549	4.43	CO WD
	0.30	38.8	8.0	0.13	48.0	–	1.058	1.624	1.080	0.544	5.09	CO(Ne) WD
	0.35	31.1	6.7	0.07	38.8	–	1.140	1.632	1.168	0.464	6.04	ONe WD
	0.40	24.9	6.0	0.04	31.6	–	1.234	2.157	1.258	0.900	9.15	ONe WD

Table 4.2 Structural properties relevant to the thermally pulsing AGB phase. We include the initial stellar mass (M_{ini}), the initial He mass fraction (Y), the H-exhausted core mass at the first thermal pulse (M_c^{TP1}), the number of calculated thermal pulses (TPs), the dredge-up efficiency λ averaged over all TPs ($\langle\lambda\rangle$), the maximum dredge-up efficiency (λ_{max}), the total TDU mass (M_{TDU}^{tot}), the maximum extent of the pulse-driven convective zone (M_{pdcz}^{max}), the maximum temperature in the He-burning shell ($T_{He-shell}^{max}$), the maximum temperature in the H-burning shell ($T_{H-shell}^{max}$), the maximum temperature at the base of the convective envelope during dredge-up or during interpulse H-burning ($T_{bce}^{max,dup}$ and $T_{bce}^{max,ip}$), the average interpulse period ($\langle\tau_{ip}\rangle$), and the total duration for which $T_{bce} > 50\,\mathrm{MK}$ (t_{hbb}).

M_{ini}	Y	M_C^{TP1} [$M_\odot$]	TPs	$\langle\lambda\rangle$	λ_{max}	M_{TDU}^{tot} [$M_\odot$]	M_{pdcz}^{max} [$10^{-3}\,M_\odot$]	$T_{He-shell}^{max}$ [MK]	$T_{H-shell}^{max}$ [MK]	$T_{bce}^{max,dup}$ [MK]	$T_{bce}^{max,ip}$ [MK]	$\langle\tau_{ip}\rangle$ [kyr]	t_{hbb} [kyr]
3 M$_\odot$	0.24	0.786	26	0.94	1.00	0.160	9.39	361	82	57	43	27.71	0
	0.30	0.847	23	0.86	0.97	0.070	5.70	338	88	63	54	11.61	82
	0.35	0.867	26	0.79	0.94	0.054	4.36	340	92	64	63	6.87	86
	0.40	0.892	48	0.70	0.91	0.065	3.00	344	98	78	86	3.63	120
4 M$_\odot$	0.24	0.864	82	0.92	0.99	0.281	4.78	350	90	74	84	9.91	683
	0.30	0.890	82	0.88	1.00	0.186	3.48	354	95	79	88	5.60	382
	0.35	0.918	75	0.81	0.93	0.114	2.59	355	100	83	93	3.41	216
	0.40	0.956	84	0.62	0.87	0.058	1.70	349	109	90	101	1.62	122
5 M$_\odot$	0.24	0.915	121	0.90	0.97	0.254	3.02	360	99	82	95	5.08	558
	0.30	0.955	104	0.84	0.98	0.137	2.13	361	105	89	99	2.85	277
	0.35	1.002	106	0.70	0.88	0.069	1.36	368	115	97	109	1.38	139
	0.40	1.077	261	0.26	0.64	0.018	0.48	356	132	118	126	0.34	91
6 M$_\odot$	0.24	0.998	136	0.81	1.01	0.140	1.82	384	111	96	108	2.39	315
	0.30	1.061	130	0.71	0.95	0.058	0.90	381	123	108	118	0.94	123
	0.35	1.143	227	0.41	0.73	0.021	0.37	382	136	124	131	0.27	65
	0.40	1.236	363	0.20	0.30	0.005	0.10	353	134	122	129	0.08	32

4.4.1. Pre-AGB evolution and stellar lifetimes

Figure 4.1 shows the evolutionary tracks of the 3 and 6 $M_\odot$ models with $Y = 0.24$ and 0.40 in a Hertzsprung-Russell diagram. In He-enhanced models, the initial compositions have a higher mean molecular weight (as H is exchanged for He), which leads to higher luminosities during the core H-burning phase (Roeser 1975). Compared with models for $Y = 0.24$, the models for $Y = 0.40$ are roughly twice as luminous during the main sequence. They are also more luminous at each corresponding stage of evolution due to the larger core masses of He-enhanced models.

As shown by the H-burning time-scales and total stellar lifetimes in Table 4.1, the increased H-burning rate and the reduced H fuel available in He-enhanced models lead to much shorter core H-burning lifetimes and shorter stellar lifetimes overall. This has important implications for chemical evolution, as He-enhanced stars will process and eject their enriched material much earlier than primordial-He stars at a given initial stellar mass. With $Y = 0.40$, the stellar lifetimes of the models are reduced by roughly 50 per cent compared to models with primordial He abundance. The shortening of stellar lifetimes by a similar factor with $Y = 0.40$ is also found by Charbonnel et al. (2013) for low-mass models between 0.66 and 0.82 $M_\odot$ at [Fe/H] = −1.56, and KMN14 for 1.7 and 2.36 $M_\odot$ models with the same metallicity of $Z = 0.0006$ as the models presented here.

4.4.2. The first and second dredge-up

After the exhaustion of H in the core, the onset of H burning in a shell around the core causes the outer layers to expand and cool as a star begins to ascend the RGB. At this stage, the envelope convection zone can move inwards in mass and dredge up the products of partial H burning, which increases the surface abundances of ^{13}C and ^{14}N and decreases the abundance of ^{12}C. Dredge-up at this evolutionary stage is known as first dredge-up (FDU).

Table 4.1 shows the innermost mass layer reached by the convective envelope during FDU for models in which FDU occurs. The depth of FDU in the 3 $M_\odot$ models decreases with increasing He abundance up to $Y = 0.40$, for which FDU does not take place. This is because these stars ignite He in their cores before their envelopes expand sufficiently to reach the first giant branch (Figure 4.1). We find no FDU for initial masses of 4 $M_\odot$ and above at any He abundance. For the $Y = 0.24$ models, the lack of FDU with initial masses of 4 $M_\odot$ and higher is consistent with the slightly higher-metallicity ($Z = 0.001$) models of Fishlock et al. (2014a), for which FDU ceases between initial masses of 3.5 and 4.0 $M_\odot$.

Following the core He-burning phase, the stars change to a dual shell-burning structure and begin their ascent of the AGB. As the He-shell is ignited and the H-shell becomes

extinguished for the first time, the inner boundary of the convective envelope moves inwards in mass and dredges up the products of complete H burning, which increases the surface abundances of ^{4}He and ^{14}N. This is the second dredge-up (SDU).

Table 4.1 shows the innermost mass later reached by the SDU for each of our models. The SDU is deeper than the FDU in every model with FDU, and the depth of the SDU decreases with increasing He abundance. However, due to the increased core mass in the 6 M$_\odot$ model with $Y = 0.40$, a "corrosive SDU" takes place (Gil-Pons et al. 2013; Doherty et al. 2014). In this model, the inner edge of the convective envelope reaches below the top of the CO core, which dredges up C and O to the surface.

4.4.3.   The thermally pulsing AGB and third dredge-up

During the AGB phase, thermal pulse (TP) cycles are driven by thermal instabilities of the thin He-burning shell (Iben 1975b; Herwig 2005). The rapid flash burning of the He-shell releases an enormous amount of energy and causes a pulse-driven convective zone to form, which homogenizes the composition of the He-intershell. As the energy moves upwards and expands the star, the H-burning shell is effectively extinguished. With the H-burning barrier removed, the envelope convection zone can penetrate into the He-intershell in an event known as a third dredge-up (TDU) episode (Iben 1975b; Sackmann 1980b).

To show how the TP cycle is altered by He-enhancement, we first measure the average time between TPs (the interpulse). The left-hand panel of Figure 4.2 shows the average interpulse period versus the average core mass during the AGB for our models from 3 to 6 M$_\odot$ with He mass fractions of $Y = 0.24, 0.30, 0.35$, and 0.40. The interpulse time-scale is mainly a function of the H-exhausted core mass (Paczyński 1974; Christy-Sackmann & Paczyński 1975), which increases with the He content (Becker & Iben 1979; Lattanzio 1986). However, the average interpulse period of a He-enhanced model is lower than that of a primordial-He model with a higher initial mass and the same average core mass. The shorter interpulse time with He-enhancement for a given core mass is connected with the increased H-burning rate. With $Y = 0.40$, the average interpulse period is up to 50 per cent shorter than with $Y = 0.24$ and the same average core mass. The right-hand panel of Figure 4.2 shows that a similar, but marginally tighter relation exists when the average core mass is replaced by the average He-intershell mass (approximated by the maximum extent of the pulse-driven convective zone).

Figure 4.3 shows the H-burning luminosity and the temperature and luminosity of the He-burning shell as a function of time from just prior to the first TP until after the second TP (of the $Y = 0.24$ case). To illustrate how a He-rich initial composition alters the behaviour of the burning shells and reduces the interpulse time-scale, the models shown
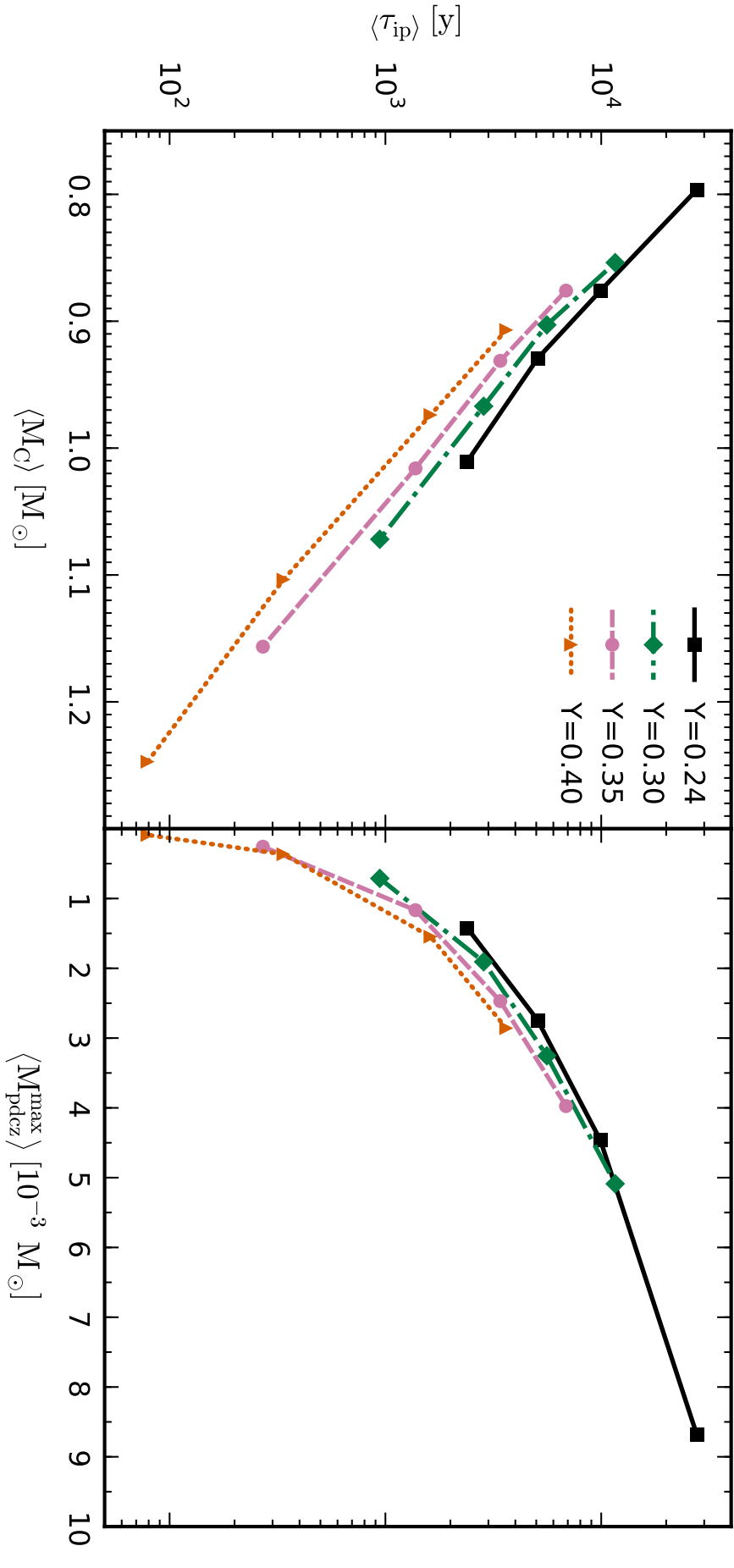
Figure 4.2 Left: the average interpulse period versus the average H-exhausted core mass during the thermally pulsing AGB phase. Right: the mean interpulse period versus the mean of the maximum extent of the pulse-driven convective zone (a proxy for the He-intershell size). Included on the plot are the 3, 4, 5, and 6 $M_\odot$ models (from left to right) with He mass fractions of $Y = 0.24$ (black squares), 0.30 (green diamonds), 0.35 (pink circles), and 0.40 (orange triangles).
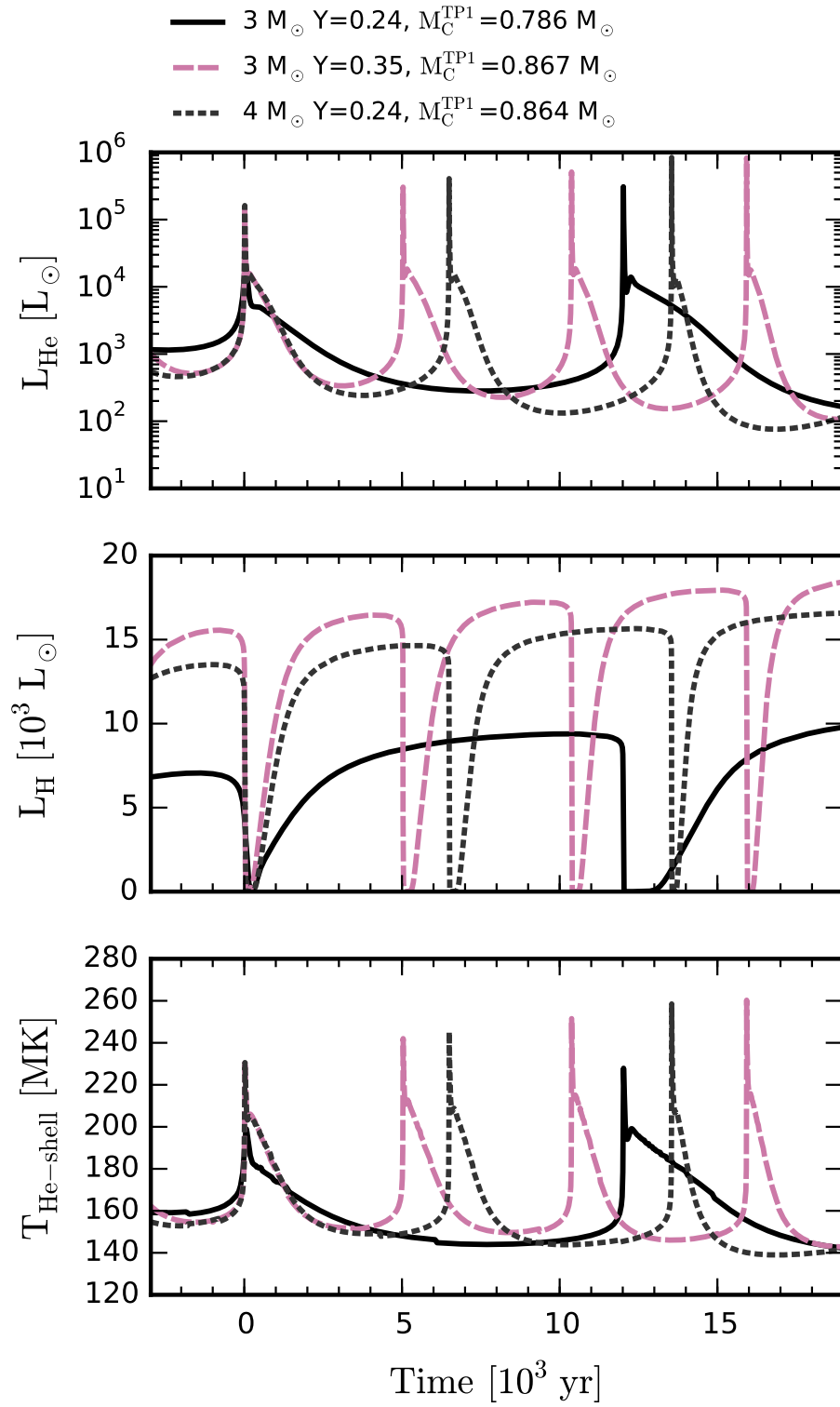
Figure 4.3 He- and H-burning luminosities, and the temperature in the He-burning shell as a function of time after the first TP for 3 $M_\odot$ models with $Y = 0.24$ and 0.35, and the 4 $M_\odot$ model with $Y = 0.24$.

are the 3 $M_\odot$ model with $Y = 0.24$, the 3 $M_\odot$ model with $Y = 0.35$, and the 4 $M_\odot$ model with $Y = 0.24$. These three models enable us to separately compare the effect of increasing the He mass fraction and increasing the initial mass, which each individually lead to a larger core mass. The 3 $M_\odot$, $Y = 0.35$ model and the 4 $M_\odot$, $Y = 0.24$ model, which have very similar core masses (0.865 ± 0.002 $M_\odot$) and intershell masses (5×10^{-3} $M_\odot$) at the time of their first TPs also exhibit a very similar time evolution of their He-shell temperature and luminosity. However, even with near-identical core masses, the onset of the next TP takes place sooner in the He-enhanced model, which has a higher H-burning luminosity.

The results in Tables 4.1 and 4.2 are derived from our evolutionary sequences which end due to convergence difficulties before the H envelopes are completely ejected (Sweigart 1999; Lau et al. 2012). The AGB lifetimes have been calculated from the time spent on the AGB up to the end of our calculations, plus an estimate of the time left to lose the remaining H envelope. This is estimated by dividing the envelope mass at the last computed model by the average mass-loss rate over the last few thousand models. For the number of TPs neglected by our calculations due to the early termination of the AGB, an upper limit is obtained by dividing the envelope ejection time by the average interpulse time. The number of additional TPs is less than 15 per cent of the numbers given in Table 4.2 for all cases except for the 6 $M_\odot$, $Y = 0.40$ model, which could experience up to ~35 per cent more TPs beyond the end of our calculations.

The total number of TPs experienced by each model depends on both the interpulse period and the time spent in the AGB phase, which is controlled by the mass-loss rate. The number of TPs has implications for the stellar yields, as a smaller number of TPs means that there will be fewer neutron-producing events and typically fewer TDU episodes. For models with HBB (Iben 1975b; Renzini & Voli 1981; Boothroyd & Sackmann 1992; Lattanzio 1992), the length of time spent in the AGB phase also has an impact on the surface abundances and yields of elements involved in proton-capture reactions at the base of the envelope. In the He-rich AGB models, the mass-loss rates are higher due to higher luminosities and generally longer pulsation periods, and thus they have shorter AGB lifetimes. Our models with $Y = 0.40$ have shorter AGB lifetimes compared with $Y = 0.24$ by a factor of 4 at 3 $M_\odot$, and by a factor of 10 at 6 $M_\odot$, although these results are dependent on the mass-loss prescription.

The models presented here for $Y = 0.24$ experience significantly more TPs than the models of SCP14 with the same initial mass. For 3, 4, 5, and 6 $M_\odot$, we find 26, 82, 121, and 136 TPs, compared with 15, 23, 35, and 72 for SCP14, and 75, 91, 103, and 116 for VD09. The smaller number of TPs in the models of SCP14 is largely due to their modification of the Vassiliadis & Wood (1993) mass-loss prescription to include a minimum rate of $10^{-7.7}$ $M_\odot$ yr^{-1} at log $P < 2.7$ (described in Straniero et al. 2006). VD09 use the Bloecker (1995) mass-loss prescription (with $\eta_R = 0.02$), which steeply increases with luminosity. For this reason, while the 3 and 4 $M_\odot$ models of VD09 experience a greater number of TPs than
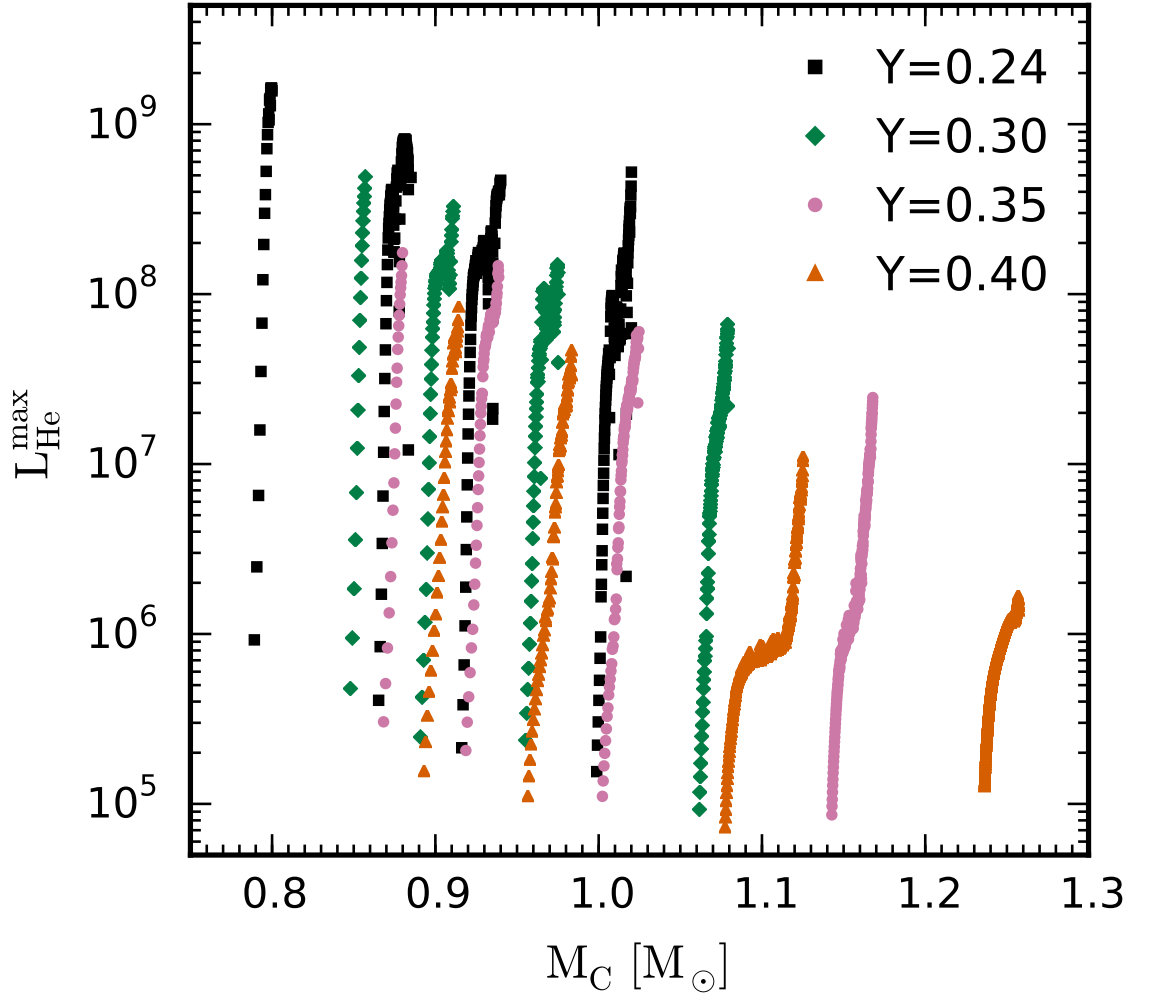
Figure 4.4 The maximum He-burning luminosity versus the H-exhausted core mass for each TP of the models at 3, 4, 5, and 6 M$_\odot$ (from left to right) with He mass fractions of $Y = 0.24$ (black squares), 0.30 (green diamonds), 0.35 (pink circles), and 0.40 (orange triangles).

our models, the opposite is the case with 5 M$_\odot$ and higher masses, for which our models experience a greater number of TPs.

For the 3 M$_\odot$ models, variation to the initial He abundance has a small (< 10 per cent) effect on the total number of TPs for $Y = 0.24, 0.30$, and 0.35. However, with $Y = 0.40$, the number of TPs almost doubles to 48 in comparison with 26 for $Y = 0.35$. The large increase in the number of TPs between $Y = 0.35$ and $Y = 0.40$ is due to the AGB lifetime shortening by about 15 per cent, while the average interpulse time drops by roughly 50 per cent.

We use the standard dredge-up efficiency parameter defined by $\lambda = \Delta M_{dredge}/\Delta M_C$, where ΔM_{dredge} is the mass of He-intershell material mixed to the surface by TDU and ΔM_C is the growth of the H-exhausted core during the preceding interpulse phase.

The TDU is generally less efficient after weaker TPs, and models with a higher core
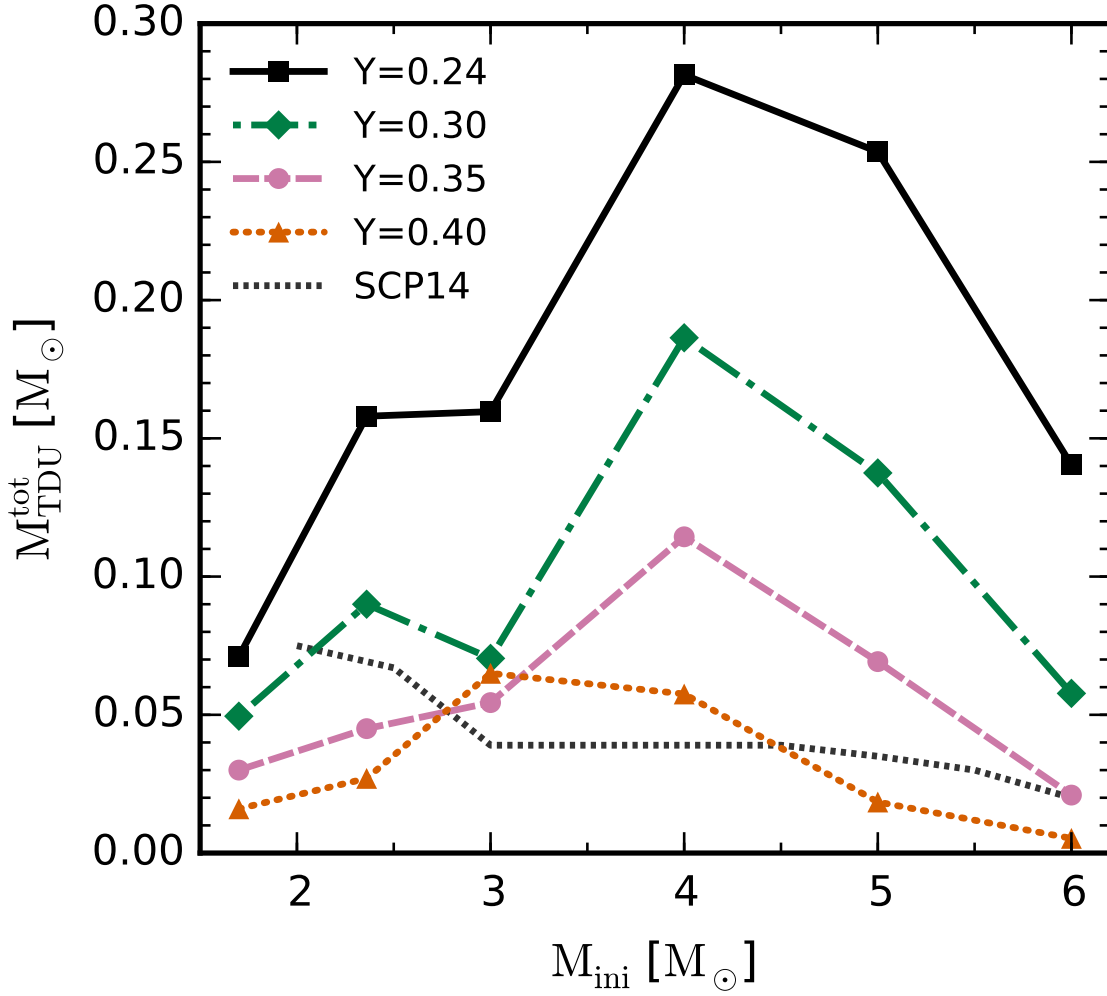
Figure 4.5 The total TDU mass during the AGB as a function of initial mass with He mass fractions of $Y = 0.24$ (black squares), 0.30 (green diamonds), 0.35 (pink circles), and 0.40 (orange triangles). Results of the 1.7 and 2.36 $M_\odot$ models are from KMN14.

mass attain a lower peak He-flash luminosity (Sackmann 1980a; Boothroyd & Sackmann 1988b; Straniero et al. 2003). This is true for changes to either the initial mass or the initial He mass fraction (Figure 4.4). However, when models of the same core mass are compared, the peak He-burning luminosity in the He-enhanced models is less than the primordial-He models by up to about 80 per cent. As a consequence, the TDU is less efficient in He-enhanced models.

Figure 4.5 shows the total mass dredged-up by TDU (hereafter TDU mass; equal to the sum of ΔM_{dredge}) during the AGB phase as a function of initial mass for several initial He abundances. Increasing the initial He mass fraction typically reduces the TDU mass for initial masses from 3 to 6 $M_\odot$, similar to what KMN14 found with their He-enhanced 1.7 and 2.36 $M_\odot$ models. For $Y = 0.24, 0.30$, and 0.35, the maximum dredge-up mass is obtained with an initial mass of around 4 $M_\odot$. With $Y = 0.40$ however, the distribution changes shape with a peak shifting downwards to approximately 3 $M_\odot$. In contrast with

our results, the SCP14 models predict that the TDU mass decreases monotonically with initial mass, and is overall much lower than for our $Y = 0.24$ models (by a factor of up to 7 at 4 $M_\odot$). The large variations between results of SCP14 and the present work reflect the significant modelling uncertainties that affect the efficiency of TDU (for a comparison of TDU efficiency between different evolution codes, see Lugaro et al. 2003). Our specific predictions for the TDU efficiency are influenced by the mass and time resolution of the extremely He-enhanced models, and our treatment of the border between radiative and convective zones (as demonstrated by Frost & Lattanzio 1996).

The TDU mass of the 3 $M_\odot$, $Y = 0.40$ model is unusual because it exceeds the TDU mass of the 3 $M_\odot$ model with $Y = 0.35$ despite the increased He abundance, which reduces the dredge-up efficiency. Indeed, both the average and maximum values of λ are lower in the 3 $M_\odot$ model with $Y = 0.40$ than $Y = 0.35$ (Table 4.2). The unusually high TDU mass with $Y = 0.40$ is the result of a near-doubling in the number of TPs, which leads to more TPs with TDU.

4.4.4.   Hot bottom burning

At $Z = 0.0006$ and primordial He abundance, AGB stars with initial masses $\gtrsim 4\ M_\odot$ experience sufficiently high temperatures at the base of the convective envelope (T_{bce}) for proton-capture nucleosynthesis to take place there. This is called hot bottom burning (HBB).

With temperatures in the envelope above about 50 MK, the resulting activation of the CN cycle begins to convert a significant fraction of C nuclei into N. In the absence of other effects, the CN-cycle would cause the C/O ratio in the envelope to decrease. However, additional primary ^{12}C nuclei from the He-burning shell are periodically transported to the envelope via TDU, leading to a surface C/O ratio that depends on the interplay between TDU and HBB. In the more massive AGB stars at solar metallicity, HBB is observationally confirmed to prevent the surface abundances from becoming C-rich (C/O > 1; Lattanzio 1992; Boothroyd et al. 1993). Further, the combined operation of both TDU and HBB in nature is confirmed by observations of C-deficient, N-rich AGB stars in the Magellanic Clouds (McSaveney et al. 2007).

Figure 4.6 shows the maximum temperature at the base of the convective envelope in our models as a function of the initial mass. The higher temperatures in models with increased initial He abundance enables HBB to take place at lower initial masses than at primordial He abundance. At masses above about 4 $M_\odot$, HBB will proceed at increased rates with He-enhancement, while models of less than about 2 $M_\odot$ will not experience HBB temperatures even with He abundances as high as $Y = 0.40$. For the 3 $M_\odot$ models,
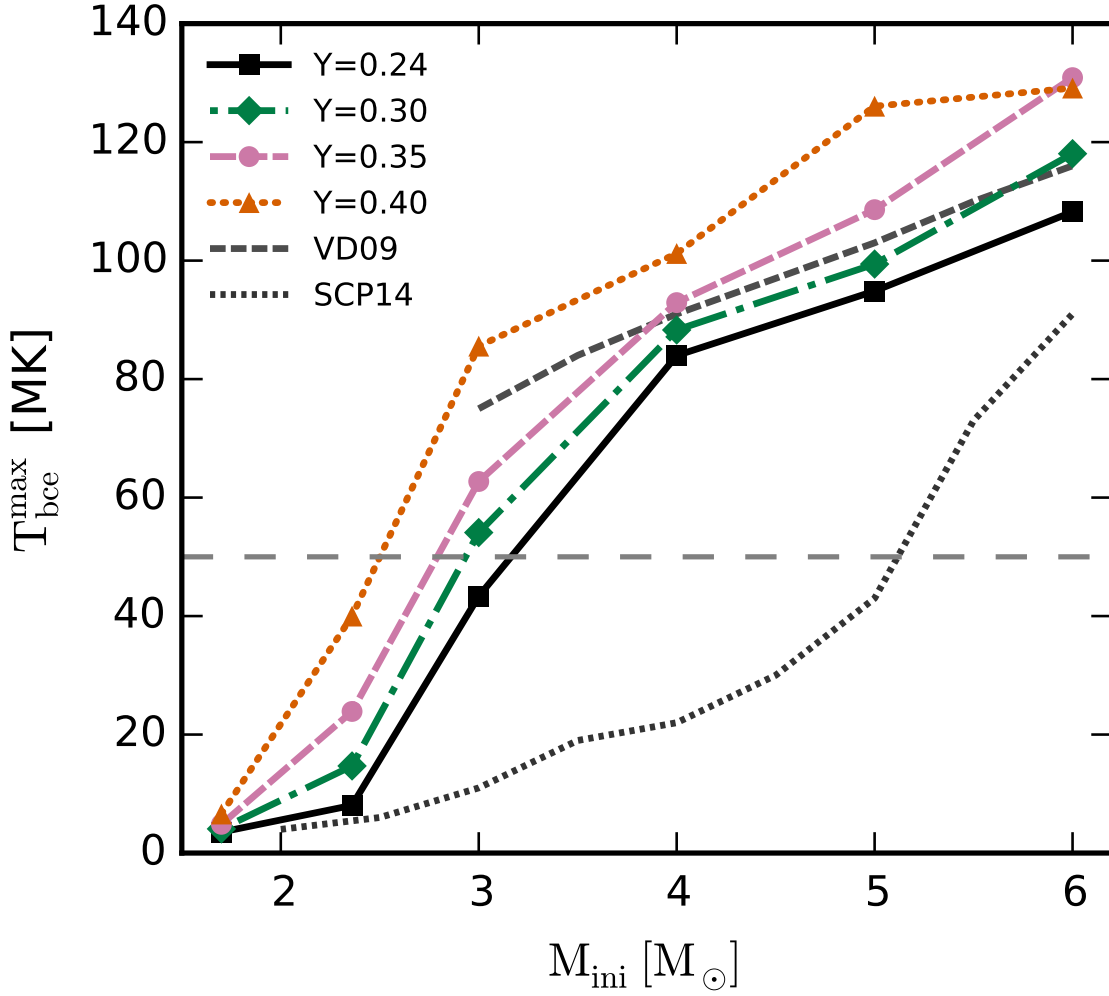
Figure 4.6 The maximum temperature at the base of the convective envelope during the interpulse phase as a function of initial mass with He mass fractions of $Y = 0.24$ (black squares), 0.30 (green diamonds), 0.35 (pink circles), and 0.40 (orange triangles). Results of the 1.7 and 2.36 M$_\odot$ models are from KMN14. The horizontal dashed line at 50 MK indicates the approximate temperature above which HBB significantly alters surface abundances.

T_{bce}^{max} increases from 43 MK with $Y = 0.24$ to 86 MK with $Y = 0.40$. This corresponds to a change from virtually no HBB to significant CN cycling in the envelope.

The maximum envelope temperatures of the primordial-He models are in reasonable agreement (< 10 per cent difference) with the models of VD09 for masses of 4 M$_\odot$ and above. The difference is more significant at 3 M$_\odot$, where our model has a maximum temperature of 57 MK during TDU and 43 MK during the interpulse phase, while the corresponding model of VD09 has a maximum temperature of 75 MK. The higher envelope temperatures in the models of VD09 are a result of the FST convection model, which predicts more efficient convective transport than the MLT theory. In contrast to the models of VD09 and the models presented here, the models of SCP14 predict much lower temperatures at the base of the convective envelope (22 MK at 4 M$_\odot$ versus 84 MK in our

model and 91 MK for VD09). SCP14 compare their models to the models of D'Orazi et al. (2013a) (calculated with the same evolutionary code used here), which experience more efficient HBB. They attribute the difference to some combination of the equation of state, interpolation of the radiative opacity tables, and their particular mixing scheme.

Figure 4.7 shows the maximum temperature at the base of the convective envelope and the surface C/O ratio for each TP of the 3 $M_\odot$ models. Over the first 10 or so TPs, the shallower initial rise of C/O in the He-enhanced models can be attributed to the less efficient TDU, as none of the models has reached HBB temperatures at this stage. In models with He-enhancement, HBB becomes active and is particularly noticeable with $Y = 0.35$ and $Y = 0.40$, for which significant CNO cycling in the envelope causes the C/O ratio to begin decreasing at around TP 16. As mass loss erodes the envelope to below a critical mass value (around 1.5 $M_\odot$ in this case) over the last few TPs, HBB ceases while dredge-up continues to take place, causing an upturn in the C/O ratio in these two models (see Frost et al. 1998). In the $Y = 0.40$ model, the cessation of HBB causes the surface to transition from O-rich to C-rich (for a second time) at the third-last TP.

Aside from CNO abundances, HBB can alter the abundances of other light elements through the NeNa cycle and the MgAl chain. Activation of the NeNa cycle can produce or destroy ^{23}Na at the expense of Ne isotopes (Arnould et al. 1999; Mowlavi 1999b; Karakas & Lattanzio 2003b). At temperatures of 50–200 MK, proton captures on to ^{23}Na produce more ^{20}Ne than ^{24}Mg, as the rate of the ^{23}Na$(p, \alpha)^{20}$Ne reaction is several times faster than ^{23}Na$(p, \gamma)^{24}$Mg (Hale et al. 2004). Activation of the MgAl chain can result in a net production of ^{26}Al and ^{27}Al (Arnould et al. 1999; Denissenkov & Herwig 2003; Ventura & D'Antona 2008), and further proton capture in the most massive AGB stars can produce ^{28}Si (Ventura et al. 2011).

4.4.5.   Core mass–luminosity relation

A well-known correlation exists between the surface luminosity of an AGB star and its H-exhausted core mass. A linear form was first proposed by Paczyński (1970), although stars undergoing HBB and TDU were found to diverge from this relation (Bloecker & Schoenberner 1991; Boothroyd & Sackmann 1992; Lattanzio 1992; Marigo et al. 1999). Figure 4.8 shows the surface luminosity versus core mass at each TP for the models of 3, 4, and 5 $M_\odot$.

We also compare the core-mass–luminosity behaviour of our models with values from the fitting formula specified by equations (29)–(34) of Izzard et al. (2004). This formula estimates the surface luminosity as a function of the core mass, the envelope mass, and the total growth in the core mass during the thermally pulsing AGB (neglecting decreases from TDU). The formula is based on the stellar evolutionary models of Karakas et al.
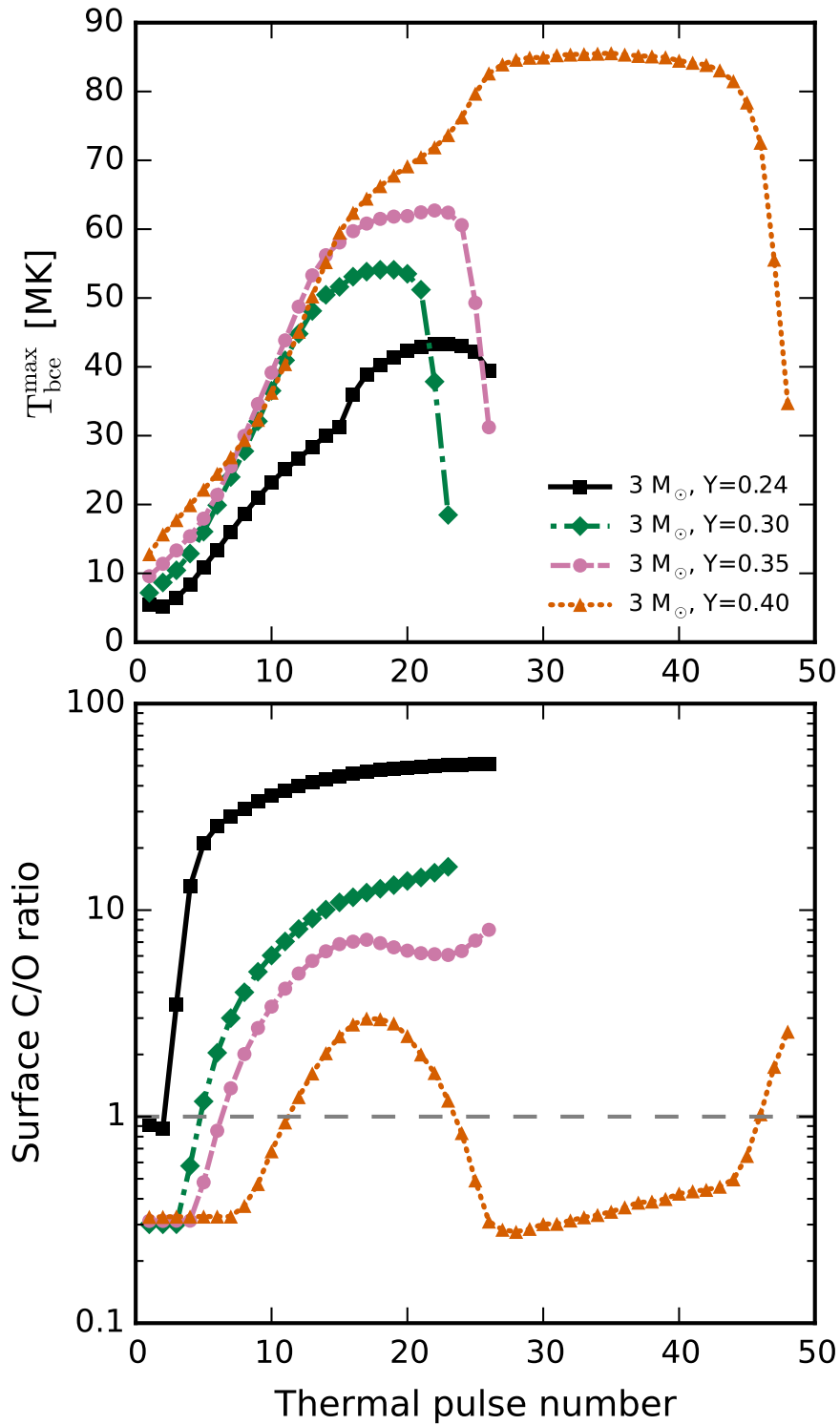
Figure 4.7 The maximum temperature at the base of the convective envelope during the preceding interpulse phase (top panel) and the surface C/O ratio (bottom panel) as a function of TP number for 3 $M_\odot$ models with He mass fractions of $Y = 0.24$ (black squares), 0.30 (green diamonds), 0.35 (pink circles), and 0.40 (orange triangles). The dashed line in the lower panel indicates a C/O ratio of 1.
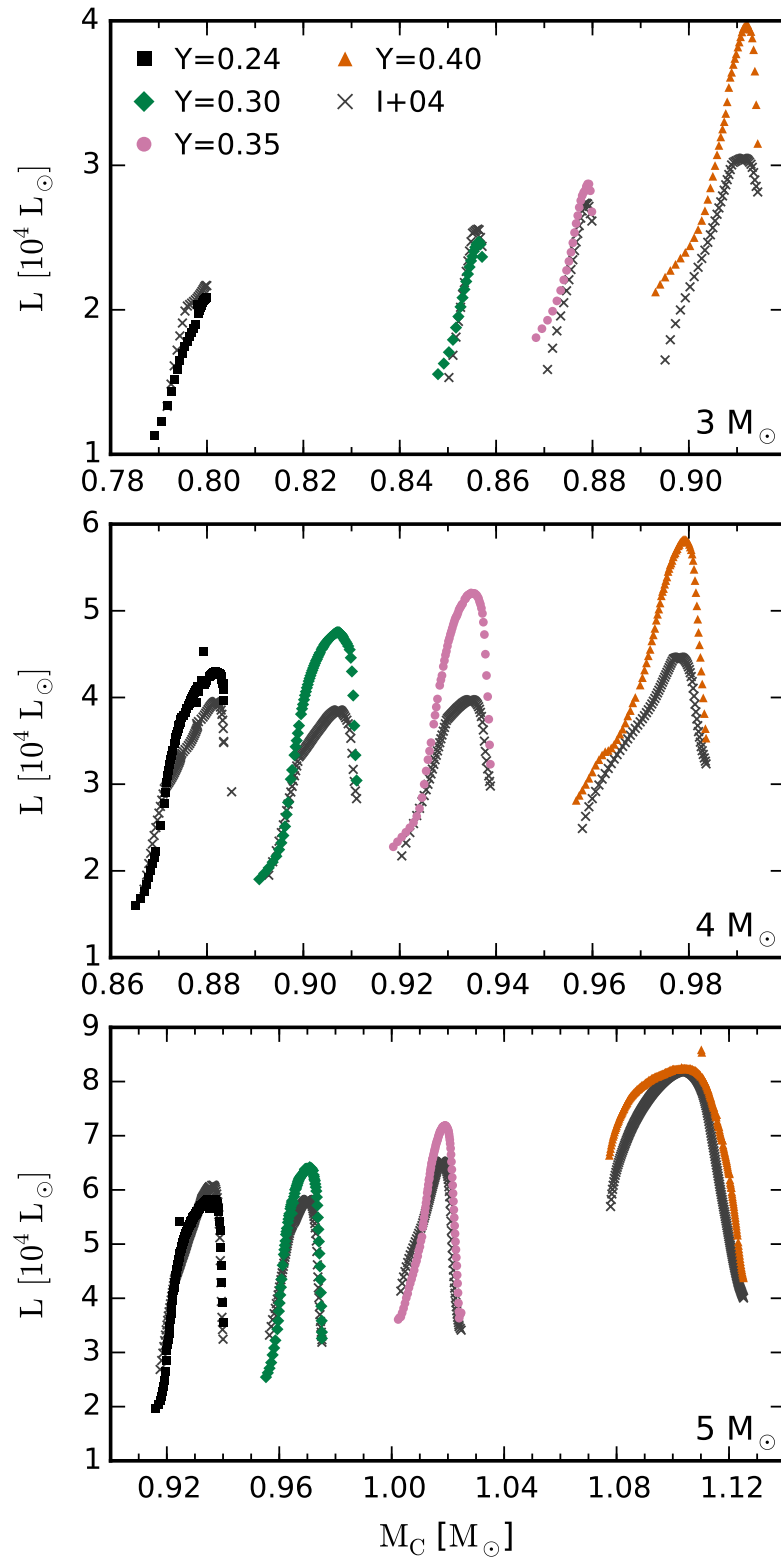
Figure 4.8 Luminosity versus H-exhausted core mass during the AGB for 3, 4, and 5 M$_\odot$ models with He mass fractions of $Y = 0.24$ (black squares), 0.30 (green diamonds), 0.35 (pink circles), and 0.40 (orange triangles). The plot also shows values from the fitting formula of Izzard et al. (2004) (I+04).

(2002) with He mass fractions that range from 0.24 to 0.30, depending on the metallicity. The grid of evolutionary models used to generate the fit extends down to $Z = 0.0001$, but only with masses of 1.25–2.25 $M_\odot$. At $Z = 0.004$ and higher metallicities, the grid includes models with initial masses up to 6 $M_\odot$. Although the updated formula of Izzard et al. (2006) improves the fit to models of low metallicity, its parametrization in terms of the initial mass causes it to be less accurate for He-rich models, which have different stellar structures compared to primordial-He models at a given initial mass.

For the 3 $M_\odot$ models, the formula is a good fit for He mass fractions between $Y = 0.24$ and extrapolation up to $Y = 0.35$. However, our 3 $M_\odot$ model with $Y = 0.40$ is consistently more luminous (by up to 25 per cent) than the formula value. Between $Y = 0.35$ and $Y = 0.40$, the maximum temperature at the base of the convective envelope during H-burning increases from 63 to 86 MK, and the more extreme HBB further increases the surface luminosity. The excess envelope luminosity with $Y = 0.40$ in comparison to the fitting formula (which accounts for the larger core mass) is probably partly due to the more He-rich envelope composition (which affects the H-burning rate) and also because of the smaller envelope mass compared to higher-mass models with primordial He and the same core mass.

The 4 $M_\odot$ models at all He mass abundances have higher peak luminosities than the formula values, although this is a small effect with $Y = 0.24$. The He-enhanced 4 $M_\odot$ models diverge from the relation in a manner characteristic of HBB, with a rise in the middle followed by a decline as the decreasing envelope mass causes a reduction in the temperature at the base of the envelope. A reasonably good fit is found for the 5 $M_\odot$ models, and this is probably because HBB is already active for this initial mass with $Y = 0.24$.

In summary, the initial He abundance alters the core-mass-luminosity relation, and a more accurate fitting formula for application to He-rich populations would require a fit to stellar evolutionary models at the appropriate He abundance.

4.4.6. Carbon burning and final fates

The C-burning behaviour and the stellar remnants of the models depend on the initial stellar mass and the initial He abundance. There is also a dependence on the initial metallicity (Cassisi & Castellani 1993; Umeda et al. 1999).

All of the models presented in this work would eventually form white dwarfs (WD) rather than exploding as electron-capture supernovae because they end with core masses well below the limiting mass of 1.37 $M_\odot$ (Miyaji et al. 1980). In Table 4.1 we classify the stellar remnants for each of our models based on the core composition at the end of our calculations, which would be similar to the composition of the resulting WD remnant.

AGB stars with initial masses below the minimum mass required for off-centre core C ignition (M_{up}, as defined by Becker & Iben 1979) end the AGB with cores composed largely of C and O in roughly equal proportions that are set by earlier core and shell He burning. Thus, we classify the remnants from our models without C ignition as CO WDs.

In stars with degenerate CO cores following central He exhaustion, the position of maximum temperature moves outwards from the centre to where the energy liberated by gravitational contraction exceeds the rate of cooling by neutrino emission (Becker & Iben 1979). In stars more massive than M_{up}, the temperature maximum exceeds about 600–700 MK (Siess 2006) and C is ignited off-centre in the core. In this case, the star is referred to as a 'super-AGB' star (Garcia-Berro & Iben 1994; Siess 2007, 2010).

C burning proceeds via the $^{12}C(^{12}C, \alpha)^{20}Ne$ and $^{12}C(^{12}C, p)^{23}Na$ reactions. The latter reaction is followed by $^{23}Na(p, \alpha)^{20}Ne$, and thus also contributes to the abundance of ^{20}Ne in the core, as does the $^{16}O(\alpha, \gamma)^{20}Ne$ reaction. The region affected by C burning will be composed largely of O and Ne, with a ratio that is affected by the rate of $^{16}O(\alpha, \gamma)^{20}Ne$. The C burning can either be aborted before reaching the centre and form a hybrid CO(Ne) WD (Doherty et al. 2010; Karakas et al. 2012; Denissenkov et al. 2013), or proceed all the way to the centre and form a ONe WD.

Bono et al. (2000) show for super metal-rich compositions ($Z = 0.04$) that the M_{up} boundary decreases with increasing He abundance from $9.5 \pm 0.5\,M_\odot$ for $Y = 0.29$ to $7.7 \pm 0.2\,M_\odot$ for $Y = 0.37$. With primordial He abundance, C burning at $Z = 0.0006$ takes place with a minimum initial mass of $6.5\,M_\odot$ (Doherty et al. 2015), and we do not find C burning in our $Y = 0.24$ models with masses up to $6\,M_\odot$. These models lead to CO WDs. The $6\,M_\odot$ model with $Y = 0.30$ experiences off-centre C burning that leaves C in the inner $0.5\,M_\odot$ unburned, and this region remains composed of C and O. We classify the remnant of this model as a hybrid CO(Ne) white dwarf (Doherty et al. 2015). The models at $5\,M_\odot$ and below with $Y = 0.30$ do not show any significant C burning.

For $Y = 0.35$, the $6\,M_\odot$ model experiences off-centre C ignition that proceeds to full central C burning and forms an ONe core. Figure 4.9 shows the C-burning luminosity and the behaviour of the C-burning convective zones in this model as a function of time. For $Y = 0.35$, the models at $5\,M_\odot$ and below do not show any significant C burning. For $Y = 0.40$, the $5\,M_\odot$ model experiences off-centre C burning that produces a CO(Ne) white dwarf and the $6\,M_\odot$ model undergoes full central C burning that produces an ONe white dwarf. The models with $Y = 0.40$ at $4\,M_\odot$ and below do not show any significant C burning.

In summary, we find that M_{up} at $Z = 0.0006$ exceeds $6\,M_\odot$ for $Y = 0.24$, decreases to between 5 and $6\,M_\odot$ for $Y = 0.30$–0.35, and decreases further to between 4 and $5\,M_\odot$ with $Y = 0.40$. Future investigations with a finer mass grid would be required to determine more precisely the dependence of M_{up} on the He abundance.
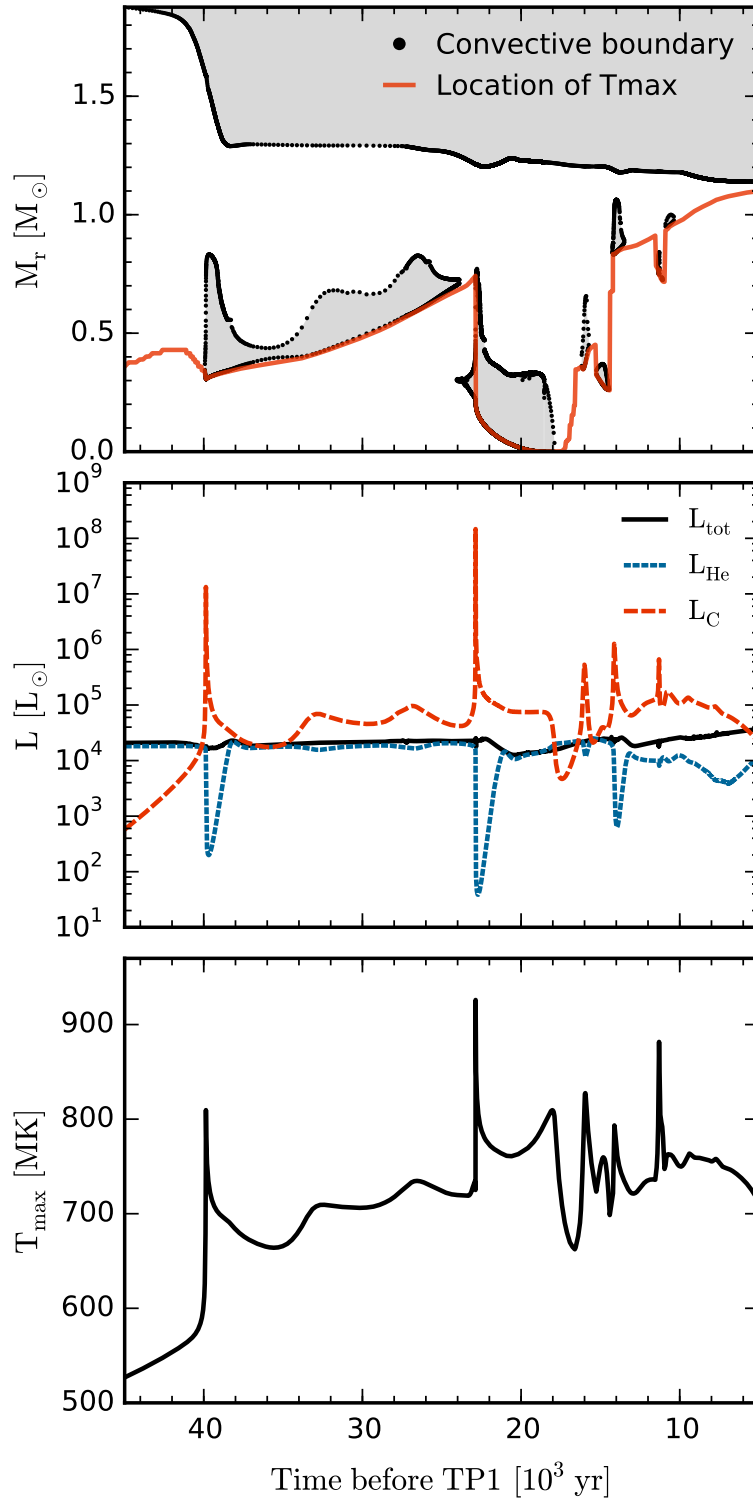
Figure 4.9   C-burning characteristics of the 6 $M_\odot$, $Y = 0.35$ model versus time before the first TP. Top: a Kippenhahn diagram showing C-burning and envelope convective zones and the location of maximum temperature (red). Middle: the total luminosity (L_{tot}) and the luminosities due to He- and C-burning (L_{He} and L_C). Bottom: the maximum temperature in the model.

4.5.   Nucleosynthesis and Stellar Yields

The stellar yield represents the contribution of a particular chemical species i (e.g., an element or nuclide) to the interstellar medium by a star over its lifetime, and is calculated using the formula

$$M_i^{\text{yield}} = \int_0^\tau X_i(t)\dot{M}(t)\,\mathrm{d}t, \tag{4.1}$$

where $X_i(t)$ is the mass fraction of species i at time t and $\dot{M}(t)$ is the stellar mass-loss rate at time t. For models with a non-zero envelope mass at the end of our calculations, we assume that all mass exterior to the core is ejected with the composition of the surface at the last computed model.

The stellar yields of all models are provided as online data tables, with an example of their form and content in Table 4.3. In the online data tables, we also include the net yields, which have the initial abundances subtracted according to

$$M_i^{\text{netyield}} = \int_0^\tau \left[X_i(t) - X_i(0)\right]\dot{M}(t)\,\mathrm{d}t, \tag{4.2}$$

where $X_i(0)$ is the mass fraction of species i in the initial composition. The net yields indicate whether a chemical species is produced or depleted in the context of chemical evolution.

4.5.1.   Yields of light elements

In AGB stars, the primary He produced by H-burning reactions is mixed to the surface during dredge-up events, with the largest increase to the surface abundance of He occurring during SDU and a smaller increase due to TDU. As we show in Figure 4.10, the average He mass fractions in the ejecta of our models are typically 0.05–0.10 higher than the initial He mass fractions, with the higher mass models releasing material that is more He-enhanced due to a deeper SDU (Karakas et al. 2006a).

For primordial-He models, the He mass fractions of our yields are generally higher than the predictions of SCP14 or VD09. At the largest difference, our predictions for $\left\langle Y_{\text{ejecta}} \right\rangle$ are higher than VD09 and SCP14 by about 0.05 and 0.03, respectively. The FRUITY data base (Cristallo et al. 2011) provides surface He mass fractions of the SCP14 models after each dredge-up event, which enables us to compare the effects of SDU and TDU. At 3 $M_\odot$, the surface Y following SDU is 0.30 (cf., 0.26, SCP14) and increases with each TDU episode up to 0.33 at the end of our calculations, while the model of SCP14 finishes with a surface Y of 0.27. The higher He mass fraction in our yield at 3 $M_\odot$ compared with SCP14 is caused by a deeper SDU and more extensive TDU in our model. For initial masses of
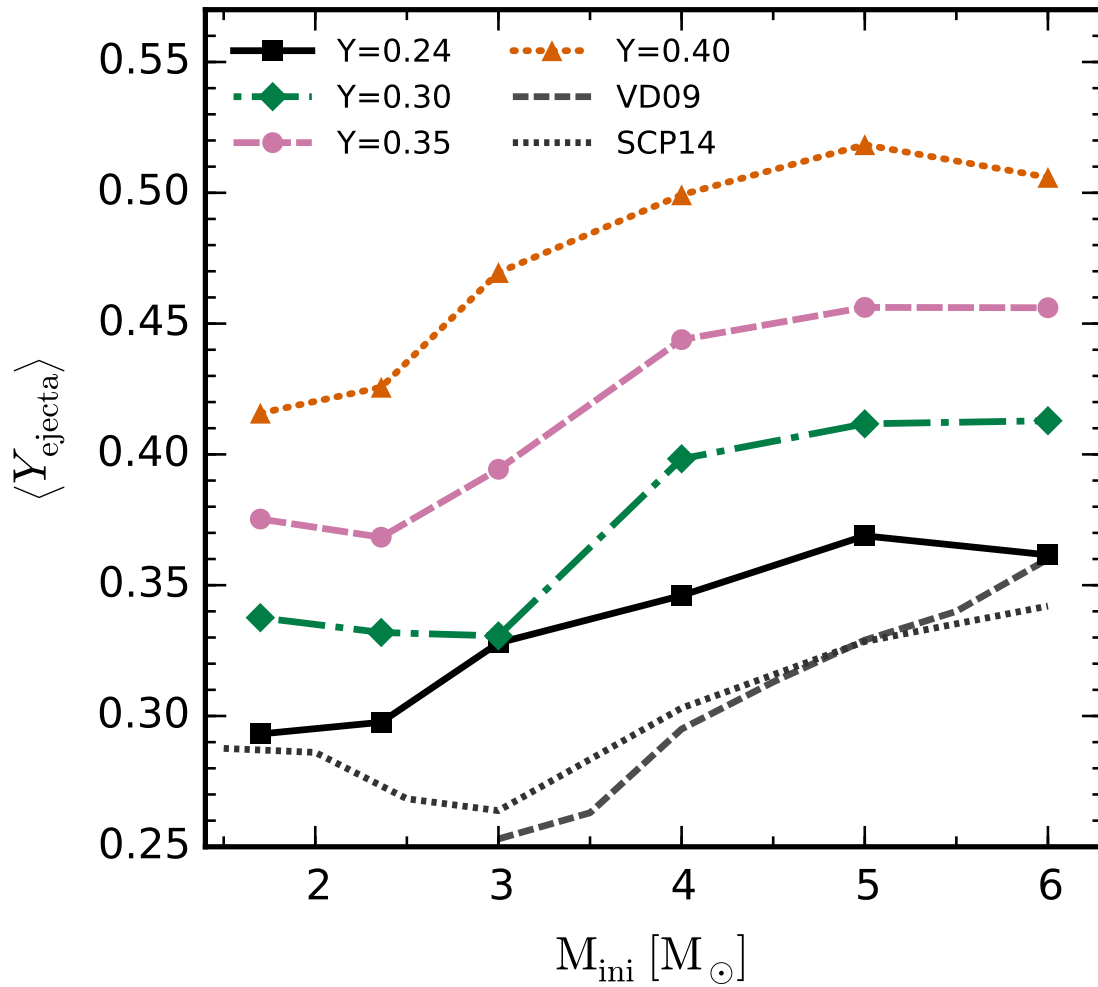
Figure 4.10 Average He mass fractions in the ejecta of the stellar models versus initial mass with He mass fractions of $Y = 0.24$ (black squares), 0.30 (green diamonds), 0.35 (pink circles), and 0.40 (orange triangles). 1.7 and 2.36 $M_\odot$ models are from KMN14.

4–6 $M_\odot$, our post-SDU He abundances are very similar to the models of SCP14, and the differences in $\langle Y_{\text{ejecta}} \rangle$ largely reflect differences in the efficiency of HBB.

Figure 4.11 illustrates the time evolution of the surface abundances of Ne, Na, Mg, Al, and Si isotopes in the 4 $M_\odot$ models with $Y = 0.24$ (left-hand panel) and $Y = 0.40$ (right-hand panel). We focus on the 4 $M_\odot$ models as they demonstrate the significant changes that can occur due to HBB with variations to the initial He abundance. As shown in Table 4.2, the maximum temperature at the base of the envelope during the interpulse phase increases from 84 MK at $Y = 0.24$ to 101 MK at $Y = 0.40$, with implications for the nucleosynthesis via proton capture reactions. However, while the maximum temperature increases, other important factors include the length of time during which the envelope is subject to high temperatures and the total mass of TDU (t_{HBB} and $M_{\text{TDU}}^{\text{tot}}$ in Table 4.2), both of which are lower in the $Y = 0.40$ model.

The surface abundance of ^{22}Ne displayed in Figure 4.11 for both $Y = 0.24$ and 0.40
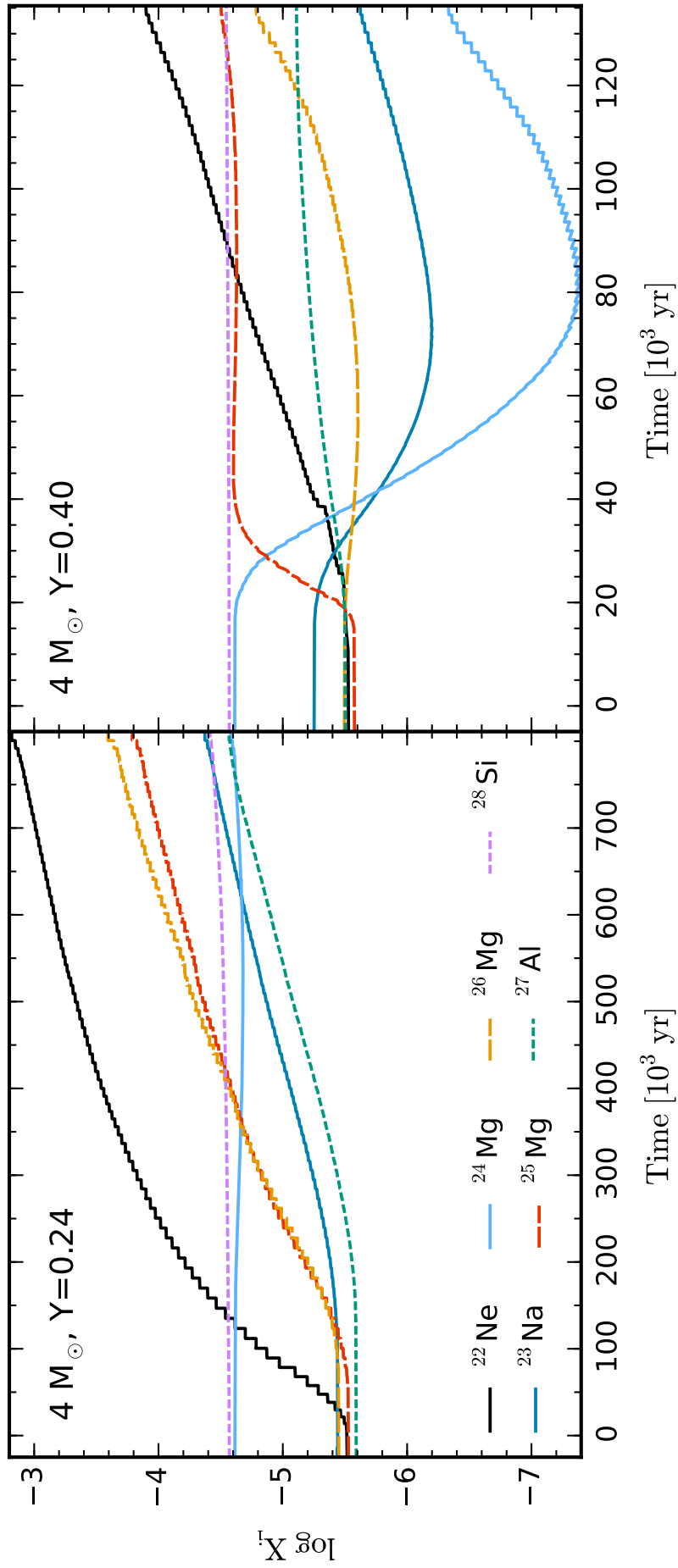
Figure 4.11 Surface abundance of selected nuclides that participate in the NeNa cycle and the MgAl chain versus time in 4 $M_\odot$ models at $Y = 0.24$ (left-hand panel) and $Y = 0.40$ (right-hand panel). Time on the horizontal axis is relative to the time of the first TP.

follows a stairstep increase as ^{22}Ne is periodically dredged up into the envelope following its production in convective pulses. The surface abundance of ^{23}Na, which increases monotonically at $Y = 0.24$, is initially destroyed by proton captures in the envelope at $Y = 0.40$. Nucleosynthesis in the convective pulses also contributes to the intershell abundances of ^{25}Mg and ^{26}Mg, which are produced via the ^{22}Ne$(\alpha, n)^{25}$Mg and ^{22}Ne$(\alpha, \gamma)^{26}$Mg reactions. At $Y = 0.24$, increases to ^{25}Mg and ^{26}Mg occur during dredge-up events, with minimal increases due to HBB. At $Y = 0.40$, however, proton captures cause the ^{25}Mg abundance to increase rapidly at the expense of ^{24}Mg. While some of the ^{24}Mg is destroyed by proton captures at $Y = 0.24$ (0.1 dex in mass fraction), the destruction of ^{24}Mg is far more extensive at $Y = 0.40$, with a decrease by almost 3.0 dex before the reduced envelope temperatures and efficient dredge-up cause the abundance to begin increasing. The production of ^{27}Al is lower at $Y = 0.40$ despite the higher $T_{\mathrm{bce}}^{\mathrm{max}}$, which indicates the greater impact of a shorter AGB phase and reduced dredge-up in the He-rich model for this nuclide. In both cases, the amount of ^{28}Si produced from proton capture on to ^{27}Al is very small (< 0.1 dex).

Figure 4.12 shows the stellar yields (in $M_\odot$) of the light elements C, N, O, F, Ne, Na, Mg, and Al as a function of initial mass.

At primordial He abundance, the yield of C increases with the initial mass (and TDU mass) up to a peak at around 3 $M_\odot$. This is the highest mass model that does not experience HBB, while HBB is highly effective in reducing the C yield and increasing the yield of N with masses of about 4 $M_\odot$ and above. With helium mass fractions from 0.30 to 0.40, the model that produces the highest C yield becomes the 2.36 $M_\odot$ model of KMN14. For the models of 3 $M_\odot$, the increase in the N yield with He abundance shows that the increased efficiency of HBB with He-enhancement overcomes the opposing effect of reduced TDU. However, this changes with $M \gtrsim 4$ $M_\odot$, where the yields of N decrease with increasing He, demonstrating that the reduced TDU and shorter AGB phases have a greater effect on the N yields than the increased temperatures at the base of the envelope.

For most of the models, the sum of the C+N+O yields is substantially reduced by helium enhancement, with the exception of the 6 $M_\odot$ model with $Y = 0.40$. The 6 $M_\odot$ model with $Y = 0.40$ experiences a corrosive SDU that dredges up C and O from the core, which affects the stellar yields of several light elements. Compared with the 6 $M_\odot$ model at $Y = 0.35$ (which does not experience a corrosive SDU), the yield of N (produced from dredged-up C) increases by 70 per cent, while O increases by 1600 per cent and the Mg yield increases by 80 per cent.

The predicted yields of C for the models of SCP14 are up to three times lower than our $Y = 0.24$ models at masses of 3 $M_\odot$ and below, and roughly two times higher for masses of 4 $M_\odot$ and above. The smaller C yields in the lower mass range reflect the significantly reduced TDU masses of the SCP14 models, which are up to 85 per cent lower than the
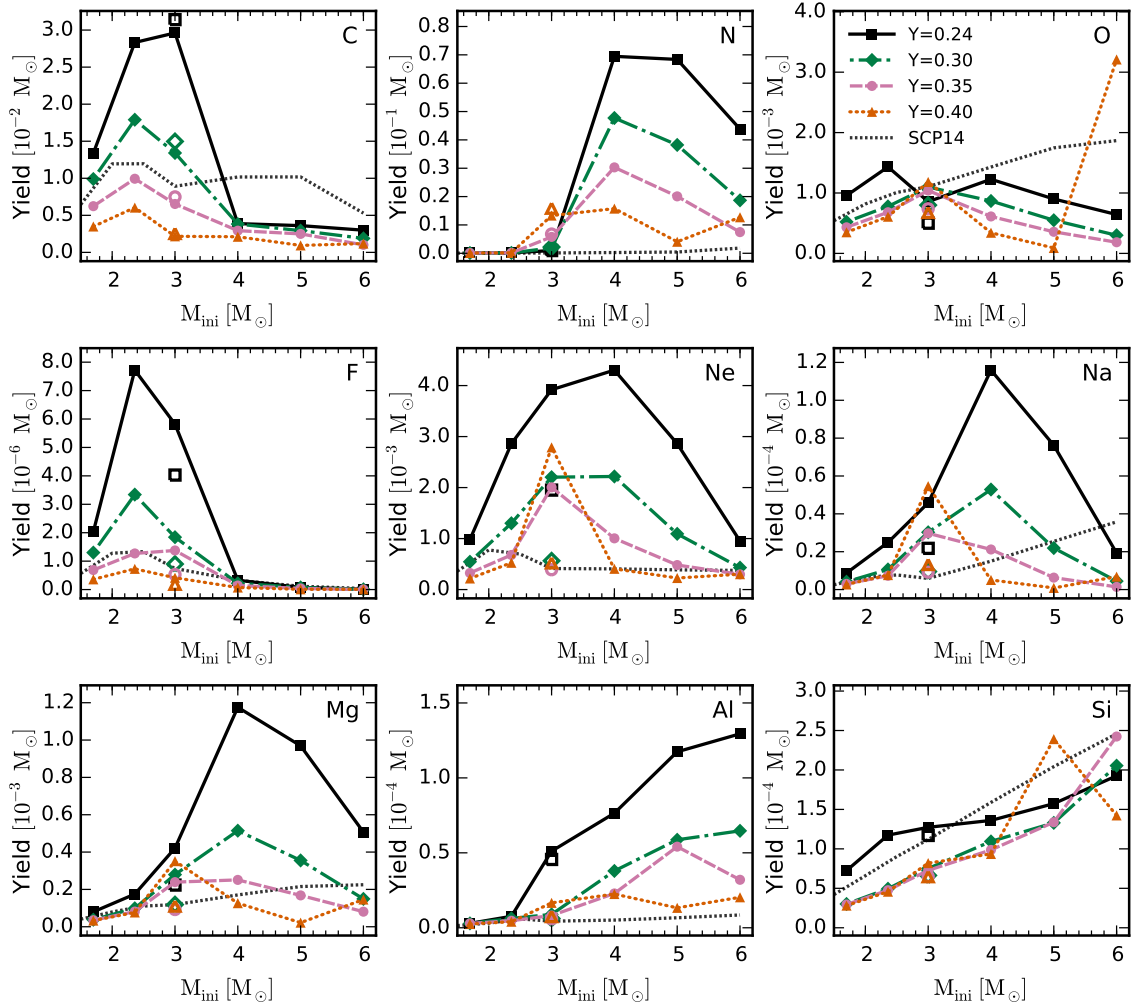
Figure 4.12 Yields of selected light elements as a function of initial mass with He mass fractions of $Y = 0.24$ (black squares), 0.30 (green diamonds), 0.35 (pink circles), and 0.40 (orange triangles). Open points represent 3 $M_\odot$ models without a PMZ. Models with masses of 3 $M_\odot$ and below otherwise include a PMZ of 1×10^{-3} $M_\odot$. 1.7 and 2.36 $M_\odot$ yields are from KMN14.

models presented here. The higher C yields of the SCP14 models in the upper mass range occur in spite of the reduced TDU and are caused by lower envelope temperatures and consequently less HBB than the models presented here.

The only stable isotope of F is ^{19}F, which is produced via ^{14}N$(\alpha, \gamma)^{18}$F$(\beta^+\nu)^{18}$O$(p, \alpha)^{15}$N $(\alpha, \gamma)^{19}$F during TPs in the He-intershell (Jorissen et al. 1992). F can be destroyed both by proton captures in the envelopes of stars with HBB via ^{19}F$(p, \alpha)^{16}$O and α captures in the He-intershells of stars more massive than about 5 $M_\odot$ via ^{19}F$(\alpha, p)^{22}$Ne (Lugaro et al. 2004; Cristallo et al. 2014). Thus, the F yields depend on both the TDU mass and the temperatures at the base of the convective envelope, causing a narrow peak of production at around 2–3 $M_\odot$ that makes F abundances a powerful indicator of stellar mass (e.g., D'Orazi et al. 2013b).

The yield of Ne is sensitive to the inclusion and extent of a PMZ (Shingles & Karakas

2013). This is because additional primary ^{14}N produced in the PMZ is converted into Ne during convective pulses via ^{14}N$(\alpha, \gamma)^{18}$F$(\beta^+\nu)^{18}$O$(\alpha, \gamma)^{22}$Ne. The very short half-life of ^{18}F (110 min) means that the additional F nuclei produced through this chain will not reach the surface (unless neutrons are captured to make ^{19}F). The increase in the yield of F with the inclusion of a PMZ is caused by the additional production of ^{15}N, which is converted into ^{19}F during TPs.

Figure 4.13 shows the isotopic fractions of ^{24}Mg, ^{25}Mg, and ^{26}Mg in the stellar yields as a function of the initial stellar mass and He abundance. The shaded regions indicate the approximate range of Mg isotopic fractions for red giants in ω Centauri with [Fe/H] $\gtrsim -1.4$, as measured by Da Costa et al. (2013).

The isotope ^{24}Mg is efficiently produced by the α-process in core-collapse supernovae, while the presence of ^{25}Mg and ^{26}Mg at low metallicities is generally a good indicator of enrichment by massive AGB stars or Wolf–Rayet stars. In the ω Centauri stars, the range of ^{24}Mg/Mg fractions of about 50–80 per cent is lower than would be expected from a pure core-collapse enrichment scenario (e.g., $\gtrsim 90$ per cent for the low-metallicity yields of Kobayashi et al. 2011) and includes values well below the solar value of 79 per cent (Asplund et al. 2009). However, a precise accounting for the contribution by AGB stars to these low ^{24}Mg/Mg values in ω Centauri would require a detailed chemical evolution model (e.g., Romano et al. 2007), and it is not immediately clear whether the yields of our He-rich models provide a better match to these observations.

This use of our yields or those of VD09 could potentially constrain the mass range of AGB polluters in ω Centauri. This is because the Mg isotope ratios in these yields vary strongly as a function of the initial stellar mass. In contrast, the limited HBB in the models of SCP14 leads to low isotopic fractions of ^{25}Mg and ^{26}Mg, which remain similar to the values in the initial composition throughout the mass range from 1 to 6 M$_\odot$. These models predict that Mg isotope ratios provide only a very weak constraint on the mass range of AGB polluters.

In our models for $Y = 0.40$, the ^{26}Mg/Mg ratio sharply decreases with initial masses greater than about 3 M$_\odot$. The envelope temperatures in these models enter the temperature range (> 110 MK) where the rate of the ^{26}Mg$(p, \gamma)^{27}$Al reaction begins to exceed that of ^{25}Mg$(p, \gamma)^{26}$Al. A similar trend is not seen at lower He abundances.

4.5.2. Yields of neutron-capture elements

Figure 4.14 shows the heavy element abundance distributions in the average of the ejecta for the 3 and 6 M$_\odot$ models. The initial masses of 3 and 6 M$_\odot$ models are chosen to represent the nucleosynthetic behaviour of low- and intermediate-mass AGB models.
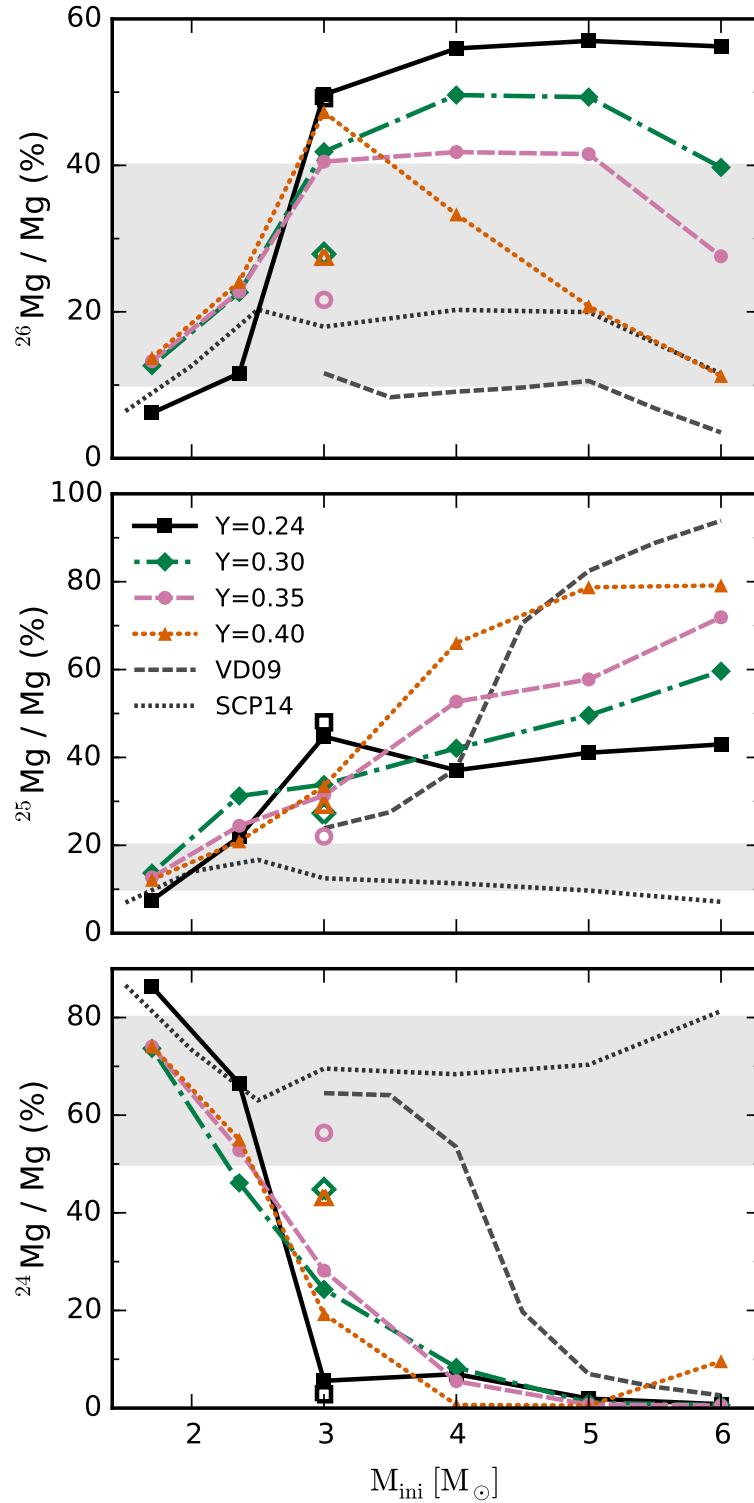
Figure 4.13 The isotopic fractions (by number) of Mg in the stellar yields as a function of initial mass for He mass fractions of $Y = 0.24$ (black squares), 0.30 (green diamonds), 0.35 (pink circles), and 0.40 (orange triangles). Open points indicate 3 $M_\odot$ models without a PMZ. Models with initial masses $\leq 3\,M_\odot$ otherwise include a PMZ of $1 \times 10^{-3}\,M_\odot$. The points at 1.7 $M_\odot$ and 2.36 $M_\odot$ are from the models of KMN14 (which have $[\alpha/\text{Fe}] = 0.4$ for $Y = 0.24$). The grey shaded regions indicate the approximate range of red giants in ω Centauri with $[\text{Fe/H}] \gtrsim -1.4$ from observations by Da Costa et al. (2013).
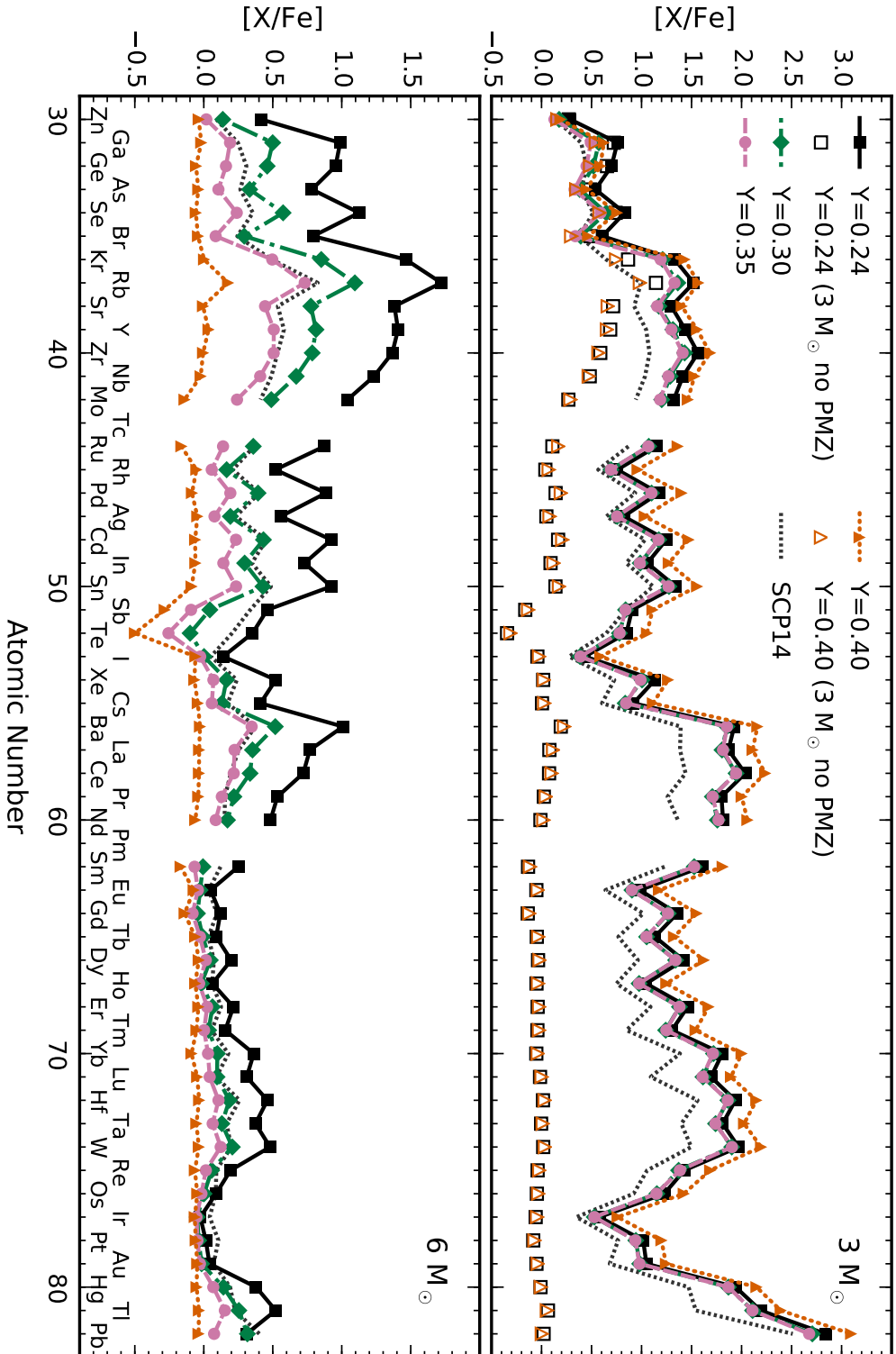
Figure 4.14 Average abundances in the ejecta versus atomic number for the 3 M$_\odot$ models (top panel) and 6 M$_\odot$ models (bottom panel) for He mass fractions of Y = 0.24 (black squares), 0.30 (green diamonds), 0.35 (pink circles), and 0.40 (orange triangles). Open points indicate 3 M$_\odot$ models without a PMZ. Models with initial masses of 3 M$_\odot$ and below otherwise include a PMZ of 1×10^{-3} M$_\odot$.

In the 3 $M_\odot$ models, the overall shape of the abundance distribution is relatively unchanged by variation to the initial He abundance. The primordial-He model is in reasonable agreement with the shape of the distribution predicted by SCP14, but we predict higher absolute abundances at the first and second s-process peaks near Y and Ba by around 0.5 dex (as represented by [X/Fe] ratios). The greater abundances of these elements in our model compared with SCP14 are caused by a significantly higher TDU mass (by a factor of 4) and possibly also our different approaches for modelling ^{13}C-pocket formation.

In contrast with the 1.7 and 2.36 $M_\odot$ yields of KMN14 that steadily decrease with increasing He mass fraction, the Ba, La, Ce, and Pb yields of our 3 $M_\odot$ models exhibit a complicated dependence on the initial He content. In the 3 $M_\odot$ model with $Y = 0.40$, the heavy-element abundances near the second s-process peak at Ba are higher than the model with $Y = 0.24$, despite the lower TDU mass. This is probably a consequence of the greater number of TPs in the $Y = 0.40$ model (48 versus 26 with $Y = 0.24$) and a more significant effect of the ^{22}Ne source.

The maximum extent of the pulse-driven convective zone (M_{pdcz}^{max} in Table 4.2) gives an indication of the size of the He-rich intershell, which decreases with increasing He content. For the 3 $M_\odot$ models, the PMZ mass of 10^{-3} $M_\odot$ increases as a fraction of the He-intershell mass from 10 per cent with $Y = 0.24$ to 33 per cent for $Y = 0.40$. However, as discussed in Section 4.3.1, the high temperatures at the base of the envelope probably prevent a significant s-process production from ^{13}C pockets in 3 $M_\odot$ stars with $Y = 0.40$. We expect that the model for $Y = 0.40$ with no PMZ is more realistic, although there could be a very small contribution from ^{13}C pockets in stars of this mass and He abundance.

For the 6 $M_\odot$ models, the reduction in TDU mass with He-enhancement causes heavy-element abundances in the yields to decrease monotonically with increases to the He abundance. In models with $M \gtrsim 4$ $M_\odot$, the main neutron source is the ^{22}Ne$(\alpha, n)^{25}$Mg reaction operating in convective pulses, which produces much lower neutron-to-Fe-seed ratios and higher neutron densities compared to the ^{13}C neutron source. As a result, the 6 $M_\odot$ abundance distributions peak at Rb, with positive [Rb/Sr] and [Rb/Zr] ratios that are characteristic of s-process production via the ^{22}Ne neutron source.

This is because the abundance ratios [Rb/Zr] and [Rb/Sr] depend on the s-process branchings at ^{85}Kr (half-life = 10.8 yr) and ^{86}Rb (half-life = 18.6 d) (Karakas et al. 2012; van Raai et al. 2012). With neutron densities above 10^8–10^9 cm^{-3}, neutron captures on to ^{85}Kr and ^{86}Rb cause the s-process path to produce ^{87}Rb. This nuclide has a magic number of neutrons, which gives it a very small neutron-capture cross-section relative to ^{85}Rb and neighbouring nuclides and hence it accumulates (Heil et al. 2008). At high neutron densities, this causes a larger production of Rb than Sr and Zr, which is not affected by branching points (D'Orazi et al. 2013a).

Pb and Bi represent the end point of the s-process chain, because heavier nuclei are
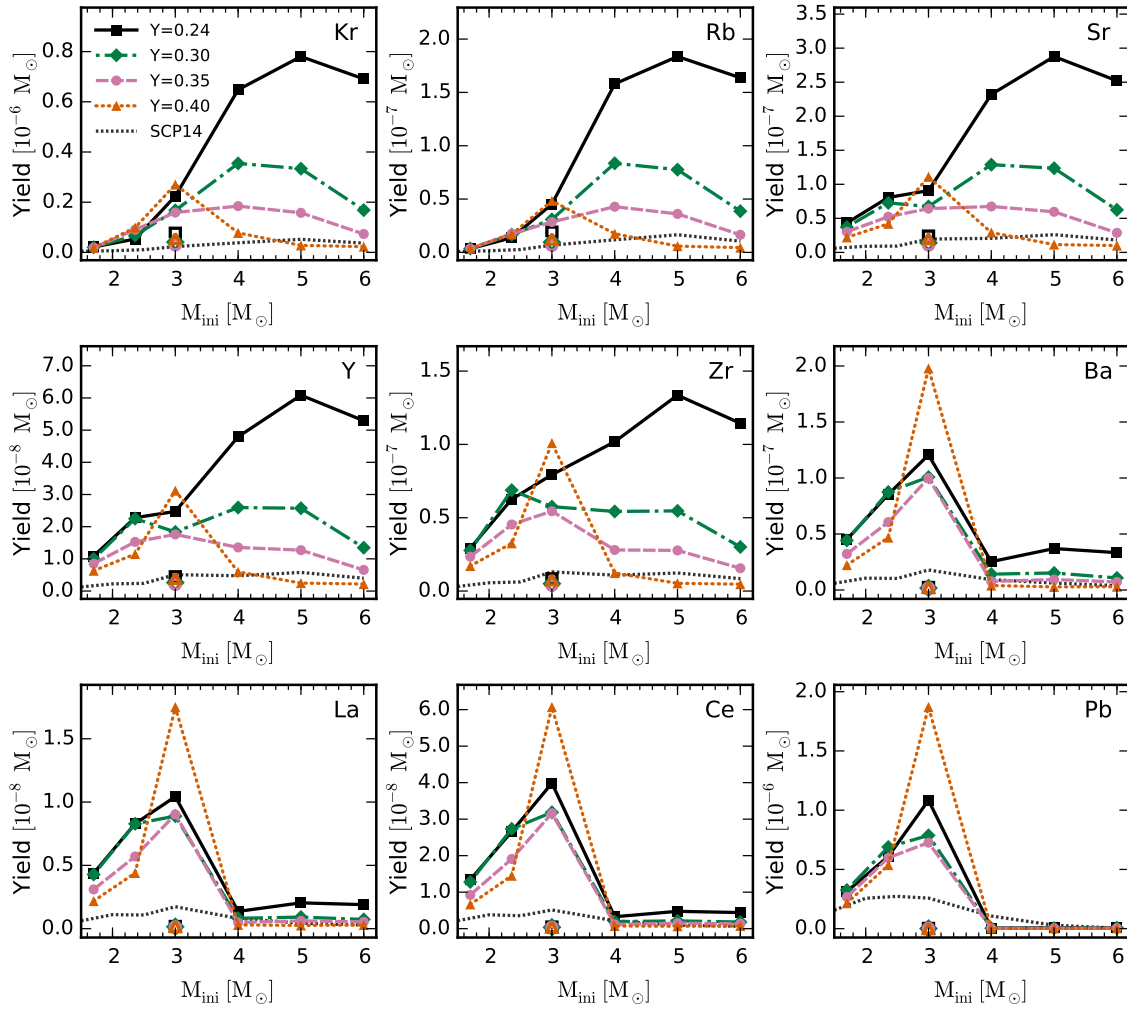
Figure 4.15 Yields of selected neutron-capture elements as a function of initial mass with He mass fractions of $Y = 0.24$ (black squares), 0.30 (green diamonds), 0.35 (pink circles), and 0.40 (orange triangles). Symbols are the same as in Figure 4.12.

unstable against α- and β-decays. Pb is not produced in significant quantities by the models that do not have a PMZ, as the low neutron-to-Fe seed ratios in these models are not sufficient to populate the s-process chain to its heaviest nuclide.

Figure 4.15 shows the stellar yields of selected s-process elements as a function of initial mass for all of our models. Overall, the yields of s-process elements exhibit a very strong reduction with He-enhancement, mostly because of the lower TDU mass.

The yields of Ba, La, Ce, and Pb increase with initial mass up to a peak near 3 M$_\odot$. The initial rise is due to the correlation between initial mass and the amount of TDU during the AGB. The trend then reverses beyond 3 M$_\odot$ due to our assumption of no PMZs (and ^{13}C pockets) in the higher mass models.

For our models between 4 and 6 M$_\odot$, in which the main neutron source is the ^{22}Ne$(\alpha, n)^{25}$Mg reaction operating in convective pulses, the elements Ba, La, Ce, and Pb are not produced

in significant quantities. With He-enhancement, the yields of these elements are reduced further to effectively zero. For the lighter *s*-process elements that are mainly produced by models in this mass range (Kr, Rb, Sr, Y, and Zr) the yields are decreased by an order of magnitude with $Y = 0.40$.

In contrast with our results for $Y = 0.24$, the SCP14 predictions for *s*-process yields are substantially lower. This is connected with the smaller number of TPs in their models, which result in fewer neutron producing events and TDU episodes, and possibly the different treatment of ^{13}C-pocket formation. The smaller variation of the yields as a function of initial mass for the models of SCP14 reflects the flatter profile of TDU mass versus the initial mass.

The top panel of Figure 4.16 shows the average [Rb/Zr] ratio in the ejecta as a function of the initial stellar mass. The transition from neutrons produced in ^{13}C pockets to neutrons produced by the ^{22}Ne source in convective pulses (which produce higher neutron densities) at around 3 M$_\odot$ is marked by [Rb/Zr] values that are negative or positive, respectively. In contrast with the stellar yields of Rb and Zr (which vary by more than 1 dex between our models and SCP14), our predictions for [Rb/Zr] agree with those of SCP14 to within 0.2 dex for initial masses between 3 and 6 M$_\odot$. This is because the [Rb/Zr] ratio is relatively independent of the TDU mass, which is substantially different in the SCP14 models.

The relative behaviour of the three *s*-process peaks is quantified by the ls and hs indices and the Pb abundances. Following Cristallo et al. (2011), we define [ls/Fe] by

$$[ls/Fe] = ([Sr/Fe] + [Y/Fe] + [Zr/Fe])/3, \qquad (4.3)$$

and [hs/Fe] by,

$$[hs/Fe] = ([Ba/Fe] + [La/Fe] + [Nd/Fe] + [Sm/Fe])/4. \qquad (4.4)$$

Figure 4.16 shows the average [hs/ls][2] and [Pb/hs] indices in the ejecta of our models as a function of the initial stellar mass. Both the [hs/ls] and [Pb/hs] indices are highly sensitive to the inclusion of a PMZ (and ^{13}C pockets), which results in positive values of these ratios for initial masses less than about 3 M$_\odot$ and negative values for higher masses.

The [hs/ls] and [Pb/hs] indices of the SCP14 models decrease more slowly with initial mass than the models presented here. This is because their treatment of the PMZ does not include an explicit cutoff at a particular initial mass. The models of SCP14 include a PMZ that gradually decreases in size and neutron production as the initial mass increases, whereas our models with masses above 3 M$_\odot$ do not include a PMZ.

---

[2][hs/ls] = [hs/Fe] − [ls/Fe]
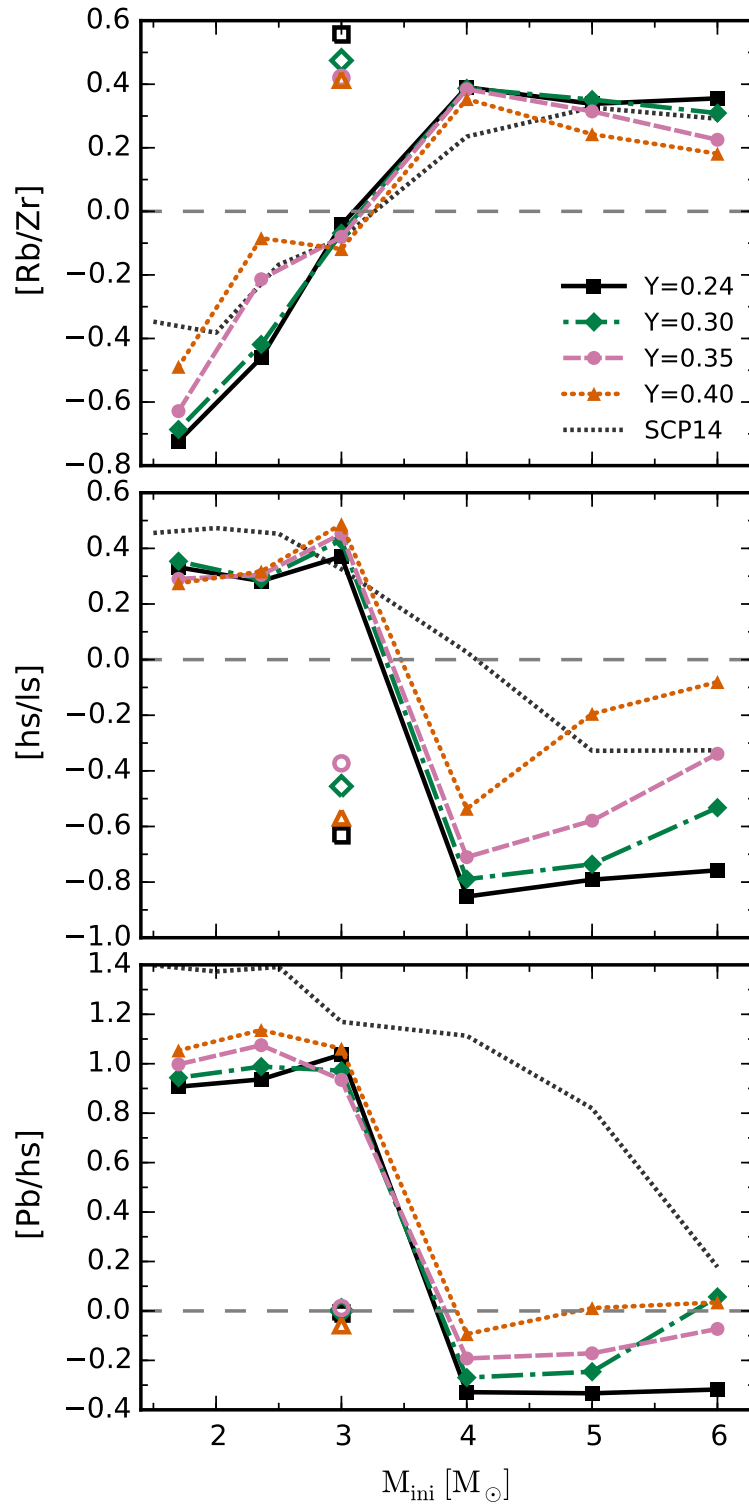
Figure 4.16 The *s*-process indices [Rb/Zr] (top), [hs/ls] (middle), and [Pb/hs] (bottom) of the yields as a function of initial mass with He mass fractions of $Y = 0.24$ (black squares), 0.30 (green diamonds), 0.35 (pink circles), and 0.40 (orange triangles). Symbols are the same as in Figure 4.12.

4.6.   Discussion and Conclusions

We have presented and analysed the results of calculations of intermediate-mass stellar models at low metallicity with initial He mass fractions of $Y = 0.24, 0.30, 0.35$, and 0.40.

The results of this study support the conclusion that the initial He abundance is a crucially important parameter for stellar evolution and chemical yields. For example, we have shown that the dredge up efficiency and the total TDU mass in intermediate-mass models are significantly reduced by He-enhanced initial compositions. In synthetic AGB models that require the value of λ as a function of mass and metallicity (e.g., Bertelli et al. 2008; Buell 2013), an improvement in accuracy would be achieved if the He abundance were incorporated as a third parameter and values were obtained from full stellar evolutionary models with the appropriate initial He abundance.

One of the objectives of this study was to discover whether the reduction in the yields of Ba-peak elements found by KMN14 with He-enhanced 1.7 and 2.36 $M_\odot$ models is also the case for higher initial masses. For 4 $M_\odot$ and higher masses, we find that it is the case that increasing the He mass fraction results in lower yields of Ba, La, and Ce. However, our models at 4 $M_\odot$ and above make a small contribution to these elements with $Y = 0.24$, and hence the reduction in these yields with He-enhancement will have minimal impact on chemical evolution. Of greater importance are the s-process yields of models with $M \lesssim 3 \, M_\odot$, which are subject to the major uncertainties of ^{13}C-pocket formation. If we assume that the same PMZs form after each TP with TDU for $Y = 0.40$ and 0.24, then predicted Ba-peak yields are higher by almost a factor of 2, due to the near-doubling of the total number of TPs in the He-enhanced model. However, the very high temperatures in the envelope during TDU and the thinner He-intershell (by a factor of 3) for $Y = 0.40$ suggest that a future, more advanced treatment of the PMZ would result in a much smaller production of free neutrons for the s-process. In this case, the production of Ba-peak elements and Pb would be significantly lower at high He abundances because of the reduced contribution from ^{13}C pockets.

Although many conclusions can be drawn from a grid of individual stellar yields, an understanding of their combined effect requires their application to a chemical evolution model (e.g., Travaglio et al. 1999; Kobayashi et al. 2011; Bisterzo et al. 2014; Shingles et al. 2014). From the stellar yields of the 1.7 and 2.36 $M_\odot$ models by KMN14 and the 3–6 $M_\odot$ models presented here, the chemical evolution of s-process elements near [Fe/H] ≈ -1.4 could be predicted as a function of He abundance, once other chemical evolution assumptions have been made (e.g., Romano et al. 2007, for light and α elements). We expect that a comparison between the chemical evolution predictions with yields of $Y = 0.40$ models and the s-process abundances in ω Centauri would be particularly insightful.

We have compared the stellar yields of our models with the primordial-He models of SCP14 and VD09, but the present lack of stellar yields for He-rich compositions makes it difficult to understand how the predicted impact of He-enhancement would be different with alternative modelling assumptions and stellar evolution codes. Of critical importance for the stellar yield predictions is the mass of intershell material that is transported to the surface by TDU. The finding of KMN14 and this work that the total mass dredged-up by TDU is highly reduced by He-enhancement (up to 96 per cent at 6 $M_\odot$) needs to be investigated with other stellar evolution codes, which already predict much less efficient dredge-up with primordial He abundance (see e.g., Mowlavi 1999a; Lugaro et al. 2003, 2012).

The increase of the core mass with initial He content is already a well-established prediction (e.g., Becker & Iben 1979; Lattanzio 1986), and therefore we expect that any predictions that are a direct consequence of larger core masses (e.g., shorter interpulse periods, shorter AGB lifetimes, and higher luminosities) would be qualitatively similar with alternative modelling assumptions. However, the predictions of AGB lifetimes and the total number of TPs are highly dependent on the chosen prescription for the mass-loss rate. The increased mass-loss rate in our models with He-rich compositions would occur to a different extent with alternative mass loss prescriptions, which have a different dependence on the stellar radius and luminosity (e.g., Bloecker 1995; Straniero et al. 2006).

The changing fates of stars with the same initial mass but different He abundances leads to questions about how other mass boundaries are shifted by He-enhancement. For example, the minimum initial mass to form an electron-capture supernova at $Z = 0.0006$ with primordial He abundance is about 8.2–8.4 $M_\odot$ (Doherty et al. 2015). With the larger core masses of He-enriched stars, this boundary would shift to lower masses, which are more numerous with a standard initial mass function. As a consequence, the rates of electron-capture supernovae and neutron star formation would be higher at a given star formation rate with He-enhancement.

Similarly, He-enhancement would increase the number of hybrid CO(Ne) WDs, which have been suggested as possible progenitors of Type Iax supernovae (Denissenkov et al. 2015a; Kromer et al. 2015). If this is the case, then the rate of Type Ia supernovae would be higher for He-rich populations.

Acknowledgements

4.7.   Example of the Online Tables

In Table 4.3 we show the first few rows of an example online table that contains the stellar yields of each chemical element.

Table 4.3 The first few rows of an example stellar yield table. Each table begins with a header describing the stellar model.

\# $M_{ini} = 3.00\ M_\odot$, $Z = 0.0006$, $Y = 0.24$, $M_{pmz} = 1.0E-03\ M_\odot$

\# Initial [Fe/H] = -1.41, [α/Fe] = 0.0

\# $M_{remnant} = 0.801\ M_\odot$, M_{yield}(all) = 2.199 $M_\odot$

El	Z	$\log \epsilon(X)$	[X/H]	[X/Fe]	M_{yield}	X_{yield}
p	1	12.000000	0.000000	1.361876	1.441618E+00	6.556237E-01
he	2	11.097055	0.167055	1.528930	7.210486E-01	3.279209E-01
c	6	9.231870	0.761870	2.123746	2.961464E-02	1.346825E-02
n	7	7.679011	-0.190989	1.170886	9.638053E-04	4.383226E-04
o	8	7.569763	-1.160237	0.201638	8.565194E-04	3.895308E-04
f	9	5.327235	0.907235	2.269111	5.818873E-06	2.646327E-06
ne	10	8.093986	0.123986	1.485862	3.918737E-03	1.782176E-03
na	11	6.140176	-0.099824	1.262052	4.578822E-05	2.082372E-05
⋮	⋮			⋮	⋮	⋮

\#	[Rb/Zr]	[ls/Fe]	[hs/Fe]	[hs/ls]	[Pb/hs]	[C+N+O/Fe]	log e (CNO)
	-0.2027	1.4595	1.9514	0.4919	0.9292	1.9422	9.5376

CHAPTER 5

Conclusions

> At terrestrial temperatures matter has complex properties which
> are likely to prove most difficult to unravel; but it is reasonable to
> hope that in the not too distant future we shall be competent to
> understand so simple a thing as a star.
>
> – Arthur Eddington (1926)[1]

In the earlier chapters, we discovered new insights into AGB evolution and nucleosynthesis and its implications for measured chemical abundances. The main findings are outlined below:

In Chapter 2, we asked if neutron-capture reactions in AGB stars are the cause of the low sulphur abundances in planetary nebulae and post-AGB stars relative to the interstellar medium. Accounting for uncertainties in the size of the partial mixing zone (PMZ; which forms ^{13}C pockets) and the rates of neutron-capture and neutron-producing reactions, our models failed to reproduce the observed levels of sulphur destruction. From this, we concluded that AGB nucleosynthesis is not the cause of the sulphur anomaly. While addressing this question, we also discovered a new technique to constrain the size of the partial mixing zone that forms ^{13}C pockets. Our constraint follows from the requirement that the AGB final surface abundances lie within the region spanned by planetary nebulae in the argon versus neon plane. This constrains the PMZ size to less than 5×10^{-3} M$_\odot$ in our 3 M$_\odot$ model at a metallicity slightly below solar.

In Chapter 3, we studied the s-process enrichment of the globular clusters M4 and M22,

---

[1]*The Internal Constitution of Stars*, Cambridge. (1926).

which are examples of inter- and intra-cluster variation, respectively. Using a basic closed-box chemical evolution code, we predicted the relative increases of light-*s* (Y, Zr) and heavy-*s* (Ba, La, Ce) elements using stellar yields from the most likely candidate polluters – rotating massive stars and AGB stars. We found that rotating massive stars alone do not explain the pattern of abundance variations, and that a contribution from both intermediate-mass AGB stars with a ^{22}Ne neutron source and low-mass stars AGB with ^{13}C pockets are required to explain the abundance variations. We also derived minimum enrichment timescales from the lowest mass (and longest-lived) stellar models in our best-fitting enrichment scenarios. Although this value depends on which assumptions are made about the partial-mixing zone, our estimate of 240 to 360 Myr for M22 is consistent with the literature value of a 300 Myr upper limit derived from isochrone fitting of the two stellar groups.

In Chapter 4, we explored the consequences of He-rich initial compositions for the stellar evolution and nucleosynthesis of intermediate-mass AGB stars. We found that the stellar yields of *s*-process elements were substantially lower in He-rich models, largely as a result of less intershell material being mixed into the envelope. We also found that envelope burning takes place at lower masses He-enhancement. The higher temperatures at the base of the convective envelope also suggest that *s*-process production by ^{13}C pockets could be restricted to lower initial masses for higher helium abundances. Overall, our results demonstrate the importance of using models of the appropriate helium abundance when assembling sets of stellar yields for chemical evolution studies.

These studies demonstrate both the utility of stellar nucleosynthesis models for interpreting chemical abundances, as well as their limitations due to the current uncertainties in stellar physics.

A central theme in this thesis has been the uncertainties related to ^{13}C-pocket formation, which is crucial for understanding the nucleosynthesis of heavy elements in low-mass stars. Despite its importance, we lack an understanding of ^{13}C-pocket formation from first principles. A variety of constraints have been discovered from measured abundances (including the upper limit to the mixing depth discussed in Chapter 2), but the physical mechanism that mixes protons into the He-rich core has not been determined conclusively. Currently there are several plausible mechanisms capable of producing ^{13}C pockets that appear to be consistent with the present observational constraints. The formation mechanism could be an example of the more general uncertainty over modelling convection in one dimension, as convective overshooting has been shown to produce adequate ^{13}C pockets for certain values of the overshoot parameter (Herwig 2000; Cristallo et al. 2009). Other candidates for the physical process responsible are rotational mixing (Langer et al. 1999; Herwig & Langer 2001), gravity-wave driven mixing (Denissenkov & Tout 2003), and semiconvection (Iben & Renzini 1982; Hollowell & Iben 1989).

With a future physical understanding of ^{13}C pocket formation, we will be able understand how the efficiency of the ^{13}C neutron source varies as a function of the initial chemical composition and the initial stellar mass. This would improve the accuracy of stellar yields of *s*-process elements for chemical evolution studies.

The uncertainty of the mass-loss rate on the AGB was mentioned in Chapter 4. The differences in the evolution, nucleosynthesis, and stellar yields of our models compared to those of Straniero et al. (2014) and Ventura & D'Antona (2009) are partly due to the use of different prescriptions for the mass-loss rate. Changes to the mass-loss rates alter the total number of thermal pulses, which affects the the number of dredge-up episodes and the nucleosynthesis that occurs in convective pulses (including via the *s*-process). The mass-loss rate also affects the duration and efficiency of hot bottom burning (Ventura & D'Antona 2005a). For these reasons, our current uncertainty in the AGB mass-loss rate propagates to uncertainty in stellar yield predictions (Stancliffe & Jeffery 2007).

5.1.   Future Directions

The general technique of using *s*-process element ratios to determine enrichment timescales demonstrated in Chapter 3 could be further applied to other globular clusters with internal *s*-process variation such as M2 (Yong et al. 2014) and NGC 5286 (Marino et al. 2015). The similarity (or variation) of the derived enrichment timescales could provide clues about the formation process of *s*-process-anomalous in general.

The enrichment timescales derived from chemical evolution models should in principle agree with age spreads derived by fitting isochrones to photometry. However, photometrically-inferred ages currently have very large uncertainties, and tend to be reliable only as upper limits. Our prediction of a 240–360 Myr enrichment timescale for M22 in Chapter 3 is larger than the 150 ± 50 Myr estimate of Straniero et al. (2014) mostly because their models include ^{13}C pockets at higher initial masses. Unfortunately, both models are consistent with the ~300 Myr age difference derived from isochrone fitting (Marino et al. 2012; Joo & Lee 2013). Assuming that the gas-cooling timescale is not a significant factor, a future measurement of the age spread in M22 from photometry that is more precise but much lower could potentially discriminate between the two models and would favour the formation of ^{13}C pockets in more massive AGB stars.

Other analysis of chemical abundance studies (in e.g., post-AGB stars) could be a continuing source of progress on ^{13}C-pocket formation. The theoretical route of using three-dimensional hydrodynamical simulations of TDU episodes will require either dramatically faster computers, new simulation codes with substantial performance optimisations and simplifications, or likely both.

With the new stellar yields described in Chapter 4 (and tabulated in Appendix A), and those of Karakas et al. (2014) for 1.7 and 2.36 $M_\odot$, we have a complete set of AGB stellar yields with a He content of $Y = 0.24, 0.30, 0.35$, and 0.40. New chemical evolution models of ω Centauri can now be constructed using yields from stellar models of the appropriate helium abundance. The comparison between the chemical evolution models using our He-rich yields and the abundances of ω Centauri stars would be an ideal way to test the validity of our yield predictions. If we have enough confidence in the validity of the model, the comparison may support or reject our prediction that the ^{13}C neutron source is suppressed at lower masses with increasing He content.

We currently do not know how our predictions for the stellar yields of He-rich stars would be altered with alternative modelling assumptions and different stellar evolution codes. Of critical importance for the stellar yield predictions is the quantity of intershell material that is transported to the surface by TDU. The finding of KMN14 and Chapter 4 of this thesis that the total mass dredged-up by TDU is significantly reduced by He-enhancement should be investigated with other stellar evolution codes, which already predict much less efficient dredge-up for models with primordial He abundance (see e.g., Mowlavi 1999a; Lugaro et al. 2003, 2012).

APPENDIX A

Tables of stellar yields

The following tables of stellar yields are included with Shingles et al. (2015) as online data tables. The stellar models are described in Chapter 4.

Table A.1 Yields for 3 M$_\odot$, Z = 0.0006, Y = 0.24, no PMZ.

El	Z	log ϵ(X)	[X/H]	[X/Fe]	M$_{yield}$	X$_{yield}$
H	1	12.000000	0.000000	1.359315	1.442128E+00	6.558556E-01
He	2	11.097060	0.167060	1.526374	7.213125E-01	3.280409E-01
C	6	9.257309	0.787309	2.146624	3.141036E-02	1.428491E-02
N	7	7.677840	-0.192160	1.167154	9.615501E-04	4.372970E-04
O	8	7.335793	-1.394207	-0.034892	4.999430E-04	2.273657E-04
F	9	5.167370	0.747370	2.106685	4.028352E-06	1.832027E-06
Ne	10	7.791710	-0.178290	1.181025	1.950436E-03	8.870260E-04
Na	11	5.817337	-0.422663	0.936651	2.178051E-05	9.905415E-06
Mg	12	6.783888	-0.856112	0.503203	2.232598E-04	1.015348E-04
Al	13	6.068462	-0.381538	0.977777	4.558582E-05	2.073167E-05
Si	14	6.460623	-1.089377	0.269937	1.170216E-04	5.321949E-05
P	15	4.297005	-1.112995	0.246319	8.858699E-07	4.028789E-07
S	16	5.803306	-1.346694	0.012621	2.944105E-05	1.338930E-05
Cl	17	3.974277	-1.255723	0.103592	4.846370E-07	2.204048E-07
Ar	18	5.081664	-1.358336	0.000978	6.329765E-06	2.878672E-06
K	19	3.773375	-1.306625	0.052690	3.350870E-07	1.523920E-07
Ca	20	4.923845	-1.366155	-0.006841	4.857517E-06	2.209118E-06
Sc	21	2.048396	-1.001604	0.357710	7.254571E-09	3.299258E-09
Ti	22	3.564495	-1.345505	0.013809	2.540155E-07	1.155220E-07
V	23	2.593294	-1.366706	-0.007391	2.883157E-08	1.311212E-08
Cr	24	4.261885	-1.378115	-0.018800	1.375631E-06	6.256142E-07
Mn	25	4.111354	-1.368646	-0.009331	1.024992E-06	4.661495E-07
Fe	26	6.180685	-1.359315	0.000000	1.224148E-04	5.567222E-05
Co	27	4.111233	-0.758767	0.600548	1.099231E-06	4.999120E-07
Ni	28	4.946031	-1.253969	0.105345	7.583346E-06	3.448780E-06
Cu	29	3.649897	-0.600103	0.759211	4.089923E-07	1.860029E-07
Zn	30	3.583904	-1.046096	0.313218	3.670452E-07	1.669260E-07
Ga	31	2.483566	-0.596434	0.762881	3.068206E-08	1.395369E-08
Ge	32	2.915020	-0.664980	0.694334	8.562187E-08	3.893940E-08
As	33	1.468066	-0.831934	0.527381	3.177834E-09	1.445226E-09
Se	34	2.761809	-0.578191	0.781124	6.545636E-08	2.976846E-08
Br	35	1.712028	-0.827972	0.531343	5.965477E-09	2.713000E-09
Kr	36	2.795765	-0.454235	0.905080	7.616920E-08	3.464048E-08
Rb	37	2.184556	-0.335444	1.023871	1.899818E-08	8.640056E-09
Sr	38	2.276326	-0.603674	0.755641	2.387831E-08	1.085946E-08
Y	39	1.537190	-0.672810	0.686504	4.421642E-09	2.010889E-09
Zr	40	1.798025	-0.731975	0.627339	8.335922E-09	3.791039E-09
Nb	41	0.572622	-0.837378	0.521937	5.013130E-10	2.279888E-10
Mo	42	0.888850	-1.051150	0.308164	1.077512E-09	4.900347E-10

Table A.1 Yields for 3 M$_\odot$, $Z = 0.0006$, $Y = 0.24$, no PMZ. (continued)

El	Z	log ϵ(X)	[X/H]	[X/Fe]	M$_{yield}$	X$_{yield}$
Ru	44	0.549225	-1.210775	0.148540	5.152165E-10	2.343119E-10
Rh	45	-0.221065	-1.281065	0.078249	8.928443E-11	4.060507E-11
Pd	46	0.471471	-1.178529	0.180786	4.530120E-10	2.060223E-10
Ag	47	-0.070990	-1.270990	0.088325	1.322789E-10	6.015824E-11
Cd	48	0.556459	-1.153541	0.205773	5.831768E-10	2.652191E-10
In	49	-0.469213	-1.229213	0.130102	5.629748E-11	2.560316E-11
Sn	50	0.890031	-1.179969	0.179346	1.325427E-09	6.027822E-10
Sb	51	-0.472169	-1.482169	-0.122854	5.883293E-11	2.675624E-11
Te	52	0.515915	-1.664085	-0.304770	5.912326E-10	2.688827E-10
I	53	0.189041	-1.360959	-0.001644	2.830405E-10	1.287221E-10
Xe	54	0.936798	-1.303202	0.056112	1.635019E-09	7.435795E-10
Cs	55	-0.234835	-1.314835	0.044480	1.116917E-10	5.079552E-11
Ba	56	1.053166	-1.126834	0.232480	2.238301E-09	1.017942E-09
La	57	-0.070916	-1.240916	0.118399	1.702562E-10	7.742969E-11
Ce	58	0.335968	-1.244032	0.115283	4.384118E-10	1.993824E-10
Pr	59	-0.536374	-1.296374	0.062940	5.913552E-11	2.689385E-11
Nd	60	0.119605	-1.330395	0.028919	2.734751E-10	1.243719E-10
Sm	62	-0.514230	-1.454230	-0.094915	6.602279E-11	3.002607E-11
Eu	63	-0.860888	-1.370888	-0.011573	3.020546E-11	1.373694E-11
Gd	64	-0.407193	-1.457193	-0.097879	8.843188E-11	4.021735E-11
Tb	65	-1.046747	-1.366747	-0.007432	2.058990E-11	9.363944E-12
Dy	66	-0.224301	-1.354301	0.005014	1.398922E-10	6.362063E-11
Ho	67	-0.899680	-1.369680	-0.010365	2.997836E-11	1.363366E-11
Er	68	-0.438176	-1.358176	0.001139	8.802372E-11	4.003172E-11
Tm	69	-1.240574	-1.360574	-0.001259	1.400608E-11	6.369734E-12
Yb	70	-0.451538	-1.371538	-0.012224	8.806425E-11	4.005016E-11
Lu	71	-1.244428	-1.334428	0.024886	1.438079E-11	6.540144E-12
Hf	72	-0.594953	-1.304953	0.054362	6.546860E-11	2.977403E-11
Ta	73	-1.443738	-1.323738	0.035577	9.396035E-12	4.273160E-12
W	74	-0.652741	-1.302741	0.056574	5.900230E-11	2.683327E-11
Re	75	-1.098575	-1.358575	0.000739	2.140688E-11	9.735492E-12
Os	76	-0.016079	-1.366079	-0.006764	2.643819E-10	1.202365E-10
Ir	77	-0.057904	-1.377904	-0.018590	2.426459E-10	1.103513E-10
Pt	78	0.217470	-1.402530	-0.043216	4.637360E-10	2.108994E-10
Au	79	-0.569924	-1.369924	-0.010609	7.647973E-11	3.478171E-11
Hg	80	-0.159734	-1.329734	0.029581	2.000581E-10	9.098309E-11
Tl	81	-0.485311	-1.255311	0.104004	9.642567E-11	4.385279E-11
Pb	82	0.741415	-1.298585	0.060730	1.648453E-09	7.496889E-10
Bi	83	-0.671914	-1.321914	0.037401	6.415583E-11	2.917700E-11

Table A.2   Yields for 3 M$_\odot$, $Z = 0.0006$, $Y = 0.24$, M$_{pmz} = 0.001$

El	Z	log ϵ(X)	[X/H]	[X/Fe]	M$_{yield}$	X$_{yield}$
H	1	12.000000	0.000000	1.361876	1.441618E+00	6.556237E-01
He	2	11.097055	0.167055	1.528930	7.210486E-01	3.279209E-01
C	6	9.231870	0.761870	2.123746	2.961464E-02	1.346825E-02
N	7	7.679011	-0.190989	1.170886	9.638053E-04	4.383226E-04
O	8	7.569763	-1.160237	0.201638	8.565194E-04	3.895308E-04
F	9	5.327235	0.907235	2.269111	5.818873E-06	2.646327E-06
Ne	10	8.093986	0.123986	1.485862	3.918737E-03	1.782176E-03
Na	11	6.140176	-0.099824	1.262052	4.578822E-05	2.082372E-05
Mg	12	7.060157	-0.579843	0.782033	4.212488E-04	1.915770E-04
Al	13	6.118289	-0.331711	1.030165	5.110963E-05	2.324381E-05
Si	14	6.496964	-1.053036	0.308840	1.272927E-04	5.789060E-05
P	15	4.682888	-0.727112	0.634763	2.153275E-06	9.792739E-07
S	16	5.812711	-1.337289	0.024586	3.008810E-05	1.368357E-05
Cl	17	3.978969	-1.251031	0.110845	4.897808E-07	2.227441E-07
Ar	18	5.080036	-1.359964	0.001912	6.304914E-06	2.867370E-06
K	19	3.775167	-1.304833	0.057042	3.363486E-07	1.529657E-07
Ca	20	4.921716	-1.368284	-0.006408	4.832749E-06	2.197854E-06
Sc	21	2.081698	-0.968302	0.393574	7.829977E-09	3.560943E-09
Ti	22	3.576810	-1.333190	0.028686	2.614948E-07	1.189235E-07
V	23	2.600276	-1.359724	0.002152	2.928843E-08	1.331989E-08
Cr	24	4.261082	-1.378918	-0.017042	1.372694E-06	6.242782E-07
Mn	25	4.105544	-1.374456	-0.012581	1.011012E-06	4.597915E-07
Fe	26	6.178124	-1.361876	0.000000	1.216570E-04	5.532760E-05
Co	27	4.113808	-0.756192	0.605684	1.105377E-06	5.027070E-07
Ni	28	4.952897	-1.247103	0.114773	7.706558E-06	3.504814E-06
Cu	29	3.668154	-0.581846	0.780030	4.263273E-07	1.938866E-07
Zn	30	3.594775	-1.035225	0.326650	3.763824E-07	1.711725E-07
Ga	31	2.516030	-0.563970	0.797906	3.306021E-08	1.503523E-08
Ge	32	2.958237	-0.621763	0.740112	9.458630E-08	4.301627E-08
As	33	1.516693	-0.783307	0.578568	3.553070E-09	1.615877E-09
Se	34	2.848239	-0.491761	0.870114	7.988955E-08	3.633244E-08
Br	35	1.826504	-0.713496	0.648380	7.759037E-09	3.528681E-09
Kr	36	3.260757	0.010757	1.372632	2.241424E-07	1.019362E-07
Rb	37	2.559778	0.039778	1.401653	4.521170E-08	2.056153E-08
Sr	38	2.855223	-0.024777	1.337098	9.072939E-08	4.126222E-08
Y	39	2.285069	0.075069	1.436945	2.473485E-08	1.124900E-08
Zr	40	2.772505	0.242505	1.604381	7.933369E-08	3.607964E-08
Nb	41	1.502444	0.092444	1.454320	4.263605E-09	1.939016E-09
Mo	42	1.939659	-0.000341	1.361534	1.213849E-08	5.520385E-09

Table A.2 Yields for 3 $M_\odot$, $Z = 0.0006$, $Y = 0.24$, $M_{pmz} = 0.001$ (continued)

El	Z	$\log \epsilon(X)$	[X/H]	[X/Fe]	M_{yield}	X_{yield}
Ru	44	1.587234	-0.172766	1.189110	5.620767E-09	2.556232E-09
Rh	45	0.494992	-0.565008	0.796868	4.641725E-10	2.110979E-10
Pd	46	1.500404	-0.149596	1.212280	4.841236E-09	2.201714E-09
Ag	47	0.698621	-0.501379	0.860496	7.790792E-10	3.543122E-10
Cd	48	1.634657	-0.075343	1.286532	6.981889E-09	3.175247E-09
In	49	0.495750	-0.264250	1.097626	5.191564E-10	2.361037E-10
Sn	50	2.089431	0.019431	1.381307	2.099575E-08	9.548516E-09
Sb	51	0.592328	-0.417672	0.944204	6.822817E-10	3.102904E-10
Te	52	1.706760	-0.473240	0.888636	9.155750E-09	4.163883E-09
I	53	0.660651	-0.889349	0.472527	8.381171E-10	3.811617E-10
Xe	54	2.052473	-0.187527	1.174348	2.147961E-08	9.768569E-09
Cs	55	0.676584	-0.403416	0.958459	9.105111E-10	4.140853E-10
Ba	56	2.784066	0.604066	1.965942	1.206260E-07	5.485872E-08
La	57	1.716468	0.546468	1.908344	1.043118E-08	4.743925E-09
Ce	58	2.294394	0.714394	2.076270	3.985463E-08	1.812522E-08
Pr	59	1.237124	0.477124	1.838999	3.509077E-09	1.595870E-09
Nd	60	1.943083	0.493083	1.854959	1.819986E-08	8.276992E-09
Sm	62	1.222332	0.282332	1.644208	3.593080E-09	1.634073E-09
Eu	63	0.170729	-0.339271	1.022605	3.247670E-10	1.476986E-10
Gd	64	1.084198	0.034198	1.396074	2.745830E-09	1.248758E-09
Tb	65	0.131356	-0.188644	1.173232	3.101724E-10	1.410612E-10
Dy	66	1.227571	0.097571	1.459447	3.961905E-09	1.801808E-09
Ho	67	0.193554	-0.276446	1.085429	3.714391E-10	1.689243E-10
Er	68	1.059111	0.139111	1.500987	2.768812E-09	1.259210E-09
Tm	69	0.101198	-0.018802	1.343074	3.075638E-10	1.398749E-10
Yb	70	1.405208	0.485208	1.847084	6.336279E-09	2.881634E-09
Lu	71	0.462041	0.372041	1.733917	7.327709E-10	3.332520E-10
Hf	72	1.325774	0.615774	1.977649	5.467637E-09	2.486590E-09
Ta	73	0.368945	0.488945	1.850820	6.102017E-10	2.775096E-10
W	74	1.297423	0.647423	2.009299	5.260536E-09	2.392404E-09
Re	75	0.365164	0.105164	1.467040	6.211539E-10	2.824905E-10
Os	76	1.255335	-0.094665	1.267210	4.902698E-09	2.229665E-09
Ir	77	0.576838	-0.743162	0.618713	1.045383E-09	4.754230E-10
Pt	78	1.314472	-0.305528	1.056347	5.797091E-09	2.636421E-09
Au	79	0.527155	-0.272845	1.089031	9.560294E-10	4.347863E-10
Hg	80	1.789377	0.619377	1.981253	1.779398E-08	8.092406E-09
Tl	81	1.637915	0.867915	2.229790	1.280151E-08	5.821913E-09
Pb	82	3.558696	1.518696	2.880571	1.083745E-06	4.928690E-07
Bi	83	2.193095	1.543095	2.904971	4.699930E-08	2.137450E-08

Table A.3 Yields for 3 M$_\odot$, Z = 0.0006, Y = 0.30, no PMZ.

El	Z	log ϵ(X)	[X/H]	[X/Fe]	M$_{yield}$	X$_{yield}$
H	1	12.000000	0.000000	1.357043	1.414479E+00	6.604008E-01
He	2	11.097673	0.167673	1.524716	7.084591E-01	3.307699E-01
C	6	8.940706	0.470706	1.827749	1.497197E-02	6.990208E-03
N	7	8.046654	0.176654	1.533697	2.204848E-03	1.029413E-03
O	8	7.548077	-1.181923	0.175120	7.996144E-04	3.733290E-04
F	9	4.523898	0.103898	1.460941	8.979423E-07	4.192370E-07
Ne	10	7.267555	-0.702445	0.654598	5.647870E-04	2.636913E-04
Na	11	5.466588	-0.773412	0.583631	9.526040E-06	4.447577E-06
Mg	12	6.528782	-1.111218	0.245825	1.186774E-04	5.540885E-05
Al	13	5.208871	-1.241129	0.115914	6.177768E-06	2.884315E-06
Si	14	6.222280	-1.327720	0.029323	6.637099E-05	3.098770E-05
P	15	4.172552	-1.237448	0.119595	6.523937E-07	3.045937E-07
S	16	5.804381	-1.345619	0.011424	2.894077E-05	1.351205E-05
Cl	17	3.907850	-1.322150	0.034893	4.072880E-07	1.901572E-07
Ar	18	5.083458	-1.356542	0.000501	6.228426E-06	2.907967E-06
K	19	3.745896	-1.334104	0.022939	3.084281E-07	1.440009E-07
Ca	20	4.930061	-1.359939	-0.002896	4.831469E-06	2.255746E-06
Sc	21	1.867471	-1.182529	0.174514	4.691154E-09	2.190235E-09
Ti	22	3.559844	-1.350156	0.006887	2.462338E-07	1.149632E-07
V	23	2.598662	-1.361338	-0.004295	2.863051E-08	1.336719E-08
Cr	24	4.264119	-1.375881	-0.018838	1.355579E-06	6.329011E-07
Mn	25	4.119945	-1.360055	-0.003012	1.025426E-06	4.787572E-07
Fe	26	6.182957	-1.357043	0.000000	1.205910E-04	5.630229E-05
Co	27	3.857755	-1.012245	0.344798	6.014555E-07	2.808113E-07
Ni	28	4.894896	-1.305104	0.051939	6.570881E-06	3.067854E-06
Cu	29	3.401495	-0.848505	0.508538	2.264558E-07	1.057291E-07
Zn	30	3.445096	-1.184904	0.172139	2.602543E-07	1.215092E-07
Ga	31	2.236802	-0.843198	0.513845	1.705005E-08	7.960434E-09
Ge	32	2.671387	-0.908613	0.448430	4.794506E-08	2.238489E-08
As	33	1.264318	-1.035682	0.321361	1.949736E-09	9.103049E-10
Se	34	2.505273	-0.834727	0.522316	3.558474E-08	1.661403E-08
Br	35	1.459469	-1.080531	0.276512	3.274000E-09	1.528586E-09
Kr	36	2.534517	-0.715483	0.641561	4.091023E-08	1.910043E-08
Rb	37	1.892265	-0.627735	0.729308	9.497048E-09	4.434042E-09
Sr	38	2.052844	-0.827156	0.529887	1.400024E-08	6.536518E-09
Y	39	1.318929	-0.891071	0.465972	2.623707E-09	1.224973E-09
Zr	40	1.587698	-0.942302	0.414741	5.028441E-09	2.347710E-09
Nb	41	0.386429	-1.023571	0.333472	3.202642E-10	1.495270E-10
Mo	42	0.735954	-1.204046	0.152997	7.431075E-10	3.469467E-10

Table A.3 Yields for 3 M$_\odot$, Z = 0.0006, Y = 0.30, no PMZ. (continued)

El	Z	log ϵ(X)	[X/H]	[X/Fe]	M$_{yield}$	X$_{yield}$
Ru	44	0.452649	-1.307351	0.049692	4.046297E-10	1.889161E-10
Rh	45	-0.249611	-1.309611	0.047432	8.200158E-11	3.828542E-11
Pd	46	0.384062	-1.265938	0.091105	3.633255E-10	1.696317E-10
Ag	47	-0.104896	-1.304896	0.052147	1.199758E-10	5.601507E-11
Cd	48	0.463480	-1.246520	0.110523	4.617734E-10	2.155957E-10
In	49	-0.529045	-1.289045	0.067998	4.811159E-11	2.246264E-11
Sn	50	0.796619	-1.273381	0.083662	1.048527E-09	4.895430E-10
Sb	51	-0.520726	-1.530726	-0.173683	5.160078E-11	2.409170E-11
Te	52	0.450352	-1.729648	-0.372605	4.988755E-10	2.329182E-10
I	53	0.193184	-1.356816	0.000227	2.802747E-10	1.308564E-10
Xe	54	0.893630	-1.346370	0.010673	1.450456E-09	6.771982E-10
Cs	55	-0.252300	-1.332300	0.024743	1.052320E-10	4.913139E-11
Ba	56	0.965007	-1.214993	0.142050	1.792695E-09	8.369847E-10
La	57	-0.115302	-1.285302	0.071741	1.507681E-10	7.039154E-11
Ce	58	0.287077	-1.292923	0.064120	3.841690E-10	1.793632E-10
Pr	59	-0.562452	-1.322452	0.034591	5.462150E-11	2.550203E-11
Nd	60	0.100677	-1.349323	0.007720	2.567826E-10	1.198883E-10
Sm	62	-0.526653	-1.466653	-0.109610	6.293497E-11	2.938347E-11
Eu	63	-0.852131	-1.362131	-0.005088	3.022974E-11	1.411385E-11
Gd	64	-0.408505	-1.458505	-0.101461	8.646939E-11	4.037137E-11
Tb	65	-1.039908	-1.359908	-0.002865	2.051569E-11	9.578492E-12
Dy	66	-0.223459	-1.353459	0.003584	1.374730E-10	6.418424E-11
Ho	67	-0.891257	-1.361257	-0.004214	2.997941E-11	1.399697E-11
Er	68	-0.438995	-1.358995	-0.001952	8.616797E-11	4.023065E-11
Tm	69	-1.236156	-1.356156	0.000887	1.387802E-11	6.479458E-12
Yb	70	-0.470496	-1.390496	-0.033453	8.268187E-11	3.860303E-11
Lu	71	-1.252117	-1.342117	0.014926	1.385614E-11	6.469244E-12
Hf	72	-0.615604	-1.325604	0.031439	6.121802E-11	2.858185E-11
Ta	73	-1.455848	-1.335848	0.021195	8.962447E-12	4.184444E-12
W	74	-0.674282	-1.324282	0.032761	5.506723E-11	2.571013E-11
Re	75	-1.095564	-1.355564	0.001479	2.114358E-11	9.871649E-12
Os	76	-0.009442	-1.359442	-0.002399	2.633371E-10	1.229485E-10
Ir	77	-0.045628	-1.365628	-0.008585	2.448176E-10	1.143020E-10
Pt	78	0.226113	-1.393887	-0.036844	4.639862E-10	2.166288E-10
Au	79	-0.561252	-1.361252	-0.004209	7.652633E-11	3.572909E-11
Hg	80	-0.182674	-1.352674	0.004369	1.861218E-10	8.689771E-11
Tl	81	-0.530150	-1.300150	0.056893	8.529841E-11	3.982466E-11
Pb	82	0.711863	-1.328137	0.028906	1.510533E-09	7.052471E-10
Bi	83	-0.690101	-1.340101	0.016942	6.034505E-11	2.817428E-11

Table A.4   Yields for 3 $M_\odot$, $Z = 0.0006$, $Y = 0.30$, $M_{pmz} = 0.001$

El	Z	$\log \epsilon(X)$	[X/H]	[X/Fe]	M_{yield}	X_{yield}
H	1	12.000000	0.000000	1.359448	1.414538E+00	6.604286E-01
He	2	11.097456	0.167456	1.526904	7.081342E-01	3.306182E-01
C	6	8.893051	0.423051	1.782499	1.341418E-02	6.262895E-03
N	7	7.980431	0.110431	1.469879	1.893103E-03	8.838639E-04
O	8	7.686088	-1.043912	0.315537	1.098727E-03	5.129804E-04
F	9	4.836002	0.416002	1.775450	1.842343E-06	8.601646E-07
Ne	10	7.853082	-0.116918	1.242530	2.203909E-03	1.028975E-03
Na	11	5.968521	-0.271479	1.087969	3.025959E-05	1.412779E-05
Mg	12	6.894356	-0.745644	0.613804	2.792229E-04	1.303654E-04
Al	13	5.369092	-1.080908	0.278540	8.934508E-06	4.171399E-06
Si	14	6.275351	-1.274649	0.084799	7.510142E-05	3.506382E-05
P	15	4.636902	-0.773098	0.586350	1.900547E-06	8.873392E-07
S	16	5.818031	-1.331969	0.027479	2.990590E-05	1.396266E-05
Cl	17	3.928785	-1.301215	0.058233	4.274854E-07	1.995871E-07
Ar	18	5.082448	-1.357552	0.001896	6.215624E-06	2.901990E-06
K	19	3.750130	-1.329870	0.029578	3.114792E-07	1.454254E-07
Ca	20	4.928399	-1.361601	-0.002153	4.814235E-06	2.247700E-06
Sc	21	1.929293	-1.120707	0.238741	5.409042E-09	2.525407E-09
Ti	22	3.574204	-1.335796	0.023652	2.548001E-07	1.189627E-07
V	23	2.605912	-1.354088	0.005360	2.911368E-08	1.359278E-08
Cr	24	4.263396	-1.376604	-0.017155	1.353446E-06	6.319054E-07
Mn	25	4.115531	-1.364469	-0.005021	1.015099E-06	4.739357E-07
Fe	26	6.180552	-1.359448	0.000000	1.199339E-04	5.599551E-05
Co	27	3.841338	-1.028662	0.330786	5.791680E-07	2.704056E-07
Ni	28	4.904292	-1.295708	0.063740	6.723968E-06	3.139329E-06
Cu	29	3.472839	-0.777161	0.582287	2.668764E-07	1.246009E-07
Zn	30	3.486492	-1.143508	0.215940	2.867570E-07	1.338829E-07
Ga	31	2.333547	-0.746453	0.612995	2.131192E-08	9.950241E-09
Ge	32	2.779273	-0.800727	0.558721	6.148472E-08	2.870637E-08
As	33	1.362264	-0.937736	0.421712	2.443091E-09	1.140646E-09
Se	34	2.667786	-0.672214	0.687234	5.176112E-08	2.416656E-08
Br	35	1.612501	-0.927499	0.431950	4.659883E-09	2.175636E-09
Kr	36	3.141195	-0.108805	1.250643	1.671499E-07	7.803999E-08
Rb	37	2.403016	-0.116984	1.242464	3.092566E-08	1.443877E-08
Sr	38	2.734540	-0.145460	1.213988	6.742909E-08	3.148172E-08
Y	39	2.164027	-0.045973	1.313475	1.836673E-08	8.575174E-09
Zr	40	2.641677	0.111677	1.471125	5.753466E-08	2.686214E-08
Nb	41	1.376151	-0.033849	1.325599	3.127871E-09	1.460360E-09
Mo	42	1.822186	-0.117814	1.241634	9.092820E-09	4.245313E-09

Table A.4 Yields for 3 M$_\odot$, Z = 0.0006, Y = 0.30, M$_{pmz}$ = 0.001 (continued)

El	Z	log ϵ(X)	[X/H]	[X/Fe]	M$_{yield}$	X$_{yield}$
Ru	44	1.512857	-0.247143	1.112305	4.647626E-09	2.169913E-09
Rh	45	0.435036	-0.624964	0.734484	3.967238E-10	1.852249E-10
Pd	46	1.431038	-0.218962	1.140487	4.048994E-09	1.890420E-09
Ag	47	0.636337	-0.563663	0.795785	6.622680E-10	3.092039E-10
Cd	48	1.562977	-0.147023	1.212425	5.808432E-09	2.711877E-09
In	49	0.427288	-0.332712	1.026736	4.351115E-10	2.031476E-10
Sn	50	2.024904	-0.045096	1.314352	1.775772E-08	8.290836E-09
Sb	51	0.530917	-0.479083	0.880365	5.811880E-10	2.713487E-10
Te	52	1.638928	-0.541072	0.818376	7.684299E-09	3.587694E-09
I	53	0.615585	-0.934415	0.425034	7.413169E-10	3.461107E-10
Xe	54	1.925263	-0.314737	1.044711	1.569430E-08	7.327452E-09
Cs	55	0.596754	-0.483246	0.876203	7.433970E-10	3.470819E-10
Ba	56	2.714291	0.534291	1.893739	1.008165E-07	4.706985E-08
La	57	1.655318	0.485318	1.844766	8.890930E-09	4.151053E-09
Ce	58	2.205704	0.625704	1.985152	3.186994E-08	1.487964E-08
Pr	59	1.148563	0.388563	1.748011	2.807998E-09	1.311016E-09
Nd	60	1.888368	0.438368	1.797816	1.573185E-08	7.344985E-09
Sm	62	1.146874	0.206874	1.566323	2.962670E-09	1.383230E-09
Eu	63	0.094776	-0.415224	0.944224	2.675213E-10	1.249020E-10
Gd	64	0.997927	-0.052073	1.307375	2.208837E-09	1.031276E-09
Tb	65	0.051594	-0.268406	1.091042	2.532827E-10	1.182542E-10
Dy	66	1.151422	0.021422	1.380870	3.262469E-09	1.523202E-09
Ho	67	0.126148	-0.343852	1.015596	3.120662E-10	1.456994E-10
Er	68	0.979690	0.059690	1.419138	2.262068E-09	1.056128E-09
Tm	69	0.041790	-0.078210	1.281238	2.632035E-10	1.228861E-10
Yb	70	1.319969	0.399969	1.759417	5.109558E-09	2.385582E-09
Lu	71	0.384734	0.294734	1.654182	6.017596E-10	2.809533E-10
Hf	72	1.254136	0.544136	1.903584	4.549185E-09	2.123952E-09
Ta	73	0.300600	0.420600	1.780048	5.115564E-10	2.388387E-10
W	74	1.232622	0.582622	1.942070	4.445717E-09	2.075644E-09
Re	75	0.311140	0.051140	1.410588	5.380538E-10	2.512099E-10
Os	76	1.183811	-0.166189	1.193259	4.080830E-09	1.905283E-09
Ir	77	0.527632	-0.792368	0.567080	9.158962E-10	4.276194E-10
Pt	78	1.243622	-0.376378	0.983070	4.832491E-09	2.256224E-09
Au	79	0.462310	-0.337690	1.021758	8.079621E-10	3.772264E-10
Hg	80	1.719181	0.549181	1.908629	1.485377E-08	6.935024E-09
Tl	81	1.560733	0.790733	2.150182	1.051569E-08	4.909632E-09
Pb	82	3.428173	1.388173	2.747621	7.871670E-07	3.675175E-07
Bi	83	2.084380	1.434380	2.793828	3.590386E-08	1.676302E-08

Table A.5 Yields for 3 M$_\odot$, $Z = 0.0006$, $Y = 0.35$, no PMZ.

El	Z	log ϵ(X)	[X/H]	[X/Fe]	M$_{yield}$	X$_{yield}$
H	1	12.000000	0.000000	1.312702	1.267917E+00	5.981164E-01
He	2	11.217161	0.287161	1.599863	8.361969E-01	3.944606E-01
C	6	8.685904	0.215904	1.528606	7.485882E-03	3.531328E-03
N	7	8.581932	0.711932	2.024634	6.778775E-03	3.197763E-03
O	8	7.560924	-1.169076	0.143626	7.381979E-04	3.482313E-04
F	9	4.342472	-0.077528	1.235174	5.300489E-07	2.500408E-07
Ne	10	7.156570	-0.813430	0.499272	3.891324E-04	1.835661E-04
Na	11	5.497265	-0.742735	0.569967	9.163964E-06	4.322932E-06
Mg	12	6.470995	-1.169005	0.143697	9.245879E-05	4.361574E-05
Al	13	5.239390	-1.210610	0.102092	5.940791E-06	2.802460E-06
Si	14	6.259926	-1.290074	0.022628	6.486730E-05	3.059996E-05
P	15	4.178746	-1.231254	0.081448	5.931960E-07	2.798294E-07
S	16	5.848366	-1.301634	0.011069	2.870488E-05	1.354100E-05
Cl	17	3.945174	-1.284826	0.027876	3.975802E-07	1.875512E-07
Ar	18	5.127579	-1.312421	0.000282	6.178715E-06	2.914696E-06
K	19	3.782802	-1.297198	0.015504	3.009748E-07	1.419793E-07
Ca	20	4.975237	-1.314763	-0.002060	4.805229E-06	2.266779E-06
Sc	21	1.858520	-1.191480	0.121222	4.119299E-09	1.943204E-09
Ti	22	3.602256	-1.307744	0.004958	2.433093E-07	1.147767E-07
V	23	2.643385	-1.316615	-0.003913	2.844759E-08	1.341963E-08
Cr	24	4.308530	-1.331470	-0.018768	1.345828E-06	6.348697E-07
Mn	25	4.165627	-1.314373	-0.001671	1.021128E-06	4.816983E-07
Fe	26	6.227298	-1.312702	0.000000	1.196910E-04	5.646202E-05
Co	27	3.829520	-1.040480	0.272222	5.051997E-07	2.383187E-07
Ni	28	4.923890	-1.276110	0.036592	6.284337E-06	2.964521E-06
Cu	29	3.337981	-0.912019	0.400683	1.754013E-07	8.274235E-08
Zn	30	3.440729	-1.189271	0.123431	2.304844E-07	1.087268E-07
Ga	31	2.174843	-0.905157	0.407545	1.325033E-08	6.250602E-09
Ge	32	2.613090	-0.966910	0.345792	3.758959E-08	1.773220E-08
As	33	1.229067	-1.070933	0.241770	1.611459E-09	7.601765E-10
Se	34	2.432770	-0.907230	0.405472	2.700013E-08	1.273682E-08
Br	35	1.422714	-1.117286	0.195416	2.694778E-09	1.271212E-09
Kr	36	2.444997	-0.805003	0.507699	2.981474E-08	1.406456E-08
Rb	37	1.785371	-0.734629	0.578073	6.650755E-09	3.137372E-09
Sr	38	1.985733	-0.894267	0.418436	1.075417E-08	5.073083E-09
Y	39	1.261836	-0.948164	0.364538	2.062133E-09	9.727735E-10
Zr	40	1.535504	-0.994496	0.318207	3.992464E-09	1.883372E-09
Nb	41	0.349521	-1.060479	0.252224	2.636909E-10	1.243913E-10
Mo	42	0.712124	-1.227876	0.084826	6.303629E-10	2.973622E-10

Table A.5 Yields for 3 M$_\odot$, $Z = 0.0006$, $Y = 0.35$, no PMZ. (continued)

El	Z	log ϵ(X)	[X/H]	[X/Fe]	M$_{yield}$	X$_{yield}$
Ru	44	0.452006	-1.307994	0.004708	3.621891E-10	1.708561E-10
Rh	45	-0.219029	-1.279029	0.033673	7.886758E-11	3.720434E-11
Pd	46	0.388509	-1.261491	0.051211	3.290331E-10	1.552153E-10
Ag	47	-0.076360	-1.276360	0.036343	1.148391E-10	5.417326E-11
Cd	48	0.464806	-1.245194	0.067508	4.151960E-10	1.958611E-10
In	49	-0.512141	-1.272141	0.040561	4.483808E-11	2.115154E-11
Sn	50	0.797905	-1.272095	0.040607	9.427499E-10	4.447250E-10
Sb	51	-0.497442	-1.507442	-0.194740	4.880157E-11	2.302125E-11
Te	52	0.468155	-1.711845	-0.399143	4.659980E-10	2.198260E-10
I	53	0.236754	-1.313246	-0.000544	2.777466E-10	1.310219E-10
Xe	54	0.922724	-1.317276	-0.004574	1.389807E-09	6.556159E-10
Cs	55	-0.214699	-1.294699	0.018003	1.028592E-10	4.852195E-11
Ba	56	0.966841	-1.213159	0.099543	1.613916E-09	7.613355E-10
La	57	-0.093136	-1.263136	0.049566	1.422229E-10	6.709104E-11
Ce	58	0.310251	-1.269749	0.042953	3.632227E-10	1.713437E-10
Pr	59	-0.529875	-1.289875	0.022827	5.277583E-11	2.489603E-11
Nd	60	0.134812	-1.315188	-0.002486	2.490014E-10	1.174618E-10
Sm	62	-0.489603	-1.429603	-0.116901	6.144022E-11	2.898330E-11
Eu	63	-0.807262	-1.317262	-0.004560	3.004675E-11	1.417401E-11
Gd	64	-0.367108	-1.417108	-0.104406	8.525951E-11	4.021961E-11
Tb	65	-0.995737	-1.315737	-0.003035	2.035875E-11	9.603869E-12
Dy	66	-0.181470	-1.311470	0.001233	1.357367E-10	6.403130E-11
Ho	67	-0.846573	-1.316573	-0.003871	2.978524E-11	1.405064E-11
Er	68	-0.397391	-1.317391	-0.004689	8.500374E-11	4.009896E-11
Tm	69	-1.192884	-1.312884	-0.000182	1.374338E-11	6.483188E-12
Yb	70	-0.435713	-1.355713	-0.043011	8.029274E-11	3.787663E-11
Lu	71	-1.213344	-1.303344	0.009358	1.357978E-11	6.406011E-12
Hf	72	-0.581763	-1.291763	0.020939	5.931670E-11	2.798156E-11
Ta	73	-1.418758	-1.298758	0.013944	8.750061E-12	4.127681E-12
W	74	-0.640436	-1.290436	0.022266	5.336195E-11	2.517252E-11
Re	75	-1.052396	-1.312396	0.000306	2.093388E-11	9.875172E-12
Os	76	0.034677	-1.315323	-0.002621	2.613028E-10	1.232648E-10
Ir	77	0.000444	-1.319556	-0.006854	2.440111E-10	1.151078E-10
Pt	78	0.270986	-1.349014	-0.036312	4.611817E-10	2.175540E-10
Au	79	-0.516353	-1.316353	-0.003651	7.606834E-11	3.588384E-11
Hg	80	-0.147444	-1.317444	-0.004742	1.809349E-10	8.535274E-11
Tl	81	-0.499629	-1.269629	0.043073	8.202710E-11	3.869478E-11
Pb	82	0.746388	-1.293612	0.019090	1.466060E-09	6.915869E-10
Bi	83	-0.652267	-1.302267	0.010435	5.901597E-11	2.783970E-11

Table A.6 Yields for 3 M$_\odot$, Z = 0.0006, Y = 0.35, M$_{pmz}$ = 0.001

El	Z	log ϵ(X)	[X/H]	[X/Fe]	M$_{yield}$	X$_{yield}$
H	1	12.000000	0.000000	1.314984	1.268083E+00	5.981951E-01
He	2	11.216942	0.286942	1.601925	8.358837E-01	3.943128E-01
C	6	8.626678	0.156678	1.471661	6.531494E-03	3.081113E-03
N	7	8.512595	0.642595	1.957578	5.779242E-03	2.726252E-03
O	8	7.710231	-1.019769	0.295215	1.041197E-03	4.911656E-04
F	9	4.756593	0.336593	1.651576	1.375606E-06	6.489167E-07
Ne	10	7.859528	-0.110472	1.204512	2.004894E-03	9.457722E-04
Na	11	6.008362	-0.231638	1.083346	2.973295E-05	1.402597E-05
Mg	12	6.875231	-0.764769	0.550215	2.390336E-04	1.127597E-04
Al	13	5.378504	-1.071496	0.243488	8.184942E-06	3.861096E-06
Si	14	6.309031	-1.240969	0.074014	7.273690E-05	3.431230E-05
P	15	4.693383	-0.716617	0.598367	1.940405E-06	9.153507E-07
S	16	5.864770	-1.285230	0.029754	2.986153E-05	1.408663E-05
Cl	17	3.970568	-1.259432	0.055552	4.217206E-07	1.989390E-07
Ar	18	5.126850	-1.313150	0.001834	6.170666E-06	2.910899E-06
K	19	3.787537	-1.292463	0.022521	3.043397E-07	1.435667E-07
Ca	20	4.973865	-1.316135	-0.001152	4.791866E-06	2.260475E-06
Sc	21	1.935365	-1.114635	0.200349	4.917287E-09	2.319640E-09
Ti	22	3.619788	-1.290212	0.024772	2.537073E-07	1.196818E-07
V	23	2.652478	-1.307522	0.007462	2.905335E-08	1.370539E-08
Cr	24	4.308362	-1.331638	-0.016654	1.345567E-06	6.347464E-07
Mn	25	4.161495	-1.318505	-0.003521	1.011593E-06	4.772006E-07
Fe	26	6.225016	-1.314984	0.000000	1.190819E-04	5.617472E-05
Co	27	3.819909	-1.050091	0.264893	4.942072E-07	2.331332E-07
Ni	28	4.931420	-1.268580	0.046404	6.402458E-06	3.020242E-06
Cu	29	3.407964	-0.842036	0.472948	2.060970E-07	9.722247E-08
Zn	30	3.484192	-1.145808	0.169176	2.552811E-07	1.204242E-07
Ga	31	2.297824	-0.782176	0.532808	1.759793E-08	8.301500E-09
Ge	32	2.755034	-0.824966	0.490018	5.215020E-08	2.460090E-08
As	33	1.355633	-0.944367	0.370617	2.156960E-09	1.017506E-09
Se	34	2.655264	-0.684736	0.630248	4.509619E-08	2.127330E-08
Br	35	1.602846	-0.937154	0.377830	4.086761E-09	1.927855E-09
Kr	36	3.166578	-0.083422	1.231562	1.589312E-07	7.497290E-08
Rb	37	2.414969	-0.105031	1.209953	2.850110E-08	1.344487E-08
Sr	38	2.761311	-0.118689	1.196295	6.429583E-08	3.033038E-08
Y	39	2.192906	-0.017094	1.297890	1.759720E-08	8.301159E-09
Zr	40	2.665293	0.135293	1.450277	5.443612E-08	2.567924E-08
Nb	41	1.402835	-0.007165	1.307819	2.981710E-09	1.406567E-09
Mo	42	1.850857	-0.089143	1.225841	8.708171E-09	4.107920E-09

Table A.6 Yields for 3 M$_\odot$, $Z = 0.0006$, $Y = 0.35$, M$_{pmz} = 0.001$ (continued)

El	Z	log ϵ(X)	[X/H]	[X/Fe]	M$_{yield}$	X$_{yield}$
Ru	44	1.552687	-0.207313	1.107671	4.566852E-09	2.154329E-09
Rh	45	0.477664	-0.582336	0.732648	3.923280E-10	1.850736E-10
Pd	46	1.473880	-0.176120	1.138864	4.006092E-09	1.889801E-09
Ag	47	0.679394	-0.520606	0.794378	6.555730E-10	3.092546E-10
Cd	48	1.603828	-0.106172	1.208812	5.720456E-09	2.698520E-09
In	49	0.467071	-0.292929	1.022055	4.274809E-10	2.016563E-10
Sn	50	2.065385	-0.004615	1.310369	1.747536E-08	8.243679E-09
Sb	51	0.574431	-0.435569	0.879415	5.759228E-10	2.716811E-10
Te	52	1.685423	-0.494577	0.820406	7.667413E-09	3.616962E-09
I	53	0.663225	-0.886775	0.428209	7.416118E-10	3.498418E-10
Xe	54	1.954949	-0.285051	1.029933	1.505249E-08	7.100735E-09
Cs	55	0.650016	-0.429984	0.885000	7.533829E-10	3.553946E-10
Ba	56	2.758313	0.578313	1.893297	1.000315E-07	4.718805E-08
La	57	1.709477	0.539477	1.854461	9.028997E-09	4.259264E-09
Ce	58	2.249937	0.669937	1.984921	3.162767E-08	1.491977E-08
Pr	59	1.195288	0.435288	1.750272	2.803208E-09	1.322362E-09
Nd	60	1.944206	0.494206	1.809190	1.603358E-08	7.563548E-09
Sm	62	1.191087	0.251087	1.566071	2.940520E-09	1.387136E-09
Eu	63	0.138257	-0.371743	0.943241	2.650753E-10	1.250444E-10
Gd	64	1.039276	-0.010724	1.304260	2.177909E-09	1.027389E-09
Tb	65	0.093020	-0.226980	1.088004	2.497841E-10	1.178311E-10
Dy	66	1.194016	0.064016	1.379000	3.226120E-09	1.521863E-09
Ho	67	0.170003	-0.299997	1.014987	3.094814E-10	1.459922E-10
Er	68	1.023661	0.103661	1.418645	2.243911E-09	1.058524E-09
Tm	69	0.092775	-0.027225	1.287759	2.653444E-10	1.251714E-10
Yb	70	1.358474	0.438474	1.753458	5.005238E-09	2.361129E-09
Lu	71	0.424464	0.334464	1.649448	5.911342E-10	2.788567E-10
Hf	72	1.296126	0.586126	1.901110	4.492191E-09	2.119109E-09
Ta	73	0.343472	0.463472	1.778456	5.061720E-10	2.387774E-10
W	74	1.278924	0.628924	1.943908	4.434130E-09	2.091719E-09
Re	75	0.367942	0.107942	1.422926	5.496932E-10	2.593077E-10
Os	76	1.223945	-0.126055	1.188929	4.013161E-09	1.893135E-09
Ir	77	0.573262	-0.746738	0.568246	9.120509E-10	4.302433E-10
Pt	78	1.282684	-0.337316	0.977668	4.740216E-09	2.236110E-09
Au	79	0.504262	-0.295738	1.019246	7.977675E-10	3.763322E-10
Hg	80	1.763325	0.593325	1.908309	1.474072E-08	6.953667E-09
Tl	81	1.604304	0.834304	2.149287	1.042178E-08	4.916285E-09
Pb	82	3.440638	1.400638	2.715622	7.260989E-07	3.425239E-07
Bi	83	2.081955	1.431955	2.746938	3.200727E-08	1.509884E-08

Table A.7 Yields for 3 M$_\odot$, $Z = 0.0006$, $Y = 0.40$, no PMZ.

El	Z	log ϵ(X)	[X/H]	[X/Fe]	M$_{yield}$	X$_{yield}$
H	1	12.000000	0.000000	1.253639	1.085439E+00	5.203824E-01
He	2	11.353737	0.423737	1.677375	9.803972E-01	4.700231E-01
C	6	8.288524	-0.181476	1.072163	2.552265E-03	1.223609E-03
N	7	9.019518	1.149518	2.403157	1.589471E-02	7.620256E-03
O	8	7.591214	-1.138786	0.114853	6.776478E-04	3.248786E-04
F	9	3.956202	-0.463798	0.789841	1.864494E-07	8.938775E-08
Ne	10	7.349891	-0.620109	0.633530	5.235993E-04	2.510245E-04
Na	11	5.724956	-0.515044	0.738595	1.325225E-05	6.353408E-06
Mg	12	6.613291	-1.026709	0.226930	1.106874E-04	5.306587E-05
Al	13	5.405767	-1.044233	0.209406	7.459953E-06	3.576459E-06
Si	14	6.326516	-1.223484	0.030154	6.474732E-05	3.104123E-05
P	15	4.287417	-1.122583	0.131056	6.522054E-07	3.126810E-07
S	16	5.908183	-1.241817	0.011822	2.820410E-05	1.352164E-05
Cl	17	4.011483	-1.218517	0.035121	3.967388E-07	1.902050E-07
Ar	18	5.187192	-1.252808	0.000831	6.068725E-06	2.909475E-06
K	19	3.847461	-1.232539	0.021100	2.990338E-07	1.433631E-07
Ca	20	5.034083	-1.255917	-0.002279	4.710890E-06	2.258500E-06
Sc	21	1.951282	-1.098718	0.154921	4.366166E-09	2.093232E-09
Ti	22	3.664372	-1.245628	0.008011	2.403753E-07	1.152410E-07
V	23	2.703147	-1.256853	-0.003214	2.794622E-08	1.339801E-08
Cr	24	4.367899	-1.272101	-0.018462	1.320992E-06	6.333113E-07
Mn	25	4.223592	-1.256408	-0.002769	9.989878E-07	4.789358E-07
Fe	26	6.286361	-1.253639	0.000000	1.174024E-04	5.628516E-05
Co	27	3.927309	-0.942691	0.310948	5.417104E-07	2.597074E-07
Ni	28	4.998898	-1.201102	0.052536	6.407556E-06	3.071917E-06
Cu	29	3.516637	-0.733363	0.520276	2.266119E-07	1.086425E-07
Zn	30	3.574252	-1.055748	0.197890	2.691549E-07	1.290385E-07
Ga	31	2.408399	-0.671601	0.582038	1.942905E-08	9.314697E-09
Ge	32	2.850970	-0.729030	0.524608	5.563876E-08	2.667440E-08
As	33	1.432700	-0.867300	0.386339	2.204787E-09	1.057021E-09
Se	34	2.704626	-0.635374	0.618265	4.321477E-08	2.071807E-08
Br	35	1.621908	-0.918092	0.335547	3.656183E-09	1.752851E-09
Kr	36	2.781224	-0.468776	0.784863	5.548883E-08	2.660251E-08
Rb	37	2.128886	-0.391114	0.862525	1.257065E-08	6.026634E-09
Sr	38	2.327388	-0.552612	0.701026	2.022085E-08	9.694301E-09
Y	39	1.609737	-0.600263	0.653375	3.933073E-09	1.885598E-09
Zr	40	1.884683	-0.645317	0.608322	7.656954E-09	3.670905E-09
Nb	41	0.667657	-0.742343	0.511295	4.696185E-10	2.251450E-10
Mo	42	1.014158	-0.925842	0.327797	1.083052E-09	5.192378E-10

Table A.7 Yields for 3 M$_\odot$, Z = 0.0006, Y = 0.40, no PMZ. (continued)

El	Z	log ϵ(X)	[X/H]	[X/Fe]	M$_{yield}$	X$_{yield}$
Ru	44	0.712566	-1.047434	0.206204	5.648639E-10	2.708076E-10
Rh	45	-0.083102	-1.143102	0.110537	9.232961E-11	4.426476E-11
Pd	46	0.628499	-1.021501	0.232138	4.894334E-10	2.346447E-10
Ag	47	0.065182	-1.134818	0.118821	1.362332E-10	6.531307E-11
Cd	48	0.702376	-1.007624	0.246015	6.141410E-10	2.944321E-10
In	49	-0.334738	-1.094738	0.158901	5.775182E-11	2.768744E-11
Sn	50	1.029703	-1.040297	0.213341	1.376077E-09	6.597203E-10
Sb	51	-0.338797	-1.348797	-0.095159	6.019958E-11	2.886095E-11
Te	52	0.655013	-1.524987	-0.271348	6.129411E-10	2.938569E-10
I	53	0.310154	-1.239846	0.013793	2.815553E-10	1.349835E-10
Xe	54	1.050206	-1.189794	0.063844	1.596625E-09	7.654557E-10
Cs	55	-0.107903	-1.187903	0.065736	1.126042E-10	5.398483E-11
Ba	56	1.191333	-0.988667	0.264971	2.316142E-09	1.110407E-09
La	57	0.071081	-1.098919	0.154720	1.777058E-10	8.519591E-11
Ce	58	0.465671	-1.114329	0.139310	4.447486E-10	2.132219E-10
Pr	59	-0.411054	-1.171054	0.082585	5.939787E-11	2.847659E-11
Nd	60	0.253925	-1.196075	0.057563	2.803584E-10	1.344097E-10
Sm	62	-0.390370	-1.330370	-0.076731	6.608887E-11	3.168440E-11
Eu	63	-0.742317	-1.252317	0.001322	2.987163E-11	1.432109E-11
Gd	64	-0.287643	-1.337643	-0.084004	8.765193E-11	4.202218E-11
Tb	65	-0.927842	-1.247842	0.005796	2.037794E-11	9.769612E-12
Dy	66	-0.104452	-1.234452	0.019187	1.387543E-10	6.652171E-11
Ho	67	-0.780677	-1.250677	0.002962	2.967649E-11	1.422753E-11
Er	68	-0.318932	-1.238932	0.014707	8.718345E-11	4.179758E-11
Tm	69	-1.119940	-1.239940	0.013699	1.391722E-11	6.672210E-12
Yb	70	-0.333375	-1.253375	0.000263	8.701048E-11	4.171465E-11
Lu	71	-1.124822	-1.214822	0.038817	1.425589E-11	6.834575E-12
Hf	72	-0.473993	-1.183993	0.069645	6.510313E-11	3.121181E-11
Ta	73	-1.322997	-1.202997	0.050641	9.338705E-12	4.477172E-12
W	74	-0.531014	-1.181014	0.072625	5.877430E-11	2.817764E-11
Re	75	-0.977164	-1.237164	0.016475	2.130839E-11	1.021569E-11
Os	76	0.101795	-1.248205	0.005434	2.610439E-10	1.251499E-10
Ir	77	0.060310	-1.259690	-0.006051	2.397668E-10	1.149492E-10
Pt	78	0.334435	-1.285565	-0.031926	4.569169E-10	2.190556E-10
Au	79	-0.453046	-1.253046	0.000592	7.533995E-11	3.611956E-11
Hg	80	-0.051467	-1.221467	0.032172	1.932041E-10	9.262612E-11
Tl	81	-0.391012	-1.161012	0.092626	9.017350E-11	4.323108E-11
Pb	82	0.828631	-1.211369	0.042270	1.516663E-09	7.271200E-10
Bi	83	-0.581419	-1.231419	0.022220	5.947482E-11	2.851348E-11

Table A.8 Yields for 3 M$_\odot$, $Z = 0.0006$, $Y = 0.40$, M$_{pmz} = 0.001$

El	Z	log ϵ(X)	[X/H]	[X/Fe]	M$_{yield}$	X$_{yield}$
H	1	12.000000	0.000000	1.256334	1.086373E+00	5.208300E-01
He	2	11.352899	0.422899	1.679234	9.793506E-01	4.695213E-01
C	6	8.217354	-0.252646	1.003688	2.168554E-03	1.039650E-03
N	7	8.941731	1.071731	2.328066	1.329961E-02	6.376113E-03
O	8	7.832737	-0.897263	0.359071	1.182765E-03	5.670426E-04
F	9	4.304199	-0.115801	1.140533	4.158450E-07	1.993648E-07
Ne	10	8.069542	0.099542	1.355876	2.788122E-03	1.336685E-03
Na	11	6.339763	0.099763	1.356097	5.463485E-05	2.619310E-05
Mg	12	7.107039	-0.532961	0.723373	3.513975E-04	1.684674E-04
Al	13	5.753280	-0.696720	0.559614	1.661969E-05	7.967829E-06
Si	14	6.427428	-1.122572	0.133762	8.199601E-05	3.931061E-05
P	15	5.153914	-0.256086	1.000248	4.800144E-06	2.301290E-06
S	16	5.991575	-1.158425	0.097909	3.453639E-05	1.655747E-05
Cl	17	4.186172	-1.043828	0.212506	5.962409E-07	2.858504E-07
Ar	18	5.193871	-1.246129	0.010205	6.177450E-06	2.961600E-06
K	19	3.884479	-1.195521	0.060814	3.262015E-07	1.563879E-07
Ca	20	5.038651	-1.251349	0.004985	4.774923E-06	2.289199E-06
Sc	21	2.326511	-0.723489	0.532845	1.036817E-08	4.970721E-09
Ti	22	3.799469	-1.110531	0.145804	3.312448E-07	1.588057E-07
V	23	2.779955	-1.180045	0.076290	3.338140E-08	1.600374E-08
Cr	24	4.384964	-1.255036	0.001298	1.376074E-06	6.597189E-07
Mn	25	4.221370	-1.258630	-0.002296	9.947435E-07	4.769010E-07
Fe	26	6.283666	-1.256334	0.000000	1.167775E-04	5.598561E-05
Co	27	3.910997	-0.959003	0.297331	5.221890E-07	2.503484E-07
Ni	28	5.003248	-1.196752	0.059582	6.482558E-06	3.107875E-06
Cu	29	3.555529	-0.694471	0.561863	2.480348E-07	1.189131E-07
Zn	30	3.602533	-1.027467	0.228867	2.878701E-07	1.380110E-07
Ga	31	2.486247	-0.593753	0.662581	2.327103E-08	1.115662E-08
Ge	32	2.951875	-0.628125	0.628210	7.029950E-08	3.370306E-08
As	33	1.535615	-0.764385	0.491949	2.796761E-09	1.340826E-09
Se	34	2.880008	-0.459992	0.796342	6.482085E-08	3.107648E-08
Br	35	1.789265	-0.750735	0.505599	5.384649E-09	2.581514E-09
Kr	36	3.463956	0.213956	1.470290	2.702809E-07	1.295783E-07
Rb	37	2.711326	0.191326	1.447660	4.833980E-08	2.317512E-08
Sr	38	3.065683	0.185683	1.442017	1.110374E-07	5.323367E-08
Y	39	2.508756	0.298756	1.555090	3.119783E-08	1.495690E-08
Zr	40	2.999933	0.469933	1.726267	1.009154E-07	4.838099E-08
Nb	41	1.722840	0.312840	1.569174	5.337059E-09	2.558699E-09
Mo	42	2.186415	0.246415	1.502749	1.616023E-08	7.747555E-09

Table A.8 Yields for 3 M$_\odot$, $Z = 0.0006$, $Y = 0.40$, M$_{pmz} = 0.001$ (continued)

El	Z	log ϵ(X)	[X/H]	[X/Fe]	M$_{yield}$	X$_{yield}$
Ru	44	1.905040	0.145040	1.401374	8.807251E-09	4.222382E-09
Rh	45	0.804264	-0.255736	1.000598	7.129846E-10	3.418199E-10
Pd	46	1.833512	0.183512	1.439846	7.856028E-09	3.766345E-09
Ag	47	1.016306	-0.183694	1.072640	1.220217E-09	5.849976E-10
Cd	48	1.964189	0.254189	1.510524	1.123565E-08	5.386609E-09
In	49	0.815988	0.055988	1.312322	8.178337E-10	3.920867E-10
Sn	50	2.408951	0.338951	1.595285	3.301735E-08	1.582921E-08
Sb	51	0.903147	-0.106853	1.149481	1.051747E-09	5.042297E-10
Te	52	2.018478	-0.161522	1.094812	1.414169E-08	6.779824E-09
I	53	0.922179	-0.627821	0.628513	1.153352E-09	5.529412E-10
Xe	54	2.288997	0.048997	1.305331	2.784211E-08	1.334809E-08
Cs	55	0.977643	-0.102357	1.153977	1.372378E-09	6.579470E-10
Ba	56	3.121733	0.941733	2.198067	1.978693E-07	9.486272E-08
La	57	2.064211	0.894211	2.150545	1.750670E-08	8.393082E-09
Ce	58	2.600293	1.020293	2.276627	6.071126E-08	2.910626E-08
Pr	59	1.544944	0.784944	2.041278	5.372078E-09	2.575487E-09
Nd	60	2.292515	0.842515	2.098849	3.063591E-08	1.468750E-08
Sm	62	1.534964	0.594964	1.851298	5.561351E-09	2.666229E-09
Eu	63	0.467838	-0.042162	1.214172	4.850404E-10	2.325386E-10
Gd	64	1.384660	0.334660	1.590994	4.132963E-09	1.981429E-09
Tb	65	0.428927	0.108927	1.365261	4.637705E-10	2.223414E-10
Dy	66	1.536920	0.406920	1.663254	6.087297E-09	2.918379E-09
Ho	67	0.501629	0.031629	1.287963	5.689728E-10	2.727775E-10
Er	68	1.373941	0.453941	1.710275	4.307453E-09	2.065084E-09
Tm	69	0.444353	0.324353	1.580688	5.107626E-10	2.448703E-10
Yb	70	1.704027	0.784027	2.040361	9.501840E-09	4.555382E-09
Lu	71	0.767966	0.677966	1.934300	1.116939E-09	5.354841E-10
Hf	72	1.641635	0.931635	2.187969	8.527118E-09	4.088080E-09
Ta	73	0.689095	0.809095	2.065429	9.610649E-10	4.607548E-10
W	74	1.628876	0.978876	2.235210	8.505564E-09	4.077746E-09
Re	75	0.729896	0.469896	1.726230	1.083629E-09	5.195147E-10
Os	76	1.555973	0.205973	1.462307	7.385530E-09	3.540779E-09
Ir	77	0.864732	-0.455268	0.801066	1.528626E-09	7.328553E-10
Pt	78	1.602848	-0.017152	1.239182	8.488695E-09	4.069659E-09
Au	79	0.827996	0.027996	1.284330	1.440259E-09	6.904906E-10
Hg	80	2.102915	0.932915	2.189249	2.760165E-08	1.323281E-08
Tl	81	1.945387	1.175387	2.431722	1.958188E-08	9.387967E-09
Pb	82	3.919272	1.879272	3.135606	1.870662E-06	8.968346E-07
Bi	83	2.585949	1.935949	3.192283	8.751328E-08	4.195571E-08

Table A.9 Yields for 4 M$_\odot$, Z = 0.0006, Y = 0.24

El	Z	$\log \epsilon(X)$	[X/H]	[X/Fe]	M$_{yield}$	X$_{yield}$
H	1	12.000000	0.000000	1.351376	1.955674E+00	6.280669E-01
He	2	11.139062	0.209062	1.560438	1.077502E+00	3.460411E-01
C	6	8.212966	-0.257034	1.094342	3.882330E-03	1.246815E-03
N	7	9.404416	1.534416	2.885791	6.947694E-02	2.231260E-02
O	8	7.593408	-1.136592	0.214784	1.227126E-03	3.940930E-04
F	9	3.945309	-0.474691	0.876685	3.276117E-07	1.052129E-07
Ne	10	8.002725	0.032725	1.384101	4.303369E-03	1.382032E-03
Na	11	6.411198	0.171198	1.522574	1.159371E-04	3.723332E-05
Mg	12	7.372561	-0.267439	1.083937	1.175518E-03	3.775188E-04
Al	13	6.160777	-0.289223	1.062153	7.646046E-05	2.455536E-05
Si	14	6.391540	-1.158460	0.192916	1.360534E-04	4.369370E-05
P	15	4.775998	-0.634002	0.717374	3.619565E-06	1.162427E-06
S	16	5.819407	-1.330593	0.020783	4.145922E-05	1.331467E-05
Cl	17	3.968709	-1.261291	0.090085	6.503649E-07	2.088654E-07
Ar	18	5.095354	-1.344646	0.006730	8.869334E-06	2.848396E-06
K	19	3.817121	-1.262879	0.088497	5.027028E-07	1.614436E-07
Ca	20	4.932817	-1.357183	-0.005807	6.729726E-06	2.161259E-06
Sc	21	2.211343	-0.838657	0.512719	1.431700E-08	4.597919E-09
Ti	22	3.601141	-1.308859	0.042517	3.751615E-07	1.204835E-07
V	23	2.611048	-1.348952	0.002424	4.073007E-08	1.308051E-08
Cr	24	4.269565	-1.370435	-0.019059	1.898860E-06	6.098210E-07
Mn	25	4.116723	-1.363277	-0.011901	1.407285E-06	4.519511E-07
Fe	26	6.188624	-1.351376	0.000000	1.691450E-04	5.432112E-05
Co	27	4.055712	-0.814288	0.537088	1.311780E-06	4.212795E-07
Ni	28	5.052442	-1.147558	0.203818	1.327690E-05	4.263891E-06
Cu	29	4.012577	-0.237423	1.113953	1.280158E-06	4.111242E-07
Zn	30	3.957551	-0.672449	0.678927	1.185061E-06	3.805836E-07
Ga	31	3.017723	-0.062277	1.289099	1.424402E-07	4.574484E-08
Ge	32	3.461735	-0.118265	1.233111	4.089638E-07	1.313392E-07
As	33	1.987156	-0.312844	1.038532	1.424013E-08	4.573235E-09
Se	34	3.365551	0.025551	1.376926	3.565607E-07	1.145099E-07
Br	35	2.305233	-0.234767	1.116609	3.171682E-08	1.018589E-08
Kr	36	3.591241	0.341241	1.692617	6.480601E-07	2.081252E-07
Rb	37	2.971498	0.451498	1.802874	1.579987E-07	5.074147E-08
Sr	38	3.131294	0.251294	1.602670	2.320777E-07	7.453202E-08
Y	39	2.440031	0.230031	1.581407	4.794215E-08	1.539667E-08
Zr	40	2.750952	0.220952	1.572327	1.018217E-07	3.270016E-08
Nb	41	1.495074	0.085074	1.436450	5.686613E-09	1.826262E-09
Mo	42	1.825162	-0.114838	1.236538	1.264377E-08	4.060562E-09

Table A.9 Yields for 4 M$_\odot$, Z = 0.0006, Y = 0.24 (continued)

El	Z	log ϵ(X)	[X/H]	[X/Fe]	M$_{yield}$	X$_{yield}$
Ru	44	1.448182	-0.311818	1.039558	5.535232E-09	1.777646E-09
Rh	45	0.367011	-0.692989	0.658387	4.689698E-10	1.506102E-10
Pd	46	1.339410	-0.310590	1.040786	4.532047E-09	1.455472E-09
Ag	47	0.546648	-0.653352	0.698024	7.446447E-10	2.391435E-10
Cd	48	1.437841	-0.272159	1.079217	6.017910E-09	1.932659E-09
In	49	0.289592	-0.470408	0.880968	4.381133E-10	1.407006E-10
Sn	50	1.798221	-0.271779	1.079597	1.454899E-08	4.672424E-09
Sb	51	0.264490	-0.745510	0.605866	4.350831E-10	1.397274E-10
Te	52	1.330210	-0.849790	0.501585	5.217265E-09	1.675531E-09
I	53	0.424609	-1.125391	0.225985	6.602518E-10	2.120406E-10
Xe	54	1.557966	-0.682034	0.669342	9.298663E-09	2.986276E-09
Cs	55	0.251276	-0.828724	0.522652	4.638997E-10	1.489819E-10
Ba	56	1.974626	-0.205374	1.146002	2.532317E-08	8.132565E-09
La	57	0.700866	-0.469134	0.882242	1.365141E-09	4.384167E-10
Ce	58	1.075808	-0.504192	0.847184	3.266656E-09	1.049090E-09
Pr	59	0.053008	-0.706992	0.644384	3.115472E-10	1.000537E-10
Nd	60	0.690383	-0.759617	0.591759	1.378997E-09	4.428663E-10
Sm	62	-0.044282	-0.984282	0.367094	2.639135E-10	8.475611E-11
Eu	63	-0.723606	-1.233606	0.117770	5.618936E-11	1.804528E-11
Gd	64	-0.092281	-1.142281	0.209094	2.478709E-10	7.960402E-11
Tb	65	-0.867549	-1.187549	0.163827	4.218370E-11	1.354734E-11
Dy	66	0.064732	-1.065268	0.286108	3.692297E-10	1.185785E-10
Ho	67	-0.751511	-1.221511	0.129864	5.718326E-11	1.836447E-11
Er	68	-0.132895	-1.052895	0.298481	2.412332E-10	7.747231E-11
Tm	69	-1.002632	-1.122632	0.228744	3.285118E-11	1.055019E-11
Yb	70	0.055793	-0.864207	0.487169	3.843259E-10	1.234267E-10
Lu	71	-0.837510	-0.927510	0.423866	4.983382E-11	1.600419E-11
Hf	72	-0.054072	-0.764072	0.587304	3.090532E-10	9.925278E-11
Ta	73	-0.978995	-0.858995	0.492381	3.715183E-11	1.193135E-11
W	74	-0.101574	-0.751574	0.599802	2.847346E-10	9.144284E-11
Re	75	-0.828681	-1.088681	0.262695	5.398396E-11	1.733701E-11
Os	76	0.161359	-1.188641	0.162735	5.382112E-10	1.728471E-10
Ir	77	-0.010508	-1.330508	0.020868	3.669717E-10	1.178534E-10
Pt	78	0.337405	-1.282595	0.068781	8.289470E-10	2.662173E-10
Au	79	-0.449938	-1.249938	0.101438	1.367176E-10	4.390700E-11
Hg	80	0.325950	-0.844050	0.507326	8.301072E-10	2.665899E-10
Tl	81	0.078379	-0.691621	0.659754	4.787408E-10	1.537481E-10
Pb	82	1.106775	-0.933225	0.418151	5.182886E-09	1.664490E-09
Bi	83	-0.402195	-1.052195	0.299181	1.619003E-10	5.199447E-11

Table A.10   Yields for 4 M$_\odot$, $Z = 0.0006$, $Y = 0.30$

El	Z	log ϵ(X)	[X/H]	[X/Fe]	M$_{yield}$	X$_{yield}$
H	1	12.000000	0.000000	1.311569	1.803502E+00	5.836954E-01
He	2	11.231976	0.301976	1.613545	1.230701E+00	3.983109E-01
C	6	8.242295	-0.227705	1.083864	3.820849E-03	1.236601E-03
N	7	9.276507	1.406507	2.718076	4.772569E-02	1.544621E-02
O	8	7.478041	-1.251959	0.059611	8.676638E-04	2.808156E-04
F	9	3.805677	-0.614323	0.697246	2.190518E-07	7.089517E-08
Ne	10	7.751336	-0.218664	1.092905	2.217578E-03	7.177096E-04
Na	11	6.105207	-0.134793	1.176776	5.285076E-05	1.710492E-05
Mg	12	7.050255	-0.589745	0.721824	5.145457E-04	1.665305E-04
Al	13	5.891327	-0.558673	0.752897	3.791471E-05	1.227093E-05
Si	14	6.333079	-1.216921	0.094648	1.094266E-04	3.541546E-05
P	15	4.551918	-0.858082	0.453487	1.992490E-06	6.448608E-07
S	16	5.854259	-1.295741	0.015829	4.140783E-05	1.340147E-05
Cl	17	3.982373	-1.247627	0.063942	6.178325E-07	1.999588E-07
Ar	18	5.132185	-1.307815	0.003754	8.893591E-06	2.878372E-06
K	19	3.825002	-1.254998	0.056571	4.719412E-07	1.527417E-07
Ca	20	4.974159	-1.315841	-0.004272	6.821952E-06	2.207895E-06
Sc	21	2.093698	-0.956302	0.355267	1.006995E-08	3.259095E-09
Ti	22	3.623932	-1.286068	0.025502	3.642740E-07	1.178957E-07
V	23	2.648619	-1.311381	0.000188	4.095489E-08	1.325487E-08
Cr	24	4.309871	-1.330129	-0.018559	1.920929E-06	6.217005E-07
Mn	25	4.160774	-1.319226	-0.007657	1.436327E-06	4.648611E-07
Fe	26	6.228431	-1.311569	0.000000	1.708378E-04	5.529091E-05
Co	27	4.011381	-0.858619	0.452950	1.092320E-06	3.535246E-07
Ni	28	5.023832	-1.176168	0.135401	1.138599E-05	3.685026E-06
Cu	29	3.848848	-0.401152	0.910417	8.093732E-07	2.619501E-07
Zn	30	3.802115	-0.827885	0.483685	7.616811E-07	2.465148E-07
Ga	31	2.813138	-0.266862	1.044708	8.201266E-08	2.654304E-08
Ge	32	3.257742	-0.322258	0.989311	2.358038E-07	7.631688E-08
As	33	1.793407	-0.506593	0.804976	8.405916E-09	2.720538E-09
Se	34	3.160055	-0.179945	1.131624	2.048996E-07	6.631487E-08
Br	35	2.056304	-0.483696	0.827873	1.651935E-08	5.346417E-09
Kr	36	3.364703	0.114703	1.426272	3.545150E-07	1.147372E-07
Rb	37	2.730062	0.210062	1.521632	8.351835E-08	2.703035E-08
Sr	38	2.910943	0.030943	1.342512	1.288263E-07	4.169408E-08
Y	39	2.208522	-0.001478	1.310091	2.594351E-08	8.396505E-09
Zr	40	2.513132	-0.016868	1.294702	5.427030E-08	1.756435E-08
Nb	41	1.261422	-0.148578	1.162991	3.062114E-09	9.910399E-10
Mo	42	1.606656	-0.333344	0.978225	7.051388E-09	2.282151E-09

Table A.10 Yields for 4 M$_\odot$, Z = 0.0006, Y = 0.30 (continued)

El	Z	log ϵ(X)	[X/H]	[X/Fe]	M$_{yield}$	X$_{yield}$
Ru	44	1.260818	-0.499182	0.812387	3.316062E-09	1.073229E-09
Rh	45	0.225950	-0.834050	0.477519	3.125387E-10	1.011518E-10
Pd	46	1.154481	-0.495519	0.816050	2.730012E-09	8.835566E-10
Ag	47	0.396812	-0.803188	0.508381	4.862125E-10	1.573606E-10
Cd	48	1.243286	-0.466714	0.844855	3.545507E-09	1.147488E-09
In	49	0.107726	-0.652274	0.659295	2.657911E-10	8.602213E-11
Sn	50	1.587322	-0.482678	0.828891	8.254435E-09	2.671512E-09
Sb	51	0.071487	-0.938513	0.373056	2.572699E-10	8.326430E-11
Te	52	1.120046	-1.059954	0.251615	2.966218E-09	9.600036E-10
I	53	0.363960	-1.186040	0.125529	5.295170E-10	1.713759E-10
Xe	54	1.362609	-0.877391	0.434179	5.461208E-09	1.767496E-09
Cs	55	0.103070	-0.976930	0.334639	3.041151E-10	9.842552E-11
Ba	56	1.757625	-0.422375	0.889194	1.417253E-08	4.586877E-09
La	57	0.513824	-0.656176	0.655393	8.183810E-10	2.648655E-10
Ce	58	0.883975	-0.696025	0.615544	1.936443E-09	6.267214E-10
Pr	59	-0.111063	-0.871063	0.440506	1.969123E-10	6.372981E-11
Nd	60	0.548752	-0.901248	0.410321	9.177296E-10	2.970192E-10
Sm	62	-0.168596	-1.108596	0.202973	1.828360E-10	5.917406E-11
Eu	63	-0.739500	-1.249500	0.062069	4.995567E-11	1.616794E-11
Gd	64	-0.174893	-1.224893	0.086676	1.889264E-10	6.114521E-11
Tb	65	-0.900122	-1.220122	0.091447	3.609040E-11	1.168050E-11
Dy	66	-0.006499	-1.136499	0.175071	2.889577E-10	9.351992E-11
Ho	67	-0.769463	-1.239463	0.072106	5.059844E-11	1.637597E-11
Er	68	-0.209755	-1.129755	0.181814	1.863282E-10	6.030431E-11
Tm	69	-1.052038	-1.172038	0.139531	2.703744E-11	8.750549E-12
Yb	70	-0.080097	-1.000097	0.311472	2.591666E-10	8.387814E-11
Lu	71	-0.943874	-1.033874	0.277695	3.596124E-11	1.163870E-11
Hf	72	-0.190941	-0.900941	0.410628	2.078785E-10	6.727899E-11
Ta	73	-1.097288	-0.977288	0.334281	2.609198E-11	8.444557E-12
W	74	-0.237713	-0.887713	0.423856	1.918975E-10	6.210678E-11
Re	75	-0.886726	-1.146726	0.164843	4.356750E-11	1.410043E-11
Os	76	0.132086	-1.217914	0.093655	4.644182E-10	1.503069E-10
Ir	77	0.016142	-1.303858	0.007711	3.598459E-10	1.164626E-10
Pt	78	0.331666	-1.288334	0.023235	7.543930E-10	2.441560E-10
Au	79	-0.455936	-1.255936	0.055633	1.243502E-10	4.024540E-11
Hg	80	0.196062	-0.973938	0.337631	5.676100E-10	1.837045E-10
Tl	81	-0.080759	-0.850759	0.460811	3.060465E-10	9.905062E-11
Pb	82	0.998214	-1.041786	0.269783	3.722891E-09	1.204897E-09
Bi	83	-0.483428	-1.133428	0.178142	1.238327E-10	4.007791E-11

Table A.11 Yields for 4 M$_\odot$, $Z = 0.0006$, $Y = 0.35$

El	Z	log ϵ(X)	[X/H]	[X/Fe]	M$_{yield}$	X$_{yield}$
H	1	12.000000	0.000000	1.275950	1.667266E+00	5.445382E-01
He	2	11.309169	0.379169	1.655119	1.359045E+00	4.438715E-01
C	6	8.161390	-0.308610	0.967339	2.930542E-03	9.571308E-04
N	7	9.113308	1.243308	2.519258	3.029995E-02	9.896128E-03
O	8	7.360337	-1.369663	-0.093713	6.117086E-04	1.997873E-04
F	9	3.652552	-0.767448	0.508502	1.423348E-07	4.648730E-08
Ne	10	7.444951	-0.525049	0.750901	1.004262E-03	3.279972E-04
Na	11	5.742179	-0.497821	0.778129	2.117933E-05	6.917284E-06
Mg	12	6.773383	-0.866617	0.409333	2.509525E-04	8.196245E-05
Al	13	5.706139	-0.743861	0.532089	2.288273E-05	7.473622E-06
Si	14	6.322705	-1.227295	0.048655	9.865005E-05	3.221964E-05
P	15	4.397117	-1.012883	0.263067	1.289686E-06	4.212183E-07
S	16	5.887186	-1.262814	0.013136	4.128288E-05	1.348321E-05
Cl	17	3.997583	-1.232417	0.043533	5.905081E-07	1.928631E-07
Ar	18	5.165954	-1.274046	0.001904	8.879810E-06	2.900194E-06
K	19	3.837092	-1.242908	0.033042	4.485444E-07	1.464970E-07
Ca	20	5.011368	-1.278632	-0.002683	6.868415E-06	2.243261E-06
Sc	21	2.004063	-1.045937	0.230013	7.573226E-09	2.473457E-09
Ti	22	3.648079	-1.261921	0.014029	3.557409E-07	1.161869E-07
V	23	2.682471	-1.277529	-0.001579	4.093042E-08	1.336810E-08
Cr	24	4.345513	-1.294487	-0.018537	1.927271E-06	6.294571E-07
Mn	25	4.201009	-1.278991	-0.003042	1.456720E-06	4.757728E-07
Fe	26	6.264050	-1.275950	0.000000	1.713399E-04	5.596053E-05
Co	27	3.937532	-0.932468	0.343482	8.519006E-07	2.782353E-07
Ni	28	5.004527	-1.195473	0.080477	1.000627E-05	3.268102E-06
Cu	29	3.666011	-0.583989	0.691961	4.910782E-07	1.603888E-07
Zn	30	3.671689	-0.958311	0.317639	5.194436E-07	1.696531E-07
Ga	31	2.603813	-0.476187	0.799763	4.681373E-08	1.528962E-08
Ge	32	3.050963	-0.529037	0.746913	1.354395E-07	4.423528E-08
As	33	1.607010	-0.692990	0.582960	5.059139E-09	1.652342E-09
Se	34	2.942412	-0.397588	0.878362	1.147733E-07	3.748558E-08
Br	35	1.826733	-0.713267	0.562683	9.008854E-09	2.942340E-09
Kr	36	3.115584	-0.134416	1.141534	1.845305E-07	6.026867E-08
Rb	37	2.474491	-0.045509	1.230441	4.284407E-08	1.399311E-08
Sr	38	2.663983	-0.216017	1.059932	6.744037E-08	2.202639E-08
Y	39	1.960639	-0.249361	1.026589	1.355295E-08	4.426467E-09
Zr	40	2.260425	-0.269575	1.006375	2.801535E-08	9.149965E-09
Nb	41	1.017607	-0.392393	0.883557	1.614711E-09	5.273732E-10
Mo	42	1.364905	-0.575095	0.700855	3.734576E-09	1.219733E-09

Table A.11 Yields for 4 $M_\odot$, $Z = 0.0006$, $Y = 0.35$ (continued)

El	Z	log ϵ(X)	[X/H]	[X/Fe]	M_{yield}	X_{yield}
Ru	44	1.035268	-0.724732	0.551218	1.823909E-09	5.956985E-10
Rh	45	0.080004	-0.979996	0.295954	2.064647E-10	6.743249E-11
Pd	46	0.938906	-0.711094	0.564856	1.536354E-09	5.017815E-10
Ag	47	0.244178	-0.955822	0.320127	3.161772E-10	1.032652E-10
Cd	48	1.024621	-0.685379	0.590571	1.981060E-09	6.470250E-10
In	49	-0.082969	-0.842969	0.432981	1.583923E-10	5.173176E-11
Sn	50	1.360084	-0.709916	0.566034	4.522011E-09	1.476913E-09
Sb	51	-0.113792	-1.123792	0.152158	1.552383E-10	5.070166E-11
Te	52	0.915492	-1.264508	0.011442	1.713054E-09	5.594925E-10
I	53	0.333878	-1.216122	0.059828	4.567583E-10	1.491797E-10
Xe	54	1.210005	-1.029995	0.245955	3.548573E-09	1.158983E-09
Cs	55	-0.003666	-1.083666	0.192284	2.198827E-10	7.181486E-11
Ba	56	1.524389	-0.655611	0.620339	7.658639E-09	2.501353E-09
La	57	0.319350	-0.850650	0.425300	4.834702E-10	1.579040E-10
Ce	58	0.695467	-0.884533	0.391417	1.159707E-09	3.787666E-10
Pr	59	-0.255050	-1.015050	0.260900	1.306694E-10	4.267734E-11
Nd	60	0.408112	-1.041888	0.234062	6.138950E-10	2.005014E-10
Sm	62	-0.279787	-1.219787	0.056163	1.308995E-10	4.275249E-11
Eu	63	-0.743700	-1.253700	0.022250	4.573854E-11	1.493845E-11
Gd	64	-0.232029	-1.282029	-0.006080	1.530719E-10	4.999409E-11
Tb	65	-0.916399	-1.236399	0.039550	3.213680E-11	1.049605E-11
Dy	66	-0.056801	-1.186801	0.089149	2.378809E-10	7.769319E-11
Ho	67	-0.776231	-1.246231	0.029718	4.605296E-11	1.504115E-11
Er	68	-0.264725	-1.184725	0.091224	1.517481E-10	4.956176E-11
Tm	69	-1.088180	-1.208180	0.067770	2.299914E-11	7.511644E-12
Yb	70	-0.204735	-1.124735	0.151215	1.797749E-10	5.871545E-11
Lu	71	-1.037168	-1.127168	0.148781	2.680767E-11	8.755529E-12
Hf	72	-0.328773	-1.038773	0.237177	1.398303E-10	4.566934E-11
Ta	73	-1.212037	-1.092037	0.183913	1.852024E-11	6.048809E-12
W	74	-0.378771	-1.028771	0.247179	1.282020E-10	4.187147E-11
Re	75	-0.934580	-1.194580	0.081370	3.608823E-11	1.178661E-11
Os	76	0.116749	-1.233251	0.042699	4.147707E-10	1.354664E-10
Ir	77	0.041150	-1.278850	-0.002900	3.523920E-10	1.150931E-10
Pt	78	0.337834	-1.282166	-0.006217	7.073486E-10	2.310239E-10
Au	79	-0.453282	-1.253282	0.022667	1.156615E-10	3.777567E-11
Hg	80	0.070553	-1.099447	0.176503	3.930224E-10	1.283632E-10
Tl	81	-0.236141	-1.006141	0.269809	1.978403E-10	6.461571E-11
Pb	82	0.905797	-1.134203	0.141747	2.782286E-09	9.087096E-10
Bi	83	-0.540214	-1.190214	0.085736	1.004472E-10	3.280659E-11

Table A.12 Yields for 4 M$_\odot$, Z = 0.0006, Y = 0.40

El	Z	log ϵ(X)	[X/H]	[X/Fe]	M$_{yield}$	X$_{yield}$
H	1	12.000000	0.000000	1.230097	1.491128E+00	4.944387E-01
He	2	11.402124	0.472124	1.702221	1.505564E+00	4.992255E-01
C	6	8.067306	-0.402694	0.827403	2.109773E-03	6.995734E-04
N	7	8.877859	1.007859	2.237956	1.575805E-02	5.225165E-03
O	8	7.156644	-1.573356	-0.343259	3.422694E-04	1.134921E-04
F	9	3.402651	-1.017349	0.212748	7.160103E-08	2.374198E-08
Ne	10	7.110607	-0.859393	0.370704	4.071789E-04	1.350153E-04
Na	11	5.169861	-1.070139	0.159958	5.071116E-06	1.681517E-06
Mg	12	6.524310	-1.115690	0.114407	1.262988E-04	4.187907E-05
Al	13	5.747638	-0.702362	0.527735	2.251730E-05	7.466445E-06
Si	14	6.348408	-1.201592	0.028505	9.352789E-05	3.101264E-05
P	15	4.290293	-1.119707	0.110390	9.019224E-07	2.990658E-07
S	16	5.931269	-1.218731	0.011366	4.085759E-05	1.354785E-05
Cl	17	4.029136	-1.200864	0.029233	5.670310E-07	1.880202E-07
Ar	18	5.210532	-1.229468	0.000629	8.795267E-06	2.916397E-06
K	19	3.865924	-1.214076	0.016021	4.286822E-07	1.421455E-07
Ca	20	5.058529	-1.231471	-0.001374	6.845859E-06	2.269998E-06
Sc	21	1.934750	-1.115250	0.114847	5.774012E-09	1.914588E-09
Ti	22	3.685936	-1.224064	0.006033	3.469240E-07	1.150355E-07
V	23	2.726714	-1.233286	-0.003189	4.053210E-08	1.343992E-08
Cr	24	4.391223	-1.248777	-0.018680	1.914604E-06	6.348579E-07
Mn	25	4.252487	-1.227513	0.002584	1.466778E-06	4.863645E-07
Fe	26	6.309903	-1.230097	0.000000	1.702345E-04	5.644757E-05
Co	27	3.851737	-1.018263	0.211834	6.253225E-07	2.073489E-07
Ni	28	5.006220	-1.193780	0.036317	8.934050E-06	2.962416E-06
Cu	29	3.443897	-0.806103	0.423994	2.633820E-07	8.733409E-08
Zn	30	3.557837	-1.072163	0.157934	3.554851E-07	1.178743E-07
Ga	31	2.348890	-0.731110	0.498987	2.326981E-08	7.715968E-09
Ge	32	2.801175	-0.778825	0.451272	6.818126E-08	2.260803E-08
As	33	1.400434	-0.899566	0.330531	2.811965E-09	9.324112E-10
Se	34	2.664066	-0.675934	0.554163	5.409178E-08	1.793614E-08
Br	35	1.600335	-0.939665	0.290432	4.778576E-09	1.584514E-09
Kr	36	2.789027	-0.460973	0.769125	7.769305E-08	2.576201E-08
Rb	37	2.134825	-0.385175	0.844922	1.751303E-08	5.807095E-09
Sr	38	2.348274	-0.531726	0.698371	2.915837E-08	9.668539E-09
Y	39	1.652218	-0.557782	0.672315	5.958308E-09	1.975698E-09
Zr	40	1.951589	-0.578411	0.651686	1.228496E-08	4.073534E-09
Nb	41	0.729618	-0.680382	0.549715	7.440725E-10	2.467248E-10
Mo	42	1.083721	-0.856279	0.373818	1.746429E-09	5.790933E-10

Table A.12 Yields for 4 M$_\odot$, Z = 0.0006, Y = 0.40 (continued)

El	Z	log ϵ(X)	[X/H]	[X/Fe]	M$_{yield}$	X$_{yield}$
Ru	44	0.786064	-0.973936	0.256161	9.191511E-10	3.047787E-10
Rh	45	-0.037879	-1.097879	0.132218	1.407579E-10	4.667349E-11
Pd	46	0.709212	-0.940788	0.289309	8.097152E-10	2.684911E-10
Ag	47	0.118183	-1.081817	0.148280	2.114671E-10	7.011976E-11
Cd	48	0.793054	-0.916946	0.313151	1.039554E-09	3.447028E-10
In	49	-0.261977	-1.021977	0.208120	9.380715E-11	3.110524E-11
Sn	50	1.124811	-0.945189	0.284908	2.353020E-09	7.802312E-10
Sb	51	-0.271647	-1.281647	-0.051550	9.652796E-11	3.200743E-11
Te	52	0.729891	-1.450109	-0.220012	1.000178E-09	3.316463E-10
I	53	0.335689	-1.214311	0.015786	4.102111E-10	1.360207E-10
Xe	54	1.104098	-1.135902	0.094195	2.483646E-09	8.235448E-10
Cs	55	-0.064762	-1.144762	0.085335	1.708457E-10	5.665022E-11
Ba	56	1.292708	-0.887292	0.342805	4.018629E-09	1.332526E-09
La	57	0.155656	-1.014344	0.215753	2.966098E-10	9.835199E-11
Ce	58	0.545016	-1.034984	0.195113	7.334593E-10	2.432057E-10
Pr	59	-0.349386	-1.109386	0.120711	9.404754E-11	3.118495E-11
Nd	60	0.315252	-1.134748	0.095349	4.435270E-10	1.470678E-10
Sm	62	-0.339751	-1.279751	-0.049654	1.020171E-10	3.382755E-11
Eu	63	-0.725377	-1.235377	-0.005280	4.267044E-11	1.414897E-11
Gd	64	-0.243249	-1.293249	-0.063152	1.333718E-10	4.422437E-11
Tb	65	-0.904219	-1.224219	0.005878	2.955919E-11	9.801447E-12
Dy	66	-0.063751	-1.193751	0.036346	2.093531E-10	6.941879E-11
Ho	67	-0.757967	-1.227967	0.002130	4.295677E-11	1.424391E-11
Er	68	-0.274427	-1.194427	0.035670	1.327015E-10	4.400210E-11
Tm	69	-1.088218	-1.208218	0.021879	2.056760E-11	6.819951E-12
Yb	70	-0.276039	-1.196039	0.034058	1.364021E-10	4.522919E-11
Lu	71	-1.081303	-1.171303	0.058794	2.165183E-11	7.179468E-12
Hf	72	-0.414414	-1.124414	0.105683	1.026094E-10	3.402396E-11
Ta	73	-1.276958	-1.156958	0.073139	1.426379E-11	4.729690E-12
W	74	-0.468369	-1.118369	0.111728	9.328102E-11	3.093078E-11
Re	75	-0.944733	-1.204733	0.025364	3.153868E-11	1.045782E-11
Os	76	0.132919	-1.217081	0.013016	3.852201E-10	1.277340E-10
Ir	77	0.077903	-1.242097	-0.012000	3.430035E-10	1.137355E-10
Pt	78	0.371500	-1.248500	-0.018403	6.835766E-10	2.266652E-10
Au	79	-0.426032	-1.226032	0.004065	1.101410E-10	3.652133E-11
Hg	80	0.002492	-1.167508	0.062589	3.004948E-10	9.964019E-11
Tl	81	-0.336412	-1.106412	0.123685	1.404681E-10	4.657741E-11
Pb	82	0.867213	-1.172787	0.057310	2.277045E-09	7.550388E-10
Bi	83	-0.548877	-1.198877	0.031220	8.806102E-11	2.919990E-11

Table A.13 Yields for 5 M$_\odot$, $Z = 0.0006$, $Y = 0.24$

El	Z	log ϵ(X)	[X/H]	[X/Fe]	M$_{yield}$	X$_{yield}$
H	1	12.000000	0.000000	1.334992	2.484846E+00	6.120689E-01
He	2	11.178007	0.248007	1.582999	1.497500E+00	3.688652E-01
C	6	8.076687	-0.393313	0.941678	3.609628E-03	8.891260E-04
N	7	9.293502	1.423502	2.758494	6.838026E-02	1.684347E-02
O	8	7.355246	-1.374754	-0.039762	9.010593E-04	2.219495E-04
F	9	3.207530	-1.212470	0.122522	7.613482E-08	1.875358E-08
Ne	10	7.723340	-0.246660	1.088332	2.860621E-03	7.046301E-04
Na	11	6.124965	-0.115035	1.219956	7.620648E-05	1.877123E-05
Mg	12	7.183723	-0.456277	0.878715	9.692234E-04	2.387398E-04
Al	13	6.243060	-0.206940	1.128052	1.174149E-04	2.892171E-05
Si	14	6.350940	-1.199060	0.135932	1.573349E-04	3.875485E-05
P	15	4.733657	-0.676343	0.658648	4.171744E-06	1.027587E-06
S	16	5.834274	-1.315726	0.019265	5.449665E-05	1.342365E-05
Cl	17	3.962018	-1.267982	0.067010	8.119650E-07	2.000038E-07
Ar	18	5.110438	-1.329562	0.005430	1.165805E-05	2.871618E-06
K	19	3.809542	-1.270458	0.064534	6.276319E-07	1.545987E-07
Ca	20	4.951876	-1.338124	-0.003132	8.931349E-06	2.199976E-06
Sc	21	2.125288	-0.924712	0.410280	1.492108E-08	3.675370E-09
Ti	22	3.610860	-1.299140	0.035852	4.871627E-07	1.199983E-07
V	23	2.628501	-1.331499	0.003493	5.387296E-08	1.327002E-08
Cr	24	4.286139	-1.353861	-0.018869	2.505707E-06	6.172075E-07
Mn	25	4.139486	-1.340514	-0.005522	1.884291E-06	4.641399E-07
Fe	26	6.205008	-1.334992	0.000000	2.230192E-04	5.493424E-05
Co	27	3.912545	-0.957455	0.377536	1.198660E-06	2.952549E-07
Ni	28	5.019051	-1.180949	0.154043	1.555566E-05	3.831680E-06
Cu	29	3.915663	-0.334337	1.000654	1.301863E-06	3.206757E-07
Zn	30	3.907709	-0.722291	0.612701	1.341360E-06	3.304047E-07
Ga	31	2.962530	-0.117470	1.217522	1.594012E-07	3.926380E-08
Ge	32	3.411374	-0.168626	1.166366	4.627965E-07	1.139964E-07
As	33	1.940864	-0.359136	0.975856	1.626389E-08	4.006133E-09
Se	34	3.320982	-0.019018	1.315974	4.089094E-07	1.007228E-07
Br	35	2.231881	-0.308119	1.026873	3.407620E-08	8.393672E-09
Kr	36	3.567709	0.317709	1.652701	7.803840E-07	1.922247E-07
Rb	37	2.932818	0.412818	1.747810	1.836409E-07	4.523454E-08
Sr	38	3.120503	0.240503	1.575495	2.876765E-07	7.086067E-08
Y	39	2.439639	0.229639	1.564631	6.085956E-08	1.499097E-08
Zr	40	2.764676	0.234676	1.569667	1.335708E-07	3.290126E-08
Nb	41	1.509448	0.099448	1.434439	7.468443E-09	1.839632E-09
Mo	42	1.855538	-0.084462	1.250530	1.723352E-08	4.244973E-09

Table A.13 Yields for 5 M$_\odot$, Z = 0.0006, Y = 0.24 (continued)

El	Z	log ϵ(X)	[X/H]	[X/Fe]	M$_{yield}$	X$_{yield}$
Ru	44	1.500559	-0.259441	1.075551	7.934919E-09	1.954535E-09
Rh	45	0.415833	-0.644167	0.690824	6.667595E-10	1.642366E-10
Pd	46	1.393559	-0.256441	1.078551	6.522867E-09	1.606717E-09
Ag	47	0.595411	-0.604589	0.730403	1.058571E-09	2.607478E-10
Cd	48	1.489550	-0.220450	1.114541	8.612782E-09	2.121506E-09
In	49	0.338088	-0.421912	0.913079	6.224219E-10	1.533154E-10
Sn	50	1.848788	-0.221212	1.113780	2.076846E-08	5.115702E-09
Sb	51	0.312909	-0.697091	0.637901	6.180075E-10	1.522280E-10
Te	52	1.379539	-0.800461	0.534531	7.426124E-09	1.829208E-09
I	53	0.458568	-1.091432	0.243560	9.071336E-10	2.234458E-10
Xe	54	1.590489	-0.649511	0.685481	1.272697E-08	3.134917E-09
Cs	55	0.295297	-0.784703	0.550289	6.523018E-10	1.606754E-10
Ba	56	2.035587	-0.144413	1.190579	3.703050E-08	9.121379E-09
La	57	0.770936	-0.399064	0.935927	2.038214E-09	5.020543E-10
Ce	58	1.134352	-0.445648	0.889344	4.748881E-09	1.169748E-09
Pr	59	0.109079	-0.650921	0.684071	4.503992E-10	1.109426E-10
Nd	60	0.754332	-0.695668	0.639324	2.029497E-09	4.999070E-10
Sm	62	0.006612	-0.933388	0.401604	3.769977E-10	9.286234E-11
Eu	63	-0.694418	-1.204418	0.130574	7.635651E-11	1.880819E-11
Gd	64	-0.048787	-1.098787	0.236205	3.481201E-10	8.574919E-11
Tb	65	-0.834138	-1.154138	0.180854	5.788404E-11	1.425804E-11
Dy	66	0.108006	-1.021994	0.312998	5.183122E-10	1.276710E-10
Ho	67	-0.718830	-1.188830	0.146162	7.833459E-11	1.929543E-11
Er	68	-0.087971	-1.007971	0.327021	3.399108E-10	8.372706E-11
Tm	69	-0.958442	-1.078442	0.256549	4.621082E-11	1.138268E-11
Yb	70	0.103926	-0.816074	0.518917	5.455676E-10	1.343846E-10
Lu	71	-0.790478	-0.880478	0.454513	7.056429E-11	1.738144E-11
Hf	72	-0.000590	-0.710590	0.624401	4.441646E-10	1.094069E-10
Ta	73	-0.927156	-0.807156	0.527836	5.318905E-11	1.310156E-11
W	74	-0.044030	-0.694030	0.640962	4.130587E-10	1.017449E-10
Re	75	-0.778705	-1.038705	0.296287	7.694341E-11	1.895275E-11
Os	76	0.196817	-1.153183	0.181809	7.419622E-10	1.827606E-10
Ir	77	0.012916	-1.307084	0.027908	4.921087E-10	1.212166E-10
Pt	78	0.371289	-1.248711	0.086281	1.138727E-09	2.804920E-10
Au	79	-0.417722	-1.217722	0.117269	1.870869E-10	4.608337E-11
Hg	80	0.379376	-0.790624	0.544368	1.192778E-09	2.938058E-10
Tl	81	0.136168	-0.633832	0.701160	6.948503E-10	1.711560E-10
Pb	82	1.163675	-0.876325	0.458666	7.507150E-09	1.849166E-09
Bi	83	-0.347770	-0.997770	0.337221	2.331715E-10	5.743495E-11

Table A.14   Yields for 5 M$_\odot$, Z = 0.0006, Y = 0.30

El	Z	log ϵ(X)	[X/H]	[X/Fe]	M$_{yield}$	X$_{yield}$
H	1	12.000000	0.000000	1.301982	2.323638E+00	5.774810E-01
He	2	11.250973	0.320973	1.622955	1.656540E+00	4.116907E-01
C	6	8.017129	-0.452871	0.849111	2.935190E-03	7.294666E-04
N	7	9.069983	1.199983	2.501965	3.821913E-02	9.498390E-03
O	8	7.169112	-1.560888	-0.258907	5.489053E-04	1.364164E-04
F	9	3.231784	-1.188216	0.113766	7.528467E-08	1.871008E-08
Ne	10	7.339364	-0.630636	0.671346	1.092895E-03	2.716112E-04
Na	11	5.613180	-0.626820	0.675162	2.193190E-05	5.450615E-06
Mg	12	6.778065	-0.861935	0.440047	3.551972E-04	8.827520E-05
Al	13	5.971118	-0.478882	0.823100	5.870163E-05	1.458879E-05
Si	14	6.308024	-1.241976	0.060006	1.329593E-04	3.304364E-05
P	15	4.451310	-0.958690	0.343292	2.036294E-06	5.060690E-07
S	16	5.861742	-1.288258	0.013724	5.426305E-05	1.348570E-05
Cl	17	3.971267	-1.258733	0.043249	7.741916E-07	1.924056E-07
Ar	18	5.140415	-1.299585	0.002397	1.166929E-05	2.900104E-06
K	19	3.813188	-1.266812	0.035170	5.917240E-07	1.470579E-07
Ca	20	4.985867	-1.304133	-0.002151	9.027045E-06	2.243442E-06
Sc	21	1.994001	-1.055999	0.245982	1.031292E-08	2.563014E-09
Ti	22	3.624949	-1.285051	0.016930	4.700790E-07	1.168261E-07
V	23	2.657407	-1.302593	-0.000611	5.384509E-08	1.338182E-08
Cr	24	4.319131	-1.320869	-0.018887	2.527516E-06	6.281496E-07
Mn	25	4.177935	-1.302065	-0.000084	1.925156E-06	4.784483E-07
Fe	26	6.238018	-1.301982	0.000000	2.248934E-04	5.589152E-05
Co	27	3.840613	-1.029387	0.272595	9.498029E-07	2.360493E-07
Ni	28	4.982296	-1.217704	0.084278	1.326089E-05	3.295655E-06
Cu	29	3.689493	-0.560507	0.741475	7.228214E-07	1.796388E-07
Zn	30	3.704659	-0.925341	0.376640	7.822422E-07	1.944063E-07
Ga	31	2.667345	-0.412655	0.889327	7.552322E-08	1.876937E-08
Ge	32	3.114160	-0.465840	0.836142	2.183063E-07	5.425445E-08
As	33	1.660914	-0.639086	0.662896	7.982591E-09	1.983869E-09
Se	34	3.008821	-0.331179	0.970803	1.863773E-07	4.631932E-08
Br	35	1.891198	-0.648802	0.653180	1.456384E-08	3.619472E-09
Kr	36	3.227960	-0.022040	1.279942	3.335390E-07	8.289261E-08
Rb	37	2.587871	0.067871	1.369853	7.756965E-08	1.927796E-08
Sr	38	2.782818	-0.097182	1.204799	1.236100E-07	3.072011E-08
Y	39	2.094802	-0.115198	1.186784	2.572532E-08	6.393372E-09
Zr	40	2.406257	-0.123743	1.178239	5.466863E-08	1.358649E-08
Nb	41	1.157974	-0.252026	1.049956	3.109033E-09	7.726707E-10
Mo	42	1.504193	-0.435807	0.866175	7.174139E-09	1.782949E-09

Table A.14 Yields for 5 M$_\odot$, Z = 0.0006, Y = 0.30 (continued)

El	Z	log ϵ(X)	[X/H]	[X/Fe]	M$_{yield}$	X$_{yield}$
Ru	44	1.167988	-0.592012	0.709970	3.450512E-09	8.575368E-10
Rh	45	0.161219	-0.898781	0.403201	3.469165E-10	8.621724E-11
Pd	46	1.070659	-0.579341	0.722641	2.900127E-09	7.207526E-10
Ag	47	0.333317	-0.866683	0.435298	5.411710E-10	1.344943E-10
Cd	48	1.163255	-0.546745	0.755237	3.799339E-09	9.442288E-10
In	49	0.036461	-0.723539	0.578443	2.906214E-10	7.222652E-11
Sn	50	1.512046	-0.557954	0.744028	8.943337E-09	2.222638E-09
Sb	51	0.010454	-0.999546	0.302436	2.880102E-10	7.157759E-11
Te	52	1.056035	-1.123965	0.178017	3.298480E-09	8.197529E-10
I	53	0.349695	-1.200305	0.101677	6.601875E-10	1.640728E-10
Xe	54	1.305820	-0.934180	0.367802	6.169341E-09	1.533232E-09
Cs	55	0.067322	-1.012678	0.289303	3.608626E-10	8.968318E-11
Ba	56	1.678156	-0.501844	0.800137	1.520799E-08	3.779558E-09
La	57	0.451597	-0.718403	0.583579	9.136515E-10	2.270648E-10
Ce	58	0.816121	-0.763879	0.538103	2.133888E-09	5.303234E-10
Pr	59	-0.163201	-0.923201	0.378781	2.250022E-10	5.591856E-11
Nd	60	0.492482	-0.957518	0.344464	1.038792E-09	2.581653E-10
Sm	62	-0.220179	-1.160179	0.141803	2.092367E-10	5.200045E-11
Eu	63	-0.751059	-1.261059	0.040923	6.267377E-11	1.557597E-11
Gd	64	-0.200950	-1.250950	0.051032	2.291983E-10	5.696138E-11
Tb	65	-0.915248	-1.235248	0.066734	4.490736E-11	1.116058E-11
Dy	66	-0.031396	-1.161396	0.140586	3.515346E-10	8.736495E-11
Ho	67	-0.780666	-1.250666	0.051316	6.353118E-11	1.578905E-11
Er	68	-0.234372	-1.154372	0.147610	2.268338E-10	5.637376E-11
Tm	69	-1.072024	-1.192024	0.109958	3.326838E-11	8.268007E-12
Yb	70	-0.136923	-1.056923	0.245059	2.929244E-10	7.279889E-11
Lu	71	-0.990356	-1.080356	0.221626	4.162430E-11	1.034466E-11
Hf	72	-0.253548	-0.963548	0.338434	2.318219E-10	5.761343E-11
Ta	73	-1.152544	-1.032544	0.269437	2.960075E-11	7.356511E-12
W	74	-0.298345	-0.948345	0.353637	2.150583E-10	5.344724E-11
Re	75	-0.909032	-1.169032	0.132950	5.332858E-11	1.325346E-11
Os	76	0.120165	-1.229835	0.072147	5.824047E-10	1.447418E-10
Ir	77	0.018781	-1.301219	0.000762	4.664645E-10	1.159278E-10
Pt	78	0.334614	-1.285386	0.016596	9.785466E-10	2.431928E-10
Au	79	-0.459420	-1.259420	0.042562	1.589332E-10	3.949880E-11
Hg	80	0.144401	-1.025599	0.276383	6.492775E-10	1.613614E-10
Tl	81	-0.138265	-0.908265	0.393717	3.454167E-10	8.584450E-11
Pb	82	0.959592	-1.080408	0.221573	4.388623E-09	1.090680E-09
Bi	83	-0.505347	-1.155347	0.146635	1.516938E-10	3.769963E-11

Table A.15 Yields for 5 M$_\odot$, $Z = 0.0006$, $Y = 0.35$

El	Z	$\log \epsilon(X)$	[X/H]	[X/Fe]	M$_\text{yield}$	X$_\text{yield}$
H	1	12.000000	0.000000	1.266999	2.137419E+00	5.377496E-01
He	2	11.326504	0.396504	1.663503	1.813235E+00	4.561887E-01
C	6	7.984301	-0.485699	0.781300	2.495241E-03	6.277733E-04
N	7	8.826695	0.956695	2.223694	2.007770E-02	5.051313E-03
O	8	7.019263	-1.710737	-0.443738	3.575814E-04	8.996327E-05
F	9	2.970233	-1.449767	-0.182768	3.792070E-08	9.540402E-09
Ne	10	7.028587	-0.941413	0.325586	4.809349E-04	1.209976E-04
Na	11	5.108581	-1.131419	0.135580	6.312448E-06	1.588138E-06
Mg	12	6.490188	-1.149812	0.117187	1.679014E-04	4.224202E-05
Al	13	5.972096	-0.477904	0.789095	5.411895E-05	1.361569E-05
Si	14	6.347471	-1.202529	0.064469	1.337585E-04	3.365207E-05
P	15	4.303212	-1.106788	0.160211	1.331875E-06	3.350841E-07
S	16	5.894674	-1.255326	0.011673	5.383432E-05	1.354408E-05
Cl	17	3.997535	-1.232465	0.034534	7.554661E-07	1.900664E-07
Ar	18	5.173918	-1.266082	0.000916	1.158852E-05	2.915535E-06
K	19	3.831362	-1.248638	0.018360	5.675214E-07	1.427817E-07
Ca	20	5.021807	-1.268193	-0.001194	9.017734E-06	2.268756E-06
Sc	21	1.916988	-1.133012	0.133987	7.944938E-09	1.998853E-09
Ti	22	3.650717	-1.259283	0.007716	4.585669E-07	1.153701E-07
V	23	2.690400	-1.269600	-0.002601	5.343915E-08	1.344466E-08
Cr	24	4.354160	-1.285840	-0.018841	2.519886E-06	6.339737E-07
Mn	25	4.217238	-1.262762	0.004237	1.938612E-06	4.877319E-07
Fe	26	6.273001	-1.266999	0.000000	2.241432E-04	5.639180E-05
Co	27	3.782963	-1.087037	0.179962	7.650764E-07	1.924842E-07
Ni	28	4.973168	-1.226832	0.040167	1.187595E-05	2.987850E-06
Cu	29	3.459681	-0.790319	0.476679	3.916518E-07	9.853499E-08
Zn	30	3.563651	-1.066349	0.200650	5.172963E-07	1.301457E-07
Ga	31	2.400866	-0.679134	0.587865	3.759956E-08	9.459608E-09
Ge	32	2.855294	-0.724706	0.542293	1.106944E-07	2.784941E-08
As	33	1.440286	-0.859714	0.407285	4.418117E-09	1.111546E-09
Se	34	2.737193	-0.602807	0.664192	9.175669E-08	2.308490E-08
Br	35	1.646741	-0.893259	0.373740	7.628518E-09	1.919245E-09
Kr	36	2.939132	-0.310868	0.956131	1.576808E-07	3.967064E-08
Rb	37	2.291965	-0.228035	1.038964	3.608693E-08	9.079047E-09
Sr	38	2.502410	-0.377590	0.889409	5.962649E-08	1.500132E-08
Y	39	1.824470	-0.385530	0.881469	1.269842E-08	3.194773E-09
Zr	40	2.147526	-0.382474	0.884525	2.771093E-08	6.971744E-09
Nb	41	0.909124	-0.500876	0.766123	1.612488E-09	4.056829E-10
Mo	42	1.264051	-0.675949	0.591049	3.794034E-09	9.545342E-10

Table A.15 Yields for 5 M$_\odot$, Z = 0.0006, Y = 0.35 (continued)

El	Z	log ϵ(X)	[X/H]	[X/Fe]	M$_{yield}$	X$_{yield}$
Ru	44	0.949305	-0.810695	0.456304	1.918588E-09	4.826943E-10
Rh	45	0.031250	-1.028750	0.238249	2.365793E-10	5.952057E-11
Pd	46	0.867387	-0.782613	0.484386	1.670696E-09	4.203275E-10
Ag	47	0.198715	-1.001285	0.265714	3.650100E-10	9.183223E-11
Cd	48	0.963059	-0.746941	0.520058	2.204193E-09	5.545492E-10
In	49	-0.131911	-0.891911	0.375087	1.814162E-10	4.564219E-11
Sn	50	1.313499	-0.756501	0.510498	5.208492E-09	1.310395E-09
Sb	51	-0.143232	-1.153232	0.113767	1.859700E-10	4.678787E-11
Te	52	0.885497	-1.294503	-0.027505	2.049890E-09	5.157281E-10
I	53	0.331383	-1.218617	0.048382	5.822052E-10	1.464760E-10
Xe	54	1.193448	-1.046552	0.220447	4.377853E-09	1.101416E-09
Cs	55	-0.010256	-1.090256	0.176743	2.776426E-10	6.985161E-11
Ba	56	1.502939	-0.677061	0.589938	9.346887E-09	2.351567E-09
La	57	0.317452	-0.852548	0.414451	6.171013E-10	1.552554E-10
Ce	58	0.697398	-0.882602	0.384397	1.493396E-09	3.757210E-10
Pr	59	-0.247758	-1.007758	0.259241	1.703535E-10	4.285894E-11
Nd	60	0.408556	-1.041444	0.225555	7.879457E-10	1.982379E-10
Sm	62	-0.279804	-1.219804	0.047195	1.678411E-10	4.222686E-11
Eu	63	-0.742846	-1.252846	0.014153	5.875416E-11	1.478186E-11
Gd	64	-0.220938	-1.270938	-0.003939	2.013011E-10	5.064500E-11
Tb	65	-0.913265	-1.233265	0.033734	4.149751E-11	1.044028E-11
Dy	66	-0.047561	-1.177561	0.089438	3.115227E-10	7.837546E-11
Ho	67	-0.772885	-1.242885	0.024114	5.949611E-11	1.496852E-11
Er	68	-0.251092	-1.171092	0.095907	2.007653E-10	5.051019E-11
Tm	69	-1.079658	-1.199658	0.067341	3.006907E-11	7.565024E-12
Yb	70	-0.200546	-1.120546	0.146453	2.326911E-10	5.854234E-11
Lu	71	-1.035064	-1.125064	0.141935	3.453478E-11	8.688544E-12
Hf	72	-0.325982	-1.035982	0.231016	1.804107E-10	4.538921E-11
Ta	73	-1.211312	-1.091312	0.175687	2.378245E-11	5.983386E-12
W	74	-0.371212	-1.021212	0.245787	1.672831E-10	4.208647E-11
Re	75	-0.923141	-1.183141	0.083858	4.749727E-11	1.194975E-11
Os	76	0.125482	-1.224518	0.042481	5.425980E-10	1.365113E-10
Ir	77	0.045284	-1.274716	-0.007717	4.560922E-10	1.147474E-10
Pt	78	0.355225	-1.264775	0.002223	9.438351E-10	2.374578E-10
Au	79	-0.443509	-1.243509	0.023490	1.516515E-10	3.815374E-11
Hg	80	0.083608	-1.086392	0.180607	5.192022E-10	1.306252E-10
Tl	81	-0.218258	-0.988258	0.278741	2.642927E-10	6.649294E-11
Pb	82	0.920889	-1.119111	0.147888	3.693023E-09	9.291212E-10
Bi	83	-0.521212	-1.171212	0.095787	1.345316E-10	3.384656E-11

Table A.16 Yields for 5 M$_\odot$, $Z = 0.0006$, $Y = 0.40$

El	Z	log ϵ(X)	[X/H]	[X/Fe]	M$_{yield}$	X$_{yield}$
H	1	12.000000	0.000000	1.214630	1.860427E+00	4.801415E-01
He	2	11.431289	0.501289	1.715919	2.008917E+00	5.184639E-01
C	6	7.620353	-0.849647	0.364983	9.386854E-04	2.422571E-04
N	7	8.193665	0.323665	1.538295	4.068249E-03	1.049939E-03
O	8	6.478995	-2.251005	-1.036376	8.970409E-05	2.315095E-05
F	9	2.407367	-2.012633	-0.798003	9.030958E-09	2.330721E-09
Ne	10	6.779980	-1.190020	0.024610	2.265756E-04	5.847492E-05
Na	11	4.305494	-1.934506	-0.719876	8.646010E-07	2.231373E-07
Mg	12	5.670251	-1.969749	-0.755120	2.194356E-05	5.663221E-06
Al	13	5.422504	-1.027496	0.187134	1.328864E-05	3.429549E-06
Si	14	6.661001	-0.888999	0.325631	2.391035E-04	6.170814E-05
P	15	4.139951	-1.270049	-0.055420	7.960223E-07	2.054384E-07
S	16	5.945620	-1.204380	0.010250	5.267379E-05	1.359412E-05
Cl	17	4.110102	-1.119898	0.094732	8.491439E-07	2.191481E-07
Ar	18	5.225189	-1.214811	-0.000181	1.134574E-05	2.928124E-06
K	19	3.874360	-1.205640	0.008990	5.453726E-07	1.407505E-07
Ca	20	5.075038	-1.214962	-0.000332	8.871044E-06	2.289450E-06
Sc	21	1.859840	-1.190160	0.024470	6.062689E-09	1.564667E-09
Ti	22	3.696196	-1.213804	0.000825	4.429693E-07	1.143221E-07
V	23	2.740907	-1.219093	-0.004463	5.225049E-08	1.348487E-08
Cr	24	4.406300	-1.233700	-0.019070	2.472761E-06	6.381732E-07
Mn	25	4.274855	-1.205145	0.009484	1.926770E-06	4.972633E-07
Fe	26	6.325370	-1.214630	0.000000	2.200384E-04	5.678778E-05
Co	27	3.698944	-1.171056	0.043573	5.487939E-07	1.416334E-07
Ni	28	4.989135	-1.210865	0.003764	1.066896E-05	2.753460E-06
Cu	29	3.110884	-1.139116	0.075513	1.527743E-07	3.942820E-08
Zn	30	3.437525	-1.192475	0.022155	3.340168E-07	8.620348E-08
Ga	31	1.966737	-1.113263	0.101366	1.202961E-08	3.104618E-09
Ge	32	2.429552	-1.150448	0.064181	3.620350E-08	9.343444E-09
As	33	1.136371	-1.163629	0.051001	1.910052E-09	4.929487E-10
Se	34	2.218604	-1.121396	0.093234	2.423111E-08	6.253596E-09
Br	35	1.365491	-1.174509	0.040121	3.457608E-09	8.923439E-10
Kr	36	2.250478	-0.999522	0.215108	2.791511E-08	7.204368E-09
Rb	37	1.563722	-0.956278	0.258352	5.851653E-09	1.510202E-09
Sr	38	1.847643	-1.032357	0.182273	1.149252E-08	2.966005E-09
Y	39	1.175010	-1.034990	0.179639	2.477493E-09	6.393946E-10
Zr	40	1.490954	-1.039046	0.175584	5.283831E-09	1.363658E-09
Nb	41	0.327327	-1.082673	0.131957	3.676407E-10	9.488117E-11
Mo	42	0.717178	-1.222822	-0.008193	9.347879E-10	2.412513E-10

Table A.16 Yields for 5 M$_\odot$, Z = 0.0006, Y = 0.40 (continued)

El	Z	log ϵ(X)	[X/H]	[X/Fe]	M$_{yield}$	X$_{yield}$
Ru	44	0.488184	-1.271816	-0.057186	5.777441E-10	1.491049E-10
Rh	45	-0.146798	-1.206798	0.007832	1.366633E-10	3.527024E-11
Pd	46	0.445600	-1.204400	0.010229	5.506140E-10	1.421032E-10
Ag	47	0.001279	-1.198721	0.015909	2.014745E-10	5.199679E-11
Cd	48	0.530404	-1.179596	0.035034	7.084582E-10	1.828398E-10
In	49	-0.439007	-1.199007	0.015623	7.785807E-11	2.009371E-11
Sn	50	0.866952	-1.203048	0.011581	1.621758E-09	4.185452E-10
Sb	51	-0.416506	-1.426506	-0.211877	8.627636E-11	2.226631E-11
Te	52	0.546923	-1.633077	-0.418447	8.198539E-10	2.115889E-10
I	53	0.322067	-1.227933	-0.013303	4.960025E-10	1.280089E-10
Xe	54	1.015481	-1.224519	-0.009889	2.524206E-09	6.514503E-10
Cs	55	-0.124811	-1.204811	0.009818	1.856322E-10	4.790818E-11
Ba	56	1.037499	-1.142501	0.072129	2.786895E-09	7.192454E-10
La	57	-0.004715	-1.174715	0.039915	2.558073E-10	6.601908E-11
Ce	58	0.401429	-1.178571	0.036059	6.574720E-10	1.696812E-10
Pr	59	-0.435283	-1.195283	0.019347	9.628283E-11	2.484880E-11
Nd	60	0.230465	-1.219535	-0.004906	4.554238E-10	1.175364E-10
Sm	62	-0.391687	-1.331687	-0.117057	1.129731E-10	2.915624E-11
Eu	63	-0.731272	-1.241272	-0.026642	5.252238E-11	1.355504E-11
Gd	64	-0.258615	-1.308615	-0.093985	1.605886E-10	4.144492E-11
Tb	65	-0.911433	-1.231433	-0.016803	3.627244E-11	9.361238E-12
Dy	66	-0.076766	-1.206766	0.007863	2.534813E-10	6.541878E-11
Ho	67	-0.761508	-1.231508	-0.016879	5.316041E-11	1.371970E-11
Er	68	-0.289097	-1.209097	0.005532	1.600490E-10	4.130564E-11
Tm	69	-1.101512	-1.221512	-0.006883	2.488786E-11	6.423091E-12
Yb	70	-0.333297	-1.253297	-0.038667	1.491272E-10	3.848693E-11
Lu	71	-1.122433	-1.212433	0.002196	2.456838E-11	6.340639E-12
Hf	72	-0.484739	-1.194739	0.019891	1.088257E-10	2.808587E-11
Ta	73	-1.335103	-1.215103	-0.000474	1.556640E-11	4.017395E-12
W	74	-0.544688	-1.194688	0.019942	9.761238E-11	2.519193E-11
Re	75	-0.968905	-1.228905	-0.014275	3.722637E-11	9.607428E-12
Os	76	0.132157	-1.217843	-0.003213	4.799074E-10	1.238551E-10
Ir	77	0.084079	-1.235921	-0.021292	4.340913E-10	1.120308E-10
Pt	78	0.386176	-1.233824	-0.019194	8.821412E-10	2.276641E-10
Au	79	-0.420062	-1.220062	-0.005432	1.393212E-10	3.595619E-11
Hg	80	-0.049332	-1.219332	-0.004702	3.326926E-10	8.586172E-11
Tl	81	-0.422508	-1.192508	0.022122	1.437475E-10	3.709854E-11
Pb	82	0.834443	-1.205557	0.009072	2.634731E-09	6.799747E-10
Bi	83	-0.559939	-1.209939	0.004691	1.071076E-10	2.764246E-11

Table A.17 Yields for 6 M$_\odot$, $Z = 0.0006$, $Y = 0.24$

El	Z	log ϵ(X)	[X/H]	[X/Fe]	M$_{yield}$	X$_{yield}$
H	1	12.000000	0.000000	1.339009	3.128908E+00	6.284591E-01
He	2	11.157866	0.227866	1.566875	1.800192E+00	3.615788E-01
C	6	7.895938	-0.574062	0.764947	2.994959E-03	6.015546E-04
N	7	9.000044	1.130044	2.469053	4.380927E-02	8.799342E-03
O	8	7.108678	-1.621322	-0.282313	6.431428E-04	1.291789E-04
F	9	2.340757	-2.079243	-0.740234	1.302877E-08	2.616903E-09
Ne	10	7.154245	-0.815755	0.523255	9.509363E-04	1.910010E-04
Na	11	5.428385	-0.811615	0.527394	1.929769E-05	3.876052E-06
Mg	12	6.802235	-0.837765	0.501244	5.071013E-04	1.018542E-04
Al	13	6.185177	-0.264823	1.074187	1.293999E-04	2.599071E-05
Si	14	6.339768	-1.210232	0.128777	1.925560E-04	3.867596E-05
P	15	4.518593	-0.891407	0.447603	3.201458E-06	6.430310E-07
S	16	5.826238	-1.323762	0.015248	6.733664E-05	1.352495E-05
Cl	17	3.937008	-1.292992	0.046017	9.624626E-07	1.933161E-07
Ar	18	5.103850	-1.336150	0.002860	1.444356E-05	2.901071E-06
K	19	3.773708	-1.306292	0.032718	7.276430E-07	1.461512E-07
Ca	20	4.950201	-1.339799	-0.000790	1.119809E-05	2.249201E-06
Sc	21	1.976813	-1.073187	0.265822	1.334806E-08	2.681035E-09
Ti	22	3.592585	-1.317415	0.021595	5.875876E-07	1.180203E-07
V	23	2.622597	-1.337403	0.001606	6.692058E-08	1.344138E-08
Cr	24	4.282068	-1.357932	-0.018923	3.124708E-06	6.276154E-07
Mn	25	4.143132	-1.336868	0.002141	2.392693E-06	4.805861E-07
Fe	26	6.200991	-1.339009	0.000000	2.780328E-04	5.584448E-05
Co	27	3.708478	-1.161522	0.177488	9.434592E-07	1.894992E-07
Ni	28	4.936371	-1.263629	0.075381	1.605580E-05	3.224899E-06
Cu	29	3.638378	-0.611622	0.727388	8.665898E-07	1.740595E-07
Zn	30	3.746317	-0.883683	0.455327	1.162009E-06	2.333960E-07
Ga	31	2.769297	-0.310703	1.028306	1.286357E-07	2.583721E-08
Ge	32	3.235991	-0.344009	0.995000	3.893527E-07	7.820372E-08
As	33	1.784872	-0.515128	0.823882	1.429968E-08	2.872173E-09
Se	34	3.167201	-0.172799	1.166210	3.614800E-07	7.260532E-08
Br	35	2.032689	-0.507311	0.831698	2.718448E-08	5.460158E-09
Kr	36	3.414951	0.164951	1.503961	6.911532E-07	1.388221E-07
Rb	37	2.783006	0.263006	1.602015	1.637460E-07	3.288932E-08
Sr	38	2.963049	0.083049	1.422058	2.520941E-07	5.063454E-08
Y	39	2.278872	0.068872	1.407881	5.292425E-08	1.063014E-08
Zr	40	2.597497	0.067497	1.406507	1.144305E-07	2.298403E-08
Nb	41	1.344730	-0.065270	1.273740	6.435849E-09	1.292677E-09
Mo	42	1.682886	-0.257114	1.081896	1.457687E-08	2.927847E-09

Table A.17 Yields for 6 M$_\odot$, Z = 0.0006, Y = 0.24 (continued)

El	Z	log ϵ(X)	[X/H]	[X/Fe]	M$_{yield}$	X$_{yield}$
Ru	44	1.335294	-0.424706	0.914304	6.829876E-09	1.371820E-09
Rh	45	0.279634	-0.780366	0.558644	6.135701E-10	1.232391E-10
Pd	46	1.236599	-0.413401	0.925608	5.722580E-09	1.149413E-09
Ag	47	0.458880	-0.741120	0.597890	9.732464E-10	1.954821E-10
Cd	48	1.334851	-0.375149	0.963860	7.595239E-09	1.525547E-09
In	49	0.191012	-0.568988	0.770022	5.586027E-10	1.121985E-10
Sn	50	1.694259	-0.375741	0.963268	1.832236E-08	3.680151E-09
Sb	51	0.171067	-0.838933	0.500077	5.613652E-10	1.127534E-10
Te	52	1.234132	-0.945868	0.393141	6.691495E-09	1.344025E-09
I	53	0.391007	-1.158993	0.180017	9.776956E-10	1.963758E-10
Xe	54	1.462679	-0.777321	0.561688	1.193471E-08	2.397155E-09
Cs	55	0.191699	-0.888301	0.450709	6.470585E-10	1.299654E-10
Ba	56	1.890071	-0.289929	1.049081	3.335631E-08	6.699805E-09
La	57	0.639739	-0.530261	0.808749	1.897348E-09	3.810932E-10
Ce	58	1.002094	-0.577906	0.761103	4.409690E-09	8.857115E-10
Pr	59	-0.005124	-0.765124	0.573886	4.360019E-10	8.757348E-11
Nd	60	0.634494	-0.815506	0.523503	1.939631E-09	3.895860E-10
Sm	62	-0.108637	-1.048637	0.290372	3.641996E-10	7.315158E-11
Eu	63	-0.739029	-1.249029	0.089981	8.676280E-11	1.742680E-11
Gd	64	-0.129305	-1.179305	0.159705	3.640848E-10	7.312851E-11
Tb	65	-0.889171	-1.209171	0.129838	6.421237E-11	1.289742E-11
Dy	66	0.029679	-1.100321	0.238689	5.449066E-10	1.094476E-10
Ho	67	-0.766466	-1.236466	0.102544	8.839158E-11	1.775395E-11
Er	68	-0.164751	-1.084751	0.254259	3.586721E-10	7.204134E-11
Tm	69	-1.023491	-1.143491	0.195518	5.009433E-11	1.006173E-11
Yb	70	-0.016862	-0.936862	0.402147	5.201093E-10	1.044669E-10
Lu	71	-0.897943	-0.987943	0.351067	6.936328E-11	1.393201E-11
Hf	72	-0.128216	-0.838216	0.500794	4.167696E-10	8.371056E-11
Ta	73	-1.044462	-0.924462	0.414548	5.112219E-11	1.026818E-11
W	74	-0.168774	-0.818774	0.520235	3.903800E-10	7.841005E-11
Re	75	-0.845177	-1.105177	0.233832	8.315233E-11	1.670162E-11
Os	76	0.139697	-1.210303	0.128706	8.198169E-10	1.646649E-10
Ir	77	-0.004176	-1.324176	0.014834	5.957722E-10	1.196642E-10
Pt	78	0.335508	-1.284492	0.054517	1.320445E-09	2.652190E-10
Au	79	-0.457743	-1.257743	0.081266	2.148404E-10	4.315192E-11
Hg	80	0.249999	-0.920001	0.419008	1.114933E-09	2.239408E-10
Tl	81	-0.007778	-0.777778	0.561231	6.281114E-10	1.261598E-10
Pb	82	1.051022	-0.988978	0.350032	7.293824E-09	1.465006E-09
Bi	83	-0.433032	-1.083032	0.255978	2.412724E-10	4.846093E-11

Table A.18   Yields for 6 M$_\odot$, $Z = 0.0006$, $Y = 0.30$

El	Z	log ϵ(X)	[X/H]	[X/Fe]	M$_{yield}$	X$_{yield}$
H	1	12.000000	0.000000	1.300956	2.866403E+00	5.826379E-01
He	2	11.248351	0.318351	1.619307	2.031180E+00	4.128668E-01
C	6	7.734738	-0.735262	0.565694	1.888207E-03	3.838055E-04
N	7	8.667838	0.797838	2.098794	1.867696E-02	3.796363E-03
O	8	6.815627	-1.914373	-0.613417	3.000565E-04	6.099083E-05
F	9	2.226262	-2.193738	-0.892783	9.169642E-09	1.863863E-09
Ne	10	6.859850	-1.110150	0.190805	4.302286E-04	8.745020E-05
Na	11	4.828960	-1.411040	-0.110085	4.446546E-06	9.038249E-07
Mg	12	6.311667	-1.328333	-0.027377	1.491687E-04	3.032071E-05
Al	13	5.922082	-0.527918	0.773038	6.468193E-05	1.314754E-05
Si	14	6.406826	-1.143174	0.157781	2.054579E-04	4.176231E-05
P	15	4.240816	-1.169184	0.131771	1.547086E-06	3.144676E-07
S	16	5.860425	-1.289575	0.011381	6.671593E-05	1.356098E-05
Cl	17	3.973387	-1.256613	0.044343	9.573451E-07	1.945943E-07
Ar	18	5.139746	-1.300254	0.000702	1.436309E-05	2.919507E-06
K	19	3.794150	-1.285850	0.015106	6.985886E-07	1.419983E-07
Ca	20	4.988277	-1.301723	-0.000768	1.119429E-05	2.275402E-06
Sc	21	1.859918	-1.190082	0.110873	9.342591E-09	1.899017E-09
Ti	22	3.615269	-1.294731	0.006225	5.666746E-07	1.151848E-07
V	23	2.656386	-1.303614	-0.002658	6.626645E-08	1.346962E-08
Cr	24	4.320057	-1.319943	-0.018987	3.123908E-06	6.349796E-07
Mn	25	4.184822	-1.295178	0.005778	2.412802E-06	4.904371E-07
Fe	26	6.239044	-1.300956	0.000000	2.779542E-04	5.649822E-05
Co	27	3.690958	-1.179042	0.121913	8.301314E-07	1.687362E-07
Ni	28	4.928494	-1.271506	0.029450	1.435001E-05	2.916847E-06
Cu	29	3.353089	-0.896911	0.404044	4.111058E-07	8.356321E-08
Zn	30	3.506663	-1.123337	0.177618	6.079095E-07	1.235664E-07
Ga	31	2.318342	-0.761658	0.539298	4.169014E-08	8.474125E-09
Ge	32	2.778466	-0.801534	0.499422	1.243946E-07	2.528501E-08
As	33	1.371443	-0.928557	0.372399	5.056400E-09	1.027787E-09
Se	34	2.653888	-0.686112	0.614844	1.015738E-07	2.064635E-08
Br	35	1.572096	-0.967904	0.333052	8.612716E-09	1.750659E-09
Kr	36	2.840413	-0.409587	0.891369	1.684182E-07	3.423345E-08
Rb	37	2.194213	-0.325787	0.975169	3.863734E-08	7.853599E-09
Sr	38	2.395010	-0.484990	0.815966	6.244927E-08	1.269372E-08
Y	39	1.722347	-0.487653	0.813302	1.346089E-08	2.736121E-09
Zr	40	2.055132	-0.474868	0.826088	3.004844E-08	6.107782E-09
Nb	41	0.818896	-0.591104	0.709852	1.756775E-09	3.570901E-10
Mo	42	1.168143	-0.771857	0.529099	4.077827E-09	8.288774E-10

Table A.18 Yields for 6 M$_\odot$, $Z = 0.0006$, $Y = 0.30$ (continued)

El	Z	log ϵ(X)	[X/H]	[X/Fe]	M$_{yield}$	X$_{yield}$
Ru	44	0.857760	-0.902240	0.398716	2.084078E-09	4.236191E-10
Rh	45	-0.035332	-1.095332	0.205623	2.721711E-10	5.532273E-11
Pd	46	0.782216	-0.867784	0.433172	1.841581E-09	3.743280E-10
Ag	47	0.131557	-1.068443	0.232512	4.193304E-10	8.523499E-11
Cd	48	0.881336	-0.828664	0.472291	2.449003E-09	4.977954E-10
In	49	-0.204848	-0.964848	0.336107	2.056775E-10	4.180693E-11
Sn	50	1.237627	-0.832373	0.468582	5.865744E-09	1.192297E-09
Sb	51	-0.207181	-1.217181	0.083774	2.152490E-10	4.375248E-11
Te	52	0.819594	-1.360406	-0.059450	2.362282E-09	4.801680E-10
I	53	0.290868	-1.259132	0.041824	7.112285E-10	1.445675E-10
Xe	54	1.143462	-1.096538	0.204417	5.233019E-09	1.063687E-09
Cs	55	-0.050236	-1.130236	0.170720	3.395886E-10	6.902632E-11
Ba	56	1.437336	-0.742664	0.558292	1.077803E-08	2.190790E-09
La	57	0.261984	-0.908016	0.392940	7.283434E-10	1.480464E-10
Ce	58	0.654494	-0.925506	0.375450	1.814591E-09	3.688419E-10
Pr	59	-0.282855	-1.042855	0.258100	2.107176E-10	4.283141E-11
Nd	60	0.360693	-1.089307	0.211648	9.468551E-10	1.924620E-10
Sm	62	-0.326836	-1.266836	0.034120	2.020298E-10	4.106549E-11
Eu	63	-0.778048	-1.288048	0.012907	7.265621E-11	1.476843E-11
Gd	64	-0.256903	-1.306903	-0.005947	2.484945E-10	5.051011E-11
Tb	65	-0.948868	-1.268868	0.032088	5.127039E-11	1.042145E-11
Dy	66	-0.083892	-1.213892	0.087064	3.842438E-10	7.810312E-11
Ho	67	-0.808168	-1.278168	0.022788	7.356195E-11	1.495253E-11
Er	68	-0.278121	-1.198121	0.102835	2.530705E-10	5.144025E-11
Tm	69	-1.106012	-1.226012	0.074943	3.794997E-11	7.713883E-12
Yb	70	-0.242489	-1.162489	0.138466	2.833174E-10	5.758837E-11
Lu	71	-1.075259	-1.165259	0.135697	4.221832E-11	8.581486E-12
Hf	72	-0.366007	-1.076007	0.224949	2.206285E-10	4.484594E-11
Ta	73	-1.250002	-1.130002	0.170953	2.917517E-11	5.930276E-12
W	74	-0.404206	-1.054206	0.246750	2.080109E-10	4.228122E-11
Re	75	-0.943918	-1.203918	0.097038	6.071624E-11	1.234146E-11
Os	76	0.091079	-1.258921	0.042035	6.723614E-10	1.366672E-10
Ir	77	0.011328	-1.308672	-0.007716	5.656473E-10	1.149760E-10
Pt	78	0.321875	-1.298125	0.002831	1.172196E-09	2.382658E-10
Au	79	-0.476962	-1.276962	0.023994	1.882960E-10	3.827390E-11
Hg	80	0.051164	-1.118836	0.182120	6.461711E-10	1.313436E-10
Tl	81	-0.236976	-1.006976	0.293980	3.394867E-10	6.900560E-11
Pb	82	1.095050	-0.944950	0.356006	7.402201E-09	1.504605E-09
Bi	83	-0.167293	-0.817293	0.483662	4.075585E-10	8.284218E-11

Table A.19   Yields for 6 M$_\odot$, $Z = 0.0006$, $Y = 0.35$

El	Z	$\log \epsilon(X)$	[X/H]	[X/Fe]	M$_{yield}$	X$_{yield}$
H	1	12.000000	0.000000	1.267631	2.618639E+00	5.419707E-01
He	2	11.323020	0.393020	1.660651	2.203717E+00	4.560958E-01
C	6	7.502193	-0.967807	0.299824	1.012836E-03	2.096232E-04
N	7	8.308984	0.438984	1.706615	7.467773E-03	1.545579E-03
O	8	6.644260	-2.085740	-0.818109	1.847479E-04	3.823663E-05
F	9	1.711648	-2.708352	-1.440721	2.561401E-09	5.301243E-10
Ne	10	6.750381	-1.219619	0.048012	2.982618E-04	6.173022E-05
Na	11	4.368355	-1.871645	-0.604014	1.406516E-06	2.911019E-07
Mg	12	6.086140	-1.553860	-0.286229	8.069237E-05	1.670062E-05
Al	13	5.655921	-0.794079	0.473552	3.201549E-05	6.626136E-06
Si	14	6.518213	-1.031787	0.235844	2.423722E-04	5.016294E-05
P	15	4.154120	-1.255880	0.011751	1.157596E-06	2.395837E-07
S	16	5.892865	-1.257135	0.010496	6.566629E-05	1.359073E-05
Cl	17	4.024279	-1.205721	0.061910	9.818526E-07	2.032107E-07
Ar	18	5.172368	-1.267632	-0.000001	1.414153E-05	2.926824E-06
K	19	3.820782	-1.259218	0.008413	6.785310E-07	1.404332E-07
Ca	20	5.022046	-1.267954	-0.000323	1.105240E-05	2.287477E-06
Sc	21	1.826109	-1.223891	0.043740	7.895818E-09	1.634170E-09
Ti	22	3.644312	-1.265688	0.001943	5.533232E-07	1.145194E-07
V	23	2.688727	-1.271273	-0.003642	6.521886E-08	1.349812E-08
Cr	24	4.353287	-1.286713	-0.019082	3.080587E-06	6.375785E-07
Mn	25	4.220469	-1.259531	0.008100	2.392807E-06	4.952311E-07
Fe	26	6.272369	-1.267631	0.000000	2.741376E-04	5.673732E-05
Co	27	3.649972	-1.220028	0.047603	6.900801E-07	1.428235E-07
Ni	28	4.939888	-1.260112	0.007519	1.341519E-05	2.776496E-06
Cu	29	3.130803	-1.119197	0.148434	2.251653E-07	4.660169E-08
Zn	30	3.420588	-1.209412	0.058219	4.530626E-07	9.376881E-08
Ga	31	2.042647	-1.037353	0.230278	2.017248E-08	4.175028E-09
Ge	32	2.513217	-1.066783	0.200848	6.175825E-08	1.278189E-08
As	33	1.178313	-1.121687	0.145944	2.961076E-09	6.128437E-10
Se	34	2.351300	-0.988700	0.278931	4.626945E-08	9.576228E-09
Br	35	1.398460	-1.141540	0.126091	5.260382E-09	1.088723E-09
Kr	36	2.518656	-0.731344	0.536287	7.325831E-08	1.516202E-08
Rb	37	1.864045	-0.655955	0.611676	1.649568E-08	3.414055E-09
Sr	38	2.096503	-0.783497	0.484134	2.870345E-08	5.940654E-09
Y	39	1.449689	-0.760311	0.507320	6.563786E-09	1.358484E-09
Zr	40	1.808792	-0.721208	0.546423	1.556029E-08	3.220459E-09
Nb	41	0.591034	-0.818966	0.448665	9.497134E-10	1.965589E-10
Mo	42	0.953176	-0.986824	0.280807	2.268445E-09	4.694923E-10

Table A.19 Yields for 6 M$_\odot$, Z = 0.0006, Y = 0.35 (continued)

El	Z	log ϵ(X)	[X/H]	[X/Fe]	M$_{yield}$	X$_{yield}$
Ru	44	0.671851	-1.088149	0.179482	1.241118E-09	2.568699E-10
Rh	45	-0.110136	-1.170136	0.097495	2.093038E-10	4.331888E-11
Pd	46	0.614746	-1.035254	0.232377	1.144165E-09	2.368038E-10
Ag	47	0.050008	-1.149992	0.117639	3.173890E-10	6.568892E-11
Cd	48	0.715905	-0.994095	0.273536	1.528690E-09	3.163877E-10
In	49	-0.325940	-1.085940	0.181691	1.421783E-10	2.942615E-11
Sn	50	1.076215	-0.993785	0.273846	3.695853E-09	7.649181E-10
Sb	51	-0.310064	-1.320064	-0.052433	1.551662E-10	3.211422E-11
Te	52	0.696148	-1.483852	-0.216221	1.625210E-09	3.363641E-10
I	53	0.296411	-1.253589	0.014042	6.580969E-10	1.362041E-10
Xe	54	1.081985	-1.158015	0.109616	4.147212E-09	8.583343E-10
Cs	55	-0.089320	-1.169320	0.098311	2.835356E-10	5.868238E-11
Ba	56	1.299178	-0.880822	0.386809	7.164640E-09	1.482841E-09
La	57	0.165351	-1.004649	0.262982	5.326490E-10	1.102405E-10
Ce	58	0.569256	-1.010744	0.256887	1.362312E-09	2.819531E-10
Pr	59	-0.336959	-1.096959	0.170672	1.699556E-10	3.517514E-11
Nd	60	0.308749	-1.141251	0.126380	7.676502E-10	1.588779E-10
Sm	62	-0.354448	-1.294448	-0.026817	1.732307E-10	3.585296E-11
Eu	63	-0.760460	-1.270460	-0.002829	6.912036E-11	1.430560E-11
Gd	64	-0.258762	-1.308762	-0.041131	2.260109E-10	4.677671E-11
Tb	65	-0.935375	-1.255375	0.012256	4.831679E-11	9.999960E-12
Dy	66	-0.082970	-1.212970	0.054661	3.517569E-10	7.280192E-11
Ho	67	-0.791087	-1.261087	0.006544	6.989930E-11	1.446682E-11
Er	68	-0.283527	-1.203527	0.064104	2.282844E-10	4.724724E-11
Tm	69	-1.105302	-1.225302	0.042329	3.472652E-11	7.187229E-12
Yb	70	-0.277155	-1.197155	0.070476	2.389358E-10	4.945172E-11
Lu	71	-1.094968	-1.184968	0.082663	3.685087E-11	7.626899E-12
Hf	72	-0.411215	-1.121215	0.146417	1.815658E-10	3.757805E-11
Ta	73	-1.283366	-1.163366	0.104265	2.468246E-11	5.108444E-12
W	74	-0.455372	-1.105372	0.162259	1.688798E-10	3.495247E-11
Re	75	-0.952675	-1.212675	0.054956	5.437220E-11	1.125323E-11
Os	76	0.105469	-1.244531	0.023100	6.350788E-10	1.314401E-10
Ir	77	0.039573	-1.280427	-0.012796	5.514845E-10	1.141389E-10
Pt	78	0.346365	-1.273635	-0.006004	1.132958E-09	2.344844E-10
Au	79	-0.455501	-1.255501	0.012131	1.807346E-10	3.740602E-11
Hg	80	0.011159	-1.158841	0.108790	5.383297E-10	1.114163E-10
Tl	81	-0.305098	-1.075098	0.192533	2.651214E-10	5.487127E-11
Pb	82	0.886940	-1.153060	0.114571	4.184800E-09	8.661138E-10
Bi	83	-0.524902	-1.174902	0.092729	1.634255E-10	3.382361E-11

Table A.20 Yields for 6 M$_\odot$, $Z = 0.0006$, $Y = 0.40$

El	Z	$\log \epsilon(X)$	[X/H]	[X/Fe]	M$_{\text{yield}}$	X$_{\text{yield}}$
H	1	12.000000	0.000000	1.223524	2.324904E+00	4.903105E-01
He	2	11.411550	0.481550	1.705074	2.398915E+00	5.059190E-01
C	6	7.622113	-0.847887	0.375637	1.190596E-03	2.510907E-04
N	7	8.591493	0.721493	1.945017	1.270680E-02	2.679799E-03
O	8	7.935902	-0.794098	0.429426	3.210529E-03	6.770842E-04
F	9	2.268295	-2.151705	-0.928182	8.193195E-09	1.727903E-09
Ne	10	6.806979	-1.163021	0.060503	3.015148E-04	6.358794E-05
Na	11	5.104894	-1.135106	0.088417	6.808097E-06	1.435793E-06
Mg	12	6.399199	-1.240801	-0.017277	1.458245E-04	3.075365E-05
Al	13	5.510643	-0.939357	0.284167	2.034286E-05	4.290205E-06
Si	14	6.338278	-1.211722	0.011801	1.423923E-04	3.002980E-05
P	15	4.189361	-1.220639	0.002884	1.114622E-06	2.350680E-07
S	16	5.936530	-1.213470	0.010053	6.447046E-05	1.359649E-05
Cl	17	4.020408	-1.209592	0.013932	8.654887E-07	1.825271E-07
Ar	18	5.216104	-1.223896	-0.000372	1.388457E-05	2.928186E-06
K	19	3.861494	-1.218506	0.005018	6.617101E-07	1.395513E-07
Ca	20	5.066157	-1.223843	-0.000319	1.086128E-05	2.290588E-06
Sc	21	1.839426	-1.210574	0.012950	7.228421E-09	1.524437E-09
Ti	22	3.686813	-1.223187	0.000337	5.417154E-07	1.142450E-07
V	23	2.731024	-1.228976	-0.005452	6.382627E-08	1.346063E-08
Cr	24	4.397403	-1.242597	-0.019073	3.027438E-06	6.384713E-07
Mn	25	4.268760	-1.211240	0.012284	2.374258E-06	5.007189E-07
Fe	26	6.316476	-1.223524	0.000000	2.693953E-04	5.681410E-05
Co	27	3.675054	-1.194946	0.028577	6.490988E-07	1.368916E-07
Ni	28	4.976975	-1.223025	0.000499	1.295846E-05	2.732872E-06
Cu	29	3.044585	-1.205415	0.018109	1.639144E-07	3.456870E-08
Zn	30	3.409663	-1.220337	0.003187	3.910429E-07	8.246895E-08
Ga	31	1.878074	-1.201926	0.021598	1.225280E-08	2.584054E-09
Ge	32	2.340423	-1.239577	-0.016053	3.686394E-08	7.774417E-09
As	33	1.076795	-1.223205	0.000318	2.080947E-09	4.388611E-10
Se	34	2.098528	-1.241472	-0.017949	2.297922E-08	4.846200E-09
Br	35	1.314585	-1.225415	-0.001892	3.839090E-09	8.096445E-10
Kr	36	2.068551	-1.181449	0.042075	2.286208E-08	4.821496E-09
Rb	37	1.352709	-1.167291	0.056233	4.487720E-09	9.464372E-10
Sr	38	1.690759	-1.189241	0.034283	1.000658E-08	2.110337E-09
Y	39	1.020946	-1.189054	0.034469	2.171405E-09	4.579382E-10
Zr	40	1.341370	-1.188630	0.034893	4.664425E-09	9.837035E-10
Nb	41	0.203815	-1.206185	0.017339	3.457040E-10	7.290721E-11
Mo	42	0.616972	-1.323028	-0.099504	9.268075E-10	1.954590E-10

Table A.20   Yields for 6 M$_\odot$, Z = 0.0006, Y = 0.40 (continued)

El	Z	log ϵ(X)	[X/H]	[X/Fe]	M$_{yield}$	X$_{yield}$
Ru	44	0.414258	-1.345742	-0.122218	6.090292E-10	1.284412E-10
Rh	45	-0.177110	-1.237110	-0.013586	1.592693E-10	3.358909E-11
Pd	46	0.380791	-1.269209	-0.045686	5.926866E-10	1.249946E-10
Ag	47	-0.030385	-1.230385	-0.006861	2.340498E-10	4.935990E-11
Cd	48	0.463826	-1.246174	-0.022650	7.594725E-10	1.601689E-10
In	49	-0.484537	-1.244537	-0.021013	8.761245E-11	1.847702E-11
Sn	50	0.797985	-1.272015	-0.048491	1.729155E-09	3.646700E-10
Sb	51	-0.456671	-1.466671	-0.243148	9.829219E-11	2.072932E-11
Te	52	0.497553	-1.682447	-0.458923	9.147287E-10	1.929116E-10
I	53	0.305857	-1.244143	-0.020619	5.971260E-10	1.259308E-10
Xe	54	0.988196	-1.251804	-0.028280	2.961689E-09	6.246052E-10
Cs	55	-0.146934	-1.226934	-0.003410	2.204564E-10	4.649314E-11
Ba	56	0.969123	-1.210877	0.012647	2.975672E-09	6.275541E-10
La	57	-0.047296	-1.217296	0.006227	2.898167E-10	6.112087E-11
Ce	58	0.361601	-1.218399	0.005125	7.496037E-10	1.580876E-10
Pr	59	-0.463580	-1.223580	-0.000056	1.127313E-10	2.377446E-11
Nd	60	0.204642	-1.245358	-0.021834	5.362963E-10	1.131022E-10
Sm	62	-0.411412	-1.351412	-0.127889	1.349123E-10	2.845232E-11
Eu	63	-0.746836	-1.256836	-0.033313	6.332472E-11	1.335486E-11
Gd	64	-0.272321	-1.322321	-0.098797	1.944408E-10	4.100657E-11
Tb	65	-0.926062	-1.246062	-0.022539	4.382681E-11	9.242852E-12
Dy	66	-0.090159	-1.220159	0.003365	3.071480E-10	6.477594E-11
Ho	67	-0.775528	-1.245528	-0.022005	6.432216E-11	1.356522E-11
Er	68	-0.302935	-1.222935	0.000588	1.937270E-10	4.085603E-11
Tm	69	-1.116481	-1.236481	-0.012958	3.004765E-11	6.336895E-12
Yb	70	-0.352747	-1.272747	-0.049223	1.781866E-10	3.757865E-11
Lu	71	-1.141421	-1.231421	-0.007898	2.938813E-11	6.197807E-12
Hf	72	-0.507093	-1.217093	0.006431	1.291629E-10	2.723979E-11
Ta	73	-1.357330	-1.237330	-0.013807	1.848219E-11	3.897799E-12
W	74	-0.569468	-1.219468	0.004055	1.152052E-10	2.429618E-11
Re	75	-0.988189	-1.248189	-0.024665	4.450144E-11	9.385126E-12
Os	76	0.119477	-1.230523	-0.006999	5.824756E-10	1.228411E-10
Ir	77	0.071010	-1.248990	-0.025467	5.263889E-10	1.110127E-10
Pt	78	0.378036	-1.241964	-0.018440	1.081895E-09	2.281662E-10
Au	79	-0.430966	-1.230966	-0.007442	1.697875E-10	3.580731E-11
Hg	80	-0.065891	-1.235891	-0.012367	4.001707E-10	8.439397E-11
Tl	81	-0.448542	-1.218542	0.004982	1.691845E-10	3.568015E-11
Pb	82	0.818396	-1.221604	0.001920	3.173124E-09	6.691956E-10
Bi	83	-0.572838	-1.222838	0.000685	1.299311E-10	2.740181E-11

APPENDIX B

Source code of Evel ChemEvol

The Evel ChemEvol chemical evolution code is written in Fortran 2008.

B.1. Main program

```fortran
 1 program echemevol
 2     use cemodel
 3
 4     implicit none
 5
 6     integer(kind=4) :: steplastoutput = 1
 7     real*8 :: serdt, sfrdt
 8     real*8 :: fetoh
 9     real*8 :: systemtimeelapsed
10     integer*8 :: sysclockstart = 0, sysclocknow, sysclockcountrate,
            sysclockcountmax
11     real*8, allocatable :: serspeciesdt(:)
12     integer :: speciesnum
13     integer :: iterations
14     logical :: acceptableerrors
15
16     open(unit=14, file=trim(filespath) // "out-log.txt", action="write",
            status="replace")
17
18     call initcemodel
19
20     allocate(serspeciesdt(size(species)))
21
22     open(unit=12, file=trim(filespath) // "out-cemodel.txt", action="write",
            status="replace")
```

```fortran
23      open(unit=13, file=trim(filespath) // "out-abundances.txt", action="write",
            status="replace")
24
25      write(12,'(A)') '#stepnum␣␣␣␣␣␣␣␣␣␣time␣␣␣␣␣␣␣␣␣␣Mgas␣␣␣␣␣␣␣␣Mstars␣␣␣␣␣␣␣␣␣␣
            SFR␣␣␣␣␣␣␣␣␣␣␣␣SER␣␣␣␣␣␣␣␣␣␣[Fe/H]'
26      write(13,'(A)') '#stepnum␣␣␣␣␣␣␣␣␣␣␣time␣[Fe/H]␣␣␣␣␣␣O␣␣␣␣␣␣Na␣␣␣␣␣␣Fe␣␣␣␣␣␣Rb␣
            ␣␣␣␣Sr␣␣␣␣␣␣Y␣␣␣␣␣Zr␣␣␣␣␣Ba␣␣␣␣␣La␣␣␣␣␣Ce&
27 ␣␣␣␣␣␣␣␣␣␣␣␣&␣␣␣␣␣Pr␣␣␣␣␣Nd␣␣␣␣␣Sm␣␣␣␣␣Eu␣␣␣␣␣Pb'
28
29      timestep = initialtimestep
30      do stepnum = 1, size(model)
31          iterations = 0
32          acceptableerrors = .false.
33          do while ((acceptableerrors .eqv. .false.) .and. (stepnum > 1)) !skip
                first model
34              iterations = iterations + 1
35              acceptableerrors = .true.
36              model(stepnum)%time = model(stepnum-1)%time + timestep
37
38              if (model(stepnum)%time > maxtime) then
39                  write(14,'(A,ES11.4,A)') 't␣>␣',maxtime,',␣finished!'
40                  goto 950
41              end if
42
43              ! all masses
44              stellarmasslow = minstellarmass
45              stellarmasshigh = maxstellarmass
46
47              !more accurate if SFR varies between model steps
48              !sfrdt = integral(starformationrate,model(stepnum-1)%time,model(
                    stepnum)%time,1,1.d0,&
49              ! error,label='sfr time integral')
50              !if (error/timestep > maxerrorser .and. timestep > mintimestep)
                    then
51              ! write(14,*),'Restepping: star formation rate error too high:',
                    error/timestep
52              ! goto 900
53              !end if
54
55              sfrdt = model(stepnum-1)%sfr * timestep
56
57              !serdt = integral(stellarejectionrate,model(stepnum-1)%time,model(
                    stepnum)%time,10,&
58              ! max(maxchangeser*model(stepnum-1)%ser,1d-8),error,label='ser time
                     integral')
59              !model(stepnum)%ser = serdt/timestep
60
61              ! this variable is read by stellarejectionrate and
                    stellarejectionrateofspecies
```

```
62          ! make sure it is accurate enough to determined whether dSER/SER >
                maxchangeser
63          maxerrorser = maxchangeser / 2.d0
64
65          model(stepnum)%ser = stellarejectionrate(model(stepnum)%time)
66          serdt = model(stepnum)%ser * timestep
67
68          if (model(stepnum-1)%ser > 1.0d-8 .and. model(stepnum)%ser > 1.0e
                -8) then
69              if (abs(model(stepnum)%ser/model(stepnum-1)%ser - 1) >
                    maxchangeser &
70                  .and. timestep > mintimestep) then
71                  write(14,'(A,ES9.2,A,ES9.2)') 'Restepping:␣dSER/SER␣=␣',&
72                      abs(model(stepnum)%ser/model(stepnum-1)%ser - 1),'␣>␣
                        ',maxchangeser
73                  goto 900
74              end if
75          end if
76
77          !$omp parallel do simd
78          do speciesnum = 1, size(species)
79              !serspeciesdt(speciesnum) = integral(
                    stellarejectionrateofspecies,model(stepnum-1)%time,&
80              ! model(stepnum)%time,10,maxchangeser,intarg=speciesnum,&
81              ! label='ser species time integral')
82              serspeciesdt(speciesnum) = stellarejectionrateofspecies(model(
                    stepnum)%time, speciesnum) * timestep
83          end do
84          !$omp end parallel do simd
85
86          model(stepnum)%starsmass = model(stepnum-1)%starsmass + sfrdt -
                serdt
87          model(stepnum)%gasmass = model(stepnum-1)%gasmass - sfrdt + serdt
88
89          if (model(stepnum)%gasmass < 0.0d0 .and. timestep > mintimestep)
                then
90              write(14,'(A,ES11.4,A,ES9.2)') 'Restepping:␣Negative␣gas␣mass.␣
                    Mgas=',model(stepnum)%gasmass,',␣SFR*dt=',sfrdt
91              goto 900
92          end if
93
94          if (abs(model(stepnum)%gasmass/model(stepnum-1)%gasmass - 1) >
                maxchangemgas .and. timestep > mintimestep) then
95              write(14,'(A,ES9.2,A,ES9.2)') 'Restepping:␣dMgas/Mgas␣=␣',&
96                  abs(model(stepnum)%gasmass/model(stepnum-1)%gasmass - 1),
                        '␣>␣',maxchangemgas
97              goto 900
98          end if
99
100         do concurrent (speciesnum = 1:size(species))
```

```
101            model(stepnum)%speciesmassfrac(speciesnum) = (1.0d0 / model(
                  stepnum)%gasmass) * &
102               (model(stepnum-1)%speciesmassfrac(speciesnum) * model(
                     stepnum-1)%gasmass + &
103               serspeciesdt(speciesnum) - model(stepnum-1)%speciesmassfrac(
                     speciesnum) * sfrdt)
104        end do
105
106        timestep = min(timestep * (1.00d0 + timestepgrowthrate),maxtimestep
              )
107        exit
108  900 continue
109        acceptableerrors = .false.
110        timestep = max(timestep * 0.5d0, mintimestep)
111        cycle
112     end do
113
114     ! will be overwritten with zero afterwards if SF is switched off
115     model(stepnum)%sfr = model(stepnum)%gasmass * sfrefficiency
116
117     if (stepnum == 1) then
118        if (model(stepnum)%gasmass > sfrstartmgasabove) then
119           write(14,'(A,ES9.2)') 'Starting␣star␣formation,␣Mgas␣>',
                  sfrstartmgasabove
120        else
121           model(stepnum)%sfr = 0.0d0
122        end if
123     elseif (model(stepnum-1)%sfr > 0.0d0) then !SF was active in the
              previous step
124        if (model(stepnum)%gasmass < sfrendmgasbelow) then
125           write(14,'(A,ES9.2)') 'Ending␣star␣formation,␣Mgas␣<',
                  sfrendmgasbelow
126           model(stepnum)%sfr = 0.0d0
127        end if
128     elseif (model(stepnum-1)%sfr <= 0.0d0) then !no SF in previous step
129        if (model(stepnum)%gasmass > sfrstartmgasabove) then
130           write(14,'(A,ES9.2)') 'Starting␣star␣formation,␣Mgas␣>',
                  sfrstartmgasabove
131        else
132           model(stepnum)%sfr = 0.0d0
133        end if
134     end if
135
136     if (stepnum - steplastoutput >= 1 .or. stepnum == 1) then
137
138        ! Asplund et al. (ARAA, 2009)
139        fetoh = logepsilon('fe') - 7.50d0
140
141        call SYSTEM_CLOCK(sysclocknow, sysclockcountrate, sysclockcountmax)
142        if (sysclockstart /= 0) then
```

```fortran
143              systemtimeelapsed = float(sysclocknow - sysclockstart) / float(
                     sysclockcountrate)
144          else
145              systemtimeelapsed = 0.0d0
146          end if
147          sysclockstart = sysclocknow
148
149          ! structure output
150          write(12,'(I7,1X,*(ES13.4))') stepnum,model(stepnum)%time,model(
                 stepnum)%gasmass,model(stepnum)%starsmass,&
151          model(stepnum)%sfr,serdt/timestep,fetoh
152          flush(12)
153
154          ! abundance output
155          write(13,'(I7,1X,ES13.4,*(F7.3))') stepnum,model(stepnum)%time,
                 fetoh,logepsilon('o'),logepsilon('na'),&
156              logepsilon('fe'),logepsilon('rb'),&
157              logepsilon('sr'),logepsilon('y'),logepsilon('zr'),logepsilon('ba
                     '),&
158              logepsilon('la'),logepsilon('ce'),logepsilon('pr'),logepsilon('
                     nd'),logepsilon('sm'),&
159              logepsilon('eu'),logepsilon('pb')
160          flush(13)
161
162          ! log output
163          write(14,'(A)')'-------------------------'
164          write(14,'(A,ES11.4,A,I6,A,ES11.4)') 't=',model(stepnum)%time,',␣
                 StepNum=',stepnum,',␣dt=',timestep
165          write(14,'(A,ES11.4,A,ES11.4)') 'Mgas=',model(stepnum)%gasmass,',␣
                 Mstars=',model(stepnum)%starsmass
166          write(14,'(A,ES11.4,A,ES11.4)') 'SFR=',model(stepnum)%sfr,',␣SER=',
                 model(stepnum)%ser
167          write(14,'(A,F6.2,A,ES11.4,A,ES11.4)') '[Fe/H]=',fetoh,',␣X(Sr)=',
                 elmassfrac('sr'),',␣X(Ba)=',elmassfrac('ba')
168          write(14,'(A,F6.2)') 'e(CNO)=',logepsiloncno()
169          if (stepnum > 1) then
170              write(14,'(A,F9.4)') 'performance␣(models/sec)=',(stepnum -
                     steplastoutput)/systemtimeelapsed
171              write(14,'(A,ES11.2)') 'performance␣(years/sec)=',&
172                  (model(stepnum)%time - model(steplastoutput)%time)/
                         systemtimeelapsed
173              !if (iterations > 1) then
174              ! write(14,'(A,I4)') 'iterations=',iterations
175              !end if
176          end if
177
178          flush(14)
179          steplastoutput = stepnum
180      end if
181  end do
```

```
182
183 950 call closefiles
184
185 contains
186 subroutine initcemodel()
187     integer :: s
188
189     write(14,'(A)',advance="no") 'Normalising␣IMF...'
190     flush(14)
191     imfnormfactor = 1.0d0 ! a value is required to calculate the following
            integral
192     imfnormfactor = 1.0d0 / integral(mimf,0.1d0,100.0d0,100,1.d-6,label='IMF␣
            normalisation')
193     write(14,'(A)') 'done.'
194     flush(14)
195
196     call initconfig
197     call initspecies
198     call inityields
199
200     allocate(model(1:maxmodelnum))
201     do s=1,size(model)
202         allocate(model(s)%speciesmassfrac(1:size(species)))
203         model(s)%speciesmassfrac = 0.0d0
204     end do
205
206     call loadinitialcomposition
207
208     model(1)%time = 0.0d0
209     model(1)%gasmass = initialgasmass
210     model(1)%starsmass = 0.0d0
211     model(1)%ser = 0.0d0
212
213 end subroutine
214
215 end program
```

B.2.   Chemical evolution module

```
 1 module cemodel
 2
 3     implicit none
 4
 5     real*8 :: minstellarmass = 0.1d0, maxstellarmass = 100.0d0
 6     real*8 :: maxtime = 1.3d10, initialgasmass = 1.4d5
 7     integer :: maxmodelnum = 10**6
 8     real*8 :: stellarmasslow, stellarmasshigh !used for integrals
 9     real*8 :: sfrefficiency = 0.0d0, maxchangemgas = 0.10, maxchangeser = 0.10
10     real*8 :: sfrstartmgasabove = 1.0d2, sfrendmgasbelow = 1.0d-6
```

```fortran
11     real*8 :: initialcompscalez = 1.0d0
12     real*8 :: timestepgrowthrate = 0.03d0
13     character(len=50), parameter :: filespath = "./"
14     real*8 :: initialtimestep = 1.0d2, mintimestep = 1.0d2, maxtimestep = 6.0
          d6
15     real*8 :: maxerrorser = 5.d-6
16     integer :: serintegralsteps = 80000
17     real*8 :: imfnormfactor = 1.0 ! to be replaced during initialisation
18
19     integer:: stepnum
20     real*8 :: timestep
21
22     type stellarmodeldata
23         real*8 :: mass
24         real*8 :: remnantmass
25         real*8 :: stellarlifetime
26         real*8 :: lifetimemassexponent ! lifetime = C * mass ^ exponent to
              match upper model set automatically on initialisation
27         real*8, allocatable :: yield(:)
28     end type
29
30     type(stellarmodeldata), allocatable :: stellarmodel(:)
31
32     type speciestype
33         character (len=6) :: name ! h, d, he4, etc
34         character (len=3) :: symbol ! h, he, c, fe, etc
35         integer :: z ! number of protons (atomic number)
36         integer :: a ! number of nucleons (mass number)
37         logical :: yieldisrelative
38         logical :: foundyields = .false.
39         logical :: foundinitialvalue = .false.
40     end type
41
42     type(speciestype), allocatable :: species(:)
43
44     type modelstate
45         real*8 :: time
46         real*8 :: gasmass
47         real*8 :: starsmass
48         real*8 :: sfr ! star formation rate (Msun / year)
49         real*8 :: ser ! stellar ejection rate (Msun / year)
50         real*8, allocatable :: speciesmassfrac(:)
51     end type
52
53     type(modelstate), allocatable :: model(:)
54
55 interface
56   pure real*8 function fi(x, realargin, intargin)
57     real*8, intent(in) :: x
58     real*8, intent(in), optional :: realargin
```

```fortran
59      integer, intent(in), optional :: intargin
60    end function fi
61 end interface
62
63 contains
64
65 pure real*8 function pastspeciesmassfrac(time,species)
66     real*8, intent(in) :: time
67     integer, intent(in) :: species
68     integer :: i
69     real*8 :: weight2
70
71     pastspeciesmassfrac = model(1)%speciesmassfrac(species)
72     do i = 2,stepnum
73        if (model(i)%time > time) then
74            weight2 = (time - model(i-1)%time) / (model(i)%time - model(i-1)%&
                  time)
75            pastspeciesmassfrac = (1-weight2) * model(i-1)%speciesmassfrac(
                  species) +&
76                weight2 * model(i)%speciesmassfrac(species)
77            exit
78        end if
79     end do
80 end function
81
82 pure integer function findmodelnum(time)
83     real*8, intent(in) :: time
84     integer :: low, middle, high
85
86     low = 1
87     high = stepnum
88
89     do while (high - low > 1)
90        middle = (high + low) / 2
91        if (model(middle)%time > time) then
92            high = middle
93        else
94            low = middle
95        end if
96     end do
97     findmodelnum = low
98 end function findmodelnum
99
100 ! calculate log epsilon abundance of an element in the current timestep
101 pure real*8 function logepsilon(symbol)
102     character (len=*), intent(in) :: symbol
103     real*8 :: eldensitysum
104     integer :: s, hydrogenindex
105
106     hydrogenindex = 1
```

```fortran
107     eldensitysum = 0.0d0
108     do s = 1,size(species)
109         if (species(s)%z == 1 .and. species(s)%a == 1) then
110             hydrogenindex = s
111         end if
112
113         if (trim(adjustl(species(s)%symbol)) == trim(adjustl(symbol))) then
114             eldensitysum = eldensitysum + (model(stepnum)%speciesmassfrac(s) /
                    species(s)%a)
115         end if
116     end do
117
118     logepsilon = log10(eldensitysum / model(stepnum)%speciesmassfrac(
            hydrogenindex)) + 12.0d0
119 end function logepsilon
120
121 ! calculate log epsilon abundance of C+N+O in the current timestep
122 pure real*8 function logepsiloncno()
123     real*8 :: eldensitysum
124     integer :: s, hydrogenindex
125
126     hydrogenindex = 1
127     eldensitysum = 0.0d0
128     do s = 1,size(species)
129         if (species(s)%z == 1 .and. species(s)%a == 1) then
130             hydrogenindex = s
131         end if
132
133         if (trim(adjustl(species(s)%symbol)) == trim(adjustl('c')) .or. trim(
                adjustl(species(s)%symbol)) == trim(adjustl('n')) &
134             .or. trim(adjustl(species(s)%symbol)) == trim(adjustl('o'))) then
135             eldensitysum = eldensitysum + (model(stepnum)%speciesmassfrac(s) /
                    species(s)%a)
136         end if
137     end do
138
139     logepsiloncno = log10(eldensitysum / model(stepnum)%speciesmassfrac(
            hydrogenindex)) + 12.0d0
140 end function logepsiloncno
141
142
143 ! calculate mass fraction of an element in the current timestep
144 pure real*8 function elmassfrac(symbol)
145     character (len=*), intent(in) :: symbol
146     real*8 :: elmassfracsum
147     integer :: s
148
149     elmassfracsum = 0.0d0
150     do s = 1,size(species)
151         if (trim(adjustl(species(s)%symbol)) == trim(adjustl(symbol))) then
```

```fortran
152            elmassfracsum = elmassfracsum + model(stepnum)%speciesmassfrac(s)
153        end if
154    end do
155
156    elmassfrac = elmassfracsum
157 end function elmassfrac
158
159 ! returns main sequence lifetime in years of a star
160 ! with initial mass in solar masses
161 pure real*8 function stellarlifetime(initmass)
162    implicit none
163    real*8, intent(in) :: initmass
164    integer :: i
165    integer :: modelindex ! reference model to interpolate from
166 ! real*8 :: c
167
168 ! stellarlifetime = 1.d+10 * (mass ** (-3.1d0))
169
170    ! interpolate lifetime from ev. model data
171    if (initmass < stellarmodel(1)%mass) then
172        modelindex = 1
173    else if (initmass > stellarmodel(size(stellarmodel))%mass) then
174 ! stellarlifetime = stellarmodel(size(stellarmodel))%stellarlifetime * &
175 ! (initmass / stellarmodel(size(stellarmodel))%mass) ** (-3.5)
176        modelindex = size(stellarmodel)
177    else
178        do i = 2, size(stellarmodel)
179            if (stellarmodel(i)%mass >= initmass) then
180                ! linear interpolation
181 ! c = (initmass - stellarmodel(i-1)%mass) / (stellarmodel(i)%mass -
      stellarmodel(i-1)%mass)
182 ! stellarlifetime = c * stellarmodel(i)%stellarlifetime + (1-c) * stellarmodel
      (i-1)%stellarlifetime
183                modelindex = i - 1
184                exit
185            end if
186        end do
187    end if
188    stellarlifetime = stellarmodel(modelindex)%stellarlifetime * &
189            (initmass/stellarmodel(modelindex)%mass) ** stellarmodel(modelindex
                )%lifetimemassexponent
190 end function stellarlifetime
191
192 ! remnant mass as a function of initial mass in solar masses
193 pure real*8 function remnantmass(initmass)
194    implicit none
195    real*8, intent(in) :: initmass
196    integer :: i
197    real*8 :: c
198
```

```
199 ! Iben & Tutukov 1984, in Pagel 2009 after eqn 7.10
200 ! if (mass <= 0.506) then
201 ! remnantmass = mass
202 ! else if (mass <= 9.5) then
203 ! remnantmass = 0.45d0 + 0.11d0 * mass
204 ! else
205 ! remnantmass = 1.5d0
206 ! end if
207
208     if (initmass < stellarmodel(1)%mass) then
209         c = (initmass - stellarmodel(1)%mass) / (stellarmodel(2)%mass -
                stellarmodel(1)%mass)
210         remnantmass = (1-c) * stellarmodel(1)%remnantmass + c * stellarmodel(2)
                %remnantmass
211         ! scale lowest mass end with initial mass
212 ! remnantmass = stellarmodel(1)%remnantmass * initmass / stellarmodel(1)%mass
213     else if (initmass > stellarmodel(size(stellarmodel))%mass) then
214         c = (stellarmodel(size(stellarmodel))%remnantmass - stellarmodel(size(
                stellarmodel)-1)%remnantmass) / &
215         (stellarmodel(size(stellarmodel))%mass - stellarmodel(size(
                stellarmodel)-1)%mass)
216         remnantmass = stellarmodel(size(stellarmodel))%remnantmass + c * (
                initmass - stellarmodel(size(stellarmodel))%mass)
217
218 ! remnantmass = stellarmodel(size(stellarmodel))%remnantmass
219     else
220     ! interpolate remnant mass from ev model data
221         do i = 2, size(stellarmodel)
222             if (stellarmodel(i)%mass >= initmass) then
223                 c = (initmass - stellarmodel(i-1)%mass) / (stellarmodel(i)%mass
                        - stellarmodel(i-1)%mass)
224                 remnantmass = c * stellarmodel(i)%remnantmass + (1-c) *
                        stellarmodel(i-1)%remnantmass
225                 exit
226             end if
227         end do
228     end if
229 end function remnantmass
230
231 ! relative or absolute yield of species in solar masses from a star with
232 ! initial mass in solar masses
233 pure real*8 function yield(species, initmass)
234     implicit none
235     real*8, intent(in) :: initmass
236     integer, intent(in) :: species
237     integer :: i
238     real*8 :: c
239
240     yield = 0.0
241
```

```fortran
242     if ((initmass >= stellarmodel(1)%mass) .and. (initmass <= stellarmodel(
            size(stellarmodel))%mass)) then
243        do i = 2, size(stellarmodel)
244           if (stellarmodel(i)%mass >= initmass) then
245              c = (initmass - stellarmodel(i-1)%mass) / (stellarmodel(i)%mass
                     - stellarmodel(i-1)%mass)
246              yield = (1-c) * stellarmodel(i-1)%yield(species) + c *
                     stellarmodel(i)%yield(species)
247              exit
248           end if
249        end do
250     end if
251 end function yield
252
253 ! stellar ejection rate in solar masses per year
254 pure real*8 function stellarejectionrate(time)
255     implicit none
256     real*8, intent(in) :: time
257
258     stellarejectionrate = integral(dserbydmass, stellarmasshigh**(-3),
            stellarmasslow**(-3), serintegralsteps,&
259        maxerrorser, realarg=time, label='ser mass integral')
260 end function stellarejectionrate
261
262 ! D stellar ejection rate / D mass
263 pure real*8 function dserbydmass(mdashexp, time, dummyint)
264     implicit none
265     real*8, intent(in) :: mdashexp
266     real*8, intent(in), optional :: time
267     integer, intent(in), optional :: dummyint
268     real*8 :: timeatbirth, mdash
269
270     mdash = mdashexp ** (-1.d0/3.d0)
271
272     timeatbirth = time - stellarlifetime(mdash)
273
274     if (timeatbirth >= 0.0d0) then
275        dserbydmass = (mdash - remnantmass(mdash)) * &
276                 starformationrate(timeatbirth) * imf(mdash)
277     else
278        dserbydmass = 0.0d0
279     end if
280     dserbydmass = dserbydmass * (1.d0/3.d0) * mdashexp ** (-4.d0/3.d0) !
            required for integral change of variables
281 end function dserbydmass
282
283 ! stellar ejection rate of species speciesnum in solar masses per year
284 pure real*8 function stellarejectionrateofspecies(time, speciesnum)
285     implicit none
286     real*8, intent(in) :: time
```

```fortran
287     integer, intent(in) :: speciesnum
288
289     stellarejectionrateofspecies = integral(dserbydmassofspecies,
            stellarmasshigh**(-3), stellarmasslow**(-3), serintegralsteps,&
290         maxerrorser, intarg=speciesnum, realarg=time, label='ser species mass
            integral')
291 end function
292
293 ! D stellar ejection rate / D mass of species
294 pure real*8 function dserbydmassofspecies(mdashexp, time, speciesnum)
295     implicit none
296     real*8, intent(in) :: mdashexp
297     real*8, intent(in), optional :: time
298     integer, intent(in), optional :: speciesnum
299     real*8 :: timeatbirth, mdash
300
301     mdash = mdashexp ** (-1.d0/3.d0)
302
303     timeatbirth = time - stellarlifetime(mdash)
304     if (timeatbirth >= 0.0d0) then
305         if (species(speciesnum)%yieldisrelative .eqv. .true.) then
306             ! use relative yields
307             dserbydmassofspecies = ((mdash - remnantmass(mdash)) * &
308                 pastspeciesmassfrac(timeatbirth,speciesnum) + &
309                 yield(speciesnum, mdash)) * &
310                 starformationrate(timeatbirth) * imf(mdash)
311 ! if (dserbydmassofspecies < 0.0d0) then
312                 !write(14,*) 'WARNING: Negative ejection rate, species:',
                        speciesnum,', mass:',mdash
313                 !dserbydmassofspecies = 0.0d0
314 ! end if
315         else
316             ! use absolute yields
317             dserbydmassofspecies = yield(speciesnum, mdash) * &
318                 starformationrate(timeatbirth) * imf(mdash)
319         end if
320     else
321         dserbydmassofspecies = 0.0d0
322     end if
323     dserbydmassofspecies = dserbydmassofspecies * (1.d0/3.d0) * mdashexp **
            (-4.d0/3.d0) !required for integral change of variables
324 end function
325
326 !integrate with Simpson's rule (and mid-point to measure error)
327 pure recursive function integral(f,x1,x2,numsteps,maxerror,intarg,realarg,
        label,recurdepth) result(integralresult)
328     implicit none
329 ! real*8, external :: f
330     procedure(fi) :: f
331     integer, intent(in), optional :: intarg
```

```fortran
332     character(*), intent(in), optional :: label
333     real*8, intent(in), optional :: realarg
334     real*8, intent(in) :: x1,x2
335     real*8, intent(in) :: maxerror
336     integer, intent(in) :: numsteps
337     integer, intent(in), optional:: recurdepth
338     integer :: precurdepth ! passed to the next function
339     integer :: i
340     real*8 :: stepsize,sum,sumloworder,loworderintegral,xdash,error
341     real*8 :: integralresult
342
343     if (present(recurdepth)) then
344        precurdepth = recurdepth
345     else
346        precurdepth = 0
347     end if
348
349     stepsize = (x2 - x1) / numsteps
350
351     ! add up the boundary terms and the first midpoint
352     if (present(intarg) .and. present(realarg)) then
353        sumloworder = f(x1,realarg,intarg) + f(x2,realarg,intarg)
354        sum = sumloworder + 4 * f(x1 + stepsize * 0.5d0,realarg,intarg)
355     else if (present(realarg)) then
356        sumloworder = f(x1,realarg) + f(x2,realarg)
357        sum = sumloworder + 4 * f(x1 + stepsize * 0.5d0,realarg)
358     else
359        sumloworder = f(x1) + f(x2)
360        sum = sumloworder + 4 * f(x1 + stepsize * 0.5d0)
361     end if
362
363     !!$omp parallel do private (i,xdash) reduction (+: sum,sumloworder)
364     do i = 1,numsteps-1
365        xdash = x1 + stepsize * i
366        if (present(intarg) .and. present(realarg)) then
367           sum = sum + 2 * f(xdash,realarg,intarg) + 4 * f(xdash + stepsize *
                 0.5d0,realarg,intarg)
368           sumloworder = sumloworder + 2 * f(xdash,realarg,intarg)
369        else if (present(realarg)) then
370           sum = sum + 2 * f(xdash,realarg) + 4 * f(xdash + stepsize * 0.5d0,
                 realarg)
371           sumloworder = sumloworder + 2 * f(xdash,realarg)
372        else
373           sum = sum + 2 * f(xdash) + 4 * f(xdash + stepsize * 0.5d0)
374           sumloworder = sumloworder + 2 * f(xdash)
375        end if
376     end do
377     !!$omp end parallel do
378
379     integralresult = sum * stepsize * (1.d0/6.d0)
```

```
380     loworderintegral = sumloworder * stepsize * 0.5d0
381     error = abs(loworderintegral/integralresult - 1.0d0)
382     if (error > maxerror .and. maxerror > 1e-14) then
383         if (precurdepth >= 19) then
384 ! if (present(label)) then
385 ! write(14,'(A,A,I8,A,ES10.3,A,ES10.3,A,ES10.3)') label,' reached maximum
        depth of ',precurdepth,', ',&
386 ! integralresult,' error ',error,' >',maxerror
387 ! else
388 ! write(14,'(A,I8,A,ES10.3,A,ES10.3,A,ES10.3)') 'Integrator recursing to ',
        precurdepth,', ',&
389 ! integralresult,' error',error,' >',maxerror
390 ! end if
391         else
392         !loworderintegral = integralresult
393 ! if (present(label)) then
394 ! write(14,'(A,A,I8,A,ES10.3,A,ES10.3,A,ES10.3)') label,' recursing to ',
        numsteps*2**(precurdepth+1),' steps ',&
395 ! integralresult,' error ',error,' >',maxerror
396 ! else
397 ! write(14,'(A,I8,A,ES10.3,A,ES10.3,A,ES10.3)') 'Integrator recursing to ',
        numsteps*2**(precurdepth+1),' steps ',&
398 ! integralresult,' error',error,' >',maxerror
399 ! end if
400             if (present(intarg) .and. present(realarg)) then
401                 integralresult = integral(f,x1,x1+(x2-x1)*0.5,numsteps,maxerror,
                    intarg=intarg,&
402                 realarg=realarg,label=label,recurdepth=precurdepth+1) +&
403                 integral(f,(x2+x1)*0.5,x2,numsteps,maxerror,intarg=intarg,&
404                 realarg=realarg,label=label,recurdepth=precurdepth+1)
405             else if (present(intarg)) then
406                 integralresult = integral(f,x1,x1+(x2-x1)*0.5,numsteps,maxerror,
                    intarg=intarg,&
407                 label=label,recurdepth=precurdepth+1) +&
408                 integral(f,(x2+x1)*0.5,x2,numsteps,maxerror,intarg=intarg,&
409                 label=label,recurdepth=precurdepth+1)
410             else if (present(realarg)) then
411                 integralresult = integral(f,x1,x1+(x2-x1)*0.5,numsteps,maxerror,
                    realarg=realarg,&
412                 label=label,recurdepth=precurdepth+1) +&
413                 integral(f,(x2+x1)*0.5,x2,numsteps,maxerror,realarg=realarg
                    ,&
414                 label=label,recurdepth=precurdepth+1)
415             else
416                 integralresult = integral(f,x1,x1+(x2-x1)*0.5,numsteps,maxerror
                    ,&
417                     label=label,recurdepth=precurdepth+1) +&
418                 integral(f,(x2+x1)*0.5,x2,numsteps,maxerror,&
419                 label=label,recurdepth=precurdepth+1)
420         end if
```

```fortran
421             end if
422         end if
423 end function integral
424
425 ! sort stellarmodel array entries by initial mass, required for interpolation
        to work
426 subroutine sortstellarmodels()
427     integer :: i,j,minkeyposition
428     real*8 :: minkeyvalue
429     type(stellarmodeldata) :: temp
430
431     do i = 1,size(stellarmodel)-1
432         minkeyposition = i
433         minkeyvalue = stellarmodel(i)%mass
434         do j = i+1,size(stellarmodel)
435             if (stellarmodel(i)%mass == stellarmodel(j)%mass) then
436                 write(14,*),"ERROR: multiple ev. models with same mass",
                        stellarmodel(i)%mass
437                 stop
438             end if
439             if (stellarmodel(j)%mass < minkeyvalue) then
440                 minkeyposition = j
441                 minkeyvalue = stellarmodel(j)%mass
442             end if
443         end do
444         if (minkeyvalue < stellarmodel(i)%mass) then
445             temp = stellarmodel(i)
446             stellarmodel(i) = stellarmodel(minkeyposition)
447             stellarmodel(minkeyposition) = temp
448         end if
449     end do
450 end subroutine sortstellarmodels
451
452 subroutine initconfig()
453     integer :: ios
454     character(len=45) :: configline
455
456     write(14,'(A)') 'reading config file...'
457     open(unit=114, file=trim(filespath) // "config.txt", action="read", status
        ="old")
458
459     do while (.true.)
460         read(114,'(A45)',iostat=ios) configline
461         if (IS_IOSTAT_END(ios)) exit
462
463         if (configline(1:25) == 'initialgasmass            ') then
464             read(configline,'(25X,D20.7)') initialgasmass
465             write(14,'(A,ES13.6)') 'initialgasmass =     ',initialgasmass
466
467         else if (configline(1:25) == 'minstellarmass           ') then
```

```
468            read(configline,'(25X,D20.7)') minstellarmass
469            write(14,'(A,F13.2)') 'minstellarmass␣=␣␣␣␣␣␣␣',minstellarmass
470
471        else if (configline(1:25) == 'maxstellarmass␣␣␣␣␣␣␣␣␣␣␣') then
472            read(configline,'(25X,D20.7)') maxstellarmass
473            write(14,'(A,F13.2)') 'minstellarmass␣=␣␣␣␣␣␣␣',maxstellarmass
474
475        else if (configline(1:25) == 'sfrefficiency␣␣␣␣␣␣␣␣␣␣␣␣') then
476            read(configline,'(25X,D20.7)') sfrefficiency
477            write(14,'(A,ES13.6)') 'sfrefficiency␣=␣␣␣␣␣␣␣',sfrefficiency
478
479        else if (configline(1:25) == 'sfrstartmgasabove␣␣␣␣␣␣␣␣') then
480            read(configline,'(25X,D20.7)') sfrstartmgasabove
481            write(14,'(A,ES13.6)') 'sfrstartmgasabove␣=␣␣',sfrstartmgasabove
482
483        else if (configline(1:25) == 'sfrendmgasbelow␣␣␣␣␣␣␣␣␣␣') then
484            read(configline,'(25X,D20.7)') sfrendmgasbelow
485            write(14,'(A,ES13.6)') 'sfrendmgasbelow␣=␣␣␣␣',sfrendmgasbelow
486
487        else if (configline(1:25) == 'maxtime␣␣␣␣␣␣␣␣␣␣␣␣␣␣␣␣␣␣') then
488            read(configline,'(25X,D20.7)') maxtime
489            write(14,'(A,ES13.6)') 'maxtime␣=␣␣␣␣␣␣␣␣␣␣␣␣',maxtime
490
491        else if (configline(1:25) == 'initialtimestep␣␣␣␣␣␣␣␣␣␣') then
492            read(configline,'(25X,D20.7)') initialtimestep
493            write(14,'(A,ES13.6)') 'initialtimestep␣=␣␣␣␣',initialtimestep
494
495        else if (configline(1:25) == 'mintimestep␣␣␣␣␣␣␣␣␣␣␣␣␣␣') then
496            read(configline,'(25X,D20.7)') mintimestep
497            write(14,'(A,ES13.6)') 'mintimestep␣=␣␣␣␣␣␣␣␣',mintimestep
498
499        else if (configline(1:25) == 'maxtimestep␣␣␣␣␣␣␣␣␣␣␣␣␣␣') then
500            read(configline,'(25X,D20.7)') maxtimestep
501            write(14,'(A,ES13.6)') 'maxtimestep␣=␣␣␣␣␣␣␣␣',maxtimestep
502
503        else if (configline(1:25) == 'timestepgrowthrate␣␣␣␣␣␣␣') then
504            read(configline,'(25X,D20.7)') timestepgrowthrate
505            write(14,'(A,ES13.6)') 'timestepgrowthrate␣=␣',timestepgrowthrate
506
507        else if (configline(1:25) == 'maxmodelnum␣␣␣␣␣␣␣␣␣␣␣␣␣␣') then
508            read(configline,'(25X,I20)') maxmodelnum
509            write(14,'(A,I13)') 'maxmodelnum␣=␣␣␣␣␣␣␣␣␣␣␣␣',maxmodelnum
510
511        else if (configline(1:25) == 'maxchangemgas␣␣␣␣␣␣␣␣␣␣␣␣') then
512            read(configline,'(25X,D20.7)') maxchangemgas
513            write(14,'(A,ES13.6)') 'maxchangemgas␣=␣␣␣␣␣␣␣',maxchangemgas
514
515        else if (configline(1:25) == 'maxchangeser␣␣␣␣␣␣␣␣␣␣␣␣␣') then
516            read(configline,'(25X,D20.7)') maxchangeser
517            write(14,'(A,ES13.6)') 'maxchangeser␣␣=␣␣␣␣␣␣␣',maxchangeser
```

```fortran
518
519         else if (configline(1:25) == 'serintegralsteps␣␣␣␣␣␣␣␣␣') then
520             read(configline,'(25X,I20)') serintegralsteps
521             write(14,'(A,I13)') 'serintegralsteps␣=␣␣␣',serintegralsteps
522
523         else if (configline(1:25) == 'initialcompscalez␣␣␣␣␣␣␣␣') then
524             read(configline,'(25X,D20.7)') initialcompscalez
525             write(14,'(A,ES13.6)') 'initialcompscalez␣=␣␣',initialcompscalez
526
527         end if
528     end do
529
530     if (mintimestep > maxtimestep) then
531         write(14,'(A)') 'STOPPING.␣mintimestep␣>␣maxtimestep'
532         stop
533     end if
534     if (sfrendmgasbelow > sfrstartmgasabove) then
535         write(14,'(A)') 'STOPPING.␣sfrendmgasbelow␣>␣sfrstartmgasabove'
536         stop
537     end if
538
539     close(114)
540     write(14,'(A)') 'finished␣reading␣config␣file.'
541     write(14,*)
542 end subroutine initconfig
543
544 subroutine initspecies()
545     integer :: s, speciescount, neutrons
546
547     write(14,'(A)') 'reading␣species.dat...'
548     open(unit=114, file=trim(filespath) // "species.dat", action="read",
            status="old")
549     read(114,'(I16)') speciescount
550     allocate(species(1:speciescount))
551     write(14,'(I4,A)') speciescount, '␣species'
552     write(14,'(A6,A4,A4,A4)') 'name','el','Z','A'
553     do s=1,size(species)
554         read(114,'(I6,A6,A6,I6)') species(s)%a, species(s)%symbol, species(s)%
                name, neutrons
555         species(s)%z = species(s)%a – neutrons
556         write(14,'(A6,A4,I4,I4)') species(s)%name,species(s)%symbol,species(s)%
                z,species(s)%a
557     end do
558     close(114)
559     write(14,'(A)') 'finished␣reading␣species.dat.'
560     write(14,*)
561 end subroutine initspecies
562
563 subroutine inityields()
564     integer :: stellarmodelcount
```

```fortran
565     integer :: ios, i, s
566     character(len=25) :: stellarmodelname
567     character(len=6) :: spname !species name
568     character(len=8) :: startyieldlist !line in yield file
569     character(len=15) :: startmodellist !line in yield file
570     character(len=10) :: absrel !absolute or relative yield
571     real*8,allocatable :: yieldrow(:)
572
573     write(14,'(A)') 'reading yields.dat...'
574     open(unit=7, file=trim(filespath) // 'yields.txt', action="read", status="
            old", access="sequential", form="formatted")
575     read(7,*,iostat=ios)
576     startmodellist = ""
577     do while (startmodellist /= "[stellarmodels]")
578         read(7,*) startmodellist
579     end do
580     read(7,*) stellarmodelcount
581     allocate(stellarmodel(stellarmodelcount))
582     write(14,'(I4,A)') size(stellarmodel), ' stellar models'
583
584     write(14,'(A25,1X,A6,A11,A14)') 'ModelName','Mini','Mremnant','lifetime'
585     do i = 1, size(stellarmodel)
586         read(7,'(A25,E14.2,14X,E14.2,E14.2)') stellarmodelname,stellarmodel(i)%
                mass,stellarmodel(i)%remnantmass,&
587             stellarmodel(i)%stellarlifetime
588         write(14,'(A25,1X,F6.2,F11.3,ES14.3)') stellarmodelname,stellarmodel(i)
                %mass,stellarmodel(i)%remnantmass,&
589             stellarmodel(i)%stellarlifetime
590         allocate(stellarmodel(i)%yield(size(species)))
591         stellarmodel(i)%yield(:) = 0.0d0
592     end do
593
594     startyieldlist = ""
595     do while (startyieldlist /= "[yields]")
596         read(7,*) startyieldlist
597     end do
598
599     allocate(yieldrow(stellarmodelcount))
600     do while (.true.)
601         read(7,'(A6,2X,A10,*(E14.6))',iostat=ios) spname, absrel, yieldrow
602         if (IS_IOSTAT_END(ios)) exit
603 ! write(14,*) name,absrel,yieldrow
604
605         do s = 1, size(species)
606             if (trim(adjustl(species(s)%name))==trim(adjustl(spname))) then
607                 write(14,'(A,A)') 'loading yields of ',species(s)%name
608                 do i = 1, size(stellarmodel)
609                     if (absrel=='  relative') then
610                         species(s)%yieldisrelative = .true.
611                     else
```

```fortran
612                          species(s)%yieldisrelative = .false.
613                      end if
614                          species(s)%foundyields = .true.
615                      stellarmodel(i)%yield(s) = yieldrow(i)
616                      !write(14,'(A,F5.2,A,E14.7)') 'M=',stellarmodel(i)%mass,',
                                yield=',stellarmodel(i)%yield(s)
617                  end do
618              end if
619          end do
620      end do
621      deallocate(yieldrow)
622      close(7)
623
624      do s = 1, size(species)
625          if (species(s)%foundyields .eqv. .false.) then
626              write(14,'(A,A,A)') 'no yields found for ',species(s)%name,',
                    setting to 0.0'
627              ! have already been initialised to zero earlier on
628          end if
629      end do
630
631      call sortstellarmodels()
632
633      ! get the exponents for lifetime = A * mass ^ B, based on each model and
                the following (higher mass) one
634      do i = 1, size(stellarmodel)-1
635          stellarmodel(i)%lifetimemassexponent = log(stellarmodel(i+1)%
                    stellarlifetime / stellarmodel(i)%stellarlifetime) / &
636              log(stellarmodel(i+1)%mass / stellarmodel(i)%mass)
637      end do
638      stellarmodel(size(stellarmodel))%lifetimemassexponent = stellarmodel(size(
                stellarmodel)-1)%lifetimemassexponent
639
640      ! debugging
641 ! do i = 1, 100
642 ! m0 = 1.0d0 + i*0.5d0
643 ! write(14,*) i,stellarmodel(i)%mass,stellarmodel(i)%stellarlifetime,&
644 ! stellarmodel(i)%remnantmass,stellarmodel(i)%yield(23)
645 ! write(14,'(F6.2,F7.3,*(ES12.3))') m0, remnantmass(m0), stellarlifetime(m0)!,
                yield(23,stellarmodel(i)%mass)
646 ! end do
647 ! stop
648
649      write(14,'(A)') 'finished reading yields.dat.'
650      write(14,*)
651
652 end subroutine inityields
653
654 subroutine loadinitialcomposition ()
655      integer :: ios, s, inmassnum
```

```fortran
656        character(len=6) :: inspname
657        real*8 :: inabund
658
659        write(14,'(A)') 'reading_initial_comp.dat...'
660        open(unit=115, file=trim(filespath) // "initial_comp.dat", action="read",
               status="old")
661        do while (.true.)
662            read(115,'(1X,A6,E14.4,I7)',iostat=ios) inspname, inabund, inmassnum
663            if (IS_IOSTAT_END(ios)) exit
664            !write(14,'(A6,E14.4,I7)') inspname, inabund, inmassnum
665            do s = 1, size(species)
666                if (trim(adjustl(species(s)%name))==trim(adjustl(inspname))) then
667                    species(s)%foundinitialvalue = .true.
668                    if (species(s)%z > 2) then
669                        model(1)%speciesmassfrac(s) = inabund * float(inmassnum) *
                                 initialcompscalez
670                    else
671                        model(1)%speciesmassfrac(s) = inabund * float(inmassnum)
672                    end if
673                    write(14,'(A,A6,A,ES14.7)') 'setting_initial_mass_fraction_of_',
                             species(s)%name,'_to_',model(1)%speciesmassfrac(s)
674                end if
675            end do
676        end do
677        close(115)
678
679        do s = 1, size(species)
680            if (species(s)%foundinitialvalue .eqv. .false.) then
681                write(14,'(A,A,A)') 'no_initial_mass_frac_for_',species(s)%name,',_
                       setting_to_0.0'
682            end if
683        end do
684
685        write(14,'(A)') 'finished_reading_initial_comp.dat.'
686        write(14,*)
687    end subroutine loadinitialcomposition
688
689    ! returns star formation rate in solar masses at time in years
690    pure real*8 function starformationrate(time)
691        real*8, intent(in) :: time
692        integer :: modelnumber
693        real*8 :: c
694
695        if (time < 0.d0) then
696            starformationrate = 0.d0
697        else
698            modelnumber = findmodelnum(time)
699            if (modelnumber >= stepnum - 1) then
700                starformationrate = model(modelnumber-1)%sfr !current model doesn't
                         have an SFR yet
```

```fortran
701          elseif (modelnumber >= 2) then
702              starformationrate = model(modelnumber)%sfr
703              c = (time - model(modelnumber)%time) / &
704                  (model(modelnumber+1)%time - model(modelnumber)%time)
705              ! this is necessary to conserve mass. The starformation rate was
                     euler integrated
706              ! to get the change in stellar/gass mass and the area must be kept
                     constant
707              ! under the interpolation
708              starformationrate = 0.5d0 * (c * (model(modelnumber)%sfr + model(
                     modelnumber+1)%sfr) +&
709                  (1-c) * (model(modelnumber-1)%sfr + model(modelnumber)%sfr))
710          else
711              starformationrate = 0.0d0
712          end if
713      end if
714
715      ! starformationrate = 0.4d1 * exp(-time/3.2d4)
716 end function starformationrate
717
718 ! initial mass function by number (dN/dM)
719 ! normalised s.t. integral of m*imf(m) from m=minstellarmass to m=
        maxstellarmass Msun is 1.0
720 ! i.e. the normalised function gives dN/dM per Msun of star formation
721 pure real*8 function imf(initmass)
722      implicit none
723      real*8, intent(in) :: initmass
724
725      ! Modified Kroupa, Tout, Gilmore 1993 IMF
726      !if (mass >= minstellarmass .AND. mass <= maxstellarmass) then
727      if (initmass > 1.0d0) then
728          imf = imfnormfactor * initmass ** (-2.7d0)
729      elseif (initmass > 0.5d0) then
730          imf = imfnormfactor * initmass ** (-2.2d0)
731      elseif (initmass > 0.08d0) then
732          imf = imfnormfactor * initmass ** (-1.50d0) / (0.5 ** (0.7d0))
733      else
734          imf = 0.0d0
735      end if
736
737      ! Kroupa 2001 IMF
738      !if (mass >= minstellarmass .AND. mass <= maxstellarmass) then
739      ! if (mass < 0.08d0) then
740      ! imf = imfnormfactor * mass ** (-0.3d0)
741      ! elseif (mass < 0.5d0) then
742      ! imf = imfnormfactor * 0.08d0 * mass ** (-1.3d0)
743      ! else
744      ! imf = imfnormfactor * 0.08d0 * 0.5d0 * mass ** (-2.3d0)
745      ! end if
746      !else
```

```fortran
747      ! imf = 0.0d0
748      !end if
749 end function imf
750
751 ! dM/dM, the mass of stars from M to M + dM,
752 ! normalised to a total stellar mass of 1 Msun
753 pure real*8 function mimf(initmass, dummyreal, dummyint)
754      implicit none
755      real*8, intent(in) :: initmass
756      real*8, intent(in), optional :: dummyreal
757      integer, intent(in), optional :: dummyint
758
759      mimf = initmass * imf(initmass)
760 end function mimf
761
762 subroutine closefiles()
763      flush(12)
764      close(12)
765      flush(13)
766      close(13)
767      flush(14)
768      close(14)
769 end subroutine
770
771 end module
```

List of acronyms

AGB

Asymptotic Giant Branch.

BBNS

Big Bang Nucleosynthesis.

CMD

Colour-Magnitude Diagram.

FDU

First Dredge-Up.

GC

Globular Cluster.

HBB

Hot Bottom Burning.

IMF

Initial Mass Function.

PDCZ

Pulse-Driven Convective Zone.

PMZ

Partially Mixed Zone.

PN(e)

Planetary Nebula(e).

r-process

rapid neutron-capture process.

RGB

Red Giant Branch.

s-process

slow neutron-capture process.

SDU

Second Dredge-Up.

SFR

Star Formation Rate.

TDU

Third Dredge-Up.

WD

White Dwarf.

Bibliography

Abia, C., et al. 2002, ApJ, 579, 817 (Link)

Alpher, R. A., Bethe, H., & Gamow, G. 1948, Phys. Rev., 73, 803 (Link)

Alpher, R. A., Follin, J. W., & Herman, R. C. 1953, Phys. Rev., 92, 1347 (Link)

Alves-Brito, A., Yong, D., Meléndez, J., Vásquez, S., & Karakas, A. I. 2012, A&A, 540, A3 (Link)

Angulo, C., et al. 1999, Nuc. Phys. A, 656, 3 (Link)

Arlandini, C., Kappeler, F., Wisshak, K., Gallino, R., Lugaro, M. A., Busso, M., & Straniero, O. 1999, ApJ, 525, 886 (Link)

Arnould, M., & Goriely, S. 2003, Physics Reports, 384, 1 (Link)

Arnould, M., Goriely, S., & Jorissen, A. 1999, A&A, 347, 572 (Link)

Asplund, M., Grevesse, N., Sauval, A. J., & Scott, P. 2009, ARA&A, 47, 481 (Link)

Audi, G., Bersillon, O., Blachot, J., & Wapstra, A. H. 2003, Nuc. Phys. A, 729, 3 (Link)

Aver, E., Olive, K. A., & Skillman, E. D. 2012, Journal of Cosmology and Astroparticle Physics, 04, 004 (Link)

Bao, Z. Y., & Kappeler, F. 1987, A&A, 36, 411 (Link)

Bastian, N., Lamers, H. J. G. L. M., de Mink, S. E., Longmore, S. N., Goodwin, S. P., & Gieles, M. 2013, MNRAS, 436, 2398 (Link)

Becker, S. A., & Iben, I. J. 1979, ApJ, 232, 831 (Link)

Bedin, L. R., Piotto, G., Anderson, J., Cassisi, S., King, I. R., Momany, Y., & Carraro, G. 2004, ApJ, 605, L125 (Link)

Beer, H., Walter, G., & Kaeppeler, F. 1992, ApJ, 389, 784 (Link)

Bekki, K., & Freeman, K. C. 2003, A&A, 346, L11 (Link)

Bennett, M. E., et al. 2012, MNRAS, 420, 3047 (Link)

Bernard-Salas, J., Pottasch, S. R., Gutenkunst, S., Morris, P. W., & Houck, J. R. 2008, ApJ, 672, 274 (Link)

Bertelli, G., Girardi, L., Marigo, P., & Nasi, E. 2008, A&A, 484, 815 (Link)

Best, A., et al. 2011, Phys. Rev. C, 83, 52802 (Link)

—. 2013, Phys. Rev. C, 87, 45805 (Link)

Bethe, H. A. 1939, Phys. Rev., 55, 434 (Link)

Biermann, L. 1948, Z. Astrophys., 25, 135 (Link)

Bisterzo, S., Gallino, R., Straniero, O., Cristallo, S., & Kappeler, F. 2010, MNRAS, 404, 1529 (Link)

—. 2012, MNRAS, 422, 849 (Link)

Bisterzo, S., Travaglio, C., Gallino, R., Wiescher, M., & Kappeler, F. 2014, ApJ, 787, 10 (Link)

Bloecker, T. 1995, A&A, 297, 727 (Link)

Bloecker, T., & Schoenberner, D. 1991, A&A, 244, L43 (Link)

Böhm-Vitense, E. 1958, Z. Astrophys., 46, 108 (Link)

Bonačić Marinović, A., Izzard, R. G., Lugaro, M. A., & Pols, O. R. 2007a, A&A, 469, 1013 (Link)

Bonačić Marinović, A., Lugaro, M. A., Reyniers, M., & van Winckel, H. 2007b, A&A, 472, L1 (Link)

Bono, G., Caputo, F., Cassisi, S., Marconi, M., Piersanti, L., & Tornambe, A. 2000, ApJ, 543, 955 (Link)

Boothroyd, A. I., & Sackmann, I.-J. 1988a, ApJ, 328, 653 (Link)

—. 1988b, ApJ, 328, 671 (Link)

—. 1992, ApJ, 393, L21 (Link)

Boothroyd, A. I., Sackmann, I.-J., & Ahern, S. C. 1993, ApJ, 416, 762 (Link)

Brown, J. A., & Wallerstein, G. 1992, AJ, 104, 1818 (Link)

Buell, J. F. 2013, MNRAS, 428, 2577 (Link)

Burbidge, E. M., Burbidge, G. R., Fowler, W. A., & Hoyle, F. 1957, Reviews of Modern Physics, 29, 547 (Link)

Busso, M., Gallino, R., & Wasserburg, G. J. 1999, ARA&A, 37, 239 (Link)

Cameron, A. G. W. 1955, ApJ, 121, 144 (Link)

—. 1957a, PASP, 69, 201 (Link)

—. 1957b, Astronomical Journal, 62, 9 (Link)

—. 1957c, Astronomical Journal, 62, 138 (Link)

—. 1960, AJ, 65, 485 (Link)

Campbell, S. W., et al. 2013, Nature, 498, 198 (Link)

Cannon, R. C. 1993, MNRAS, 263, 817 (Link)

Cannon, R. D., Croke, B. F. W., Bell, R. A., Hesser, J. E., & Stathakis, R. A. 1998, MNRAS, 298, 601 (Link)

Canuto, V. M., Goldman, I., & Mazzitelli, I. 1996, ApJ, 473, 550 (Link)

Canuto, V. M., & Mazzitelli, I. 1991, ApJ, 370, 295 (Link)

Carretta, E., Bragaglia, A., Gratton, R., D'Orazi, V., & Lucatello, S. 2009a, A&A, 508, 695 (Link)

Carretta, E., Lucatello, S., Gratton, R. G., Bragaglia, A., & D'Orazi, V. 2011, A&A, 533, 69 (Link)

Carretta, E., et al. 2009b, A&A, 505, 117 (Link)

Cassisi, S., & Castellani, V. 1993, A&AS, 88, 509 (Link)

Caughlan, G. R., & Fowler, W. A. 1988, Atomic Data and Nuclear Data Tables, 40, 283 (Link)

Chaboyer, B., Demarque, P., Kernan, P. J., & Krauss, L. M. 1996, Science, 271, 957 (Link)

Charbonnel, C., Chantereau, W., Decressin, T., Meynet, G., & Schaerer, D. 2013, A&A, 557, L17 (Link)

Chiappini, C., Matteucci, F., & Romano, D. 2001, ApJ, 554, 1044 (Link)

Chieffi, A., & Limongi, M. 2002, ApJ, 577, 281 (Link)

Chieffi, A., & Straniero, O. 1989, A&AS, 71, 47 (Link)

Chiosi, C., & Maeder, A. 1986, ARA&A, 24, 329 (Link)

Christy-Sackmann, I. J., & Paczyński, B. 1975, Mem. Soc. R. Sci. Liège, 8, 335 (Link)

Clayton, D. D. 1988, MNRAS, 234, 1 (Link)

Clayton, D. D., & Rassbach, M. E. 1967, ApJ, 148, 69 (Link)

Cohen, J. G. 1978, ApJ, 223, 487 (Link)

Cohen, J. G., & Kirby, E. N. 2012, ApJ, 760, 86 (Link)

Constantino, T., Campbell, S., Gil-Pons, P., & Lattanzio, J. C. 2014, ApJ, 784, 56 (Link)

Cottrell, P. L., & Da Costa, G. S. 1981, ApJ, 245, L79 (Link)

Cristallo, S., Gallino, R., & Straniero, O. 2004, Mem. Soc. Astron. Ital., 75, 174 (Link)

Cristallo, S., Imbriani, G., Piersanti, L., Abia, C., Gialanella, L., & Straniero, O. 2014, A&A, 570, A46 (Link)

Cristallo, S., Straniero, O., Gallino, R., Piersanti, L., Dominguez, I., & Lederer, M. T. 2009, ApJ, 696, 797 (Link)

Cristallo, S., et al. 2011, ApJS, 197, 17 (Link)

Cyburt, R. H., et al. 2010, ApJS, 189, 240 (Link)

Da Costa, G. S., Held, E. V., Saviane, I., & Gullieuszik, M. 2009, ApJ, 705, 1481 (Link)

Da Costa, G. S., & Marino, A. F. 2011, Publ. Astron. Soc. Aust., 28, 28 (Link)

Da Costa, G. S., Norris, J. E., & Yong, D. 2013, ApJ, 769, 8 (Link)

de Laverny, P., & Recio-Blanco, A. 2013, A&A, 560, 74 (Link)

de Mink, S. E., Pols, O. R., Langer, N., & Izzard, R. G. 2009, A&A, 507, L1 (Link)

De Silva, G. M., Gibson, B. K., Lattanzio, J. C., & Asplund, M. 2009, A&A, 500, L25 (Link)

De Smedt, K., van Winckel, H., Kamath, D., Karakas, A. I., Siess, L., Goriely, S., & Wood, P. 2014, A&A, 563, L5 (Link)

De Smedt, K., van Winckel, H., Karakas, A. I., Siess, L., Goriely, S., & Wood, P. R. 2012, A&A, 541, A67 (Link)

Decressin, T., Charbonnel, C., Prantzos, N., & Ekström, S. 2007, A&A, 464, 1029 (Link)

Denisenkov, P. A., & Denisenkova, S. N. 1990, SvAL, 16, 275 (Link)

Denissenkov, P. A., & Hartwick, F. D. A. 2014, MNRASL, 437, L21 (Link)

Denissenkov, P. A., & Herwig, F. 2003, ApJ, 590, L99 (Link)

Denissenkov, P. A., Herwig, F., Truran, J. W., & Paxton, B. 2013, ApJ, 772, 37 (Link)

Denissenkov, P. A., & Tout, C. A. 2003, MNRAS, 340, 722 (Link)

Denissenkov, P. A., Truran, J. W., Herwig, F., Jones, S., Paxton, B., Nomoto, K., Suzuki, T., & Toki, H. 2015a, MNRAS, 447, 2696 (Link)

Denissenkov, P. A., VandenBerg, D. A., Hartwick, F. D. A., Herwig, F., Weiss, A., & Paxton, B. 2015b, MNRAS, 448, 3314 (Link)

D'Ercole, A., D'Antona, F., & Vesperini, E. 2011, MNRAS, 415, 1304 (Link)

Descouvemont, P. 1993, Phys. Rev. C, 48, 2746 (Link)

Dicke, R. H., Peebles, P. J. E., Roll, P. G., & Wilkinson, D. T. 1965, ApJ, 142, 414 (Link)

Dillmann, I., Heil, M., Kappeler, F., Plag, R., Rauscher, T., & Thielemann, F.-K. 2006, in CAP-TURE GAMMA-RAY SPECTROSCOPY AND RELATED TOPICS: 12th International Symposium. AIP Conference Proceedings, Institut für Kernphysik, Forschungszentrum Karlsruhe, Postfach 3640, D-76021 Karlsruhe, Germany; Departement Physik und Astronomie, Universität Basel, Klingelbergstrasse 82, CH-4056 Basel, Switzerland, 123–127 (Link)

Doherty, C. L., Gil-Pons, P., Lau, H. H. B., Lattanzio, J. C., Siess, L., & Campbell, S. W. 2014, MNRAS, 441, 582 (Link)

Doherty, C. L., Gil-Pons, P., Siess, L., Lattanzio, J. C., & Lau, H. H. B. 2015, MNRAS, 446, 2599 (Link)

Doherty, C. L., Siess, L., Lattanzio, J. C., & Gil-Pons, P. 2010, MNRAS, 401, 1453 (Link)

D'Orazi, V., Biazzo, K., Desidera, S., Covino, E., Andrievsky, S. M., & Gratton, R. G. 2012, MNRAS, 423, 2789 (Link)

D'Orazi, V., Campbell, S. W., Lugaro, M. A., Lattanzio, J. C., & Carretta, E. 2013, MNRAS, 433, 366 (Link)

D'Orazi, V., Gratton, R., Lucatello, S., Carretta, E., Bragaglia, A., & Marino, A. F. 2010, ApJL, 719, L213 (Link)

D'Orazi, V., Lugaro, M. A., Campbell, S. W., Bragaglia, A., Carretta, E., Gratton, R. G., Lucatello, S., & D'Antona, F. 2013a, ApJ, 776, 59 (Link)

D'Orazi, V., & Marino, A. F. 2010, ApJL, 716, L166 (Link)

D'Orazi, V., et al. 2013b, ApJ, 763, 22 (Link)

Dotter, A., Kaluzny, J., & Thompson, I. B. 2009, IAU, 4, 171 (Link)

Dotter, A., et al. 2010, ApJ, 708, 698 (Link)

Drake, J. J., Smith, V. V., & Suntzeff, N. B. 1992, ApJ, 395, L95 (Link)

Dunbar, D. N., Pixley, R. E., Wenzel, W. A., & Whaling, W. 1953, Phys. Rev., 92, 649 (Link)

Dupree, A. K., & Avrett, E. H. 2013, ApJL, 773, L28 (Link)

Ekström, S. 2006, A&A, 447, 623 (Link)

Ekström, S., & Charbonnel, C. 2008, A&A, 479, L9 (Link)

Ekström, S., & Matteucci, F. 2006, A&A, 449, L27 (Link)

Fabbian, D., Nissen, P. E., Asplund, M., Pettini, M., & Akerman, C. 2009, A&A, 500, 1143
    (Link)

Fenner, Y., Campbell, S., Karakas, A. I., Lattanzio, J. C., & Gibson, B. K. 2004, MNRAS, 353,
    789 (Link)

Fishlock, C. K., Karakas, A. I., Lugaro, M. A., & Yong, D. 2014a, ApJ, 797, 44 (Link)

Fishlock, C. K., Karakas, A. I., & Stancliffe, R. J. 2014b, MNRAS, 438, 1741 (Link)

Freeman, K. C. 1993, Why Galaxies Care about AGB Stars II: Shining Examples and
    Common Inhabitants, 48, 608 (Link)

Friedmann, A. 1922, Z. Astrophys., 10, 377 (Link)

Frischknecht, U., & Thielemann, F.-K. 2012, A&A, 538, L2 (Link)

Frost, C. A., Cannon, R. C., Lattanzio, J. C., Wood, P. R., & Forestini, M. 1998, A&A, 332,
    L17 (Link)

Frost, C. A., & Lattanzio, J. C. 1996, ApJ, 473, 383 (Link)

Gallino, R., Arlandini, C., Busso, M., Lugaro, M. A., Travaglio, C., Straniero, O., Chieffi, A.,
    & Limongi, M. 1998, ApJ, 497, 388 (Link)

Gallino, R., Heil, M., Wiescher, M., Kappeler, F., Herwig, F., & Bisterzo, S. 2010, ApJ, 710,
    1557 (Link)

Gallino, R., Herwig, F., & Wiescher, M. 2008, ApJ, 687, L95 (Link)

Gamow, G. 1946, AJ, 70, 572 (Link)

Garcia-Berro, E., & Iben, I. 1994, ApJ, 434, 306 (Link)

García-Hernández, D. A., Zamora, O., Yagüe, A., Uttenthaler, S., Karakas, A. I., Lugaro,
    M. A., Ventura, P., & Lambert, D. L. 2013, A&A, 555, L3 (Link)

Gil-Pons, P., Doherty, C. L., Lau, H., Campbell, S. W., Suda, T., Guilani, S., Gutiérrez, J., &
    Lattanzio, J. C. 2013, A&A, 557, A106 (Link)

Goriely, S. 1999, A&A, 342, 881 (Link)

Goriely, S., & Mowlavi, N. 2000, A&A, 362, 599 (Link)

Goriely, S., & Siess, L. 2004, A&A, 421, L25 (Link)

Gratton, R., Sneden, C., & Carretta, E. 2004, ARA&A, 42, 385 (Link)

Gratton, R. G., Sneden, C., Carretta, E., & Bragaglia, A. 2000, A&A, 354, 169 (Link)

Gratton, R. G., et al. 2001, A&A, 369, 87 (Link)

Guo, B., et al. 2012, ApJ, 756, 193 (Link)

Hale, S. E., Champagne, A. E., Iliadis, C., Hansper, V. Y., Powell, D. C., & Blackmon, J. C. 2004, Phys. Rev. C, 70, 045802 (Link)

Harris, W. E. 1996, AJ, 112, 1487 (Link)

Hayashi, C. 1950, Progress of Theoretical Physics, 5, 224 (Link)

Heil, M., Kappeler, F., Uberseder, E., Gallino, R., & Bisterzo, S. 2008, Phys. Rev. C, 78, 025802 (Link)

Henry, R. B. C., Kwitter, K. B., & Balick, B. 2004, AJ, 127, 2284 (Link)

Henry, R. B. C., Speck, A., Karakas, A. I., Ferland, G. J., & Maguire, M. 2012, ApJ, 749, 61 (Link)

Henyey, L. G., Forbes, J. E., & Gould, N. L. 1964, ApJ, 139, 306 (Link)

Henyey, L. G., Wilets, L., Böhm, K. H., Lelevier, R., & Levee, R. D. 1959, ApJ, 129, 628 (Link)

Herwig, F. 2000, A&A, 360, 952 (Link)

—. 2004, ApJ, 605, 425 (Link)

—. 2005, ARA&A, 43, 435 (Link)

Herwig, F., Blöcker, T., Langer, N., & Driebe, T. 1999, A&A, 349, L5 (Link)

Herwig, F., & Langer, N. 2001, Mem. Soc. Astron. Ital., 72, 277 (Link)

Herwig, F., Langer, N., & Lugaro, M. A. 2003, ApJ, 593, 1056 (Link)

Herwig, F., Pignatari, M., Woodward, P. R., Porter, D. H., Rockefeller, G., Fryer, C. L., Bennett, M., & Hirschi, R. 2011, ApJ, 727, 89 (Link)

Herwig, F., et al. 2008, in "Proceedings of the 10th Symposium on Nuclei in the Cosmos (NIC X). July 27 - August 1, 23 (Link)

Hirschi, R. 2007, A&A, 461, 571 (Link)

Hollowell, D., & Iben, I. J. 1989, ApJ, 340, 966 (Link)

Hoyle, F. 1948, MNRAS, 108, 372 (Link)

—. 1954, Astrophysical Journal Supplement, 1, 121 (Link)

Hubble, E. 1929, in Proceedings of the National Academy of Sciences of the United States of America, 168–173 (Link)

Hunter, J. D. 2007, Comput. Sci. Eng., 9, 90 (Link)

Iben, I. J. 1975a, ApJ, 196, 549 (Link)

—. 1975b, ApJ, 196, 525 (Link)

Iben, I. J., Kaler, J. B., Truran, J. W., & Renzini, A. 1983, ApJ, 264, 605 (Link)

Iben, I. J., & Renzini, A. 1982, ApJ, 259, L79 (Link)

Iglesias, C. A., & Rogers, F. J. 1996, ApJ, 464, 943 (Link)

Iliadis, C. 2007, Nuclear physics of stars (LibreDigital) (Link)

Iliadis, C., Longland, R. L., Champagne, A. E., Coc, A., & Fitzgerald, R. 2010, Nuc. Phys.
    A, 841, 31 (Link)

Ivans, I. I., Kraft, R. P., Sneden, C., Smith, G. H., Rich, R. M., & Shetrone, M. 2001, AJ, 122,
    1438 (Link)

Ivans, I. I., Sneden, C., Kraft, R. P., Suntzeff, N. B., Smith, V. V., Langer, G. E., & Fulbright,
    J. P. 1999, AJ, 118, 1273 (Link)

Izzard, R. G., Dray, L. M., Karakas, A. I., Lugaro, M. A., & Tout, C. A. 2006, A&A, 460, 565
    (Link)

Izzard, R. G., Glebbeek, E., Stancliffe, R. J., & Pols, O. R. 2009, A&A, 508, 1359 (Link)

Izzard, R. G., Tout, C. A., Karakas, A. I., & Pols, O. R. 2004, MNRAS, 350, 407 (Link)

Jaeger, M., Kunz, R., Mayer, A., Hammer, J. W., Staudt, G., Kratz, K. L., & Pfeiffer, B. 2001,
    Physical Review Letters, 87, 202501 (Link)

Jahn, D., Rauch, T., Reiff, E., Werner, K., Kruk, J. W., & Herwig, F. 2007, A&A, 462, 281
    (Link)

James, G., Francois, P., Bonifacio, P., Carretta, E., Gratton, R. G., & Spite, F. 2004, A&A,
    427, 825 (Link)

Johnson, C. I., & Pilachowski, C. A. 2010, ApJ, 722, 1373 (Link)

Johnson, H. L., & Sandage, A. R. 1955, ApJ, 121, 616 (Link)

Jones, S., et al. 2013, ApJ, 772, 150 (Link)

Joo, S.-J., & Lee, Y.-W. 2013, ApJ, 762, 36 (Link)

Jorissen, A., Smith, V. V., & Lambert, D. L. 1992, A&A, 261, 164 (Link)

Kamath, D., Karakas, A. I., & Wood, P. R. 2012, ApJ, 746, 20 (Link)

Karakas, A. I. 2010, MNRAS, 403, 1413 (Link)

—. 2014, MNRAS, 445, 347 (Link)

Karakas, A. I., Campbell, S. W., Lugaro, M. A., Yong, D., & Chieffi, A. 2010a, Mem. Soc.
    Astron. Ital., 81, 1010 (Link)

Karakas, A. I., Campbell, S. W., & Stancliffe, R. J. 2010b, ApJ, 713, 374 (Link)

Karakas, A. I., Fenner, Y., Sills, A., Campbell, S. W., & Lattanzio, J. C. 2006a, ApJ, 652, 1240 (Link)

Karakas, A. I., García-Hernández, D. A., & Lugaro, M. A. 2012, ApJ, 751, 8 (Link)

Karakas, A. I., & Lattanzio, J. C. 2003a, Publ. Astron. Soc. Aust., 20, 393 (Link)

—. 2003b, Publ. Astron. Soc. Aust., 20, 279 (Link)

—. 2007, Publ. Astron. Soc. Aust., 24, 103 (Link)

—. 2014, Publ. Astron. Soc. Aust., 31, e030 (Link)

Karakas, A. I., Lattanzio, J. C., & Pols, O. R. 2002, Publ. Astron. Soc. Aust., 19, 515 (Link)

Karakas, A. I., & Lugaro, M. A. 2010, Publ. Astron. Soc. Aust., 27, 227 (Link)

Karakas, A. I., Lugaro, M. A., Wiescher, M., Gorres, J., & Ugalde, C. 2006b, ApJ, 643, 471 (Link)

Karakas, A. I., Marino, A. F., & Nataf, D. M. 2014, ApJ, 784, 32 (Link)

Karakas, A. I., van Raai, M. A., Lugaro, M. A., Sterling, N. C., & Dinerstein, H. L. 2009, ApJ, 690, 1130 (Link)

Kennicutt, R. C., & Evans, N. J. 2012, ARA&A, 50, 531 (Link)

King, I. R., et al. 2012, AJ, 144, 5 (Link)

Kobayashi, C., Karakas, A. I., & Umeda, H. 2011, MNRAS, 414, 3231 (Link)

Kobayashi, C., Umeda, H., Nomoto, K., Tominaga, N., & Ohkubo, T. 2006, ApJ, 653, 1145 (Link)

Koehler, P. E. 2002, Phys. Rev. C, 66, 55805 (Link)

Kraft, R. P., Sneden, C., Smith, G. H., Shetrone, M. D., Langer, G. E., & Pilachowski, C. A. 1997, Astronomical Journal v.113, 113, 279 (Link)

Kraft, R. P., Suntzeff, N. B., Langer, G. E., Trefzger, C. F., Friel, E., Stone, R. P. S., & Carbon, D. F. 1982, Astronomical Society of the Pacific, 94, 55 (Link)

Kromer, M., et al. 2015, MNRAS, 450, 3045 (Link)

Kroupa, P., Tout, C. A., & Gilmore, G. 1993, MNRAS, 262, 545 (Link)

Langer, G. E., Hoffman, R., & Sneden, C. 1993, PASP, 105, 301 (Link)

Langer, N. 2012, ARA&A, 50, 107 (Link)

Langer, N., Heger, A., Wellstein, S., & Herwig, F. 1999, A&A, 346, L37 (Link)

Lattanzio, J. C. 1986, ApJ, 311, 708 (Link)

—. 1992, Astron. Soc. Aust. Proc., 10, 120 (Link)

Lau, H. H. B., Gil-Pons, P., Doherty, C. L., & Lattanzio, J. C. 2012, A&A, 542, A1 (Link)

Lebzelter, T., & Wood, P. R. 2007, A&A, 475, 643 (Link)

Lederer, M. T., & Aringer, B. 2009, MNRAS, 494, 403 (Link)

Lemaître, G. 1927, Annales de la Société Scientifique de Bruxelles, 47, 49 (Link)

Limongi, M., & Chieffi, A. 2012, ApJS, 199, 38 (Link)

Lodders, K. 2003, ApJ, 591, 1220 (Link)

Longland, R. L., Iliadis, C., & Karakas, A. I. 2012, Phys. Rev. C, 85, 65809 (Link)

Longland, R. L., Iliadis, C., Rusev, G., Tonchev, A. P., deBoer, R. J., Gorres, J., & Wiescher, M. 2009, A&A, 80, 055803 (Link)

Lugaro, M. A., Herwig, F., Lattanzio, J. C., Gallino, R., & Straniero, O. 2003, ApJ, 586, 1305 (Link)

Lugaro, M. A., Karakas, A. I., Stancliffe, R. J., & Rijs, C. 2012, ApJ, 747, 2 (Link)

Lugaro, M. A., Ugalde, C., Karakas, A. I., Görres, J., Wiescher, M., Lattanzio, J. C., & Cannon, R. C. 2004, ApJ, 615, 934 (Link)

Maeder, A., & Meynet, G. 2000, ARA&A, 38, 143 (Link)

Magic, Z., & Asplund, M. 2014, eprint arXiv:1405.7628 (Link)

Maiorca, E., Magrini, L., Busso, M., Randich, S., Palmerini, S., & Trippella, O. 2012, ApJ, 747, 53 (Link)

Marigo, P. 2002, A&A, 387, 507 (Link)

Marigo, P., & Aringer, B. 2009, A&A, 508, 1539 (Link)

Marigo, P., Bernard-Salas, J., Pottasch, S. R., Tielens, A. G. G. M., & Wesselius, P. R. 2003, A&A, 409, 619 (Link)

Marigo, P., Girardi, L., Weiss, A., & Groenewegen, M. A. T. 1999, A&A, 351, 161 (Link)

Marino, A. F., Milone, A. P., Piotto, G., Villanova, S., Bedin, L. R., Bellini, A., & Renzini, A. 2009, A&A, 505, 1099 (Link)

Marino, A. F., Villanova, S., Milone, A. P., Piotto, G., Lind, K., Geisler, D., & Stetson, P. B. 2011a, ApJL, 730, L16 (Link)

Marino, A. F., Villanova, S., Piotto, G., Milone, A. P., Momany, Y., Bedin, L. R., & Medling, A. M. 2008, A&A, 490, 625 (Link)

Marino, A. F., et al. 2011b, A&A, 532, 8 (Link)

—. 2012, A&A, 541, 15 (Link)

—. 2014, MNRAS, 437, 1609 (Link)

—. 2015, MNRAS, 450, 815 (Link)

McSaveney, J. A., Wood, P. R., Scholz, M., Lattanzio, J. C., & Hinkle, K. H. 2007, MNRAS, 378, 1089 (Link)

Merrill, S. P. W. 1952, ApJ, 116, 21 (Link)

Meyer, B. S. 1994, ARA&A, 32, 153 (Link)

Miglio, A., et al. 2012, MNRAS, 419, 2077 (Link)

Milingo, J. B., Kwitter, K. B., Henry, R. B. C., & Souza, S. P. 2010, ApJ, 711, 619 (Link)

Miller Bertolami, M. M., & Althaus, L. G. 2006, A&A, 454, 845 (Link)

Milone, A. P., et al. 2008, ApJ, 673, 241 (Link)

Miszalski, B., et al. 2013, MNRAS, 436, 3068 (Link)

Miyaji, S., Nomoto, K., Yokoi, K., & Sugimoto, D. 1980, PASJ, 32, 303 (Link)

Mocák, M., Siess, L., & Müller, E. 2011, A&A, 533, 53 (Link)

Moehler, S. 2001, PASP, 113, 1162 (Link)

Mowlavi, N. 1999a, A&A, 344, 617 (Link)

—. 1999b, A&A, 350, 73 (Link)

National Research Council. 2008, Minerals, Critical Minerals, and the U.S. Economy (The National Academies Press) (Link)

Nomoto, K., Kobayashi, C., & Tominaga, N. 2013, ARA&A, 51, 457 (Link)

Norris, J. E. 2004, ApJ, 612, L25 (Link)

Norris, J. E., & Da Costa, G. S. 1995, ApJ, 447, 680 (Link)

Paczyński, B. 1970, Acta Astron., 20, 47 (Link)

—. 1974, ApJ, 192, 483 (Link)

Pagel, B. E. J. 2009, Nucleosynthesis and Chemical Evolution of Galaxies, second edition edn. (Cambridge University Press) (Link)

Pasquini, L., Mauas, P., Käufl, H. U., & Cacciari, C. 2011, A&A, 531, A35 (Link)

Paxton, B., Bildsten, L., Dotter, A., Herwig, F., Lesaffre, P., & Timmes, F. X. 2011, ApJS, 192, 3 (Link)

Pellegriti, M., et al. 2008, A&A, 77, 042801 (Link)

Penzias, A. A., & Wilson, R. W. 1965, ApJ, 142, 419 (Link)

Peters, J. G. 1968, ApJ, 154, 225 (Link)

Peterson, R. C. 1980, ApJ, 237, L87 (Link)

Piersanti, L., Cristallo, S., & Straniero, O. 2013, ApJ, 774, 98 (Link)

Piotto, G. 2009, The Ages of Stars, 258, 233 (Link)

Piotto, G., et al. 2005, ApJ, 621, 777 (Link)

—. 2007, ApJ, 661, L53 (Link)

Pottasch, S. R., & Bernard-Salas, J. 2010, A&A, 517, 95 (Link)

Pottasch, S. R., Surendiranath, R., & Bernard-Salas, J. 2011, A&A, 531, 23 (Link)

Prantzos, N., & Charbonnel, C. 2006, A&A, 458, 135 (Link)

Prantzos, N., Charbonnel, C., & Iliadis, C. 2007, A&A, 470, 179 (Link)

Raiteri, C. M., Gallino, R., & Busso, M. 1992, ApJ, 387, 263 (Link)

Raiteri, C. M., Gallino, R., Busso, M., Neuberger, D., & Kaeppeler, F. 1993, The Astrophysical Journal, 419, 207 (Link)

Rauscher, T., & Thielemann, F.-K. 2000, Atomic Data and Nuclear Data Tables, 75, 1 (Link)

Reimers, D. 1975, Mem. Soc. R. Sci. Liège, 8, 369 (Link)

Renzini, A., & Voli, M. 1981, A&A, 94, 175 (Link)

Roederer, I. U., Marino, A. F., & Sneden, C. 2011, ApJ, 742, 37 (Link)

Roeser, M. 1975, A&A, 45, 335 (Link)

Romano, D., Karakas, A. I., Tosi, M., & Matteucci, F. 2010, A&A, 522, 32 (Link)

Romano, D., Matteucci, F., Tosi, M., Pancino, E., Bellazzini, M., Ferraro, F. R., Limongi, M., & Sollima, A. 2007, MNRAS, 376, 405 (Link)

Rose, W. K. 1966, ApJ, 146, 838 (Link)

Sackmann, I.-J. 1980a, ApJ, 241, L37 (Link)

—. 1980b, ApJ, 235, 554 (Link)

Salpeter, E. E. 1955, ApJ, 121, 161 (Link)

Sanders, R. H. 1967, ApJ, 150, 971 (Link)

Scalo, J. M. 1978, ApJ, 221, 627 (Link)

Schmidt, M. 1959, ApJ, 129, 243 (Link)

Schoenberner, D. 1979, A&A, 79, 108 (Link)

Schwarzschild, M., & Harm, R. 1965, ApJ, 142, 855 (Link)

Shetrone, M. D. 1996, AJ, 112, 1517 (Link)

Shingles, L. J., Doherty, C. L., Karakas, A. I., Stancliffe, R. J., Lattanzio, J. C., & Lugaro, M. A. 2015, MNRAS, 452, 2804 (Link)

Shingles, L. J., & Karakas, A. I. 2013, MNRAS, 431, 2861 (Link)

Shingles, L. J., Karakas, A. I., Hirschi, R., Fishlock, C. K., Yong, D., Da Costa, G. S., & Marino, A. F. 2014, ApJ, 795, 34 (Link)

Siess, L. 2006, A&A, 448, 717 (Link)

—. 2007, A&A, 476, 893 (Link)

—. 2010, A&A, 512, A10 (Link)

Siess, L., Goriely, S., & Langer, N. 2004, A&A, 415, 1089 (Link)

Simmerer, J., Sneden, C., Cowan, J. J., Collier, J., Woolf, V. M., & Lawler, J. E. 2004, ApJ, 617, 1091 (Link)

Simmerer, J., Sneden, C., Ivans, I. I., Kraft, R. P., Shetrone, M. D., & Smith, V. V. 2003, AJ, 125, 2018 (Link)

Smith, V. V., Suntzeff, N. B., Cunha, K., Gallino, R., Busso, M., Lambert, D. L., & Straniero, O. 2000, AJ, 119, 1239 (Link)

Sneden, C., Cowan, J. J., & Gallino, R. 2008, ARA&A, 46, 241 (Link)

Sneden, C., Johnson, J., Kraft, R. P., Smith, G. H., Cowan, J. J., & Bolte, M. S. 2000, ApJ, 536, L85 (Link)

Sneden, C., Kraft, R. P., Shetrone, M. D., Smith, G. H., Langer, G. E., & Prosser, C. F. 1997, AJ, 114, 1964 (Link)

Sobeck, J. S., et al. 2011, AJ, 141, 175 (Link)

Stancliffe, R. J., Dearborn, D. S. P., Lattanzio, J. C., Heap, S. A., & Campbell, S. W. 2011, ApJ, 742, 121 (Link)

Stancliffe, R. J., & Jeffery, C. S. 2007, MNRAS, 375, 1280 (Link)

Stancliffe, R. J., Tout, C. A., & Pols, O. R. 2004, MNRAS, 352, 984 (Link)

Sterling, N. C., & Dinerstein, H. L. 2008, ApJS, 174, 158 (Link)

Straniero, O., Cristallo, S., & Piersanti, L. 2014, ApJ, 785, 77 (Link)

Straniero, O., Dominguez, I., Cristallo, S., & Gallino, R. 2003, Publ. Astron. Soc. Aust., 20, 389 (Link)

Straniero, O., Gallino, R., Busso, M., Chieffi, A., Raiteri, C. M., Limongi, M., & Salaris, M. 1995, ApJ, 440, L85 (Link)

Straniero, O., Gallino, R., & Cristallo, S. 2006, Nuc. Phys. A, 777, 311 (Link)

Sweigart, A. V. 1999, New Views of the Magellanic Clouds, 190, 370 (Link)

The, L.-S., El Eid, M. F., & Meyer, B. S. 2007, ApJ, 655, 1058 (Link)

Thielemann, F.-K., et al. 2011, Progress in Particle and Nuclear Physics, 66, 346 (Link)

Travaglio, C., Galli, D., Gallino, R., Busso, M., Ferrini, F., & Straniero, O. 1999, ApJ, 521, 691 (Link)

Travaglio, C., Gallino, R., Busso, M., & Gratton, R. 2001, ApJ, 549, 346 (Link)

Tur, C., Heger, A., & Austin, S. M. 2009, ApJ, 702, 1068 (Link)

Tytler, D., O'Meara, J. M., Suzuki, N., & Lubin, D. 2000, Particle Physics and the Universe, 85, 12 (Link)

Umeda, H., Nomoto, K., Yamaoka, H., & Wanajo, S. 1999, ApJ, 513, 861 (Link)

Uttenthaler, S., Hron, J., Lebzelter, T., Busso, M., Schultheis, M., & Käufl, H. U. 2007, A&A, 463, 251 (Link)

Van Eck, S., Goriely, S., Jorissen, A., & Plez, B. 2001, Nature, 412, 793 (Link)

—. 2003, A&A, 404, 291 (Link)

van Raai, M. A., Lugaro, M. A., Karakas, A. I., García-Hernández, D. A., & Yong, D. 2012, A&A, 540, A44 (Link)

van Winckel, H. 2003, ARA&A, 41, 391 (Link)

Vassiliadis, E., & Wood, P. R. 1993, ApJ, 413, 641 (Link)

Ventura, P., Carini, R., & D'Antona, F. 2011, MNRAS, 415, 3865 (Link)

Ventura, P., & D'Antona, F. 2005a, A&A, 439, 1075 (Link)

—. 2005b, ApJ, 635, L149 (Link)

—. 2008, A&A, 479, 805 (Link)

—. 2009, A&A, 499, 835 (Link)

Ventura, P., D'Antona, F., Mazzitelli, I., & Gratton, R. 2001, ApJ, 550, L65 (Link)

Ventura, P., Di Criscienzo, M., Carini, R., & D'Antona, F. 2013, MNRAS, 431, 3642 (Link)

Villanova, S., & Geisler, D. 2011, A&A, 535, 31 (Link)

Villanova, S., Geisler, D., & Piotto, G. 2010a, ApJL, 722, L18 (Link)

Villanova, S., Piotto, G., Marino, A. F., Milone, A. P., Bellini, A., Bedin, L. R., Momany, Y., & Renzini, A. 2010b, IAU, 5, 326 (Link)

Wagoner, R. V., Fowler, W. A., & Hoyle, F. 1967, ApJ, 148, 3 (Link)

Ward, R. A., Newman, M. J., & Clayton, D. D. 1976, Astrophysical Journal Supplement, 31, 33 (Link)

Weigert, A. 1966, Z. Astrophys., 64, 395 (Link)

Werner, K., Heber, U., & Hunger, K. 1991, A&A, 244, 437 (Link)

Werner, K., & Herwig, F. 2006, PASP, 118, 183 (Link)

Werner, K., Rauch, T., & Kruk, J. W. 2005, A&A, 433, 641 (Link)

Werner, K., Rauch, T., Kruk, J. W., & Kurucz, R. L. 2011, A&A, 531, 146 (Link)

Werner, K., Rauch, T., Reiff, E., & Kruk, J. W. 2009, Ap&SS, 320, 159 (Link)

Wiescher, M., Kappeler, F., & Langanke, K. 2012, A&A, 50, 165 (Link)

Woodward, P. R., Herwig, F., & Lin, P.-H. 2015, The Astrophysical Journal, 798, 49 (Link)

Yong, D., Aoki, W., Lambert, D. L., & Paulson, D. B. 2006, ApJ, 639, 918 (Link)

Yong, D., & Grundahl, F. 2008, ApJ, 672, L29 (Link)

Yong, D., Karakas, A. I., Lambert, D. L., Chieffi, A., & Limongi, M. 2008a, ApJ, 689, 1031 (Link)

Yong, D., Lambert, D. L., & Ivans, I. I. 2003, The Astrophysical Journal, 599, 1357 (Link)

Yong, D., Lambert, D. L., Paulson, D. B., & Carney, B. W. 2008b, ApJ, 673, 854 (Link)

Yong, D., et al. 2014, MNRAS, 441, 3396 (Link)

Zamora, O., García-Hernández, D. A., Plez, B., & Manchado, A. 2014, A&A, 564, L4 (Link)